Characterising KMOS and Scaling Relations in the Rich Cluster MS0451.6-0305

Richard John Masters

Keble College, Oxford

A thesis submitted for the degree of Doctor of Philosophy
at the University of Oxford.

Hilary Term 2012

For Chris, John and Jess. Always for you guys...

Declaration

I declare that no part of this thesis has been accepted, or is currently being submitted, for any degree or diploma or certificate or any other qualification in this University or elsewhere. Except where explicit reference is made to the work of others, the work contained in this thesis is my own, and is not the outcome of work done in collaboration.

Richard Masters

(January 2012)

Acknowledgements

Firstly I would like to thank my supervisor Professor Niranjan Thatte, not only for giving me the opportunity and guidance to pursue a DPhil here at Oxford, but also the chance to attend this great institution for my undergraduate degree seven years ago. Equally, the support and tutelage of my supervisor Dr. Matthias Tecza since my undergraduate days has been invaluable and I am forever grateful for all of the time he has given up to help me through.

Huge thanks are owed to Professor Roger Davies for bringing me on board with the galaxy clusters project and giving me direction and invaluable guidance in pursuing this side of my Thesis, despite the busiest of schedules.

My advisors Dr. Ian Lewis (for my work on KMOS) and Dr. Ryan Houghton (for my work on galaxy evolution) are owed my deepest thanks for their constant enthusiasm and unending patience. I have learned so much and I could not have completed this work without either of you.

I would like to thank Dr. Bob Watkins and Andy Clack. Their years of experience and inhuman patience & endurance truly ensured the successful completion of the KMOS project.

Thanks to Phil Rees at the UK ATC for accommodating my visits during integration and testing runs of KMOS.

Many thanks to Fraser Clarke and Aprajita Verma for their patience and help during my week at Palomar Observatory with SWIFT and for many interesting discussions throughout the DPhil. Also to Dr. Tim Goodsall for giving my inspiration in instrumentation.

Thanks to Jane and Jenny for always greeting me with smiles during the earlier mornings in the department.

Dr. Lisa Fogarty and Henry Tillson have been the best office mates over the past couple of

years. The great discussions on academic & non-academic topics and mutual support have really helped keep me going. Thanks to all the Oxford astrophysics graduate students, researchers and faculty that I have worked or conversed with over the past three years. There a too many to name, but my time here would not have been the same without you all.

Thanks to my friends in the Keble MCR for their support and laughs over the past three years. I'd like to say a personal thanks, in no particular order, to AJ, Sameer, Ross, Dan G, Mandeep, Tom, Hannah, Gareth, Anbara, Jess, Rob and Jorick.

An enormous thanks to Leah for being so patient with me over the last year, for always understanding and for always being there. I don't know how to express how much it's meant to me.

Lastly and most importantly I would like to thank my family. Thanks to Nan and Grandad for helping me whenever I needed somewhere to stay, for their amazing support during the final stages of the Thesis and for their patience in not seeing me for months at a time! I'll be forever grateful.

Mum, Dad and Jess. Thank you isn't enough. Your encouragement, support, love and understanding have kept me going throughout all of my endeavours. It's all for you guys.

Abstract

This Thesis contains two parts. **Part I** details my work on KMOS, a new instrument for the VLT and **Part II** details my research on scaling relations for the massive galaxy cluster MS0451.6-0305.

Part I: The K-Band Multi-Object Spectrograph (KMOS) is a new near infra-red (NIR) instrument to be installed at the Very Large Telescope (VLT). KMOS is capable of spatially resolved kinematics via 24 deployable integral field units (IFUs), each with a 2.8″ field of view. I describe my contribution to the construction and optical characterisation of the spectrograph modules and instrument as a whole.

Part II: GMOS-N spectroscopy has been used to obtain velocity dispersions (σ) and archival HST photometry has been used to determine the effective radii (R_e) & average surface brightnesses within R_e ($\langle I \rangle_e$) of 26 confirmed cluster members of MS0451.6-0305 at $z = 0.55$. The Kormendy Relation, Faber-Jackson Relation and Fundamental Plane have been produced for the cluster and have been compared to the results for a local reference sample in Coma. GMOS-N g' and r' band photometry has also been used to produce a Colour-Magnitude Relation for MS0451.6-0305.

It is found that the KR and FJR disagree at the 2.1σ level with respect to luminosity evolution since $z = 0.55$. When correcting for size-evolution (SE), the magnitude offsets agree and are consistent with passive evolution of the galaxy stellar populations from a single burst of star formation $9.8^{+4.5}_{-1.7}$ Gyrs ago or $z = 1.7^{+\infty}_{-0.6}$. The median offset in the FP relation for the SE corrected data is also consistent with this formation epoch. Evidence is found for the evolution of the FP tilt in MS0451.6-0305, where it is shown to be steeper than that of the Coma FP, when expressed as a relation between galaxy mass and M/L.

Contents

I Characterising KMOS **1**

1 Introduction **3**
1.1 Astronomical Spectroscopy . . . 3
1.2 KMOS Overview . . . 8
1.2.1 Full System Description . . . 9
1.2.2 KMOS Subsystems . . . 9
1.2.3 The Pick-Off Module . . . 9
1.2.4 The IFU Modules . . . 11
1.2.5 The Spectrographs . . . 14
1.2.6 Housekeeping Systems . . . 14

2 The KMOS Spectrographs **17**
2.1 The Spectrographs and their Sub-Assemblies . . . 17
2.1.1 Optical bench/structure . . . 19
2.1.2 Fold Mirror . . . 20
2.1.3 Collimator . . . 21
2.1.4 Gratings and the grating exchange . . . 22
2.1.5 Camera barrel . . . 25
2.1.6 The Hawaii-2RG detectors . . . 28
2.2 The Oxford Facility . . . 30
2.2.1 Design and Construction of the Test Facility . . . 30
2.2.2 Thermal modeling . . . 32
2.2.3 The Control Setup . . . 39
2.3 Test Setup at the UK ATC . . . 47
2.4 Summary . . . 49

3 KMOS testing **51**
3.1 The Oxford Test Results . . . 53
3.1.1 Mechanical Checks . . . 54
3.1.2 Best Focus Determination . . . 54
3.1.3 Spectrograph PSF . . . 56
3.1.4 Determination of central wavelengths and R at λ_c . . . 60
3.2 Edinburgh ATC tests . . . 68
3.2.1 Mechanical tests . . . 68
3.2.2 The KMOS spectrograph focal plane and PSF variation . . . 70

3.2.3 KMOS Throughput . . . 76
3.3 Hyper-sampling of the KMOS spectral PSF . . . 78
3.3.1 Using Spectral Flexure . . . 79
3.4 Observing and Science with KMOS . . . 82
3.4.1 Configurations and Observing Modes . . . 82
3.4.2 Reconstructing the Data . . . 82
3.4.3 Calibrations . . . 83
3.4.4 Sky subtraction . . . 84
3.4.5 Science Cases for KMOS . . . 86
3.5 Summary . . . 88

II Scaling Relations in the Rich Cluster MS0451.6-0305 89

4 Introduction 91
4.1 A Brief Introduction to Galaxies and Clusters . . . 91
4.1.1 Scaling Relations . . . 93
4.2 The Gemini/HST cluster project . . . 95
4.2.1 X-ray selection of clusters . . . 95
4.3 MS0451 - a rich galaxy cluster at $z = 0.55$ . . . 97

5 GMOS/HST reductions and analysis 99
5.1 The Data . . . 99
5.2 GMOS data reduction . . . 104
5.2.1 GMOS imaging . . . 104
5.2.2 Spectroscopic Reduction . . . 109
5.3 Integrated Photometry . . . 110
5.4 Determining velocities and velocity dispersions . . . 111
5.5 Extracting kinematics . . . 112
5.6 HST imaging . . . 119
5.6.1 HST Reduction and *MultiDrizzling* . . . 119
5.7 R_e and $\langle I \rangle_e$ Determination . . . 121
5.7.1 Preparing the galaxies . . . 121
5.7.2 The COG Algorithm . . . 122
5.7.3 PSF creation . . . 124
5.8 HST Photometric zero-points, corrections and conversions . . . 126
5.8.1 Magnitude systems . . . 126
5.8.2 Cosmological corrections . . . 127
5.8.3 Photometric Errors . . . 129
5.9 The Local Reference Sample . . . 130

6 GMOS/HST Results 133
6.1 Ensemble characteristics of MS0451 . . . 133
6.2 Galaxy Scaling Relations . . . 135
6.2.1 The Colour-Magnitude relation (CMR) . . . 135
6.2.2 The Kormendy and Faber-Jackson Relations . . . 138

6.3 The Fundamental Plane 144

7 Discussion and Conclusions **155**
7.1 The CMR 155
7.2 The Kormendy Relation and Faber-Jackson Relation 156
7.3 The Fundamental Plane 156
7.4 MS0451 in the context of Previous Gemini/HST Rich Cluster Studies 158
7.5 Caveats 160
7.5.1 Outliers 160
7.5.2 Colour gradients 161
7.5.3 Sample effects 161
7.6 Summary and Future Work 163

Bibliography **165**

List of Figures

1.1 3D datacube - dimensions from KMOS specification. 5
1.2 Illustrating the decomposition of a 2D field into slices 7
1.3 Full optical path through one pick-off unit and IFU. 8
1.4 3D CAD model of one pick-off unit. Image courtesy Phil Rees, UK ATC. 11
1.5 KMOS Pick-Off module. 12
1.6 Example IFU and image slicer stack. 12
1.7 KMOS at the ATC. 15

2.1 A fully populated Science Grade Spectrograph module. 1.) Fold mirror assembly, 2.) Collimator, 3.) Grating exchange mechanism, 4.) Camera barrel, 5.) Detector focus stage, with detector inside housing. The spectrograph module sits on the cold plate. The brass resistors were used for plate heating and the yellow wires were linked to PT100 resistive temperature sensors. 19
2.2 The fold mirror sub-assembly and its alignment 21
2.3 The collimator sub-assembly and its alignment 23
2.4 The grating exchange wheel. 24
2.5 Wavefront map of Iz grating. 24
2.6 On-axis aberrations to the wavefront as a function of axis rotation 27
2.7 Hawaii-2RG engineering grade detector and kinematic mount. 29
2.8 CAD model of a single KMOS spectrograph module in the end-cap chamber. 31
2.9 Schematic of the test rig thermal model. 34
2.10 Geometries involved in defining the view factors for the radiation transfer model. . . 35
2.11 Schematic view of the control systems for the Oxford test. 40
2.12 Left: Copper cooling loop attached to underside of cold plate. Right: Radiation shield over spectrograph module. The aluminium cylinder in the foreground is the control pot, containing a temperature sensor to ensure liquid LN2 was not passing through the copper cooling loop. 41
2.13 Plots of the thermal data during the Oxford testing phase. 44
2.14 KMOS test source and fiber baffle system. 46

3.1 Central pixel flux against focus position for KMOS arc line and model PSF. 55
3.2 Gaussian fits to the spectral and spatial cuts to an arc line. 56
3.3 False-colour images of an arc line at best-focus and out of focus. 57
3.4 Achievable spatial PSF σ for the central arc line in the H-band Oxford data. 59
3.5 A representative sample of the centre-field focus positions across the KMOS I/z, YJ, H and K grating configurations. 60

3.6 H-band argon spectrum through the central pixel of the central slitlet in the full KMOS optical train. . . . 67
3.7 Grating mechanism repeatability measurements. . . . 69
3.8 Spatial and spectral flexure plots 70
3.9 A false colour image of the full H-band focal plane 71
3.10 Focal plane contours and residual plots. . . . 73
3.11 Effect on surface profile of a reversal in sign of curvature. . . . 75
3.12 The residuals for the corrected focal plane - H-band. . . . 76
3.13 K-band throughput for Arm 12. Adapted from a plot, group email from Gert Finger. 77
3.14 Line spread profiles at wavelengths in he H-band for one slitlet. . . . 81
3.15 Data-cube reconstruction. Reproduced from Davies (2007). . . . 85

4.1 X-ray surveys and cluster project sample 96

5.1 HST ACS WFC and GMOS-N chip layouts. . . . 100
5.2 False colour image of MS0451.6-305. . . . 105
5.3 GMOS r'-band scttered light removal 107
5.4 Example spectra for Galaxy I.D. 1931. . . . 113
5.5 GH fit to GMOS arc line and TF for convolution with CFLIB stellar templates. . . . 115
5.6 σ, σ_λ and the even GH parameters as a function of λ. . . . 116
5.7 Example of source contamination and COG fit. . . . 125
5.8 MGE approximation and residuals to COG fits. . . . 125

6.1 Histogram of the V_{los} of the confirmed cluster members of MS0451. . . . 135
6.2 The $g' - r'$ vs r' CMR for MS0451 136
6.3 $g' - r'$ colour as a function of projected cluster-centric distance. . . . 137
6.4 The Kormendy and Faber Jackson Relations for MS0451 142
6.5 The BC03 and M05 stellar population model results 144
6.6 The Fundamental Plane for MS0451 152
6.7 FP residuals as a function of cluster-centric distance (projected). . . . 153

7.1 FP plots for Rich Clusters at $z = 0.28, 0.8 - 0.9, 1$. . . . 159

List of Tables

2.1 Fold mirror sub-assembly alignment data for one spectrograph module 21
2.2 Collimator sub-assembly alignment data for one spectrograph module. The primary tolerance is on the spherical radius at ±0.5%, or ±10.4mm. 23
2.3 KMOS calculated (expected) spectral properties and grating properties. 25
2.4 Detector specifications, adapted from Finger et al. (2004) 30
2.5 Parameters used for thermal calculations 38

3.1 KMOS Image Quality Requirements 53
3.2 KMOS spectral requirements and measured values 63
3.3 Expected & Measured Spectral FWHM and R (H-band - Oxford tests). 64
3.4 Measured Spectral FWHM and R across detector (H-band - Edinburgh tests - with out of specification L6 and collimator). 65
3.5 Measured Spatial FWHM across detector (H-band - Oxford tests). 66

5.1 Summary of HST ACS F814W imaging data 100
5.2 GMOS-N instrumental setup. 101
5.3 Details of the GMOS-N raw imaging data in the r' and g' bands. 103
5.4 Details of the GEMINI/GMOS imaging standard stars 103
5.5 Overview of cluster data. 131

6.1 KR and FJR parameters. 143
6.2 FP parameters. 150

7.1 Summary of Fundamental Plane coefficients across the Gemini/HST Cluster Project 158

Part I

Characterising KMOS

Chapter 1

Introduction

The K-band Multi-Object Spectrograph (KMOS) is a new instrument to be installed at the Nasmyth focus of the Very Large Telescope (VLT) UT 2 in Paranal, Chile. Summarising in one sentence:

KMOS is a multi-object spectrograph, capable of spatially resolved spectroscopy of 24 simultaneous targets via deployable image-slicing integral field units, operating in the 0.8-2.5 μm spectral range.

To describe the case for such an instrument and the instrument itself, we must first briefly discuss the field of astronomical spectroscopy and the instrumentation used.

1.1 Astronomical Spectroscopy

The analysis of spectra is a fundamental aspect of modern astronomy. The process has traditionally involved a setup involving light from an object sent through a slit, along one spatial dimension of the source, or collected over a small aperture and into a standard spectrograph comprising of a collimator, dispersing element, camera and detector. The objects I am concerned with in this thesis are galaxies and the spectra from these objects allow us to use certain markers in the form of absorption and emission features of the chemical constituents to measure properties such as relative chemical abundances to infer star formation histories and velocity dispersions & rotation curves to

indicate dynamical masses. Of course, the method of limiting the spectra over an extended source in one spatial dimension results in the loss of a large amount of information on the kinematics and composition of these stellar systems. For example, in determining rotation curves the alignment of the slits must be along the desired axis to a high degree of precision. Misalignment can lead to substantial error. Velocity dispersions derived from these limited cuts through the galaxies must be extrapolated across the rest of the object and thus require certain assumptions about the distribution of the stellar or interstellar gas motions.

It is possible to move these one dimensional slits across the projected face of the object to improve the spatial sampling, in essence a spatial scanning technique, creating a *datacube* with two spatial dimensions and one spectral dimension. However, there is a practical limitation on the achievabl signal to noise (S/N) using this method due to exposure time overheads and availability of facilities. Variation in atmospheric transmission between exposures can be significant and there is still a limit to the accuracy with which the slit(s) can be placed and aligned with respect to an object. The problem of alignment can be removed by scanning the object in wavelength via a Fabry-Perot interferometer (Monnet, 1984). This allows multiple narrow band images to be taken of the object or several objects in a field of view, reconstructing a spectrum. However, this is again limited by exposure overheads and so reduces the available spectral resolution or wavelength range - potentially losing features for analysis. These points highlight two main areas when considering detailed observations of large numbers of (potentially faint) objects:

- The requirement for higher observing efficiency (as VLT costs are ~ 1€/second)
- Homogeneity in the final datacube - of increased importance in the near infrared (NIR) due to the strong temporal variation in the sky background in addition to atmospheric transmission variation.

To address these problems, integral field spectrographs (IFS) have become the tools for spatially resolved spectral analysis. In essence, an IFS samples a 2D field of view and obtains a spectrum for each resolved element in a *single exposure*. This produces a datacube, as with the previous methods. However, the field is spatially sampled in more homogeneous fashion, as is the spectral dimension - achieving resolutions identical to long-slit spectra. An example of a datacube is shown

in Figure 1.1, showing 14 spatial slices of a 2D field, projected in λ displaying different features at different wavelengths.

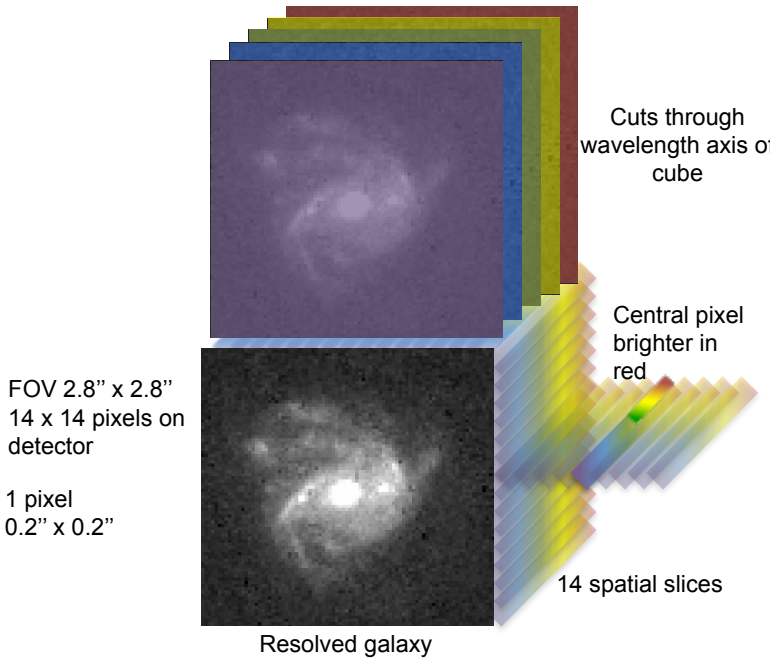

Figure 1.1: 3D datacube - dimensions from KMOS specification.

Instruments capable of IFS operation include SINFONI (Thatte et al., 1998), VIMOS (Le Fevre et al., 2000) and FLAMES (Pasquini et al., 2000) on the VLT, GMOS-N/GMOS-S on the Gemini North and South telescopes (Davies et al., 1997) and OSIRIS on Keck (Larkin et al., 2006) to name a few. Current IFS use three primary methods of spatially sampling the field of view (FoV). These are via image slicing mirror stacks, optical fibers or lenslet arrays (or possibly combinations of these).

- *Lenslet array*

A lenslet array IFS employs small lenses arranged to image sub-fields across the FoV of the telescope. Each pupil is then dispersed and the spectra recorded. The arrangement of the sub-fields is such that the dispersed spectra from each do not overlap. The problem of spectral overlap is also reduced by limiting the wavelength ranges with filters. The rearranged sub-fields must also fit their spectra onto a square detector. This ultimately limits the spectral range if each element

is to be matched to create a coherent datacube. The technique was pioneered in the TIGER instrument (Bacon et al., 1988) and a recent example of a lenslet-array IFS is OSIRIS on Keck II (Larkin et al., 2006).

- *Fibers*

Fiber fed IFS systems consist of bundles of fibers, as tightly packed arrays or single feeds, that can usually be positioned anywhere within the FoV of the telescope. The flexibility in these fibers then allow the outputs to be arranged along the input slit of a long-slit spectrograph. The limitation of this setup include the lossy nature of the fibers at certain wavelengths (particularly in the NIR) and the discrete nature of the sampling caused by the finite thickness of the cladding of fibers (although this can be overcome by employing lenslets to direct sub-fields into the fibers). A great advantage with this method, however, is the ability to sample many different sources and to redeploy the sub-fields. An example of a fiber-fed IFS is FLAMES on the VLT (Pasquini et al., 2002).

- *Image Slicers*

Image slicers are formed of a stack of rectangular mirrors. These slice up the FoV into several slitlets and each element is sent out to a pupil array formed of mirrors or lenses. The pupil array rearranges these slitlets into a pseudo-long-slit for input into a standard spectrograph (see Figure 1.2). This type of integral field unit (IFU - the field sampling component) allows contiguous placement of field-sampling elements and has a high efficiency across its operating wavelengths. An example of an image slicing IFS is the Oxford SWIFT instrument at Palomar Observatory (Thatte et al., 2010b).

The ability to acquire these datacubes has proven invaluable for the detailed investigation of many objects. A particularly successful series of investigations has been carried out using the SAURON IFS (lenslet configuration - (Bacon et al., 2001; de Zeeuw et al., 2002), with over eighteen key publications(e.g., Bureau et al., 2011). However, to gain a true understanding of the common (and apparently not so common) processes occurring throughout the Universe, large statistical samples are crucial. Multi-object capability is key to making the most out of the collecting power

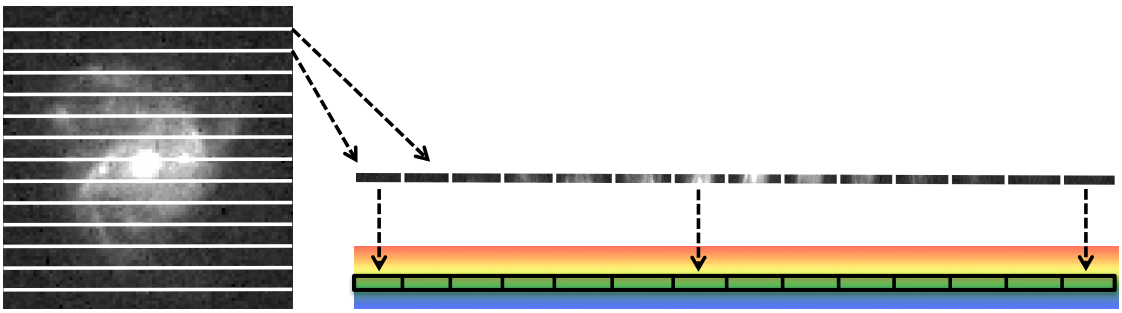

Figure 1.2: Illustrating the decomposition of a 2D field into slices, re-imaged by a pupil mirror array into a pseudo-long-slit.

of 8m class telescopes and the limited observing time available for a project. One of the first methods used in undertaking multi-object spectroscopy (MOS) involved the use of slit masks, still used regularly today. These are plates (originally metal, but now also carbon fiber) that have slits cut into them at the positions of the objects of interest within the telescope FoV. Their coordinates are measured from previous images of the field. Many objects can be analysed with a mask, but closely packed sources are difficult to separate and a configuration change requires a whole new mask to be made and reinstalled at the telescope focal plane. They also, of course, lack the spatial resolution and scanning capability for datacube reconstruction.

The most successful method of MOS, in terms of large statistical surveys, has been fiber-fed spectroscopy. The close packing of positionable optical fibers over sources and the ability to route their outputs through regular spectrographs has made extremely large redshift surveys possible. Originally, the fibers still required plate-masks to be produced for positioning at the telescope focal plane. However, instruments such as the two degree field (2dF) facility at the Anglo-Australian Observatory (now the Australian Astronomical Observatory) pioneered automated fiber positioning over the full telescope FoV via robot arm deployment (Lewis et al., 2002). The ability to allocate a set of fibers to sky while simultaneously observing targets is also a key advantage of fiber MOS instruments, to help improve the signal to noise (S/N) of the spectra through accurate background estimation and the removal of telluric features. Again, the limitations of the discrete spatial sampling of fibers and their lossy nature at certain wavelengths has made them less than ideal for more detailed 3D studies of many sources at once.

There is a need for spatially resolved information in the form of datacubes for many objects

at once or over the course of an observing run and the need for fully deployable IFUs with high throughput in the NIR to study faint and distant objects. To fill this gap a multi-object, image slicing integral field spectrograph is required. This has been addressed in the form of KMOS (Sharples et al., 2010). The exact requirements on such an instrument were informed by the science programs foreseen to be carried out with such an instrument (Lehnert et al., 2003). A discussion of some of the science cases is given at the end of the KMOS sections of the thesis.

1.2 KMOS Overview

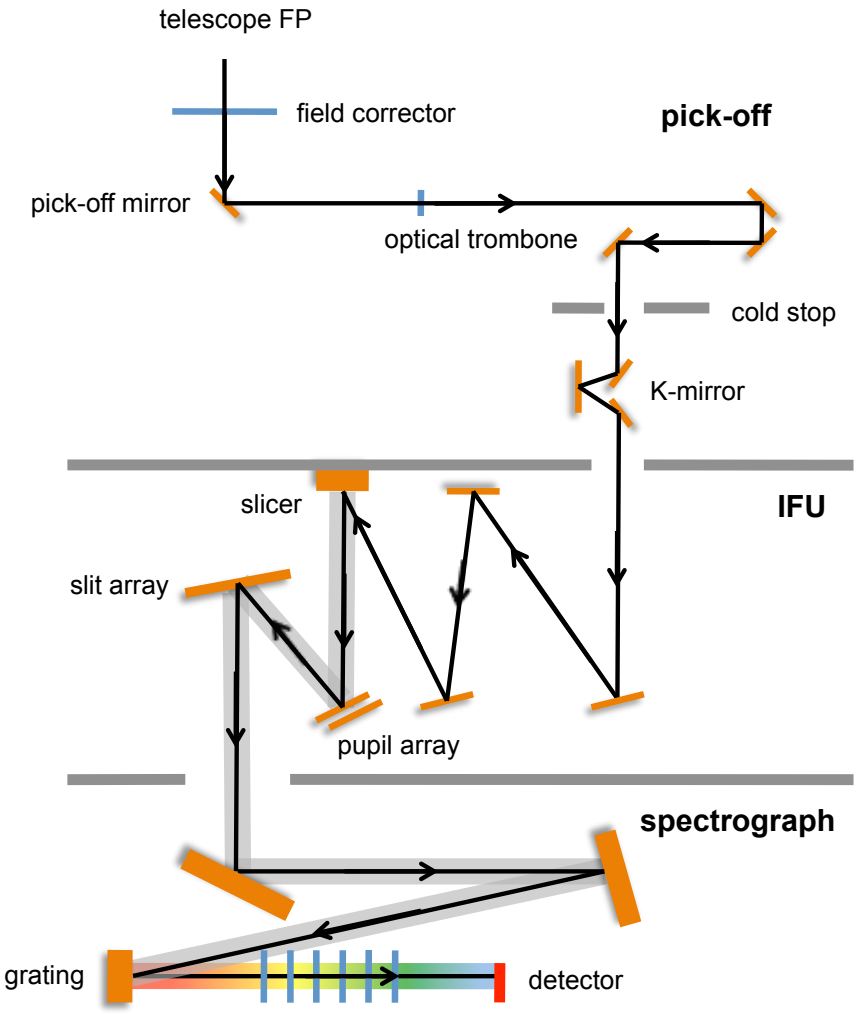

Figure 1.3: Full optical path through one pick-off unit and IFU.

1.2.1 Full System Description

KMOS consists of 24 fully-deployable robot arms, each able to direct a $2.8'' \times 2.8''$ field to one of 24 image slicing IFUs. Each IFU splits its field into 14 slices, which are then reformatted into pseudo-long-slits for input into a standard spectrograph. There are three spectrograph modules, each fed by 8 IFUs. The size of the sliced field and the rearrangement of the slitlets leads to a spatial resolution of $0.2''$, integrated over $0.2''$ in the spectral direction. This enables better than Nyquist sampling of the median seeing PSF of $\sim 0.5''$-$0.7''$(across the operational wavelength range) at Paranal (Gilmozzi, 1999). The operational wavelength range is 0.8 to 2.5μm, split across I, z, Y, J, H and K bands. These are selectable through one five reflection gratings and corresponding filters (split into gratings covering I/z, Y/J, H, K and HK at lower spectral resolution). Due to the operating wavelength range, where thermal background from room temperature sources can be overwhelming, KMOS is operated in a cryogenic environment, under high vacuum.

1.2.2 KMOS Subsystems

KMOS is split into three main subsystems. These are the pick-off module, the integral field units (IFUs) and the spectrographs (containing the detector subsystems). The 24 deployable IFUs, slicing each sub-field into 14 slits results in 336 separate optical paths. So, because of such a complex arrangement, these modules have been designed to be independently constructed, tested and adjusted prior to integration into the full instrument[1]. The full optical train through one arm, IFU and spectrograph is displayed in Figure 1.3. I will now detail these modules and highlight their key capabilities.

1.2.3 The Pick-Off Module

The KMOS pick-off module contains 24 mechanical arms that can be freely positioned to select sub-fields in the full $7.2'$ Nasmyth field of view of a VLT telescope. The FoV is modified by a field corrector lens to produce a flat and telecentric focal plane for the pick-off units to probe.

Each arm contains an elliptical, gold coated pick-off mirror orientated at 45° to the focal plane,

[1]The logistics of the modular KMOS project management are detailed in Rees et al. (2008).

producing a circular sub-field when projected onto the FoV, oversized to contain a $2.8'' \times 2.8''$ square. This redirects the target beam through a collimating lens, off three other fold mirrors (a trombone configuration - with the first surface being a roof mirror on the same rail as the pick-off mirror) that send the beam down through a cold stop in the arm support shaft (see Figures 1.3 & 1.4). To maintain the distance between the lens and the pupil at the cold stop, (and thus the optical path length for each arm) the roof mirror-lens and the roof mirror-first fold mirror distances vary as the arm moves. Past the cold stop is a K-mirror system for field rotation and direction of the output beam through the filter wheel, where the intermediate image field is available to the IFU subsystem after passing through the appropriate filter. The nominal outputs of the each pick-off unit are telecentric with f/16.67. The plate scale varies with wavelength over the range 624.9 μm per arcsecond at 0.84 μm to 615.9 μm at 2.5 μm. The filter thickness also varies between wavebands to ensure that each central wavelength shares a common focal point (limiting chromatic aberration to effects within each band). The fully-populated pick-off module with the calibration sphere in the centre is shown in Figure 1.5. The design and testing of the arms is detailed in Bennett et al. (2008).

The arm layout can be seen in Figure 1.5. The arrangement of the arms is split over two levels, with twelve arms in each. This is due to space and manoeuvrability constraints on the pick-off units. Each level of arms has 100 % coverage of the field. The upper level is set 20mm above the telescope focal plane and the lower level is set 20mm below the telescope focal plane. The ring of arms covers a circular area of diameter 540 mm. There are two cryogenic stepper motors contained in each unit, one for rotation and one for radial insertion into the field. The form of an arm is displayed in Figure 1.4, highlighting the key optical and mechanical components. Collision prevention has been built in at various levels of control. Mechanically, there is a system to physically stop the arms colliding by causing a cut-off in arm power should they touch (completing a control circuit that then switches off arm power). Position tracking is built into the software at the engineering control level and at the higher level user interface.

Calibration through each arm is possible via an integrating sphere, 180 mm in diameter, situated on the central instrument axis, offset 137 mm from the input focal plane on the opposite side of the

roaming plane of the arms. Light from the calibration sources in a primary integration sphere (70 mm diameter), located externally, reaches the internal integration sphere via a gold coated light pipe, 900mm long, along the instrument axis. The numerical aperture of the light passing through the pipe is restricted to <0.74, via a compound parabolic concentrator, to ensure a narrow beam hits the top of the internal integrating sphere. The sphere has 24 ports that send the homogeneous output up to mirrors located 50mm above the input focal plane, and just outside the telescope focal plane - creating a circle of diameter 270mm. The narrow spread of the input beam ensures that all ports see the light-pipe at the same level. The pick-off units can be positioned underneath these mirrors for spectral calibration and flat-fielding. A full analysis of the Pick-Off module design is given in Clark et al. (2007).

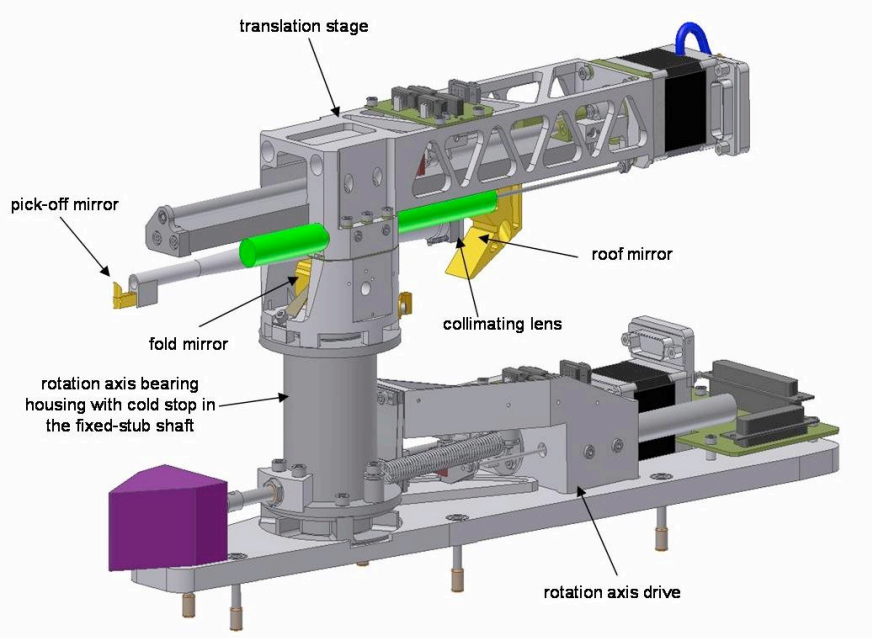

Figure 1.4: 3D CAD model of one pick-off unit. Image courtesy Phil Rees, UK ATC.

1.2.4 The IFU Modules

Each pick-off unit sends its output beam to an individual integral field unit (IFU). The principal function of each IFU is to reformat the input 2.8″ x 2.8″ field (1.74mm x 1.74mm) into a pseudo long-slit of dimensions 0.56″ x 39.2″ (0.35mm x 31.5mm) to form part of the entrance slit of a

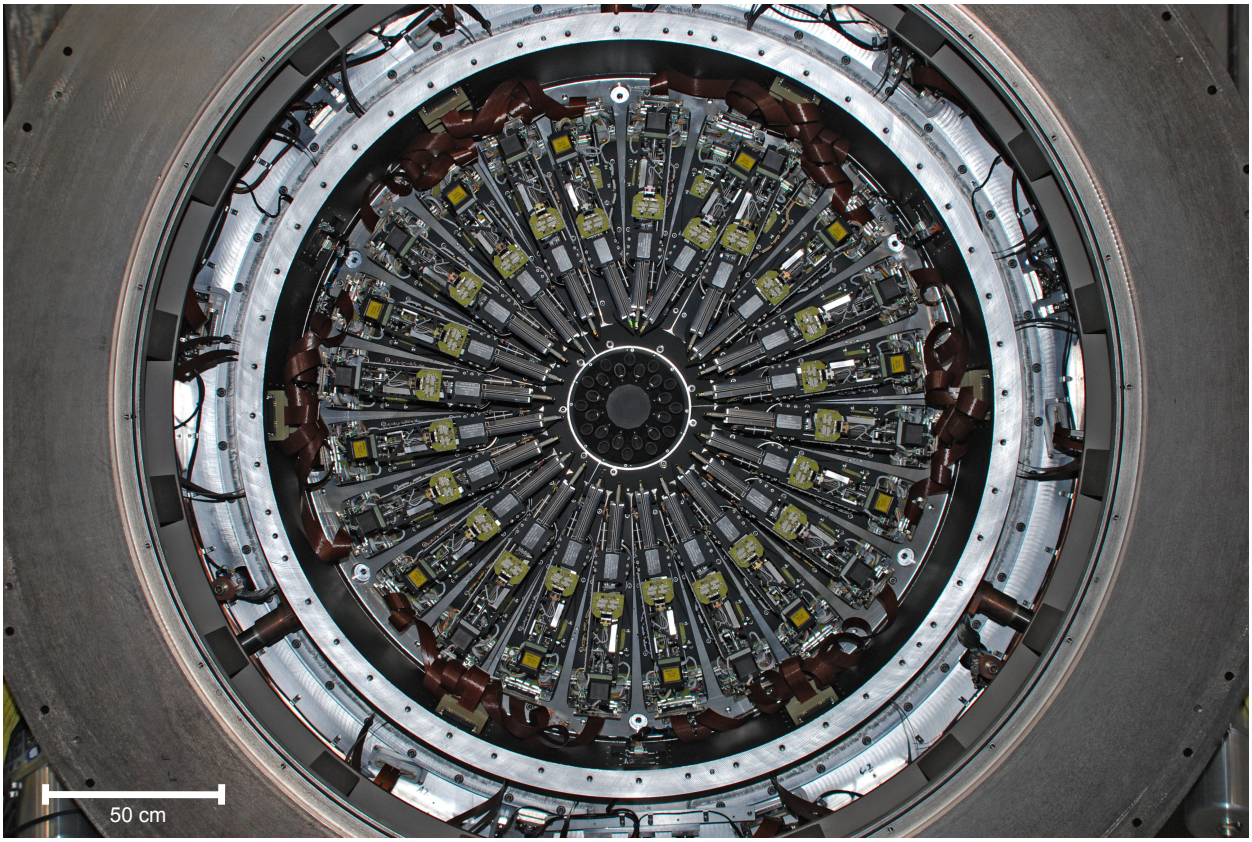

Figure 1.5: KMOS Pick-Off module. Image courtesy Phil Rees, UK ATC.

spectrograph module. There are 8 IFUs allocated to each spectrograph - creating a full entrance slit for each of $\sim$ 252.6mm x 0.35 mm.

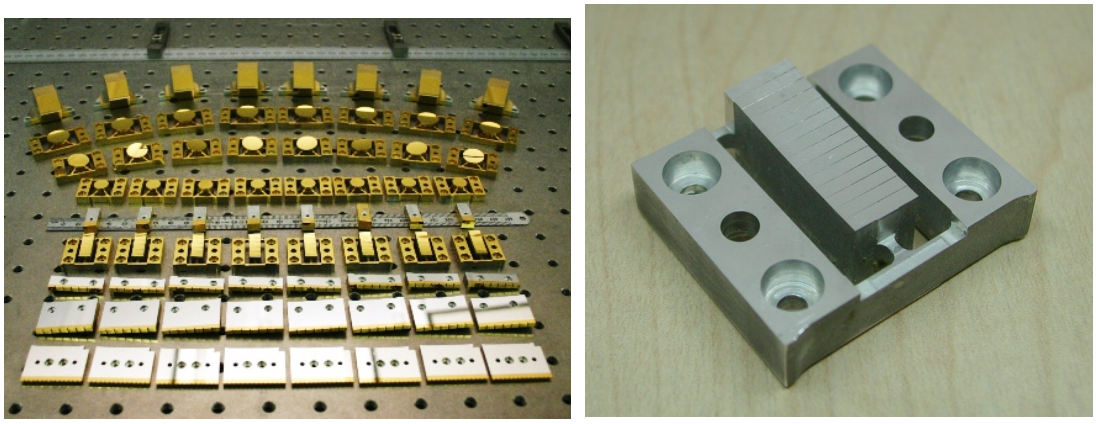

Figure 1.6: Example IFU and image slicer stack. Images adapted from Rees (2007)

The IFUs were designed and produced by the Centre for Advanced Instrumentation (CfAI) at

Durham and are based on the Advanced Image Slicer concept developed there (Content, 1998). An IFU assembly is in two main parts: the fore optics and the image slicer. The fore optics section re-images the input field from the pick-off output and produces an image onto the image slicer. The image slicer then cuts the image into fourteen slitlets and rearranges these into a pseudo-long-slit for input into a spectrograph module. The exploded view of the components of 8 IFUs is shown in the left image in Figure 1.6. From top to bottom; there are three fore optics mirrors, an image slicer, the top and the bottom levels of the pupil array and the slit array. The right image in Figure 1.6 shows a close up of an uncoated aluminium image slicer stack, showing the 14 slices. Form errors in the mirror surfaces across a full IFU unit are in the range 10-15 nm, with surface roughnesses <10nm.

The fore optics add an anamorphic magnification to the beam. The spectral direction is magnified to 2.8 times the size of the spatial direction, with an actual magnification of 4 spatially and 11.2 spectrally. When the output of the IFU at this ratio enters the spectrograph and reflects off the gratings, the beam is anamorphically magnified again and the spectral magnification reduces to 2 times the spatial size. This ensures Nyquist sampling of the spectral point spread function (PSF) once incident on the detector, as the slitlet image covers 2 pixels. The fore optics section is made up of two aspheric re-imaging mirrors and a third re-imaging mirror, defined by Zernike polynomials[2].

The image slicer is constructed of a monolithic slicing array (or a mirror stack), made of diamond turned aluminium mirrors (spherical), coated in gold and is fourteen slices high. The techniques in the surfacing of the mirrors was developed initially as part of the Gemini Near-Infrared Spectrograph (GNIRS) project (Dubbeldam et al., 2000). Each slice is oriented differently to send their output beams to one of fourteen pupil mirrors. They are also oversized to accommodate any iterated misalignment or potential movement of components over the lifetime of the instrument. The field hitting the slicer stack is 7mm in the spatial direction and 19.6 mm in the spectral dimension as a result of the anamorphic magnification by the fore optics.

The pupil mirrors are arranged in a two level array, each containing 7 slices. Each pupil mirror sees one slice and isotropically demagnifies by a factor of 4 & re-images the beam onto its

[2]Explained in section2.1.5.

corresponding mirror in a slit-mirror array, located in the focal plane of a spectrograph module and comprising of 14 toroidal facets along the full slit. These slit mirrors are toroidal to account for astigmatism present in the arm images formed near the pupil mirrors. The f-numbers in the spectral and spatial directions as the beam leaves the IFU are f/44.8 and f/16 respectively.

1.2.5 The Spectrographs

There are three identical spectrographs. Each is fed by 8 pick-off units via 8 IFUs. These modules were the focus of my work on KMOS. The optical layout involves a standard spectrograph setup. A 254mm entrance slit is formed by a combination of eight slit-mirror assemblies from the IFUs and enters through the bottom of the optical bench. A fold mirror, set at 45° to the plane of the bench redirects the input beam to a spherical collimator mirror. This sends the collimated beam to one of five reflection gratings. The dispersed output from the grating then passes through a six lens camera onto a 2k×2k pixel infrared array detector. In each spectrograph there are 112 slitlets that make up the entrance slit (14 slices from each IFU over 8 IFUs) and there are 14 spatial pixels (spaxels) per slice. This provides 1568 individual spectra per spectrograph and 4704 in the whole instrument. The spectrograph components are described in more detail (optically and mechanically) in the following Chapter.

1.2.6 Housekeeping Systems

The full instrument sits inside a cryostat containing an aluminium cold bench, conductively linked to the KMOS modules. The cooling is achieved and maintained via Gifford-McMahon cryocoolers (described in more detail in Section 2.3). The cryostat window is composed of the field corrector lens. The housekeeping electronics are situated in the Cable Co-Rotator (CACOR) section that is secured to the instrument platform and does not rotate with the Nasmyth mount. The compressors for the cryocoolers are also fixed to the instrument platform. The external setup of KMOS can be seen in Figure 1.7. The aluminium cryostat is seen in the centre, the CACOR is the red assembly containing a light grey electronics rack. In the fully populated instrument, the centre of the CACOR is populated by three electronics racks, each responsible for the control of a third of the instrument

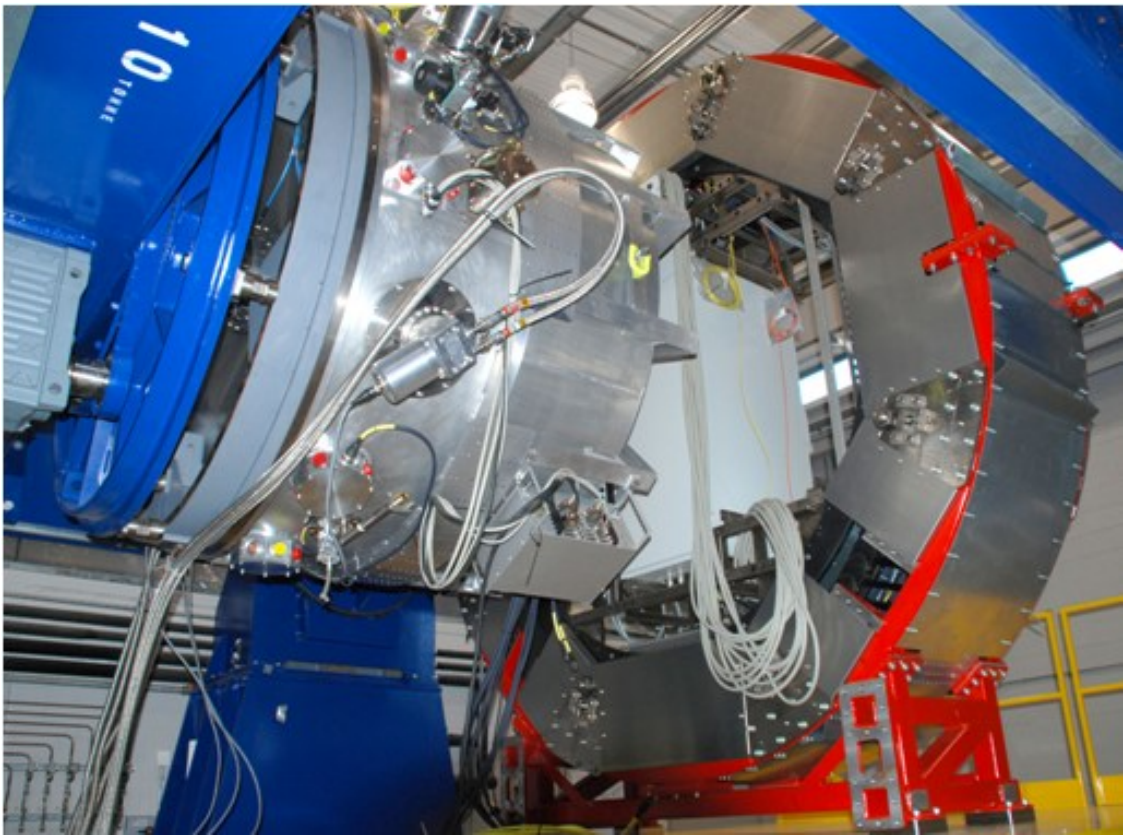

Figure 1.7: KMOS at the ATC.

(one spectrograph, fed by 8 arms). Each rack contains thermal control units, power units for the detectors and optical relays for image readout (similar to the setup described later in Section 2.2). They also control other housekeeping systems such as the LN_2 exhaust heater, window defogger (for the field window), flow sensors and proximity switches for the robot arms. The instrument is suspended on a rig (blue assembly) mimicking the Nasmyth mount at the VLT UT2. Controlled rotation is possible.

Chapter 2

The KMOS Spectrographs

The KMOS project team is composed of a consortium of institutes. The UK Astronomy Technology Centre (UK ATC) in Edinburgh have been responsible for the construction and testing of the pick-off module and the robot arms. It is also where the full instrument is integrated and full testing is conducted prior to delivery. The Centre for Advanced Instrumentation (CfAI) at Durham has been primarily responsible for the design and construction of the IFUs. The Max Planck Institut Für Extraterrestriche Physik (MPE) in Garching, Germany has been responsible for the reduction packages. The Ludwig Maximilian University of Munich (LMU) has designed and constructed the electronics & control software. The Optical Instrumentation Group in Oxford has been responsible for the spectrograph modules.

2.1 The Spectrographs and their Sub-Assemblies

For any consortium effort on a large instrument, such as KMOS, independent verification of the instrument's sub-assemblies is crucial in determining any problems with the design or manufacture of parts. The wavelength range and precision of operation of KMOS required a low contamination, high vacuum, cryogenic environment, thus increasing the need for such verifications. The design of the three identical spectrographs was carried out in Oxford. The assembly, integration and testing (AIT) of these modules and their sub-assemblies was my responsibility. A shorter overview of the Oxford tests can be found in Masters et al. (2010), although much of the detail and results is

updated here.

The spectrograph units were expected, as part of the design specifications, to meet certain image quality, stability and repeatability requirements, shown in Table 3.1 (next Chapter). To ensure this, verification of the individual modules was required prior to and after their integration with the front end IFU/pick-off unit. Our objectives in Oxford were to assemble the modules and to design and carry out tests to ensure that they were within the specifications. This section provides detail on the spectrographs and their components. I discuss each sub-assembly, its optical properties, mechanical properties, design modification decisions, alignment processes and individual verification of quality. I then go on to describe our processes in constructing and operating the test facility, the requirements for testing the full modules and the optical tests carried out. The results from these tests are then presented in the context of the spectrograph design requirements and as guides for future testing of instrumentation under similar conditions, with similar facilities.

As a note for the remainder, there were two versions of spectrograph that were constructed as part of the testing and development phase. These were the Engineering Spectrograph (ES) and the Science Grade Spectrographs (SGS). The ES was a reduced version of the final spectrograph assemblies and contained an alternative material fold mirror, uncoated collimator, single grating and engineering grade detector. The SGS modules were the finalised assemblies containing the full compliment of coated optical surfaces and engineering or science grade detector. A fully populated SGS module is shown in Figure 2.1. The optical bench/baseplate sits on a cold plate for conductive cooling during the Oxford tests (explained in Section 2.2). The sub-assemblies can be seen and from 1-5 we have the fold mirror, collimator, grating exchange, camera and the focus mechanism/detector housing respectively. The yellow cables are for temperature sensors and the temporary brass resistors on the plate are for controlled warming of the module (again see 2.2). A stiffening frame can be seen arching behind the collimator and focus mechanism.

The mass budget for each fully populated spectrograph was initially 100 kg. This was revised to a total mass of 310 kg for all three during the design reviews. The final measured mass for all three modules is 336 kg. Although this is over budget, it does not affect mechanical operation. The total mass of the full KMOS instrument has been measured to be 2529 kg, under the 3000 kg maximum

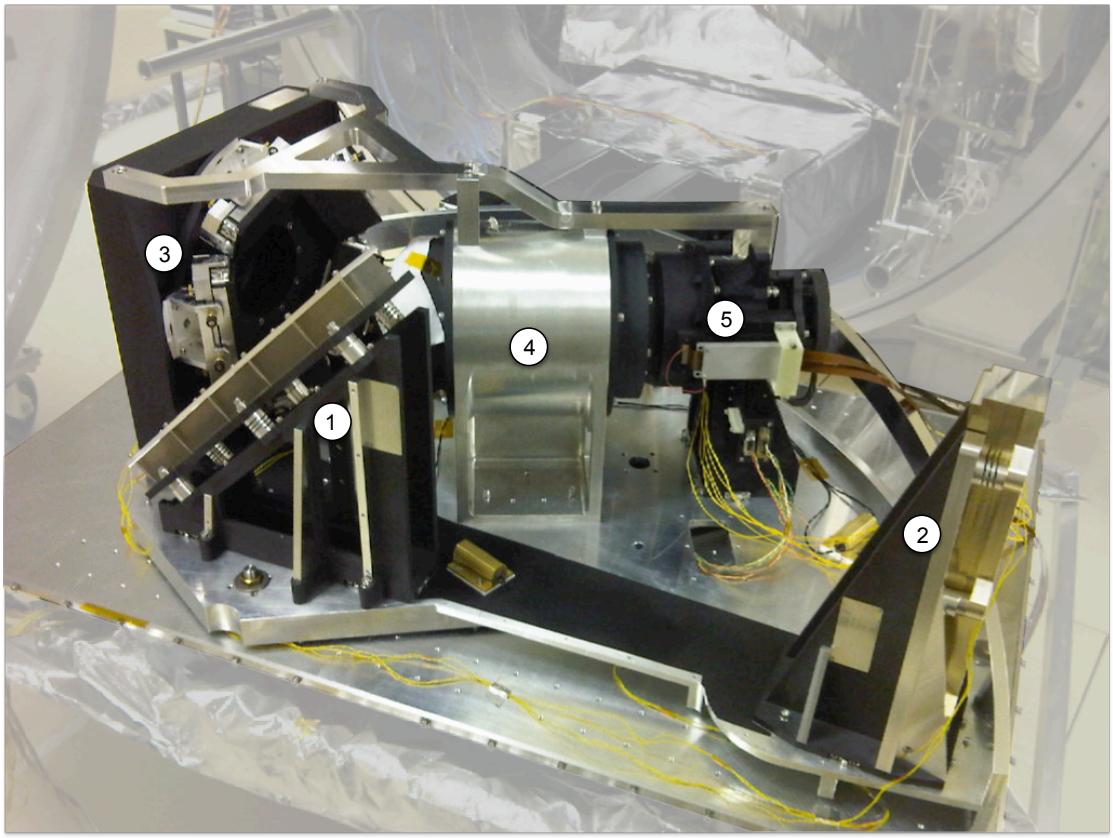

Figure 2.1: A fully populated Science Grade Spectrograph module. 1.) Fold mirror assembly, 2.) Collimator, 3.) Grating exchange mechanism, 4.) Camera barrel, 5.) Detector focus stage, with detector inside housing. The spectrograph module sits on the cold plate. The brass resistors were used for plate heating and the yellow wires were linked to PT100 resistive temperature sensors.

requirement. All of these figures are taken from the latest mass specification document (Rees, 2011).

2.1.1 Optical bench/structure

Each spectrograph optical bench occupies one third of the full circular configuration of the units. The baseplates are made from aluminium with the underside (facing the focal plane) light weighted to minimise mass while maintaining strength. The modules also have a stiffening frame bolted along their outer edges to limit flexure of the plate during rotation of the instrument on the Nasmyth mount. The sub-assembly locations are defined by dowels set into the baseplate that contact machinable shims (adjustable as part of the alignment processes described in the following

subsections) attached to the sub-assembly bases. Each sub-assembly was secured to the baseplate by screws involving spring washers to maintain pressure while thermally cycling the module. The track on the baseplate following the optical path between the fold, collimator and grating exchange was painted with NEXTEL®[1] black paint to reduce scattered light.

In the full instrumental setup, the spectrograph modules are attached to the cryostat bench and the IFU module via three aluminium feet, providing a conductive link to the KMOS cold bench (see Section 2.3). There are two ports cut into the baseplate for installation of the D-type connector blocks for accessing the grating mechanisms, focus mechanisms and detector readout & thermal control.

2.1.2 Fold Mirror

The fold mirror assembly consists of a black organically anodised, aluminium triangular frame, angling an optically flat, fold mirror surface at 45° to the plane of the optical bench (Figure 2.2). This directs the input beam from the entrance slit towards the collimator. The mirror material was BK7 (Schott designation for borosilicate glass) for the ES and Zerodur® glass ceramic (another Schott product) for the three final SGS modules. BK7 was used in the ES due to its lower cost. Zerodur® experiences less volumetric variation during thermal cycling and is also less prone to stress fractures under such conditions (as seen by VLT mirror blanking work in Morian et al. (1997)) and so was used for the final SGS modules for operational use. The fold mirror optical surface was gold coated for improved reflection of the required wavelengths. The following numerical references are to Figure 2.2.

Alignment was achieved using a co-ordinate measuring machine (CMM), by defining a plane parallel to the mirror support frame at (4) and measuring the angle between that plane and the plane of the datum. The assembly was located on the spectrograph optical bench against three dowels, using three machinable shims. The CMM probe (2) was used to define planes at (1) (the fixed datum plate - to mimic positioning on the final baseplate) and (4) (the mirror frame/support). Adjustment to the relative angles of the two planes (in the XZ and YZ planes) was achieved via three screws compressing three spring supports (5). Once the design specifications of the angles

[1] Mankiewicz Gebr. & Co.

Table 2.1: Fold mirror sub-assembly alignment data for one spectrograph module

Reference plane	Nominal [°,′,″]	Measured [°,′,″]
XY	149, 40, 00	149, 46, 29
YZ	179, 50, 00	00, 00, 34
ZX	45, 00, 00	44, 59, 27

were met, rigid supports were secured at the vacant positions between the triangular web frames and the mirror support (4). If the specified orientations could not be met using the sprung screws alone, the shims were available for adjustment. Fortunately, modification of the shims was not necessary. (3) indicates a shim position - used to locate the assembly against the datum during alignment. The final angles of the three fold mirrors were $\sim 0.02\%$ of the nominal values (see Table 2.1).The nominal values are taken from the fold mirror assembly drawing sets and Lewis et al. (2007).

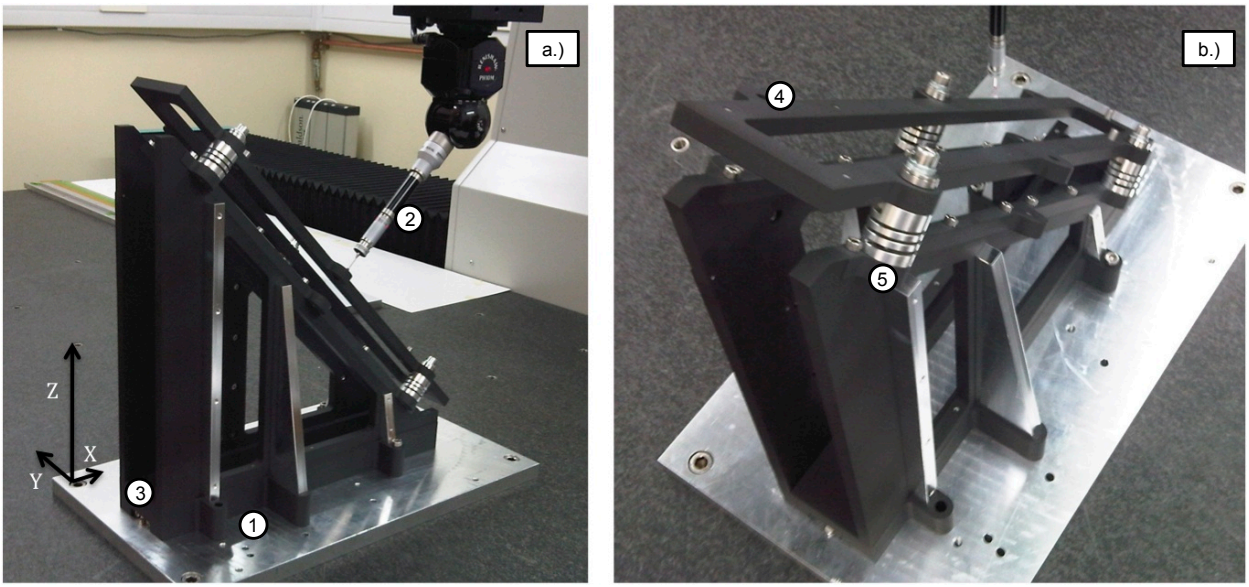

Figure 2.2: The fold mirror sub-assembly and its alignment

2.1.3 Collimator

The collimator assembly consists of a black organically anodised, aluminium support frame holding a spherical, gold coated, diamond turned, aluminium mirror. The mirror surface roughness, prior

to gold coating, was <4nm rms. The initial collimator mirror surfaces, used during the testing at Oxford and in the initial full instrument tests at the ATC, suffered from out of specification RMS form error in off-axis positions. The initial test of the mirror form error by the manufacturer only sampled a 50nm aperture on-axis, which was found to be within specification (< 100nm RMS). This would have contributed to the focal plane curvature described later in Section 3.2.2. These mirrors were re-surfaced and the off-axis RMS form error was found to be within specification for the final build.

Alignment of the mirror with the sub-assembly base was performed using the CMM. The assembly was located on the spectrograph optical bench against three dowels, as with the fold mirror. The following numerical references are to Figure 2.3.

The height of the mirror block above the sub-assembly base plate and separation of the mirror block from the support sides (2) were set using slip gauges. Gauges combined to the design specification separation were positioned and the mirror was secured against them via the three screws compressing the three spring supports, below (2). The CMM probe (6) was used to define planes through the mirror block in the XY, YZ and XZ planes, along the sides and through the centre of the block. These planes were used to set the specified Z, X and Y positions of the block respectively, relative to the sub-assembly base plate, via the three adjustment screws, below (2). The probe was then used to measure six points on the surface of the mirror to define a sphere. The sphere's projected centre was used to angle the mirror correctly to direct the optical path from the fold mirror to the grating. The alignment of the collimator spherical surface with the required projected centre (i.e. radius of the nominal sphere) was typically $\sim 0.01\%$ of the nominal design value. Table 2.2 shows the vectorial positions along the X,Y and Z axes along with the radius of the projected sphere for one of the collimators. The nominal values are taken from the collimator drawing sets and Lewis et al. (2007).

2.1.4 Gratings and the grating exchange

The grating exchange wheel involves five reflection gratings (covering the I/z, Y/J, H, K, HK ranges), positionable into the optical path using a computer controlled motor. The following

Table 2.2: Collimator sub-assembly alignment data for one spectrograph module. The primary tolerance is on the spherical radius at ±0.5%, or ±10.4mm.

Vectorial position [mm]	Nominal [mm]	Measured [mm]
X	79.20	78.74
Y	65.10	63.71
Z	409.30	409.33
Sphere radius [mm]:	2082.90	2082.71

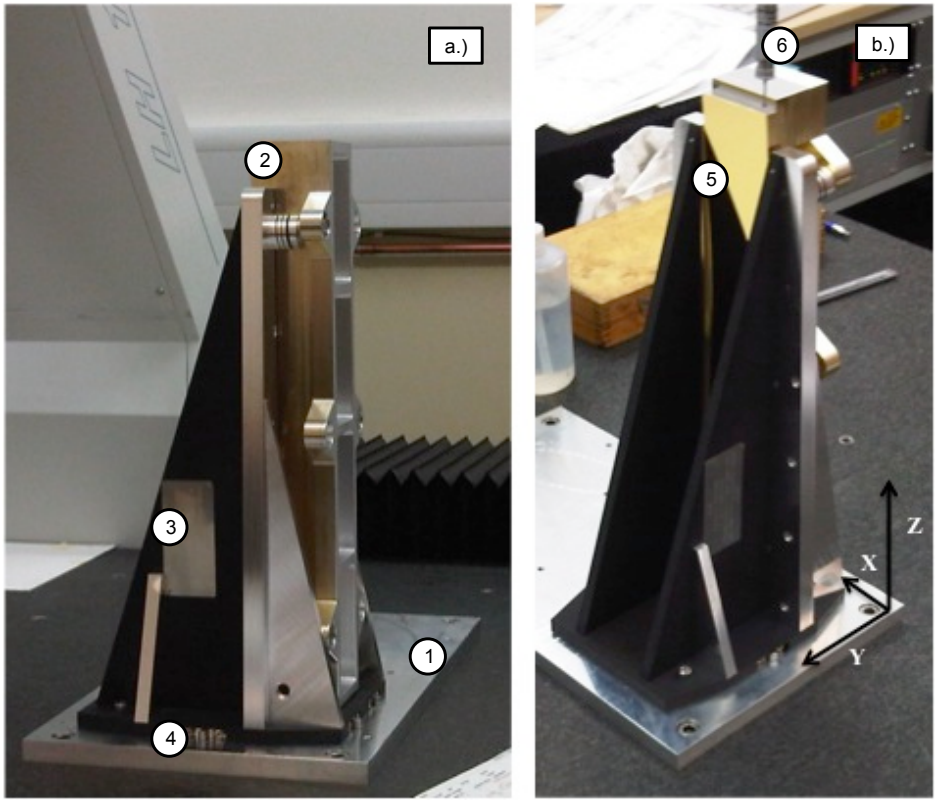

Figure 2.3: The collimator sub-assembly and its alignment

numerical references are to Figure 2.5. These gratings were produced by Newport Optics. The master gratings were ruled and then used to replicate each grating in a soft epoxy on an aluminium substrate, coated in gold for high reflective throughput. The grating surface spans 50mm by 110mm (dispersion and spatial directions respectively), oversized by 5mm spatially to accommodate the collimated beam. A representation of the surface variation is given in Figure 2.5 in the form of a wavefront map, provided by the manufacturer. It can be seen that towards the optical axis, in the centre of the grating, the rms variation is typically <0.08 of a wave. Each grating block

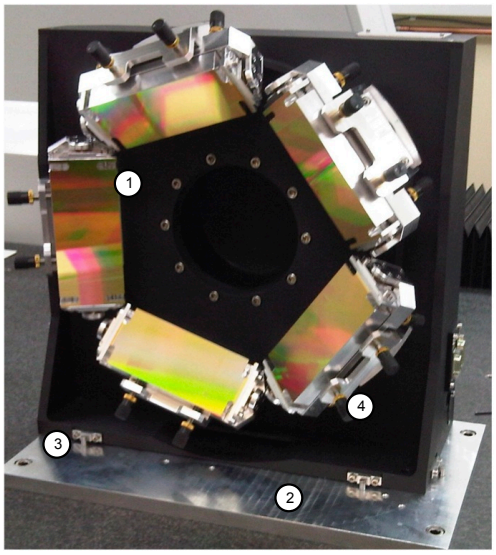

Figure 2.4: The grating exchange wheel.

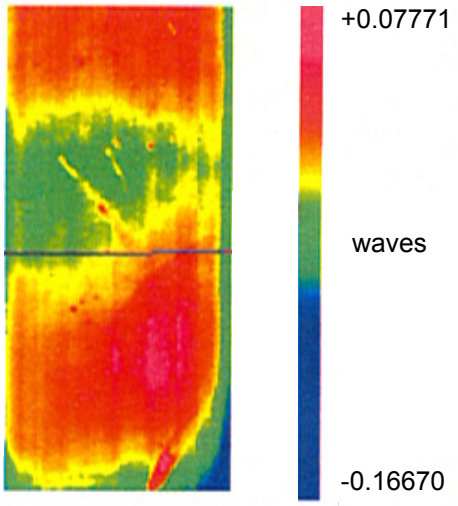

Figure 2.5: Wavefront map of Iz grating.

was held by a custom made (in-house) cradle that was attached to the wheel mechanism. The cradles were each orientated to ensure the incident beam would be at the required Blaze angle (θ_b), to ensure maximum throughput at the central wavelength of each filter. Four fine-thread screws with locking rings were attached to each cradle, pushed against the gratings with two for central wavelength adjustment - pressing against the side of the grating block allowing tip/tilt adjustment perpendicular to the optical path and two contacting the back of the grating block for fine tuning of orientation angle during alignment with the CMM.

The exchange wheel casing was NIR-black anodised. The same datum plate (2) as used with the fold mirror and collimator was used when aligning the gratings. Three shims (3) again defined its nominal position on the datum and on the final spectrograph optical bench. All measurements were measured with the CMM probe. To set the initial position of a grating, a plane was defined through the grating (measuring off the side of the grating mount/cradle), with its lower face towards the datum plate. The grating wheel was rotated until this plane was parallel to the datum plate (2). The front face of the grating wheel, inside the pentagon made by the gratings themselves, was defined as the plane from the which the orientation angles for the gratings were taken (1). The outside edges of the gratings were aligned to be nominally perpendicular to the datum plate (allowing for adjustment of dispersion direction during later optical tests) and the tilt was also

adjusted to ensure the 2nd order dispersed beam was sent to the camera. The 1st order beams are at least 32° separated from the 2nd order beams, thus the camera barrel is orientated at 32° to the collimator-grating optical path. The adjustments were also made to ensure that the nominal central wavelength on the detector would be correct. This procedure was identical for all gratings and across all three spectrographs. The properties of the gratings are given in Table 2.1.4 along with the expected spectral properties. The Bragg angle for the 1st order beam is given as $\theta_b[^\circ]$ (2nd order beam angle, θ, is calculable via the grating equation: $d \sin\theta = m\lambda$ - where d is ruling separation and m is order). $\langle E \rangle$ is the average efficiency over the wavelength range for each grating, taken from the manufacturer's report.

Grating	λ range [μm]	λ_c [μm]	$1/d$ lines/mm	θ_b [°]	$\langle E \rangle$ [%]	R_{exp} ($\equiv \lambda/\Delta\lambda$)
Iz	0.80 - 1.08	0.98	425.8	24.67	75	3327
YJ	1.02 - 1.35	1.18	361.2	25.23	78	3387
H	1.45 - 1.85	1.65	287.3	28.30	83	3840
K	1.95 - 2.50	2.23	219.0	29.23	88	3766
HK	1.50 - 2.38	1.94	272.3	31.89	90	2052

Table 2.3: KMOS calculated (expected) spectral properties and grating properties.

2.1.5 Camera barrel

The KMOS camera barrels were assembled and tested at Rutherford Appleton Laboratories (RAL) by members of the Optical System Group. The assembly and alignment of each of the six lenses followed the methods used in the assembly of the UK-FMOS NIR spectrograph camera (Froud et al., 2006). The coated lenses were supported within flexures cut away from aluminium rings. Low thermal expansion pads were attached to the ring flexures to hold the lenses. These pads were then bonded to the glass before the lenses were co-aligned in the barrel.

Optical testing of the camera employed an Optical Surfaces collimator (involving a pinhole, source, collimator and filters in one assembly) illuminating the lens barrel with a high quality collimated beam, 65 mm in diameter. The output beam from the lens barrel was then re-collimated by a high quality microscope objective, demagnifying the beam diameter to 4 mm and onto a

Shack-Hartmann wavefront sensor (WFS) from Thor labs. This wavefront sensor employs a focally homogeneous lenslet array that samples the wavefront at each lenslet position and measures wavefront shape and therefore any aberrations by registering the position of each focal spot on the detector.

Aberrations to the wavefront (such as tip/tilt, defocus, coma off-axis distortions, spherical aberrations etc) are parameterised by Zernike polynomials. These are an orthogonal set of polynomial terms, where higher order terms describe more intricate or irregular aberrations. A given lens will have intrinsic aberrations (parameterised by Zernike terms - primarily Z4 & Z6 (astigmatism), Z8 & Z9 (coma) and Z13 (spherical)) due to manufacturing limitations. The KMOS lens barrels were designed as six lens systems, and so the alignment of the barrels allowed for the axial rotation of each lens to minimise the Zernike terms and thus reduce the aberrations in the full lens system. The main Zernike terms affected by the relative axial rotation of the lenses are the coma terms (Z8 & Z9) and astigmatic terms (Z4 & Z6). The spherical aberration terms are limited by the manufactured optical surfaces of the lenses. Iterative rotations of the lenses to minimise the coma residuals (via WFS checks) were undertaken. Practically, the spherical term (Z13) dominated the RMS wavefront error.

During the optical testing (discussed later), the results with the initial builds of the KMOS camera barrels indicated image quality issues towards the edge of the field, stemming from the use of the incorrect sign for the curvature term of the sag equation (see Section 3.2.2) during the manufacture of lens six (L6). The on-axis wavefront aberrations as a function of rotation about the optical axis are shown in Figure 2.6. The top plot shows the measurements for the camera barrel setup containing the original, incorrectly manufactured L6 and the bottom plot relates to the corrected L6. It can be seen that the RMS wavefront error is nearly halved by the reworking of the lens. This is also seen in the off-axis (at 7°) aberrations. The full details and results of the assembly processes for all of the camera barrels used in KMOS are given in Tosh (2011). A more in-depth discussion of the effect of the incorrect L6 optical surfaces given in Section 3.2.2, along with the optical test results indicating the effect this had on the end-to-end KMOS tests.

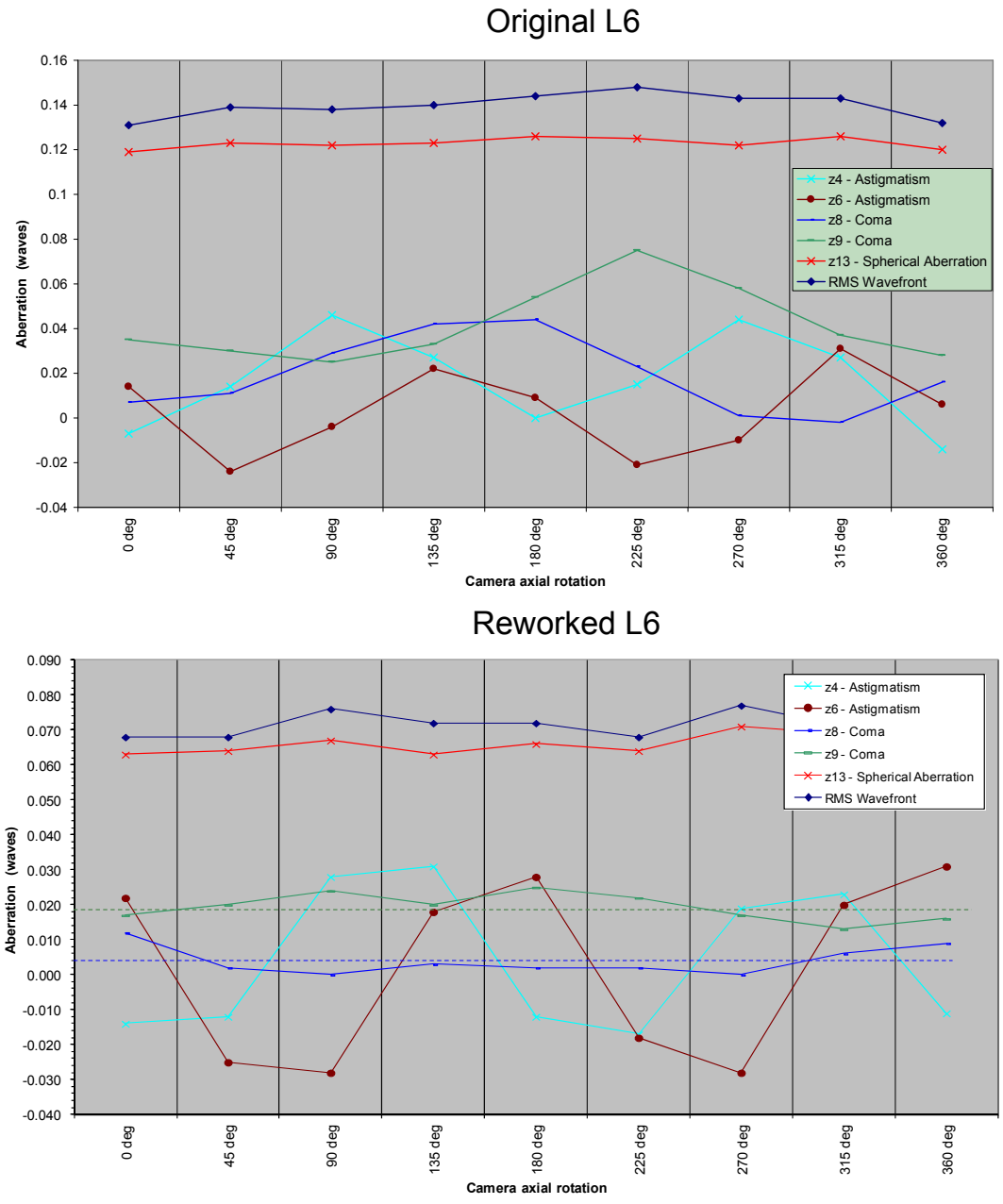

Figure 2.6: On-axis aberrations to the wavefront as a function of axis rotation. Adapted from Tosh (2011).

2.1.6 The Hawaii-2RG detectors

KMOS employs three infrared diode array detectors, one in each spectrograph module. Each is comprised of a 2048 x 2048 pixel HgCdTe array, grown by molecular beam epitaxy (MBE) onto a CdZnTe substrate, hybridized to a Hawaii-2RG multiplexer. For the delivered detectors, the CdZnTe substrate was removed to reduce fringing effects, reduce cosmic ray events and to extend the spectral response and increase quantum efficiency (QE) for shorter wavelengths. They have been developed by Teledyne Imaging Sensors (see Finger et al., 2004 for a description of their performance). These IR arrays perform exceptionally well at the required KMOS wavelengths and show low shot noise at their operational temperature of $\sim$ 80K. Having relatively thin layering for photon detection generally results in very low cosmic ray events, even with the CdZnTe substrate in place. Some features of the KMOS Hawaii-2RG detectors are given in Table 2.4.

For initial setup of the detector tip/tilt on the final instrument, a travelling microscope is used to measure the focus distance to the corners of each detector. The tip/tilt is then adjustable via a three-point kinematic mount. The detector delivered for the Oxford tests was already nominally set up with minimal tip/tilt. However, we were unable to perform a second, more detailed measurement of the tip/tilt in Oxford, as we did not have the appropriate equipment. Detector tip/tilt was measurable via focus scans across the focal plane during the optical testing, but was not crucial in our tests of specifications detailed in Chapter 3.

The full housing and open front are shown in Figure 2.7. The Hawaii-2RG engineering grade detector can be see in the housing on the left. The housing is NIR-black anodised and the front contains a ridge that creates a recess for the detector to sit in. This ridge contacts the end of the camera barrel when they are attached to the spectrograph optical bench. A baffle from the end of the camera barrel slides over the housing ridge to create a folded-baffle light guard to ensure no scattered light hits the detector before passing through the camera. The three stage kinematic mount is visible in the open-fronted image on the right of Figure 2.7, with the detector sitting on its molybdenum base, conductively linked to potential cooling reservoirs by a copper busbar. The yellow cables feed into a heater and diode resistor at the back for thermal control and the internal casing is constructed of G10 resin to ensure thermal isolation from any other conductive sources.

The display readout ribbon is connected on the right of the image.

For the KMOS testing in Oxford, an engineering grade detector was supplied. This had a significant number of dead pixels ($\sim$ 30%), which affected analysis (as detailed in Chapter 3). A science grade Hawaii 2RG has typically <1% bad pixels (Finger et al., 2004). The data taken at the ATC (presented later in this document) was obtained with both engineering grade and science grade detectors, depending on the stage of the project.

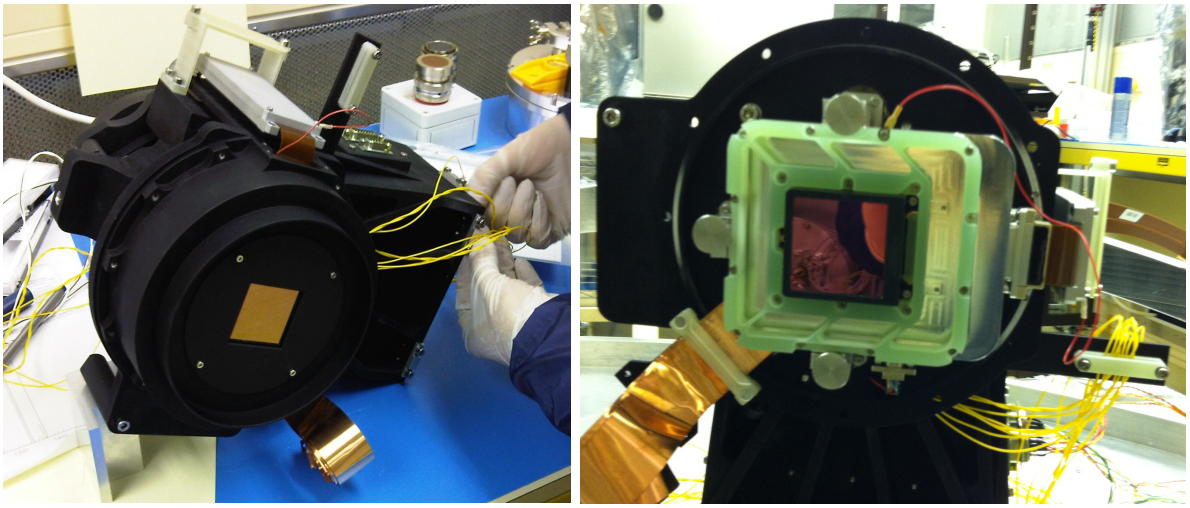

Figure 2.7: Hawaii-2RG engineering grade detector and kinematic mount.

Feature	Specification
Detector Material	MBE HgCdTe double planar heterostructures (DLPH) CdZnTe substrate removed
Format	2048 x 2048 pixels
Pixel size	18.0 μm
Wavelength range	0.8 - 2.5 μm
Mean QE ($\pm$5%) at 80K $\lambda = 1.05 - 1.37\mu$m (J) $\lambda = 1.45 - 1.85\mu$m (H) $\lambda = 1.95 - 2.50\mu$m (K)	 > 80 % > 85 % > 85 %
Readout noise	Double correlated: < 20 e$^-$ rms measured: 8-9 e$^-$ rms 16 Fowler pairs < 7 e$^-$ rms measured 64 Fowler pairs at 2.3 e$^-$ rms
Dark current (80K, Vbias = 0.5V)	< 36 e$^-$/hour
Fringing	< 1 % when illuminated by narrow band light at $\lambda = 1.2, 1.65, 2.1\mu$m

Table 2.4: Detector specifications, adapted from Finger et al. (2004)

2.2 The Oxford Facility

2.2.1 Design and Construction of the Test Facility

As part of the design of an adequate operational environment for the Oxford testing of the spectrograph modules, basic modelling of the test facility was required in order to understand the thermal and mechanical response of the chamber and the instrument inside. My main focus was on the thermal and optical properties. The outline requirements for the test rig were:

- Vacuum capability - able to achieve and maintain pressures $\sim 5 \times 10^{-6}$ mbar.
- Recreate the KMOS arc and continuum calibration sources for optical testing.
- Cryogenic capability - able to cool the spectrograph modules down to KMOS operational temperatures in a controlled way and to maintain a stable temperature for the length of time required for the optical testing (particularly for the detector, maintaining a gradient of less than 2.0 K/minute).
- Allow control of instrument mechanisms and the detector via work stations supplied by LMU & ESO respectively.

The 2.2m HIRDLS facility (Dials et al., 1998) in the Oxford University Atmospheric, Oceanic and Planetary Physics (AOPP) department was available to meet these requirements. This facility was comprised of a class 100 clean-room, containing a cylindrical thermal vacuum chamber. The chamber measured 2.2m x 2.2m x 4m and had a removable cap towards one end. This end-cap was pivotable and was large enough to contain a full spectrograph module and any supporting structure. The required vacuum pressure was achievable via initially rough-pumping the chamber down to $\sim 10^{-4}$mbar and then employing a turbo pump to achieve 5×10^{-6} mbar. A CAD model of a spectrograph module can be seen in the end-cap of this facility in Figure 2.8

Access to any instrumentation inside the chamber during vacuum operation was possible via four vacuum interface flanges. Two were prepared for electronic access (for mechanisms, temperature control & monitoring and detector readout), one for coolant injection into the cryogenic system and one for optical input (a fiber fed flange - see section 2.2.3).

What follows is a description of how we decided on the thermal setup, the electronic control system and the optical setup for the testing in Oxford.

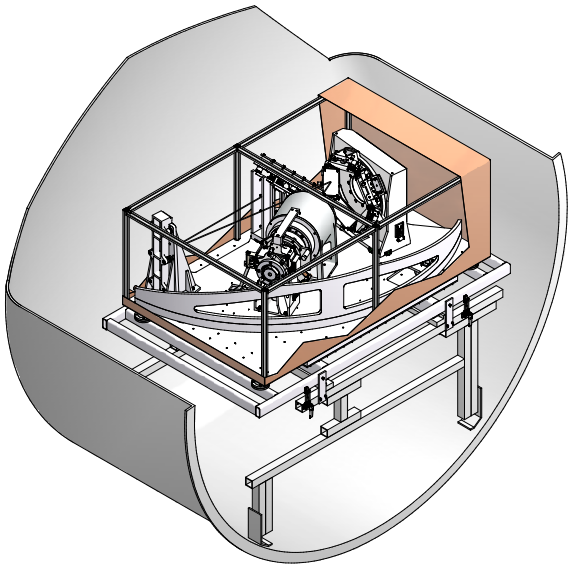

Figure 2.8: CAD model of a single KMOS spectrograph module in the end-cap chamber. Image courtesy James Lynn, OUPD Design Office.

2.2.2 Thermal modeling

With the available setup in the 2.2m facility, consideration of the thermal behaviour of the instrument and the test chamber was required to understand the materials & mechanisms available for the support structure, the method & timescale of cooling and the amount of any coolant required. The potential hold time at operational temperature, along with realistically achievable gradients in cooling and warming needed to be predicted so that the full range of tests could be planned and conducted properly.

Most crucial was the thermal gradient between the detector and its surroundings. The cooling/warming rate of the H2RG detector must not have exceeded 2K/minute (Finger et al., 2004). This is due to the layering of the HgCdTe detector. Rates exceeding 2K/min for the temperature variation of a Hawaii-2RG detector could shatter the surface owing to the differing rates of thermal expansion of the detector materials. We opted to aim for a controlled rate of 0.5 K/minute, to ensure any fluctuations in the rate would not cause it to exceed 2K/minute.

These factors were determined in a two stage investigation. Initially a basic thermal model was constructed and then this was tested with a dummy spectrograph to refine our understanding of how the final modules would perform. In constructing the thermal model I considered conductive and radiative power sources, linearly combining them (see Figure 2.9). The assembly of the model was performed by writing a program enabling user choice of various parameters (emissivity of various surfaces, masses etc), so that the model could be adjusted more easily.

For the initial ES set of through-focus tests with the H-band grating only, a back of the envelope calculation included the exposure times for the arc frames, dark-frames, halogen frames and overheads for readouts and focus mechanism movement. In total, this came to $\sim$ 30 minutes of required stable cold time (assuming around 20 to 30 stacked exposures of 1s at 21 positions along the 2.1mm of focus movement to provide reasonable S/N). However, for the SGS data, the total test time needed to be at least 5 times the ES test time (due to five gratings in total). In addition to this, considerations of longer exposure times for the HK and K band data sets (due to worse throughput along the input fibers), movements of the grating mechanism, repeatability tests and filter changeover time (manual exchange as described in section 2.2.3) took the required stable

window up to at least 4 hours. So, not only did we need to have a good idea of how long the cool down would take, we also had to calculate how much coolant would be available for uninterrupted testing given the available facilities.

The Model

The spectrograph was initially represented as an aluminium plate (**BP**), as only the baseplate of one of the modules was available for testing in the chamber. The option of changing the mass to that of the full assembly encompassed by a dummy block (**S**) was included, to give a better representation of the fully populated spectrograph module. The **BP** sat on a cold plate (**CP**), thermally connected by three disc-shaped feet. Prior to the design of the model, it was understood that the cooling material available would be liquid Nitrogen (LN_2). The nature of the available setup enabled injection of the coolant boil-off gas into a cooling loop attached to an aluminium plate (see section 2.2.3) - creating a cold reservoir (**CP**). The **CP** was set to be thermally isolated (conductively) from the chamber and the whole spectrograph setup was considered thermally disconnected from any other part of the system. A radiation shield (**RS**) was represented as an aluminium box around the **BP**, connected conductively to the **CP**. The final surface in the model was the vacuum chamber wall (**C**). Due to the conductive isolation of the spectrograph, only radiative processes were considered for the thermal interaction of **C** and the spectrograph. The setup can be seen as a reduced schematic in Figure 2.9.

Computing the radiative heat flow and conductive heat flow simply involved considering the magnitude of the heat flux and the direction of the heat flow, relative to a particular component. The conductive flow is governed by Fourier's Law, represented by the heat transfer equation

$$P_c = kA\frac{\Delta T}{x} \tag{2.1}$$

where P_c is the conductive power, k is the thermal conductivity of the material, A is the surface area of contact, ΔT is the temperature difference of the two reservoirs in the flow and x is the length of the conductive link.

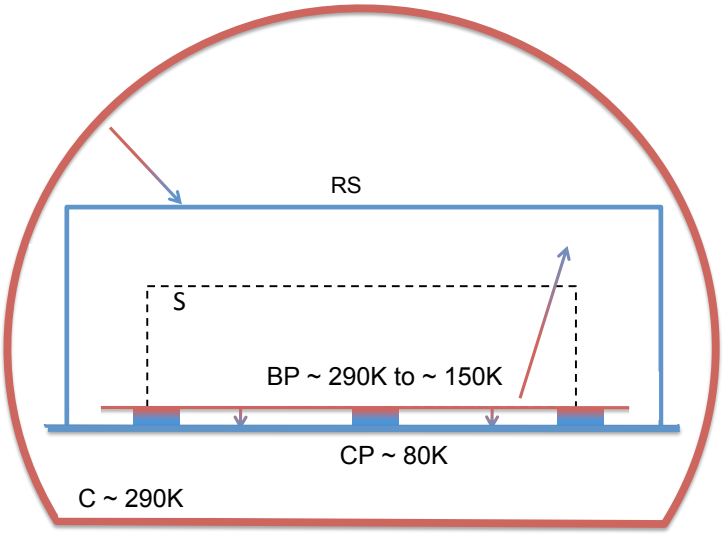

Figure 2.9: Schematic of the test rig thermal model.

Radiative flow is governed by a modification to the Stefan-Boltzmann law, shown by equation 2.2

$$P_r = C_t \sigma (T_2^4 - T_1^4) \tag{2.2}$$

where P_r is the radiative power, C_t is the radiative transfer coefficient, σ is the Stefan-Boltzmann constant and T_1 & T_2 are the temperatures of the two surfaces involved in the power flow. The exact form of the radiative flow, parameterised by C_t, is a function of the surface areas, emissivities and orientations of the surfaces involved,

$$\frac{1}{C_t} = \left[\left(\frac{1-\epsilon_2}{A_2 \epsilon_2} \right) + \frac{1}{A_2 F_{2-1}} + \frac{1-\epsilon_1}{A_1 \epsilon_1} \right] \tag{2.3}$$

Where, ϵ_i represents emissivity of surface i and A_i represents the visible area of surface i. F_{j-i} is the view factor and is a function of the geometries of the surfaces involved.

The model was decomposed into four primary pieces or configurations. We first considered the radiative flow between **C** & the **RS** (configuration 1) and the conductive flow between the **RS** and the **CP** (configuration 2). Configuration 1 was modelled as a hemispherical surface radiating onto a plane, with adjustable height between the two areas (see Figure 2.10a). The required view-factor

for this configuration is

$$dF_{2-1} = \frac{zR^2}{[R^4 + 2R^2(2z^2 - 1) + 1]^{\frac{1}{2}}} \tag{2.4}$$

where z is the height between the two radiating elements and R is the radius of the concentric disc. Although the radiation shield top surface was actually rectangular in the final test setup, the view factors available from Howell (1982) only provided this model. For an approximate estimate to inform the practical setup, the geometry assumed here was deemed adequate. Incorporating this factor into equation 2.2, we get the maximum power flow between the **C** (293K) and **RS** (106K - midpoint of the conductively linked **CP** temperature and ambient) as $\sim$ 330W. The assumed values are given in Table 2.5. Configuration 2 involves the conductive flow between the top of the **RS** and

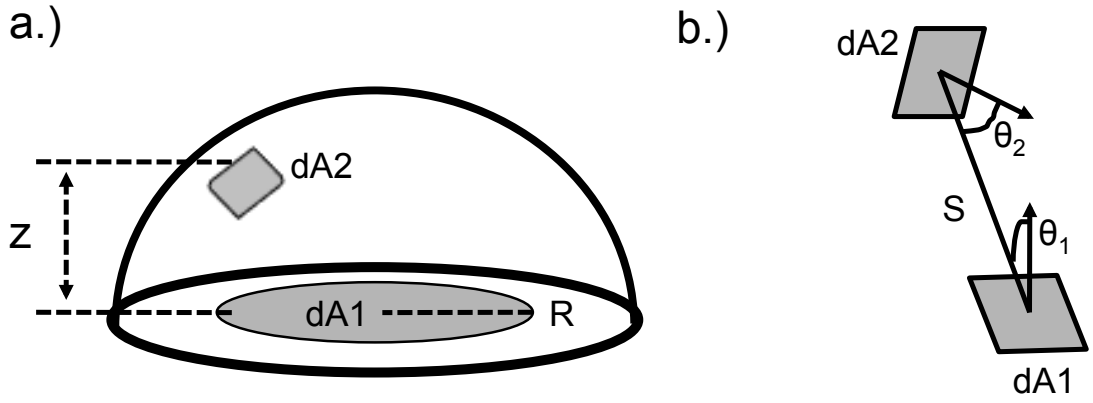

Figure 2.10: Geometries involved in defining the view factors for the radiation transfer model.

the **CP**, and thus requires no view factor calculation, but simply the dimensions of the **RS** walls and some assumptions about the thermal contacts. The maximum conductive power flow between the **RS** and the **CP** (using Equation 2.1) becomes $\sim$ 197W assuming perfect contact between the **RS** walls and the **CP**. In reality, this is of course not the case. A dry, surface to surface, resting interface results in $\sim$ 50% actual compliance. Thus, we modified the calculation to account for this and the cooling power becomes $\sim$ 98.5W.

The conductive heat load into the top of the **RS**, P_{RS}, balanced with the radiative heat load from the **C** would result in a temperature of $\sim$ 271K for the **RS** in the steady state.

Now, assuming this steady state temperature for the **RS**, we can investigate the effect this would have on the power flow into the **BP** and how this would affect the cool down rate and

stability. We take the **RS** as fixed at 271K and the **CP** fixed at 80K. The configurations here involve the radiative flow between the **RS** and the **BP** (configuration 3) and the conductive flow between the **BP** and the **CP** (configuration 4).

Configuration 3 involved consideration of two elemental areas in an arbitrary configuration, as show in Figure 2.10b. It is the geometry of this setup that allows us to define F_{j-i}. If the **BP** is surface 1 and a wall of the **RS** is surface 2 (where S is the distance between them - ie the linear size of **BP**), then the required view-factor is

$$dF_{2-1} = \frac{cos\theta_1 cos\theta_2}{\pi S^2} dA_1 \tag{2.5}$$

and we can, again, obtain F by integrating over the full area of A_1. So, we simply take θ_1 as 90° and θ_2 as 0° for the radiative flow between the walls of the **RS** and the **BP** and θ_1 as 0° & θ_2 as 0° for the ceiling of the **RS** onto the **BP**. The values employed are given in Table 2.5

We took the **BP** at its maximum operational temperature (150K, with 130K being optimal) and the **RS** at 271K, considering it would be held up by the **C**. The combined power from the walls and the roof emitting onto a flat **BP** was found to be $\sim$ 382W. This is an underestimate, as the surface area (A_1) is a lot larger with the sub-assemblies populating the **BP**.

Configuration 4 involves the application of equation 2.1. The conductive flow through all of the three mounting feet (stainless steel) was found to be $\sim$ 225W. Thus, at 150K, the **BP** would not be thermally stable. The stable temperature of the **BP** in this setup would be $\sim$ 196K, which is outside of the operational specification. In fact, this would be even worse as we have assumed zero thermal resistance between the **BP** feet and the **CP**. For a dry connection, the compliance is usually assumed to be 50%.

Due to the above findings, it was decided that the **RS** temperature should follow that of the **BP** and its sub-assemblies as closely as possible (reducing the ΔT to zero). To achieve this, we decided to cover the external surface of the **RS** in a sheet of multi-layered-insulation (MLI). This would radiatively isolate the **RS** from the **C** and it would allow it to cool solely conductively at the same rate as the **BP**. So, assuming purely conductive cooling of the **BP** via the fixed reservoir

of the **CP**, we were able to predict an approximate cool-down time for the spectrograph. We used

$$E_S = c_{al} m \Delta T \tag{2.6}$$

$$\tau_{cd} \sim E_S / P_c$$

where E_S is the thermal energy contained in the spectrograph (assumed a block of aluminium), c_{al} is the specific heat capacity of aluminium ($\sim$ 897 kJkg^{-1}K^{-1}), m is the mass of the model spectrograph - defined earlier (**S** at $\sim$ 108kg), ΔT is the change in temperature of **S** (from ambient to operational $\sim$ 290K to $\sim$ 150K), P_c is the conductive power between the **BP** and the **CP** and τ_{cd} is the cool-down time. The result from this predicted a cool down time, to the up limit of operation of 150K, of around **26 hours**.

To calculate the amount of LN_2 required for the cool down, I considered the thermal energy E_S that needed to be removed from the spectrograph ($\sim$ 13.5MJ) and the heat capacity of the LN_2 boil-off gas($c_{\mathrm{LN_2},gas} \sim$ 1.04 kJ/kgK), used to bring the **CP** down to temperature - the method of cooling is described in section 2.2.3). An assumption needed to be made on the average amount of heat transferring from the spectrograph to the LN_2 gas, in the form of the temperature differential between the **S** and the gas. This was taken as an average of the ambient and LN_2 temperature, multiplied by a factor of 0.5 to account for the efficiency of heat transfer, giving $\sim$ 55K. Thus the mass of LN_2 required (assuming perfect heat transfer) was simply given as

$$m_{\mathrm{LN_2}} \approx \frac{E_S}{c_{\mathrm{LN_2},gas} \Delta T_{\mathbf{CP}-gas}} \tag{2.7}$$

which comes to $\sim$ 236kg. A 160L (128kg) LN_2 dewar was available as the supply to the **CP**. Thus, one refill was predicted to be required during cool down.

Practically, the **CP** would take time to reach LN_2 temperatures. By ensuring good thermal coupling between the **RS** and the **CP** and between the **BP** and the **CP**, these components were expected to follow the **CP** cool down at a suitable rate (not letting the ΔT get so large that such a gradient would cause stresses on moving parts or large radiative loading onto the detector housing).

The cooling of the detector was achievable via a direct conductive link to the **CP**. The housing

of the detector operated as a radiation shield. The conductive link was comprised of a copper busbar attached to a copper column, which was secured to the **CP**. This was wrapped in MLI to ensure any radiative effects would not hinder the conductive link. The other end of the copper busbar would be attached to the back of the detector mount, inside the detector housing (see Section 2.1.6 for detector description). The high thermal conductivity of the copper link enabled us to predict that the detector cool down should follow that of the **CP**, with only a small ΔT. To decide on an acceptable temperature gradient between the detector and **CP**, a simple conductive calculation was performed using Equation 2.1 and the time constant, τ_{cd}. The copper conductive link contained several thermal resistance points and the busbar was made of several thin strips of copper, reducing the conductive area further still. The detector was modelled as a molybdenum block. A rough calculation resulted in the need to keep the ΔT between the detector and cold plate less than $\sim$ 35K to prevent thermal movement greater than 2K/minute of the detector.

Configuration 1			**Configuration 2**	
Governing equations	2.2, 2.3, 2.4			2.1
Nomenclature	1 = RS, 2 = C			
Parameter	Assumed value		Parameter	Assumed value
$A_C \sim 2\pi r_C^2$	$r_C \sim 1.1$m, $A_C \sim 7.6$m^2			
A_{RS}	1.5m^2		k_{Al}	$\sim$ 250 Wm^{-1}K^{-1}
z	0.5m		A_{RS}^{thick}	0.0015m^2
R	0.75m		x_{RS}^{height}	0.6m
ϵ_{RS} and ϵ_C	0.2			
Heat load	**330W**			**-532W/2 = -266W**
Configuration 3			**Configuration 4**	
Governing equations	2.2, 2.3, 2.5			2.1
Nomenclature	1 = RS, 2 = C			
Parameter	Assumed value		Parameter	Assumed value
$A_{BP} \sim 0.3\pi r_{BP}^2$	$r_C \sim 1.5$m, $A_{BP} \sim 2.12$m^2			
$A_{RS}^{w/r}$	1.5m^2		k_{stst}	$\sim$ 13 Wm^{-1}K^{-1}
S	0.6m		A_{BP}^{foot}	0.008m^2
θ_1^w, θ_2^w	90°, 0°		x_{BP}^{foot}	0.03m
θ_1^r, θ_2^r	0°, 0°			
ϵ_{RS} and ϵ_{BP}	0.2			
Heat load	**382W**			**-75W$\times$3 = -225W**

Table 2.5: Parameters used for thermal calculations and the resulting heat loads through the four main configurations.

The preceding calculations have relied on various assumptions and approximations, but were required and crucial to the final design choices on the thermal setup of the test rig. The details of thermal control and the success of these predictions are given in section 2.2.3.

2.2.3 The Control Setup

Control of the tests required five distinct areas: detector control, mechanism control, cooling via LN_2, temperature monitoring & control and control/operation of a light source.

Detector and Mechanism Control

Control of the optical testing was achieved via two workstations supplied by ESO & LMU. One ran the mechanisms and the other was dedicated to the detector. The control, monitoring and acquisition systems can be seen in a schematic view in Figure 2.11. The cabling between the control units and the chamber was wired in-house.

The detector control system (DCS) was comprised of the detector power supply, New General detector Controller (NGC) (Baade et al., 2009) and workstation PC running Scientific Linux. The power supply was connected to the NGC via a 128 pin cable into a custom PCB, as was the NGC to the detector interface cables (comprising clock & bias lines and video signal) via the vacuum port. A 2Gb/s, full duplex fiber optic link ran from the NGC to the DCS PC, carrying the detector readout signal. At the DCS PC the detector readout could be displayed and stored. To set the detector properties (bias voltages, exposure times, number of frames etc) the supplied NGC operation software was used. This also coupled to a real time display (RTD) to monitor the exposures as they were acquired.

The instrument control system (ICS) was comprised of a local control unit (LCU) and the ICS PC. The LCU provided the power to the grating and focus mechanism motors, as well as the limit/reference switches for initialisation and positioning. Control of the mechanisms was possible via a graphical user interface (GUI) on the ICS PC patched through an ethernet link to the LCU. An ethernet link to the DCS PC allowed acces to the DCS user account via the ICS PC, enabling synchronisation of detector readouts and focus/grating positioning. This allowed acquisition scripts

to be run and a range of optical tests to be automated (see section 3). This setup is very similar to that of the full KMOS control system utilised at the UK ATC and the system that will be used at the VLT.

The output of the acquisitions took the form of a single readout of the full array of the 2k x 2k detector, with varying exposure times (or detector integration times - DITs) depending on the waveband measured (due to the wavelength dependence of the throughput of our optical input system and brightness of the arc sources at different λ - see 2.2.3). Exposures were combined by the NGC acquisition software and their number specified as a number of DITs (NDITs). Basic header information was written into the acquisition scripts to aid reductions and attached to the output FITS files. These could be accessed by external users via the internet link.

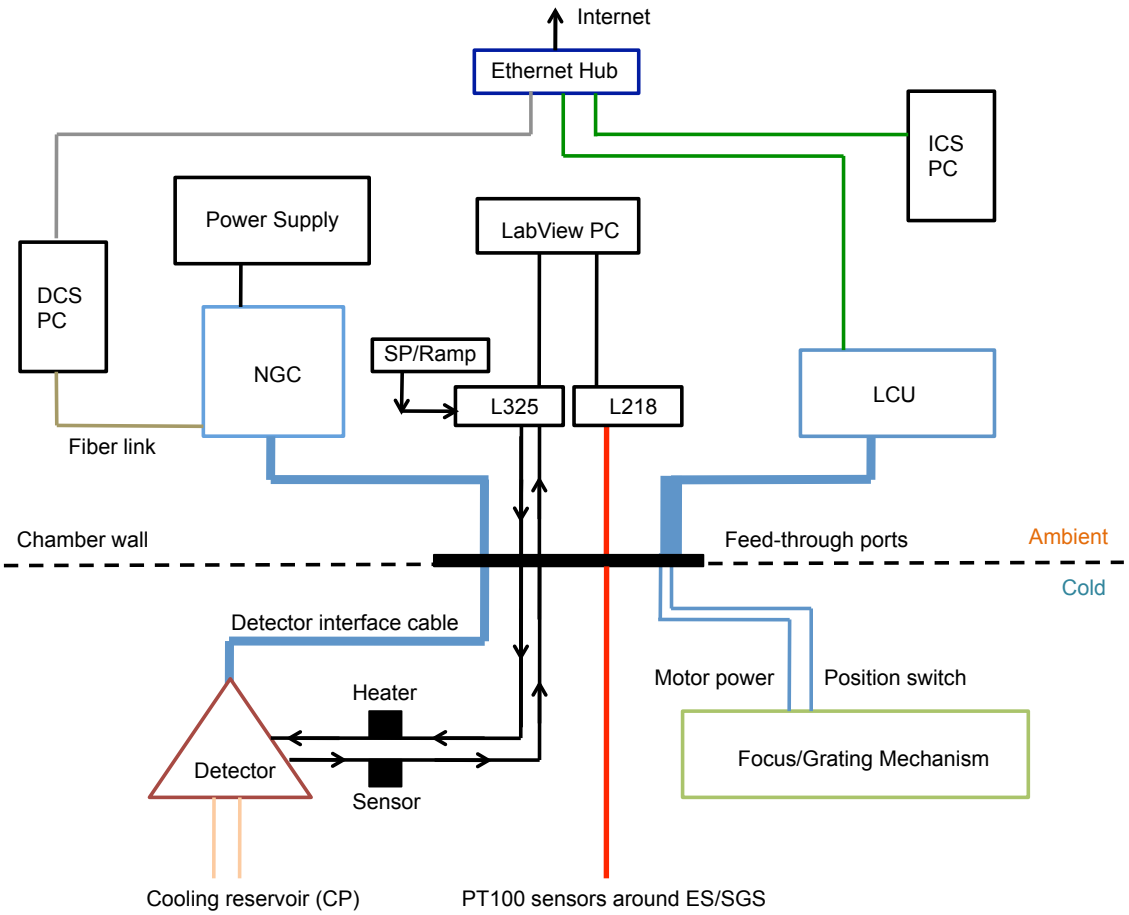

Figure 2.11: Schematic view of the control systems for the Oxford test.

Cooling and Temperature Control

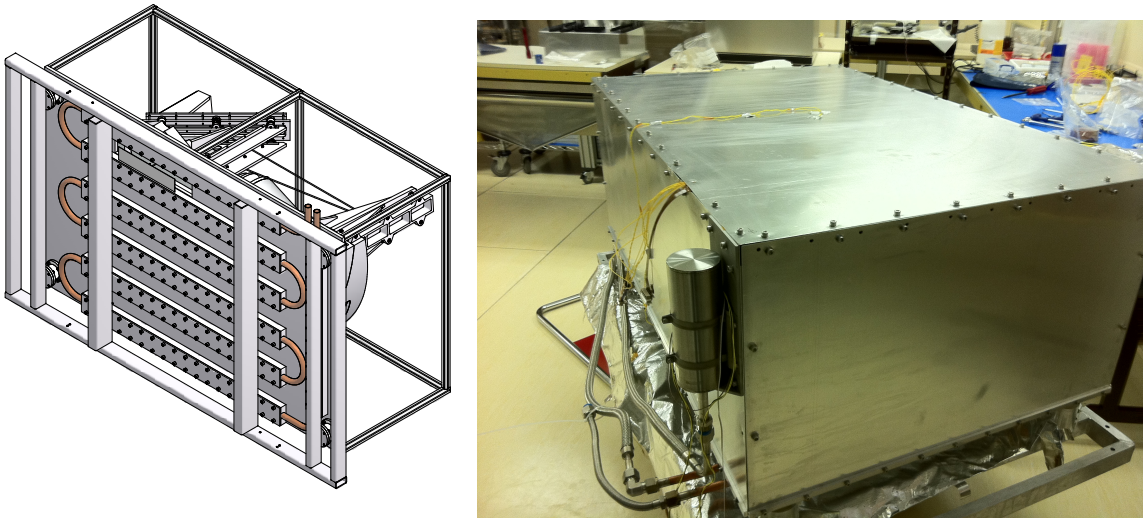

Figure 2.12: Left: Copper cooling loop attached to underside of cold plate. Right: Radiation shield over spectrograph module. The aluminium cylinder in the foreground is the control pot, containing a temperature sensor to ensure liquid LN2 was not passing through the copper cooling loop.

The cooling process involved LN_2 gas fed through a meandering copper tube imbedded in aluminium blocks, attached to the underside of an aluminium plate (the cold plate see Figure 2.12). The blocks aided conduction into the plate (less radiative loss from copper tube). The rate of LN_2 gas flow was controlled by a valve linking an LN_2 dewar to the cooling loop input in the side of the chamber (with the dewar located outside the chamber). This valve was held open while the temperature of a control pot was above a certain set-point. The control pot was located on a corner of the radiation shield, at the end of the cold loop - after the tube had passed along the plate (see Figure 2.12). This was to ensure efficient heat transfer between the gas and the cold plate. If the pot was getting down to the set temperature too quickly, then this would indicate the gas was getting to it too quickly at too low a temperature, so less heat would have been transported from the plate. Thus the valve would automatically close to allow the gas in the system to slow and remove heat from the plate more efficiently. As a second control of heat transfer, the pressure of the gas out of the dewar was maintained at around 10-13 psi by a hand operated valve.

Due to the limited size of the dewar available and the inevitable limited efficiency of the cooling

process, a refill was required once during each cool-down. This required a 'down time' of around three hours. The operational required temperatures of the detector and sub-assemblies were reached soon after this refill in each cooling run. The control setup then allowed the temperature of the detector to be stable over the optical testing period, with the sub-assemblies experiencing a few K change over this time. Warming up to the clean room ambient temperature took significantly longer and was achieved by passing ambient temperature nitrogen through the cooling loop to warm the cold plate, heating the baseplate via three resistor heaters and by directly ramping up the detector temperature with its inbuilt heater. Direct control of the detector temperature enabled a low ΔT between it and the bus bar to be maintained, to prevent the detector warming too rapidly.

During these tests the most important things to monitor were the cold plate containing the LN_2 loop, the copper busbar providing the conductive link between the detector and the cold plate, the baseplate of the spectrograph module, the radiation shield covering the setup and the detector itself. In order to record and monitor the temperatures we used PT100 sensors, connected to a Lakeshore 218E temperature monitor. To record the temperature and control the detector temperature directly, a Lakeshore 325 controller with a diode sensor and resistance heater were used (see Figure 2.11). In the Engineering and Science spectrographs, six PT100s were placed throughout the test rig (with five having their readouts logged), held by aluminium tape to maintain a good thermal contact, in the following positions:

- On the cold plate, underneath the spectrograph baseplate.
- On the copper bus bar connecting the cold plate to the copper braid attached to the detector.
- On the top of the radiation shield, towards the centre. The sensor was underneath the MLI blanket to ensure a true measure of the radiation shield's aluminium plate temperature.
- In the centre of the baseplate, by the base of the camera barrel.
- On top of the camera barrel.
- On top of the collimator mirror.

A LabView Virtual Instrument (VI) was designed to log these temperatures to a file and to update a graphical display of the readouts every 5 seconds. This provided a real time indication of the cool-down, to better monitor the rates and in particular the rate of the detector (via the copper bus bar acting as an indirect measure once the detector was at temperature). The dummy spectrograph had extra PT100s on the radiation shield and dummy detector instead of the camera barrel and collimator, as they were not in place.

Figure 2.13 shows the cool-down data for the dummy (test) module, engineering module (ES) and science (SGS) module. The dummy module cool down shows rapid cooling due to the absence of the full mass. The dashed purple rectangles indicate the down-time & turnover period and the dashed black rectangles indicate the optical test windows. The zoomed in views underneath the Engineering and Science plots show the stability achieved during the tests (with the black line indicating the cold plate and the green indicating the copper busbar, indirectly monitoring the detector), with little variation during the testing of the final science spectrographs. The variation over the cold-time ($\sim$ 5 hours) for the ES was around 0.5-1K and the SGS had a standard deviation of $\sim$ 0.02K over the full test period. The improvement here resulted from more efficient use of the LN_2 gas as the operational temperature was approached. This increased efficiency was achieved through better thermal coupling, via mechanical adjustments and the application of thermally conductive, low outgassing Apiezon grease (after the dummy and ES runs) between the copper cooling loop and the heat transfer blocks they were imbedded in (see Figure 2.12). Recall that in Section 2.2.2 I stated $\sim$ 50% contact between two solid surfaces. The grease would have increased the area of contact substantially.

An important observation is the gradient of the baseplate temperature variation (light blue in the Test plot, dark blue in the other two plots) and camera barrel temperature variation (light blue in the Engineering and Science plots). They experienced significant cooling over the course of the optical tests with a ΔT of $\sim$ 10-15K. This was difficult to control during this phase of testing, due to the limitations in cryogenic control in the facility. This variation did not significantly affect results, but is worth noting in the context of image quality, discussed later in Chapter 3. The red line indicates the radiation shield thermal response.

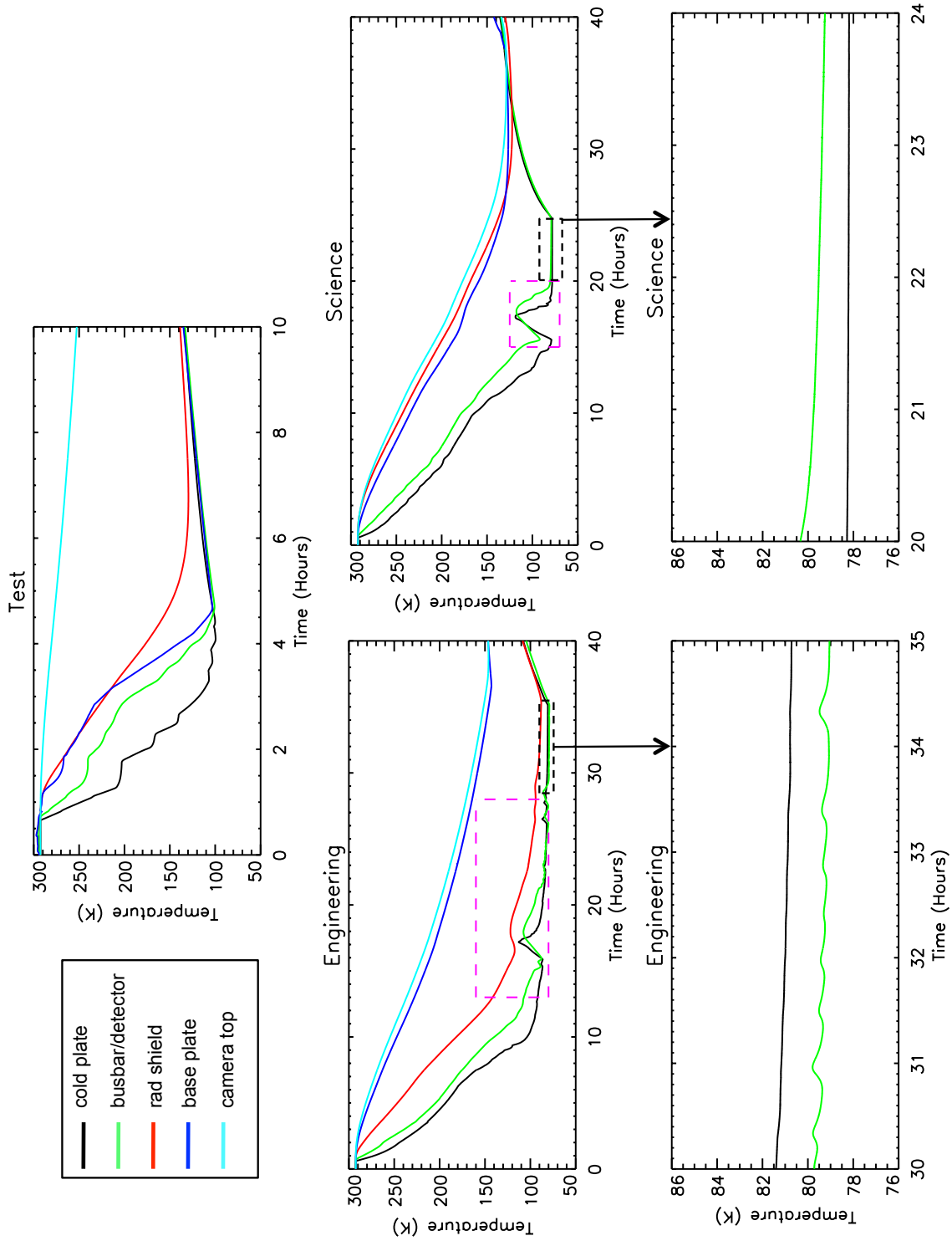

Figure 2.13: Plots of the thermal data during the Oxford testing phase.

The control of the detector temperature was achieved via a proportional-integral-derivative (PID) loop from the Lakeshore 325 controller. This control loop requires a set-point (desired temperature) and a ramping rate with which to approach the set-point from the current (read) temperature. The basic outline of the PID control loop is as follows:

The controller takes the difference between the set-point and the current temperature and, depending on this difference, adjusts the heater output power accordingly (proportional control). If the current temperature does not update at the required ramp rate (either too quickly or too slowly) the controller is able to adjust the heater output again to compensate (integral control). As the set-point is reached, the heater output may overshoot the required value and as it self-corrects oscillatory effects about the set-point can occur. The control loop can be set to reduce the effects of these as it approaches the set-point (derivative control - to decay the sinusoidal oscillation). This method provided adequate control over the detector to maintain the required rate of around 0.5K/min. It was particularly required once the ΔT between the detector and the copper bus bar became significant ($\geq$ 10K), mainly during the warming up process.

The Optical Setup and Light Source Control

As the full KMOS instrument was being integrated at the ATC, the output beams of the IFUs were not available to us for the testing of the spectrograph modules in Oxford. So, we had to create a light source that would mimic the output beams of the IFUs, or at least provide the correct focal ratios in the spatial and spectral directions (f/16.7 and f/46.8 respectively). It was decided that this would be best achieved, under the allowed budget and time constraints, by an optical fiber input system incorporating cone baffles to change the output beams to the required f-ratio.

A vacuum fiber feedthrough assembly was acquired from Ceramoptec®. This consisted of seventeen optical fibers, with core diameters of 50 μm, fed through a CF vacuum flange. The CF flange provided a metal-to-metal seal by compressing a soft copper gasket between two grooved plates, ensuring a full seal down to 10^{-11} pa if required. The fibers inside the chamber were sleeved in a stainless steel braid to protect the fiber cladding & core and limit any outgassing, while the external fibers were sleeved in rubber. These fibers would link a light source, external

to the chamber, through the vacuum port to a baffle block attached along the input slit of the spectrograph module. This block was comprised of two sub-blocks. The first was an aluminium block containing the brass SMA (screw) connectors for the fibers, with a circular beam output. The second was a brass block,[2] between the stainless steel connector block and the baseplate entrance slit. This block contained wire eroded elliptical cone apertures that reformed the output beams from the fibers (see Figure 2.14) to provide the replication of the spectral/spatial relative f-ratios.

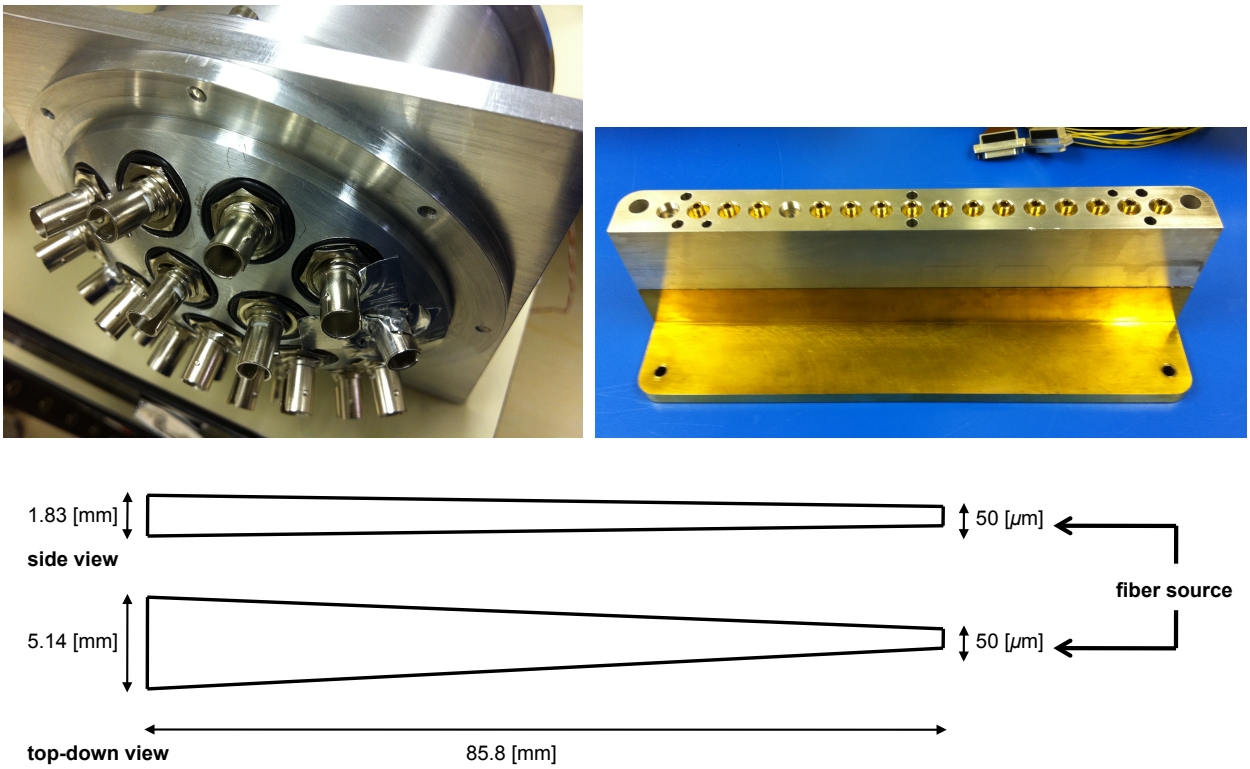

Figure 2.14: KMOS test source and fiber baffle system. *Top left:* Front of test source light-box, showing the fiber plug-plate. *Top right:* Cone baffle system, showing the brass end-block and aluminium connector-block, containing SMA connectors. *Bottom:* Basic schematic illustrating the baffle dimensions. The **side view** indicates the spectral direction, perpendicular to the slit. The **top-down view** indicates the spatial direction, along the length of the slit.

The light source itself was comprised of an aluminium light box, built in-house, containing a halogen lamp with a variable power supply and Newport PenRay arc lamps (Argon, Neon and Xenon - exchangeable), with a filter (manually exchangeable to I/z, Y/J, H, K or HK) between

[2]the material needed to be brass for the wire erosion cutting technique

the lamps and the front. The front of the light box was a hemispherical fiber plug-plate, with each of the fiber ports containing ST (bayonet) connectors and pointed towards the filter to try and achieve homogenous illumination of the fibers and therefore the slit (see Figure 2.14).

The spectrograph optical setups changed slightly (between two types) as the testing developed. The two types were the Engineering Spectrograph (ES) and Science Grade Spectrographs (SGS x 3). The three SGS would be the final modules to be permanently integrated with the full instrument, whereas the ES was designed as a temporary setup for pre-SGS construction checks.

The ES contained a BK7 fold mirror, an uncoated aluminium collimator mirror, a single grating (H-band) on the grating exchange mechanism (the other grating locations contained dummy gratings to maintain an even mass distribution), a full camera barrel and an engineering grade detector on a fully functional focus stage. The lack of coatings and non-optimal materials for mirror surfaces were not a requirement for the ES as throughput and stability under thermal cycling were not an issue at this stage. The intent of the ES was to provide a preliminary check of the optical requirements (central wavelength, wavelength coverage, repeatability under cryogenic conditions and ability to achieve focus/required IQ/resolution). The ES optical bench would then be installed in the cryostat at the ATC and the full optical path would be characterised through two fully operational pick-off arms (see section 3.2).

The three SGS contained gold coated collimator surfaces and gold coated Zerodur® fold mirrors. They also contained fully populated grating mechanisms and complete camera barrels. The detector used in Oxford was an engineering grade model throughout all of the tests. This was exchanged for a science grade detector in each spectrograph prior to final integration at the UK ATC.

2.3 Test Setup at the UK ATC

When testing was conducted on the full instrument, through the full optical path of KMOS at the UK ATC, the test setup was pre-determined by the team there. After integration of each spectrograph module into the KMOS cryostat, the full cooling procedure, outlined in Burch et al. (2006), was adopted to cool and control all of the components. The cold mass of the instrument is defined as the pick-off unit (surrounded by an aluminium radiation shield) and spectrographs

(also surrounded by a radiation shield), sandwiching the optical bench (with a third radiation shield surrounding this section). The full cold mass is connected to the vacuum vessel by 12 G10 thermally isolating 'A' frame trusses. The only thermal links between the cold mass and the ambient vacuum vessel are fill exhaust tubes for an annular LN_2 can (attached to the pick-off arm end of the optical bench), instrument cabling and copper cooling wicks connected to closed-cycle coolers. The outline of the cooling procedure follows:

- LN_2 is fed into the annular can surrounding the optical bench for pre-cooling.
- Once a set-point is reached the closed cycle cryo-coolers are enabled to aid the final cooling and control at operation temperature. They are connected in two separate stages:
  - The first stage of each cooler (one cooler per spectrograph/8 IFU segment) is attached to the optical bench via a copper cooling wick.
  - The second stage cold fingers are linked to the three detectors via copper busbars running through the optical bench (thermally isolated from the bench by smaller G10 trusses), attached to detector cooling wicks (much like the detector links in the Oxford setup).
- Closed loop resistive heating is operated on each detector.
- Once the operational temperatures are reached (130K for the optical bench, pick-off unit, spectrograph and sub-assemblies, 80K for the detectors), the LN_2 can is evacuated and the cryo-coolers control the temperatures at the set-points (allowing continuous operation).
- The controlled cool down time of the full KMOS instrument is 48 hrs for minimum operational conditions and 1 week for full stability across all wavebands.

It can be seen that the thermal control is very similar to the setup in Oxford, but the small-scale nature of the Oxford tests required the use of an LN_2 cold-reservoir only, with no cryo-cooler capability for maintaining the temperature. The considerations that went into the thermal modelling of the full KMOS instrument can again be found in Burch et al. (2006). Section 5.6 in this document details a similar heat flux schematic considering conductive and radiative loads.

An important addition to the full instrument thermal loads is the heat load from the instrument wiring (considered negligible in the cooling of a single spectrograph in Oxford).

The control electronics were similar to those described during the Oxford tests. The software also shared the same interfaces and the end data was tagged with similar header information for data reduction procedures. The key differences in the UK ATC setup were the ability to stabilise the sub-assemblies for longer periods and the ability to rotate the full instrument to impose varying gravity vectors on the setup. The full setup at the UK ATC is the same as the setup planned for the instrument on the VLT UT2. The tests I carried out using the UK ATC setup are presented in the next chapter.

2.4 Summary

In this Chapter I have described the KMOS spectrographs and their sub-assemblies in the Engineering model and Science grade setups, along with the methods and results of the alignment procedures. The design of the cryogenic test facility in Oxford, the suitability of a basic thermal model to predict thermal response and the setup of the various control systems have also been presented. The achievability of an operational environment for optical testing of the modular components of a large project in the Oxford HIRDLS facility (and possibly facilities like it) has been demonstrated, with the procedures now available as a potential reference for future large, module-based projects that will begin to be developed for other large telescopes (e.g. Harmoni (Thatte et al., 2010a) for the European-Extremely Large Telescope (E-ELT)). The next Chapter details the range of optical and mechanical tests of the spectrographs conducted at the Oxford Test facility and at the UK ATC using the full KMOS instrument.

Chapter 3

KMOS testing

In this Chapter I describe the tests carried out in the Oxford facility and at the Edinburgh ATC. These were carried out to check performance against the design specifications. The areas in which the initial configuration did not meet specifications are also presented along with the solutions employed for reference in future projects. The amount of data gathered was substantial and so I only provide a representative sample here, with any key or useful results summarised in tables for reference.

Oxford Tests

The list of tests carried out during the testing in the Oxford facility was as follows:

- Ensuring cryogenic operability of components and repeatability of mechanisms.

This was the first simple test to make sure a thermal cycling of assembled components did not cause distortions or loosening of secured parts. It was also crucial to have a preliminary check of the repeatability of the cryogenic motors before more strenuous testing at the ATC.

- Through focus run for each band to determine the best focus position across the detector.

This was intended to make sure best focus was achievable within the run of the focus stage (which had a range of 2.1mm in 0.01 mm increments), that the best focus positions of each band coincided

(confirming the achromatic nature of the camera) and to characterize the tip/tilt and form of the focal plane.

- Central wavelength determinations for each band and a preliminary assessment of spectral and spatial resolution.

The nominal alignment of the gratings needed to be checked and possibly adjusted to confirm that the spectral coverage was adequate for each band across the detector and that the specifications for the resolutions at the central wavelengths were met, along with spatial resolution checks.

UK ATC Tests

The tests carried out at the UK ATC were:

- Repeatability of cryogenic mechanisms under varying gravity vectors and flexure measurements.

The cryogenic motors needed to be tested while the instrument was held in an 'on-scope' environment, under rotation and suspended. The flexure measurements were used to find sources of movement within the instrument and to determine if the movement in the spatial and spectral directions of slitlets on the detector were within specification.

- Measurement of the spectral and spatial PSFs at their true focus position along with focal plane mapping.

This was performed to ensure the specified PSF size in each waveband was achieved and to measure any variation or distortion in the focal plane.

- Spectral resolution measurement at best focus.

This was to get a final determination of R at central wavelength (λ_c) and a measure of the curvature in resolution ($R(\lambda)$).

The specifications on the image quality are summarised in the original KMOS Technical Specification document: Ramsay Howat et al. (2005a), sections 3.5.6 and 3.5.11. The wavelength coverage

and spectral resolving power requirements are given in sections 3.5.20 and 3.5.19 in the same document respectively and are also found in Ramsay Howat et al. (2007). They are summarised in Table 3.1.

Requirement	**Specification**
Image Quality	Instrumental FWHM $< 0.2''$ across the entire FoV
Spatial Sampling	$0.2'' \pm 0.025$
Wavelength Ranges [1] (minimum range to be covered)	(I/z) 0.80 - 1.08 μm (Y/J) 1.05- 1.37 μm (H) 1.45 - 1.85 μm (K) 1.95 - 2.50 μm (HK) 1.50 - 2.38 μm
Spectral Resolving Power[1], R (minimum in band)	I/z > 2800 Y/J > 3200 H > 3800 K > 3000 HK > 1800
Throughput For KMOS opto-mechanical system only. Excludes telescope efficiency, atmospheric transmission and detector QE	I/z $> 20\%$ Y/J $> 20\%$ H $> 30\%$ K $> 30\%$ $> 60\%$ of peak throughput at the extremes of the bands
Flexure	$< \pm 0.72$ spatially $< \pm 0.45$ spectrally
Repeatability	< 0.2 resolution elements

Table 3.1: KMOS Image Quality Requirements
[1] I/z and HK requirements updated in more recent document by Ramsay Howat et al. (2007)

3.1 The Oxford Test Results

In order to analyse the Oxford test data, a series of `IDL` programmes and `IRAF` scripts were written. The main `IDL` script allowed user choice of a single PSF measurement in the desired waveband, a through focus determination (producing FWHM determinations in the spectral and spatial direction at the centre-of-field best focus position) and a focal plane map displaying any curvature or irregularities in the focal plane. Prior to analysis by the `IDL` programme a basic reduction was performed of the data, which involved dark-frame subtraction from the arc and halogen frames in each band. Interpolation across the bad pixels was attempted, but due to the large percentage of

bad pixels, this was abandoned as the PSF image shapes were being affected too greatly.

3.1.1 Mechanical Checks

The mechanical checks in the Oxford setup were simple. Repeatability of the grating mechanisms were within the ±0.2 pixel specification and the focus stage and grating mechanisms both operated smoothly and without complication. The method of determining this shift and details of more rigorous testing are given in section 3.2.1.

3.1.2 Best Focus Determination

To determine the best focus position of points across the detector, the through-focus run (arc source) data was fed to the custom `IDL` programme. This data consisted of 0.1 mm increments along the focus stage for each waveband (totalling 21 focus positions per band). Dark frames were taken before the first focus position and after the last focus position for each band - to remove background noise. Exposure times varied depending on waveband due to the spectral dependence on the input fiber throughput and source flux. The analysis software first required selection (via cursor input or coordinate file) of a single point or several points across the field. An image at mid-focus position was used for selection. The arc line selected would then be centred via a 2D Gauss fit.

Determining the best-focus position proved difficult using the standard method of taking spectral and spatial cuts across the PSFs and measuring the FWHMs of fits to the arc line profiles. The large number of bad pixels on the detector meant that a large number of profile cuts would give unreliable results, particularly far from best focus. To more reliably constrain the best-focus positions a central power method (CPM) was employed. The total flux contained within an emission line is assumed constant. As we move through-focus the size of the PSF reduces. As the flux is conserved, it becomes more centrally concentrated. To illustrate how this central flux increases, a basic model PSF was created adopting the elliptical beam profile (the shape caused by the input cone-baffle system) of the real data. In the model, the total power under the beam was fixed and the counts in the central pixel were measured as best-focus was approached (setting the best focus

PSF size as 1 pixel along the spatial axis). The approach to max-power/best-focus can be fit by a Lorentzian profile (see Figure 3.1).

In the test data, the Gauss centroid positions were used in each image at each focus position to sum the 4 pixels in the spatial and spectral directions (4x4) in the centre of each emission line selected. This enabled the central PSF flux to be compared between each image (focus position). A 4 pixel central aperture was adopted due to movement in the PSF centre of $\sim \pm 0.2$ pixels, with beam defocus. So, in the test data we see that as best focus is approached, the flux in the centre of the PSF reaches it's maximum (assuming a constant input source and after dark-frame subtraction). The left plot in Figure 3.1 shows the central pixel flux (in normalised counts) against focus position for an argon arc line at $\sim 1.7\mu$m close to the centre of the field. The approach to maximum central flux followed a Lorentzian profile, as expected from the model fit, seen on the right of Figure 3.1. For beam sizes close to the best focus position, the 4x4 pixel aperture encompassed the full flux of the PSF. This resulted in a flattening of the profile around the peak.

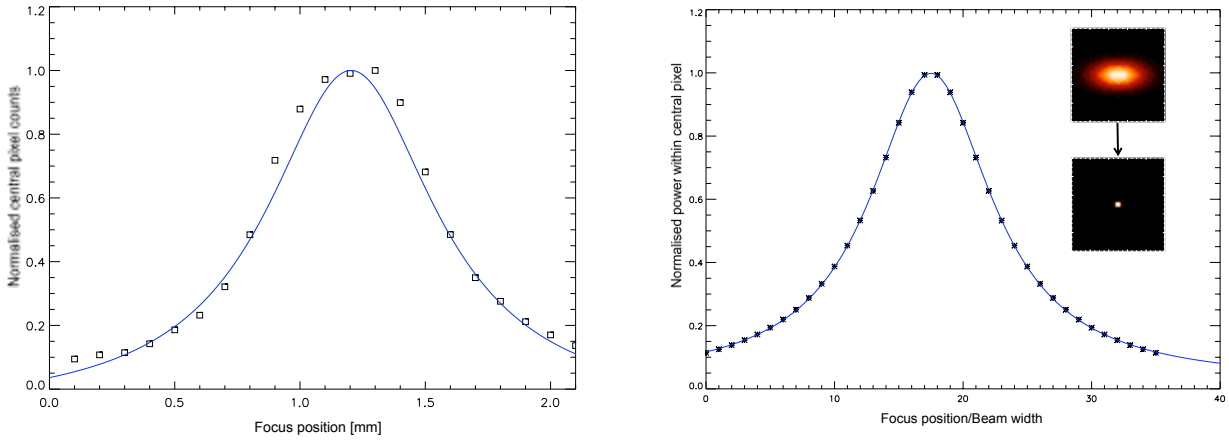

Figure 3.1: Central pixel flux against focus position for KMOS arc line and model PSF.

Figure 3.3 shows the arc line PSF from an image taken nearest best focus[1]. Slight ghosts from back-reflections in the input cone-baffle system can be seen, but the levels are of the order of 5-10% of the central peak, as can be seen in Figure 3.2. The Gaussian fits to the spatial and spectral cuts in this plot (corresponding to the horizontal and vertical lines in Figure 3.3) indicate the

[1]As the images were taken in 0.1 mm steps, the PSF at predicted best focus was not available in the Oxford test data.

achievability of equal spectral (red line) and spatial (blue line) focus positions. The measured σ here are 0.58±08 and 0.63±0.10 pixels for the spectral and spatial PSFs respectively. The PSF FWHM were equal close to best focus due to diffraction effects dominating in the spectral direction (explained in the next section).

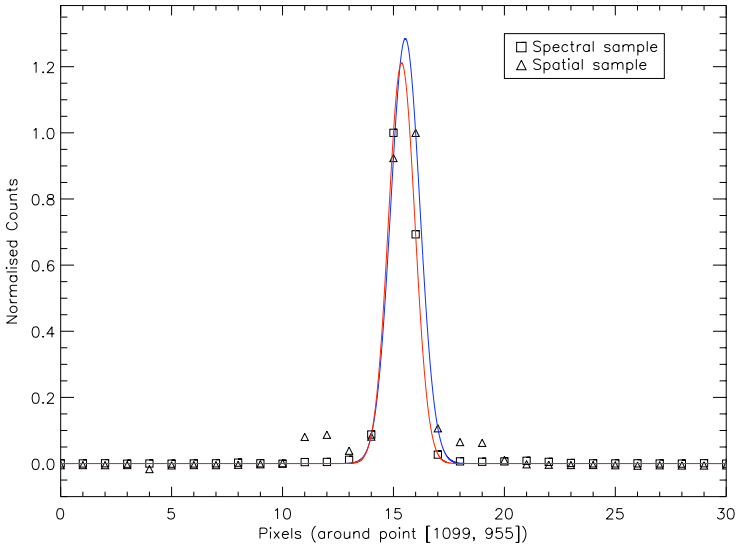

Figure 3.2: Gaussian fits to the spectral and spatial cuts to an arc line.

3.1.3 Spectrograph PSF

Using the observed PSF in our tests, it was required that we showed that the true spectrograph PSF was within specification (1 pixel spatially and various R specifications across the wavebands - See Table 3.1). To recover the spectrograph PSF from our measurements we needed to consider finite source effects (finite size of fiber input) and diffraction effects.

The full input slit is 254 mm along the spatial axis. This is demagnified to 2048 pixels across the detector. Taking the detector pixel size as 18μm, this translates to a demagnification factor, $m \sim 0.145$. Thus, spatially the fiber diameter is 0.4 pixels and spectrally the diameter is 0.29 pixels due to additional anamorphic demagnification by the grating. The demagnification by the grating is wavelength dependent, but I adopt the average factor of 1.4 here, taken from Lewis et al. (2007).

Due to the finite f-ratio of the input beam, diffraction was important. Fraunhofer diffraction by the camera would produce an Airy profile for the diffraction pattern. The width of the output

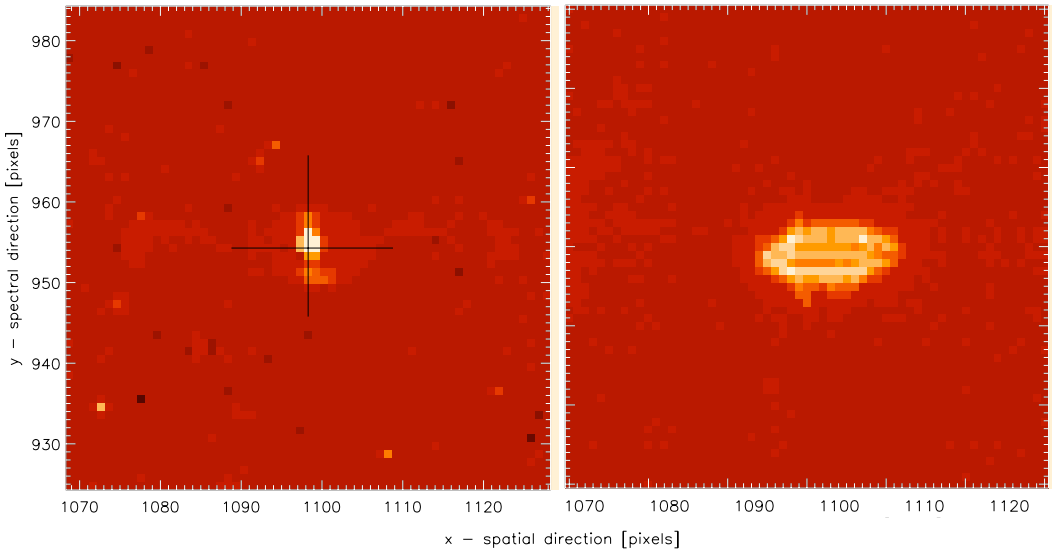

Figure 3.3: False-colour images of an arc line at best-focus and out of focus.

beam would be approximated by,

$$\sigma_{Dir} \approx \frac{\lambda}{2.35} \left(\frac{f}{d}\right)_{Cam,Dir} \tag{3.1}$$

where λ is the wavelength of the input and $\left(\frac{f}{d}\right)_{Cam,Dir}$ is the f/# in the spectral or spatial direction (Dir) for the camera, which relates to the input f/#s (produced by the cone baffle system, mimicking the IFU output) via,

$$\left(\frac{f}{d}\right)_{Cam,Dir} = m \left(\frac{f}{d}\right)_{In,Dir} \tag{3.2}$$

The input f/# is 16.7 in the spatial direction and 46.8 in the spectral direction. The fits shown in Figure 3.2 were to an arc line at $\lambda = 1.7\mu$m. This results in,

$$\sigma_{spatial} = 1.69 \text{ [}\mu\text{m]} \text{ or } 0.09 \text{ [px]}$$

and

$$\sigma_{spectral} = 4.77 \text{ [}\mu\text{m]} \text{ or } 0.26 \text{ [px]}$$

If we neglect the slight broadening effect of detector cross-talk, we can determine values for the instrumental width (σ_I) by performing deconvolutions of the measured profiles (σ_m) with the effects of a finite source (σ_f) and diffraction (σ_d),

$$\sigma_I = \sqrt{\sigma_m^2 - \sigma_f^2 - \sigma_d^2} \tag{3.3}$$

giving

$$\sigma_{I,spatial} = 0.55^{+0.08}_{-0.09} \text{ [px]}$$

and

$$\sigma_{I,spectral} = 0.56^{+0.09}_{-0.09} \text{ [px]}$$

The requirements state $0.2''$ (FWHM) instrumental resolution in the spatial direction (Ramsay Howat et al., 2005a) and $0.064''$ FWHM for the spectrograph only (Ramsay Howat et al., 2005b). The results here indicate an instrumental resolution of $0.26''^{+0.01}_{-0.02}$ (FWHM) in the spatial direction, in the centre of the H-band. The σ_m obtained was not from an image at best-focus and there was not a best focus image available from the Oxford dataset. To predict the spatial FWHM of an in-focus point source through the spectrograph, the through-focus measurements for the H-band arc data were analysed with the `IDL` script mentioned earlier. The approximate best focus position was determined using the central-pixel-power method. Images at four focus positions either side of this best focus were then used to measure the FWHM of a central H-band arc line (at $\lambda \sim 1.7\mu$m). These then enabled a prediction of the FWHM ($2.35\sigma_{p,spatial}$) of the arc line at the *true* best focus position. A plot of $\sigma_{m,spatial}$ against focus position is given in Figure 3.4. The fit to the relation in Equation 3.4 is shown in blue. The errors shown are on the standard deviations of the Gaussian fits to the PSFs. These errors increase to $\sim \pm 0.2$ pixels for the out of focus PSFs, due to lower S/N and bad pixels. The fit is severely under-sampled at the turnover and so the minimum σ has a an error of $\sim 20\%$. The approach to best-focus for σ is approximately linear far out from focus and adopts a decaying profile towards the turnover. Of course, a linear approach is not well fit to the turnover and thus under predicts the PSF. Polynomial fitting is also adopted in other best-focus determinations, but this too fails to fit the turnover adequately, primarily because of

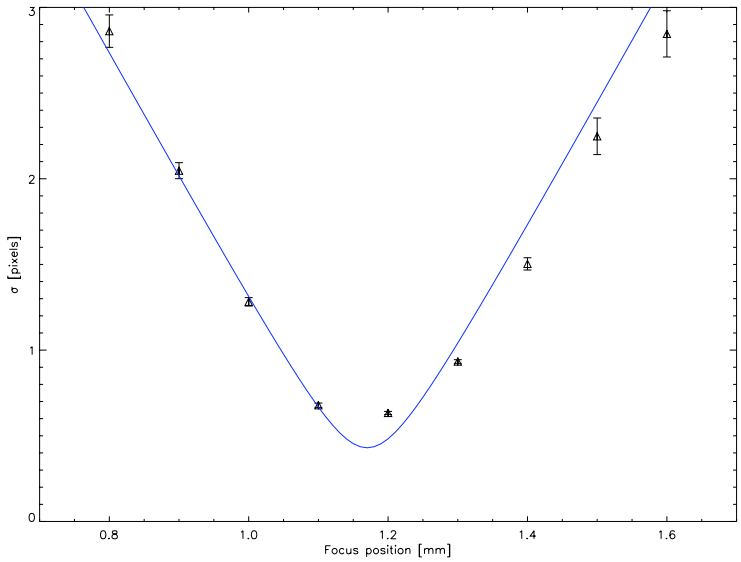

Figure 3.4: Achievable spatial PSF σ for the central arc line in the H-band Oxford data.

the under-sampling in this case. The true form of the approach is represented by equation 3.4. This describes the change in spot size of a finite Gaussian beam with distance from the best-focus position.

$$\sigma(z) = \sigma_{bf}\sqrt{1 + (\frac{z}{z_R})^2} \tag{3.4}$$

where

$$z_R = \frac{\pi\sigma_{bf}^2}{\lambda}$$

and is called the Rayleigh range (indicating the distance along the optical path that the beam profile would appear double that of the in-focus image). This does assume the system is diffraction limited, which we are not here, and a quality factor is usually applied to z_R, decreasing it. Applying this factor would act to decrease $\sigma_{p,spatial}$. Therefore, the presented $\sigma_{p,spatial}$ is a conservative prediction.

A fit of this function to the test data indicates a $\sigma_{p,spatial}$ of $\sim 0.43 \pm 0.1$ pixels, which indicates an instrumental (spatial) FWHM of 1.01 ± 0.24 pixels ($0.20'' \pm 0.05$) . There is an error on this from the poorer fitting further out from focus. This is due to the small number of pixels involved in the cuts of the PSF and by the deviation from a Gaussian profile of the actual beam. However, this did indicate the ability to achieve the required spatial resolution at the centre of the field. The predicted spatial resolution degraded as measurements were made towards the edges of the

detector, as seen later in Table 3.5, due to an irregular focal plane, discussed in Section 3.2.2.

To test the achromatic nature of the camera barrel, arc lines towards the centre of the detector (centre of the slit and near the λ_c of the band) were used across all bands to determine predicted best focus positions. The results of this can be seen in Figure 3.5. The best focus predictions across the four high resolution bands (Iz, YJ, H, K) are given, with errors increasing towards the K-band due to lower S/N data available in this setup (errors are typically <0.01 mm). The common focus position is arbitrary, however the slope is slight at 0.01 and the spread is small at 0.007 mm (within the errors), below the resolution of the focus stepper motor mechanism. Equation 3.4 can be used to translate this focus position variation to PSF variation. A change in focus position of 0.01 mm indicates a $\sim 2\%$ spatial PSF FWHM variation.

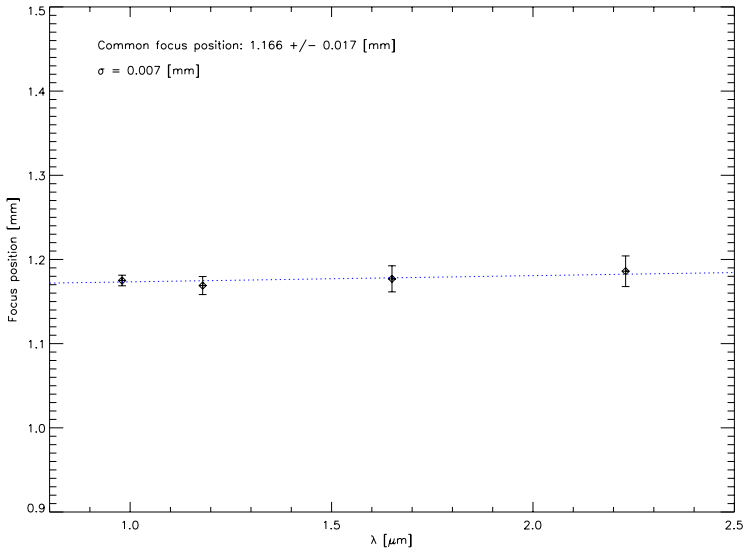

Figure 3.5: A representative sample of the centre-field focus positions across the KMOS I/z, YJ, H and K grating configurations.

3.1.4 Determination of central wavelengths and R at λ_c

To determine the central wavelengths of the five grating configurations an **IRAF** script was created. The task required an arc frame, a halogen frame and their appropriate dark frames for noise subtraction. Quick reductions were initially performed on the files and the halogen frame was used to trace apertures. This was possible using the **IRAF** task `aptrace` that fits a Legendre polynomial

to sampled points along the vertical axis of the image, determining aperture positions. For the Oxford tests, this traced the $\sim$ 1pixel wide, near-focus halogen lines through the 17 inputs fibers and for the Edinburgh tests this traced the gaps in between the slitlets (in-focus). The task `apsum` was then run on the arc frame, using the halogen frame and the trace reference file as markers for the apertures over the which the arc spectra were to be extracted. Once a single aperture was chosen, the task `autoidentify` matched the emission lines in the cut to arc line positions given in reference files that related to the lamps used for each band. It then applied a Legendre polynomial fit to the identified line positions to determine a wavelength grid. Initial values of the required dispersions and wavelength ranges were fed to the task as a starting point to aid in the auto-identification (interactive identification was also possible if too few lines or the wrong positions were identified by the task).

The coordinate fit from `autoidentify` was used in `fitcoords` to produce a wavelength solution that could be evaluated per pixel with `fceval`. So, for a solution using an H-band arc frame, for the central slitlet on the detector, the wavelength range was found to be 1.462 to 1.846μm and the central wavelength was 1.652μm. The solution varied depending on the slitlet chosen, due to the slit curvature. Once the wavelength grid had been determined, an `IDL` routine was designed to evaluate the spectral resolution (R) across the band. The routine identified the arc lines along the spectrum and fit Gaussian profiles to each. The FWHMs of these fits were then used to compute $R = \lambda/\Delta\lambda$. Preliminary checks of R in the KMOS spectrograph module setup in Oxford required consideration of the source size in the spectral direction before computing R. As the fiber size was nominally 0.29 pixels on the detector, the Gaussian fit first needed to be deconvolved with a top-hat of 0.29 pixels in the width and then convolved with a top-hat function representing a fully illuminated slit at 2 pixels (otherwise the R calculated from the measured FWHM of the fit would indicate a much higher resolution than in the final instrument). The lack of a truly in-focus image in the Oxford data also reduced the measured spectral resolutions. However, these were still found to be close to specification (with the H-band $R_c^{oxford} \sim 3500$).

A sample dataset is given across Tables 3.3, 3.4 & 3.5 for a set of H-band images. Table 3.3 shows the expected FWHM in the spectral direction and expected R corresponding to these for six

positions along the slit and across five wavelength positions. These are derived from the simulation results in (Lewis et al., 2007). Adjacent to these are the measured values of FWHM and R at similar positions from a set of near-focus (centrally) Oxford arc-line data. It can be seen that the spectral resolution approaches (but is still below) the required value (H > 3800 - see Table 3.1) towards the centre of the field (slit position $\sim$ 127mm, $\lambda \sim 1.65\mu$m), getting much worse at the wavelength and spatial extremes. When we look at the data from the H-band frame taken through the full instrumental setup (at the UK ATC with a fully illuminated slit and in focus at the centre) in Table 3.4, we see that, at the centre, the achieved resolution far exceeds requirements at $R \sim 4900$, as stated earlier, but this gets progressively much worse out to the corners of the field. The results from an H-band arc frame (full-instrument data set) cut can be seen in Figure 3.6. The image at the top shows the dispersed slitlet, with the spectrum plotted underneath. Several lines are highlighted, fit with Gaussian profiles. The variation of R with λ is shown by the red dashed line. Three lines are shown below the full spectrum with R values (at λ) of $\sim$ 3500 (1.52), 4660(1.60) and 4570(1.793).

The measured R values at the λ_c for each band, at the centre of the slit, in the full instrument setup are summarised in Table 3.2. These all indicate the requirements are surpassed in the centre of the field. The wavelength ranges measured are just for the central slitlet and will obviously vary with slitlet due to the slit curvature, as stated earlier.

Table 3.5 refers back to the spatial FWHM measurements described in Section 3.1.3. The data from the Oxford tests are presented again. Spatial PSF cuts to the arc lines at the same positions as in Table 3.3 were used to determine the spatial FWHM as a function of position in the focal plane. To convert the finite-source Oxford data to the expected point-source results through the full instrument, the measured PSFs were deconvolved with a top-hat function of width 0.4 pixels (the spatial diameter of the input fibers on the detector). We can see that in the centre of the field the image quality requirement ($0.2'' \pm 0.025$) is met (1.01 ± 0.05 pixels $= 0.20'' \pm 0.01$), but towards the extremes the image quality degrades to at least $0.7''$.

This irregular focal plane (seen across all wavebands) is discussed in more detail in Section 3.2.2, where I also discuss the source of the problem and the solution implemented, along with evidence

for the corrected, flattened focal plane.

Grating/Band	λ^r range [μm]	λ_c^r [μm]	λ^m range [μm]	λ_c^m [μm]	R_r	R_{exp}	R_m
Iz	0.80 - 1.08	0.98	0.82 - 1.10	0.96	> 2800	3580	3430
YJ	1.02 - 1.35	1.18	1.01 - 1.36	1.19	> 3200	3660	3430
H	1.45 - 1.85	1.65	1.46 - 1.85	1.65	> 3800	4220	4940
K	1.95 - 2.50	2.23	1.97 - 2.51	2.24	> 3000	4150	4550
HK	1.50 - 2.38	1.94	1.48 - 2.41	1.93	> 1800	2260	2310

Table 3.2: KMOS spectral requirements and measured values - r = required, exp = expected, m = measured. The λ ranges are defined for the central slitlet. The R_{exp} values are taken from the predictions of Lewis et al., 2007, calculated assuming the nominal wavelength range over 2048 pixels, with the nominal λ_c and a dispersion of 2 pixels. The R_m values are also taken at the centre of the band, with full illumination of the slit with out of specification L6 and collimator. All R values to 3.s.f.

Slit position [mm] :	0	25	50	75	100	127
λ [μm]	Expected FWHM (px)					
1.85	2.11	2.11	2.11	2.17	2.17	2.17
1.75	2.06	2.06	2.11	2.11	2.11	2.22
1.65	2.06	2.06	2.06	2.06	2.06	2.11
1.55	2.00	2.00	2.00	2.00	2.00	2.11
1.45	2.00	2.00	2.00	2.00	2.06	2.39
	Measured FWHM (px)					
1.85	3.04 ± 0.13	2.68 ± 0.08	3.78 ± 0.35	4.27 ± 0.23	4.48 ± 0.19	4.15 ± 0.20
1.75	2.55 ± 0.13	2.02 ± 4.92	2.87 ± 0.47	2.55 ± 0.12	2.32 ± 0.02	2.42 ± 0.05
1.65	2.33 ± 0.04	2.27 ± 0.11	2.27 ± 0.43	2.41 ± 0.03	2.32 ± 0.06	2.49 ± 0.11
1.55	2.17 ± 0.18	2.73 ± 0.37	2.63 ± 0.30	2.07 ± 4.77	2.30 ± 0.07	2.16 ± 0.35
1.45	3.38 ± 0.26	3.42 ± 0.17	3.16 ± 0.43	3.06 ± 0.33	4.18 ± 0.41	3.07 ± 0.29
	Expected R					
1.85	4486	4486	4486	4371	4371	4371
1.75	4358	4358	4244	4244	4244	4032
1.65	4132	4132	4132	4132	4132	4023
1.55	3968	3968	3968	3968	3968	3759
1.45	3712	3712	3712	3712	3611	3107
	Measured R					
1.85	3018^{+129}_{-119}	3414^{+104}_{-98}	2481^{+249}_{-207}	2195^{+123}_{-110}	2092^{+94}_{-86}	2259^{+111}_{-101}
1.75	3505^{+187}_{-169}	4406^{+1000}_{-1000}	3095^{+599}_{-432}	3486^{+173}_{-157}	3824^{+39}_{-39}	3667^{+71}_{-68}
1.65	3639^{+55}_{-54}	3731^{+193}_{-175}	3712^{+859}_{-587}	3578^{+41}_{-40}	3680^{+105}_{-100}	3426^{+151}_{-138}
1.55	3620^{+323}_{-274}	2875^{+447}_{-341}	2982^{+384}_{-305}	3779^{+1000}_{-1000}	3400^{+100}_{-94}	3627^{+699}_{-504}
1.45	2289^{+188}_{-162}	2259^{+116}_{-105}	2437^{+381}_{-290}	2516^{+302}_{-243}	1789^{+195}_{-160}	2433^{+248}_{-206}

Table 3.3: Expected & Measured Spectral FWHM and R (H-band - Oxford tests - with out of specification L6 and collimator). Expected R values are calculated using the model predictions of the FWHM in pixels, assuming the nominal wavelength range over 2048 pixels. Caveats on these results include a lack of consideration for slit curvature (wavelength range constant along slit) and the errors on the Gaussian FWHM fits neglect any line-spread function deviation.

Slit position [mm] :	0	25	50	75	100	127
λ [μm]	Measured FWHM (px)					
1.85	5.95 ± 0.40	3.76 ± 0.19	3.51 ± 0.83	2.92 ± 0.44	2.74 ± 0.44	2.09 ± 0.28
1.75	2.32 ± 0.03	2.10 ± 0.03	1.90 ± 0.01	1.02 ± 0.27	1.87 ± 0.02	1.80 ± 0.03
1.65	2.43 ± 0.06	2.32 ± 0.07	2.12 ± 0.06	2.01 ± 0.04	1.89 ± 0.05	1.73 ± 0.01
1.55	5.05 ± 0.24	4.34 ± 0.17	3.23 ± 0.12	2.56 ± 0.11	2.10 ± 0.10	2.01 ± 0.10
1.45	7.37 ± 0.49	6.63 ± 0.42	4.74 ± 0.23	3.56 ± 0.13	2.81 ± 0.07	2.74 ± 0.10
	Measured R					
1.85	1571^{+113}_{-99}	2499^{+133}_{-120}	2692^{+828}_{-512}	3235^{+572}_{-422}	3442^{+667}_{-480}	4514^{+698}_{-533}
1.75	3857^{+44}_{-43}	4266^{+72}_{-69}	4694^{+32}_{-32}	8782^{+1000}_{-1000}	4751^{+43}_{-42}	4942^{+75}_{-73}
1.65	3507^{+84}_{-80}	3659^{+105}_{-100}	3992^{+108}_{-103}	4220^{+92}_{-88}	4486^{+119}_{-113}	4942^{+42}_{-41}
1.55	1574^{+79}_{-71}	1829^{+76}_{-70}	2454^{+95}_{-88}	3087^{+143}_{-131}	3763^{+194}_{-176}	3936^{+213}_{-192}
1.45	1034^{+73}_{-64}	1149^{+78}_{-69}	1602^{+83}_{-75}	2131^{+80}_{-74}	2702^{+72}_{-68}	2740^{+106}_{-98}

Table 3.4: Measured Spectral FWHM and R across detector (H-band - Edinburgh tests - with out of specification L6 and collimator).

λ [μm]	Measured FWHM (px)					
1.85	3.44 ± 0.25	2.38 ± 0.15	3.57 ± 0.38	3.91 ± 0.21	4.34 ± 0.22	3.75 ± 0.12
1.75	3.02 ± 0.43	2.78 ± 0.35	2.25 ± 0.50	2.21 ± 0.13	1.84 ± 0.09	1.23 ± 0.01
1.65	2.70 ± 0.50	2.62 ± 0.41	3.32 ± 0.72	1.98 ± 0.19	1.38 ± 0.09	1.01 ± 0.05
1.55	3.09 ± 0.35	6.80 ± 3.33	2.38 ± 0.49	2.13 ± 0.49	1.28 ± 0.04	1.23 ± 0.03
1.45	9.78 ± 1.42	7.09 ± 0.48	2.63 ± 0.74	1.10 ± 1.04	4.29 ± 2.19	1.83 ± 0.08

Table 3.5: Measured Spatial FWHM across detector (H-band - Oxford tests - with out of specification L6 and collimator). The high percentage of bad pixels on the engineering grade detector ($> 30\%$) resulted in unreliable FWHM determinations further out from the centre, however the trend in PSF size can be seen to worsen (increase) radially.

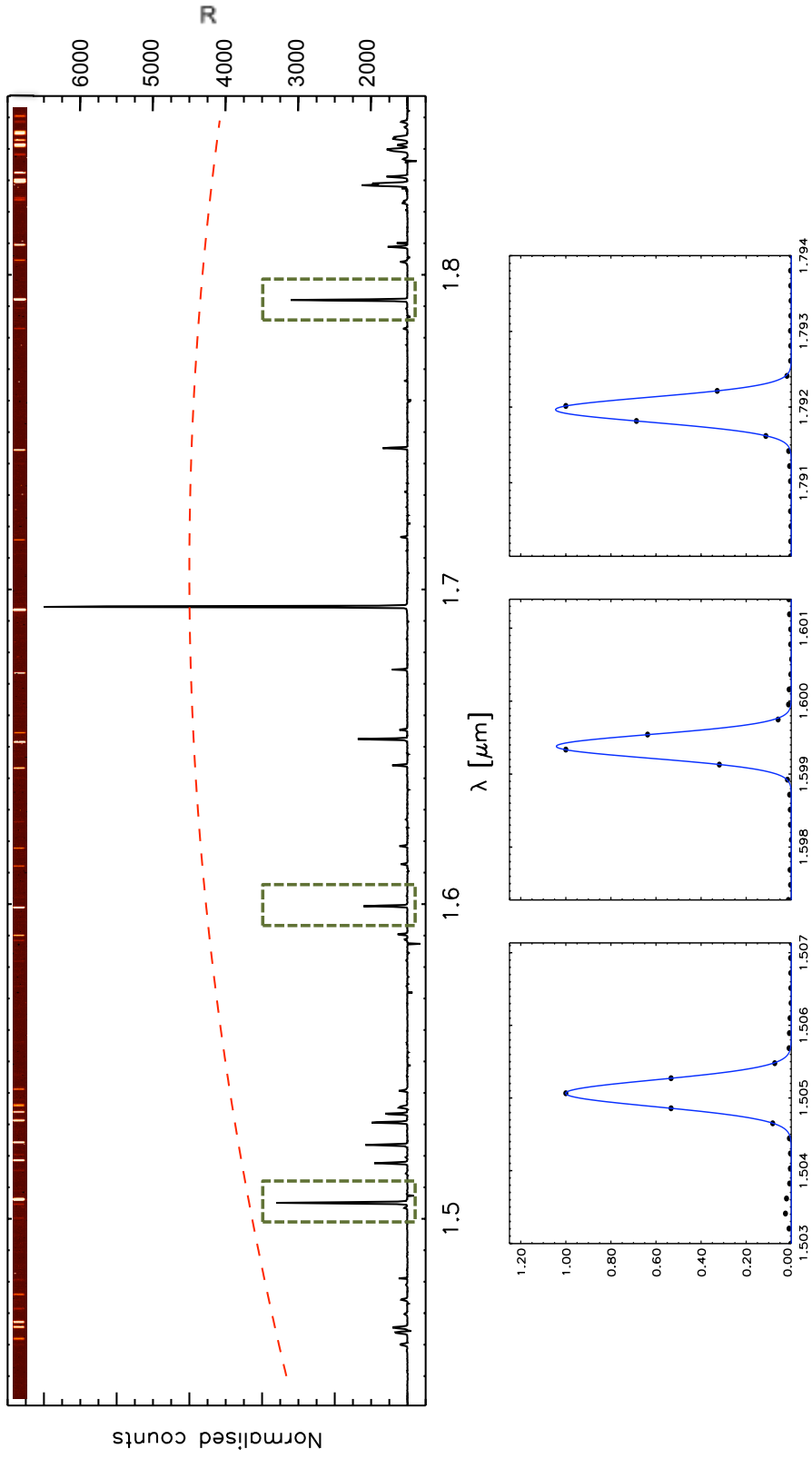

Figure 3.6: H-band argon spectrum through the central pixel of the central slitlet in the full KMOS optical train. This cut is taken from an out of specification focal plane image, with the centre of the field in focus only.

3.2 Edinburgh ATC tests

3.2.1 Mechanical tests

There were two major mechanical tests that needed to be carried out as part of the checks of spectrograph compliance. These were the repeatability of the grating mechanism(s) and the inherent flexure in the modules/instrument as a whole. The preliminary tests of these were carried out on the ES, integrated into the full KMOS structure at the Edinburgh ATC. The status of the instrument at this stage in the testing involved the full optical paths of two pick-off units through the H-band configured ES. One arm/IFU sent its output through the centre of the spectrograph entrance slit, while the other occupied the end of the slit nearest the collimator.

The facility at the ATC involved a full Nasmyth rotator to mimic the gravity vectors KMOS would experience on the VLT UT 2. The two arms were set in their calibration positions, outside the FOV, and were observing the argon arc source. Basic reductions were undertaken involving dark frames taken between arc frame exposures. The detector was an engineering grade model.

Repeatability

The requirements on repeatability related to the grating wheel and the repeatability of its cryogenic motors. The requirement was that a slitlet should be repeatable to within 0.2 resolution elements, which translates to 0.2 pixels spatially and 0.4 pixels spectrally, upon a full rotation of the grating wheel and under slew of the telescope. To test this on the grating wheel, an in-focus slitlet arc-line had its spatial and spectral edge positions determined in pixel space. The grating wheel was then rotated to various positions, while operating the Nasmyth rotator. The grating was then moved back into its original position (approaching from the same direction to avoid hysteresis in the mechanism) and the slitlet position was then re-measured relative to the detector pixel grid. This was performed fifty times.

This may seem like a lot of repetitions, but as shown in Figure 3.7 (right plot), there is a jump in the position spatially of $\sim$ 3 pixels and spectrally $\sim$ 2 pixels after 23 repetitions. On closer inspection of the grating wheel it was discovered that a small indentation in the edge was causing the end-position to jump randomly. Upon re-chamfering this edge and performing the

repeatability tests again, we can see that the as-designed performance of the grating mechanism is within specifications (left plot), with a movement in the spectral and spatial directions of less than 0.1 pixels.

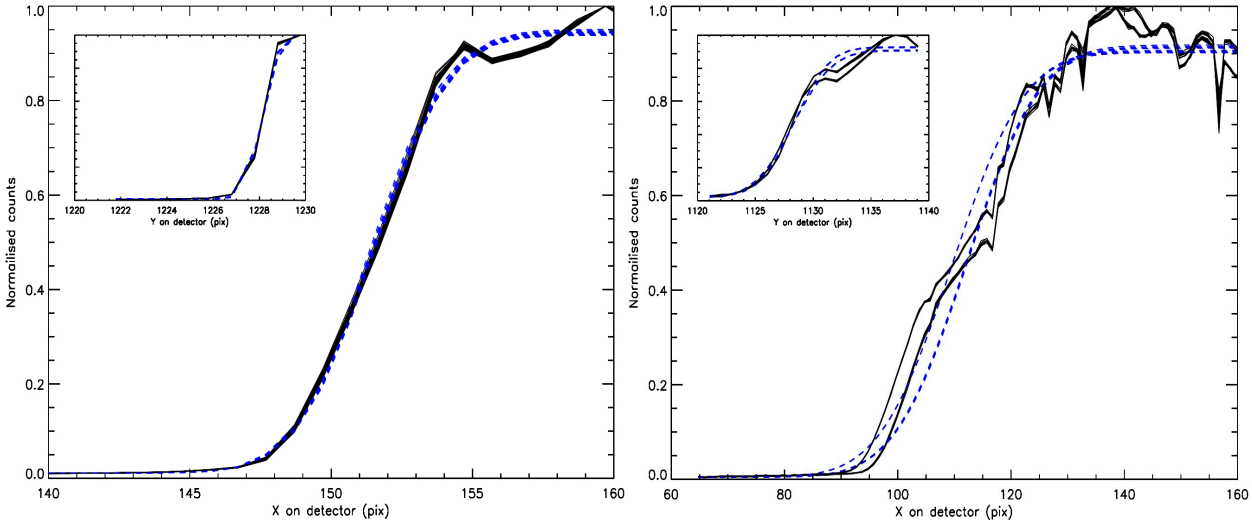

Figure 3.7: Grating mechanism repeatability measurements. *Right plot: Before re-chamfering.* Cut along spatial direction of a slitlet arc-line (x, in pixel space). The black line indicates the sampled data, blue dashed line is an edge-function fit to monitor the position of the slitlet edge. The plot inset is a cut along the spectral direction (y, in pixel space). *Left plot: After re-chamfering.* The same cuts were taken and this time the repeatability was within 0.1 pixels.

Flexure

Flexure is unavoidable in any instrument that is undergoing rotation and slewing motion at a telescope. A certain level of flexure is acceptable, provided it is predictable and repeatable. If the flexure is too great there is a risk of losing predictability and increased difficulty in tracking spaxels during the data reduction phase. The requirements on the flexure were $< \pm 0.72$ pixels in the spatial direction and $< \pm 0.45$ pixels in the spectral direction, peak to peak (see Table 3.1).

To gauge the flexure, slitlet positions were measured at various points along the outputs of both arms. The Nasmyth rotator, at this point in the project, had a rotational range of $\sim 180°$. This allowed measurements of the slitlet positions to be taken at 10° intervals from $-55°$ to $+125°$, defining 0° as the position where the grating wheel back face was perpendicular to the ground. Figure 3.8 shows the spatial (left) and spectral (right) flexure in the instrument. It can be seen

that in the ES there was ±3.5 pixels of spatial and ±0.45 pixels of spectral flexure. This was outside of the specifications on flexure. It was determined that the source of the flexure was across the grating-camera barrel-detector optical path on each spectrograph. An extra stiffening frame (aluminium) was attached along the tops of these three sub-assemblies to inhibit their movement along the optical path. Repeating the same analysis indicated a final flexure of $< \pm 1$ pixels spatially and $< \pm 0.4$ pixels spectrally. Thus the spectrograph flexure was deemed to be outside specification in the spatial direction.

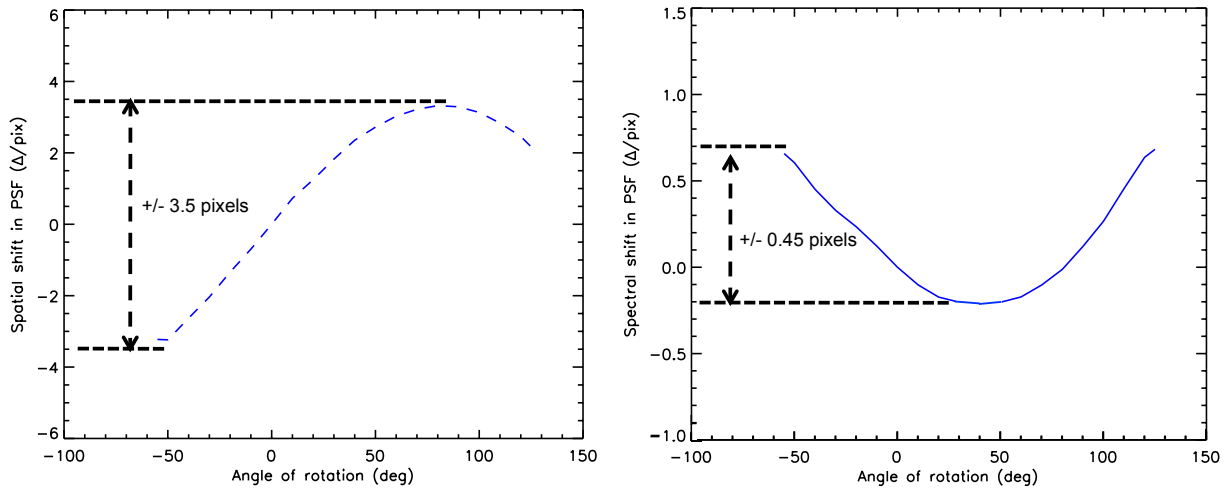

Figure 3.8: Spatial (left) and spectral (right) flexure plots in terms of slitlet movement in detector pixel space. As the gravity vector rotates, the translational movement on the detector follows a sinusoidal pattern. The blue lines (dashed and solid) indicate fits to the data, taken at 10° intervals.

3.2.2 The KMOS spectrograph focal plane and PSF variation

It was discovered that the KMOS PSF varied across the detector, radially worsening out from the centre of the field. This issue was not simply tip/tilt, but it was a curved or irregular focal plane. The effect in an arc frame image from testing in the full instrument can be seen in Figure 3.9.

Using the CPM described earlier to find the best focus positions across the grid of an arc frame, we can map the defocus as a function of x and y on the detector. We are thus able to map the focal plane. This was initially tested on the Oxford data set, but due to the poor quality of the detector the plane was severely under-sampled in the top-left corner and at several other locations

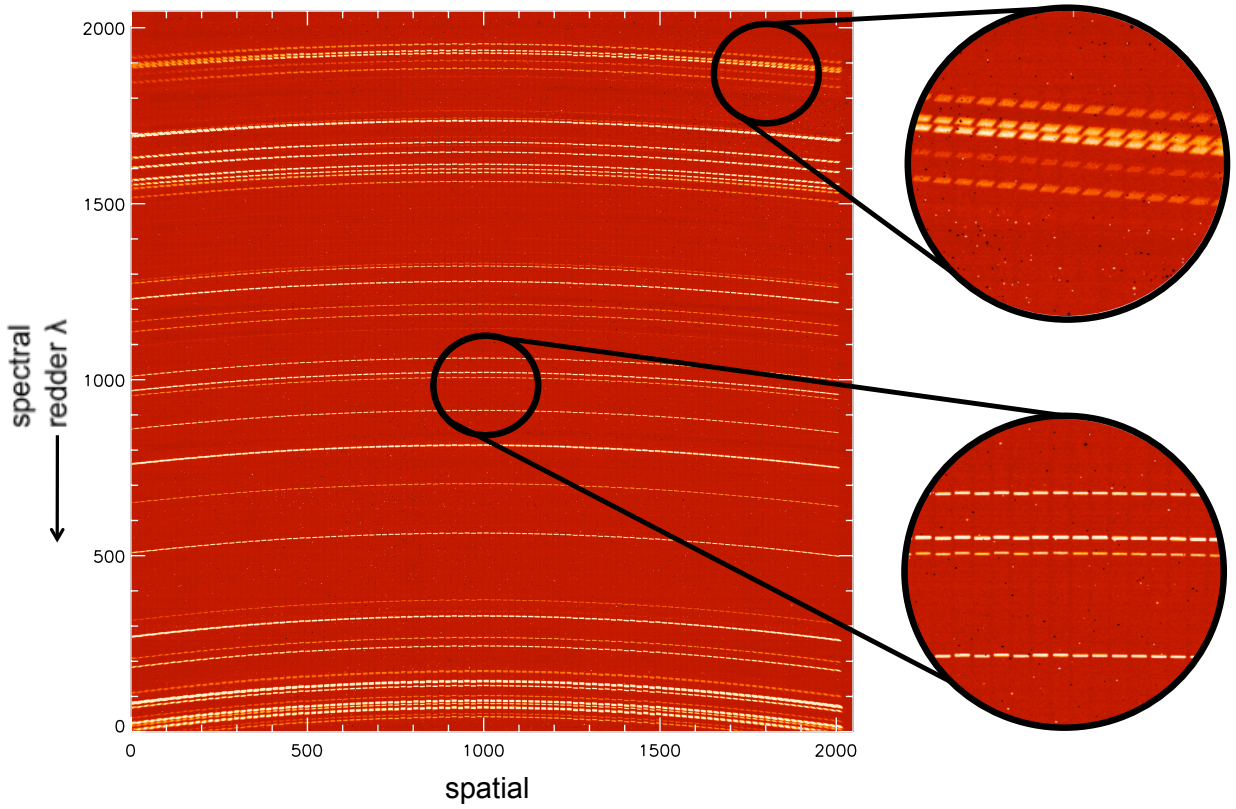

Figure 3.9: A false colour image of the full H-band focal plane, through a fully populated spectrograph being fed by 8 arms/IFUs.

on the chip. We could only determine a 1st order plane fit (tip/tilt) to the defocus positions. The science grade detectors on the integrated module(s) in Edinburgh allowed sampling across the full field of the detector. To obtain a focal plane map, one hundred points were taken across the chip, across several arc-lines and slitlets.

A first order 2D plane was fit to the defocus positions across the field (see Figure 3.10 - top right contour plot) and the residuals between the defocus points and the fit were obtained (bottom two scatter plots). Curvature in the residuals indicates a curvature in the focal plane. A 3rd order polynomial fit to the residuals in x and y (physical coordinates on-chip) highlights the apparent curvature in the focal plane (top left contour plot). The spectral curvature is large, with a maximum deviation of nearly 0.4mm, from the best focus position in the centre, at the edges of the field (bottom right plot). The spatial residuals exhibit a large scatter, with a maximum deviation close to 0.3 mm at the extremes (bottom left plot). The dashed lines in the two residual plots in

Figure 3.10 indicate the scatter allowed by the requirements. These requirements state that the PSF size shall not deviate by more than $\pm 0.025''$ of the required $0.2''$ nominal width (see Table 3.1). Using the relation between PSF σ and focus position in Section 3.1.3, this becomes $\sim 55\mu$m at $\lambda = 1.65\mu$m (ranging from 60 down to 50 microns over the H-band range $\sim 1.45 - 1.85\mu$m). The red and blue dashed lines in the spatial-residuals plot indicate the longer and shorter wavelength ends of the chip respectively (. It can be seen that in the centre of the chip the required focal plane scatter is nearly met, whereas the edge deviations are completely outside the requirement.

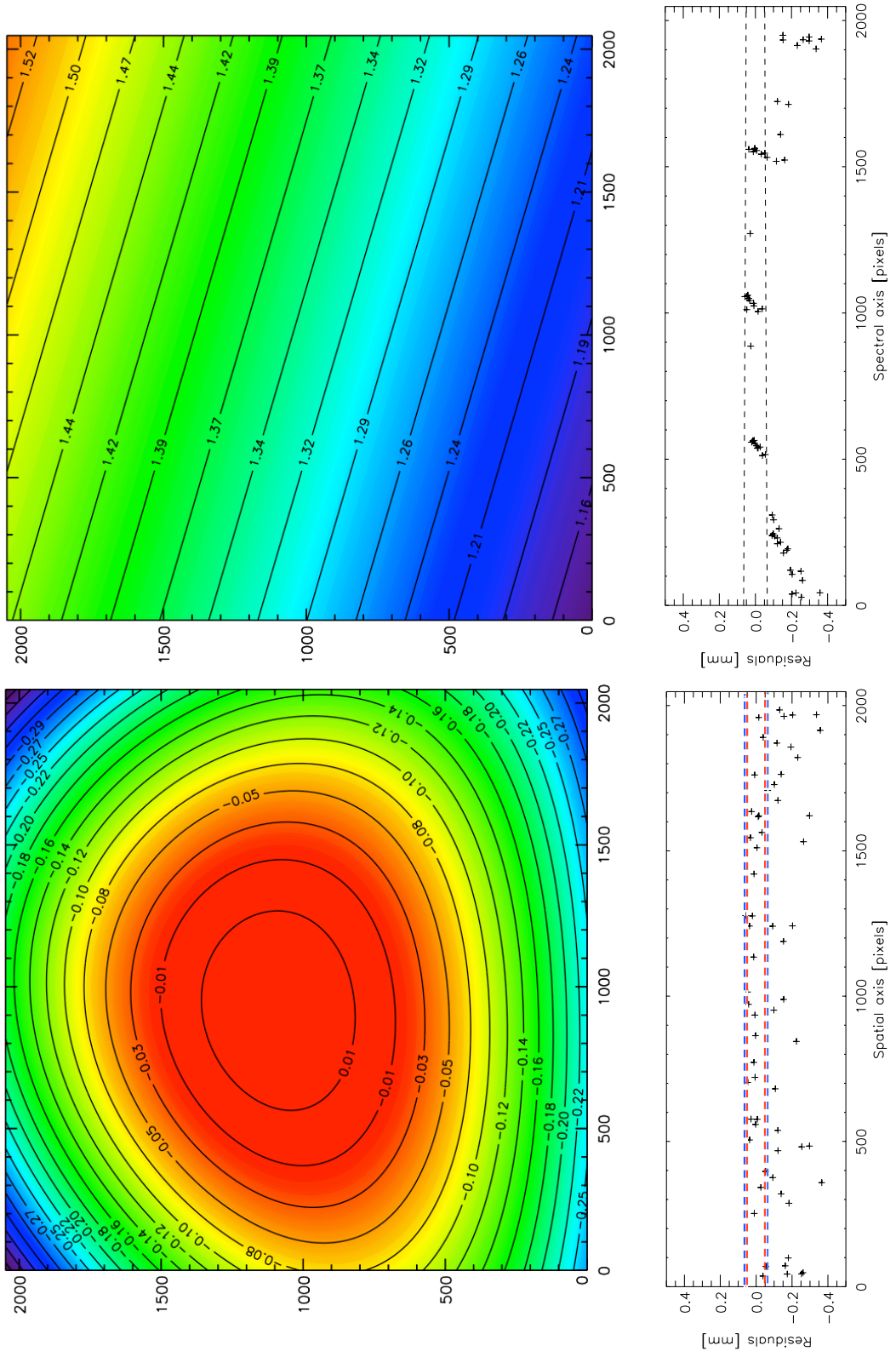

Figure 3.10: Focal plane contours and residual plots.

It can bee seen in Figure 3.9, that the out of focus slitlets at the top right of the field are of a different shape to the slitlets in the centre of the field. The central slitlets do not take on this shape if they are placed out of focus. Closer inspection of the Oxford arc frames show tails on the PSFs in the corners of the field. The image quality problem was in a component of the spectrograph.

There were two possible explanations for this PSF variation and focal plane curvature. As the PSF shape was a function of spatial and spectral position, the source of the aberrations could be tracked down to the camera barrel. The surfaces of six lenses of the barrel (L1 to L6 in designation) were defined in terms of their 'sag' (surface profile). The last lens (L6 constructed from Zinc Selenide - ZnSe) had aspheric surfaces (rotationally symmetric about the optical axis, with a radially varying radius of curvature). The sag of a surface on L6 is parameterised by a summation of the expression for a conic profile of the surface and higher order aspheric terms,

$$z(r) = \frac{cr^2}{1 + \sqrt{1 - (1+k)c^2r^2}} + \alpha r^4 + \beta r^6 + \gamma r^8 + ... \tag{3.5}$$

where $z(r)$ is the surface profile/sag, r is the radial distance from the optical axis, c is the curvature[2], k is conic constant (0 = sphere, >-1 = ellipse etc) and $\alpha, \beta, \gamma...$ are the aspheric coefficients. Equation 3.5 is used to derive the parameters and aspheric coefficients to be sent to the manufacturer. The form of the coefficients change with temperature, as the physical dimensions of the lens change. So, the terms are initially defined at the required operating temperature of the lens(es) (at 130K) and scaled up to ambient ($\sim$ 293K) for manufacture and assembly. It was initially thought that an oversight apparent in the drawings sent for manufacture, meant that the unscaled cold coefficients were used. However, the effect on the aspheric terms (the terms that would have more effect on the extremities of the image, as in Figure 3.9), although noticeable, were not significant enough to explain the aberrations. They were within the surface tolerances on the lens.

Another source of potential error was the curvature term, as an incorrect sign for c would result in an incorrect sign for the sag and an incorrect absolute value. Computing the absolute value of the sag ($z(r)$) for various points, moving radially outward from the lens centre for a negative curvature and a positive curvature, adopting the same aspheric coefficients in each case, indicates

[2]Inverse of radius of curvature.

a significant divergence as the edge of the lens is reached, as shown in Figure 3.11. Centrally we see little change between the curves representing the correct sign for c (black) and the positively signed c (blue), but out towards the edges divergence occurs. So, if a positive sign for c had been used (as opposed to the negative sign originally in the design for L6 as part of the full barrel) in the manufacture of L6, this divergence would lead to the distorted PSFs at the corners of the field. Thus, a misinterpretation or miscommunication of the sign convention during manufacture was determined to be the cause of the PSF distortion and was verified with CMM measurements of the L6 sag profile (please see the full report in Tosh, 2011).

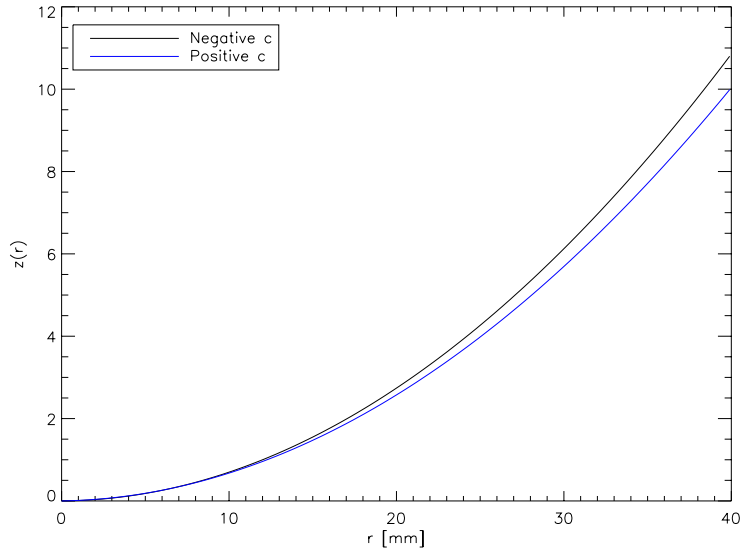

Figure 3.11: Effect on surface profile of a reversal in sign of curvature.

The corrected Focal Plane

The L6 lenses from all three spectrographs were re-machined and re-coated to correct the curvature. A through focus-run of arc frames taken with the H-band setting was conducted to re-fit the focal plane. The residuals of the new focal plane can be seen in Figure 3.12. The top plot shows the residuals along the spatial axis and the bottom plot shows the residuals along the spectral axis. The scatter in the plane has been reduced to $\pm 30\mu$m in the centre of the field, and is less than 50μm at the extremes. The corrected focal plane for KMOS thus meets the spectral resolving power and spatial FWHM requirements in H-band (of > 3800 and $0.2 \pm 0.025''$ respectively) across the full

field. The same is also true across the other wavebands.

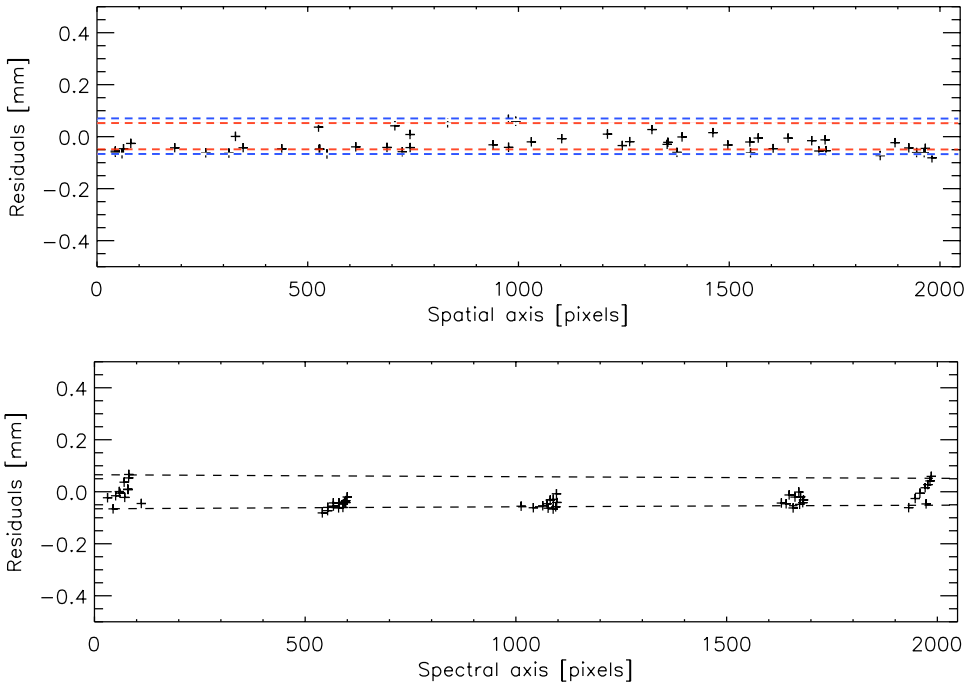

Figure 3.12: The residuals for the corrected focal plane - H-band.

3.2.3 KMOS Throughput

The current state of KMOS at the Edinburgh ATC makes end-to-end efficiency of the optical train difficult to measure. To provide an approximate measure of the throughput, a black body source was employed. The source was observed through each arm via the full optical path of each pick-off unit, IFU and a full SGS onto a science grade detector. The representative sample given here in Figure 3.13 is a measurement in the K-band of a black-body source at 383K and 343K through one of the pick-off unit/IFU optical paths (undertaken by Phil Rees and Gert Finger). Each coloured line represents the throughput through each of the 14 slitlets produced by the IFU. The counts were averaged over the central 9 pixels of each slitlet (the full spatial extent of a slitlet is 14 pixels). To obtain the pure optical train throughput, certain assumptions were made. The emissivity of the black-body source was taken as 0.94 and the quantum efficiency of the detector, which of course had to be divided out to gauge the true optical throughput, was taken as the manufacturer's

stated value of 0.8 over this range (2.0 to 2.5μm). This measurement was also taken with an out of specification L6 lens in the camera barrel, so the focal ratio at the detector varies across the wavelength range and the wavelength solution is not optimal. However, the arm chosen here was located towards the centre of the detector, and thus the centre of the camera field where the effects of L6 are minimal at the central wavelength and the PSF size deviates by $\sim 5\%$ at the wavelength extremes. The uniform illumination of the slitlets reduces the effect of the PSF deviation as the power lost from one pixel due to defocus moves into the adjacent pixels and thus the central 9 pixels used to obtain the average throughput would not be as heavily affected by the central power loss as the pixels at the edges of the slitlets.

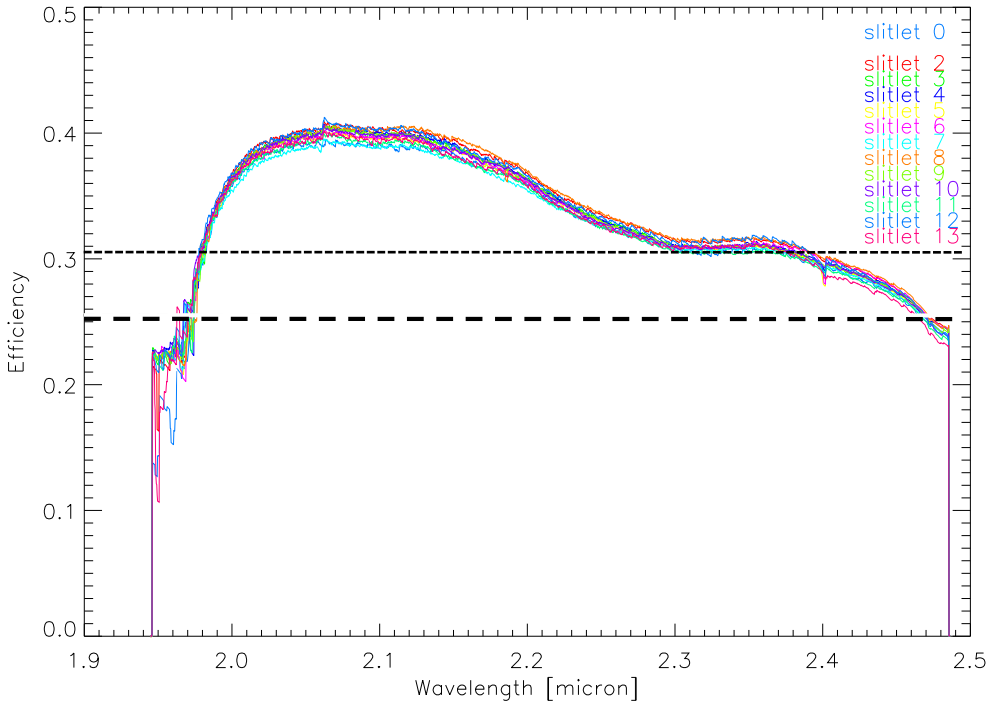

Figure 3.13: K-band throughput for Arm 12. Adapted from a plot, group email from Gert Finger.

The throughput for the pick-off unit in Figure 3.13 peaks at 0.4 around 2.1μm, moving down to 0.35 at the central wavelength $\lambda_c^K = 2.2\mu$m, with the entire range averaging ~ 0.3 (dotted black line in Figure 3.13). The standard deviation in the throughput of the slitlets around the peak is typically $\pm 1\%$. The noisy rise between $\sim 1.95\mu$m and 2.0μm is a result of the slit curvature and slight misalignment of the slitlets. The sharp cut-off towards 2.49μm is an artifcial limit imposed

in the creation of the plot (cutting off at the maximum required wavelength). This result indicates exceptional throughput at the central wavelength in the K-band for the full KMOS optical train. Even with the possibility of fluctuations in the λ_c^K efficiency, the requirement of a K-band central throughput > 0.3 is met (see Table 3.1). The requirement of 60% of the peak throughput at the extremes of the waveband is difficult to rigorously test with the current data (due to slitlet misalignment and an undefined final wavelength range), however the efficiency out at the cut-off can be determined (close to the nominal wavelength limit) as seen by the dashed black line in Figure 3.13, and is found to be ~ 0.25 (63%). Calculations by Phil Rees indicate the peak efficiency in the H and YJ bands are 37% and 34% respectively.

3.3 Hyper-sampling of the KMOS spectral PSF

Measuring the KMOS PSF with a static detector and a finite pixel size prevents a true determination of the instrument line spread function (LSF). The just Nyquist sampled spectra require an assumption of a purely Gaussian line shape. It is important to know the true line shape in the case of spectroscopy, primarily for achieving good sky subtraction. Ideally, we would like to move the sampling grid of the detector across the static line profile of the instrument to sample more points along the profile, *hyper-sampling* the PSF.

To illustrate the importance of measuring the line spread function of the optical train, consider the following scenario. The results of the techniques demonstrated in section 3.4.4 and Davies (2007) have been achieved through observations using the same optical components. If we were to observe an object through one of the KMOS pick-off units and measure the sky background through another arm (in stare mode, as explained in section 3.4.4), the act of subtracting the sky frame from the object frame is optimal if the line profiles of the arms are identical. If they are not, the shape of the OH sky lines, for example, will be different in the two exposures and so they will not be cleanly subtracted. To a level of accuracy, this will of course not be the case for observations through two separate arms. If we can measure the LSFs of each arm and find significant deviations in line shape, deconvolution could be applied to the spectra taken through each arm and the LSF of each IFU could be matched for cleaner reductions.

To achieve this measurement through hyper-sampling there needs to be some form of spectral dithering. This is usually achieved by control of the grating mechanism in the instrument to shift the spectrum by small amounts on the detector (shifting the central wavelength). This is more common than moving the detector around, as usually there is no need to have detector movement other than along its through-focus path, whereas the grating mechanism will be adjustable to switch between several gratings. The resolution of the sampling is then limited by the resolution of the grating mechanism stepper motor. Instruments such as SINFONI contain turret grating exchange mechanisms that allow accurate control of the spectrum position. However, the mechanism in KMOS, as outlined in section 2.1.4, is rotary in a plane perpendicular to the optical path. Thus, there is limited movement of the spectrum across the detector before the grating is moved completely out of the optical path. A novel idea was required to produce a shift in the spectrum.

3.3.1 Using Spectral Flexure

The corrections to the KMOS instrument flexure, outlined in section 3.2.1, still left ± 0.45 pixels of spectral movement over a rotation. This movement would potentially be enough to better sample the spectral PSF. To show how this flexure can be used to hyper-sample the KMOS spectral PSF, the first set of flexure data used in the investigations of section 3.2.1 was utilised (using a setup with out of specification flexure).

Initially a slitlet was traced using the halogen flat-field taken at the beginning of the rotation run and the wavelength solution determined, as in section 3.1.4. The same aperture trace was then applied to each of the subsequent arc frames taken at the other rotator positions, thus extracting the Argon arc lamp spectra over the same aperture, along the same column of pixels. For each extracted 1D spectrum a wavelength solution was determined using a 4th order Legendre polynomial fit to wavelength against pixel position. The line identifications were checked by hand to reduce the r.m.s deviation of the fit to ~ 0.1 waves (at $\lambda_c \sim 1.65\mu$m). Once the wavelength solutions had been determined and applied to each set of data, the wavelength arrays and intensity arrays read out from the 1D image files were concatenated into two large arrays. The wavelength array was then sorted in ascending order and the rearranged array indices were used to organise the intensity

array. Thus, over a certain wavelength interval there were now N× more points (with N begin the number of files/rotator positions). Figure 3.14 shows line spread profiles (LSP) of eight H-band arc lines of several wavelengths, centred on one slitlet. The figure also displays the residuals of a Gaussian fit to the lines, as a percentage of the flux at each sample point (in red in the line profile plots and magnified in the adjacent plots). Further out from the central wavelength, ($\sim 1.65\mu$m) it can be seen that the line profile is broad. This is due to the out of specification L6 present in the flexure tests. Also, the LSP do not cover the extremes of the wavelength range, due to the poorer Engineering grade detector used (the extremes of the chip were crowded by dead or hot pixels).

One of the main problems to overcome in hyper-sampling is the normalisation of the counts. As each of the rotator positions provides a PSF with only a few sampling points, the peak of the emission line is not actually measured (sampling occurs either side of the peak - it is unlikely the true peak value will be sampled). Ideally there should be flat-field and dark images taken at each rotator position before/after each arc frame is taken. This would remove external background noise and changes in pixel response. However, this was not undertaken in this set of flexure tests. So, each hyper-sampled line was fit with a Gaussian profile at each rotator position. This enabled a determination of the likely peak value of the line with which to normalise the counts. The noise in the hyper-sampled line was thus reduced. However, as the line was not necessarily purely Gaussian, the peak could still be inaccurate.

A way of overcoming this with the current data could include bootstrapping by fitting B-splines to the initial hypersampled line shape and then weighting the counts by this line profile on subsequent iterations. However, we are fundamentally limited by the quality of the data and the out-of-specification nature of the test setup. The large spatial flexure in this data severely reduces the likelihood that we are tracing the same spaxel when the wavelength solution is obtained at each rotator position. Also, the availability of only the single central IFU meant that we could not produce a full LSF map across all spaxels. The results here serve as a proof of concept, but repetitions of this work would be required across all bands with the current, in specification, KMOS setup.

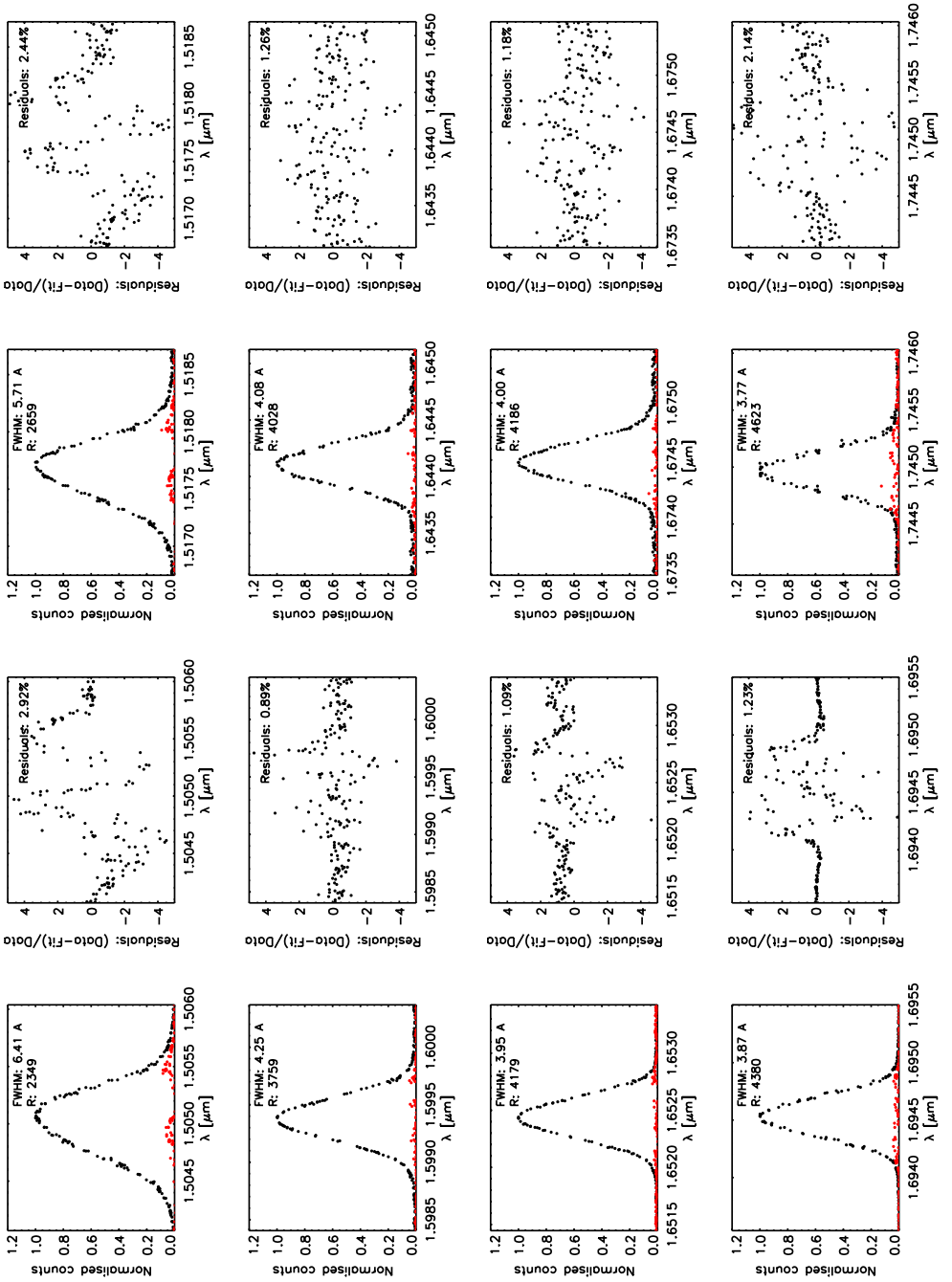

Figure 3.14: Line spread profiles at wavelengths in he H-band for one slitlet.

3.4 Observing and Science with KMOS

This section describes some of the nuances in the observing strategies to be considered when using KMOS. The configuration aspects and some of the observing modes are first discussed and then a brief description of some of the key aspects of the reduction steps is given. This section is in no way intended to be an exhaustive source on the unique aspects of the KMOS operation and data structure and more in-depth detail in all areas can be found in Davies et al. (2010). It is also noted that these processes and operations have not been tested on sky, but with simulated data. Any results presented in the following subsections are not my own, they are a review of previous work on the instrument. Some representative science cases are then presented for the use of KMOS. Again, this is by no means an exhaustive list.

3.4.1 Configurations and Observing Modes

Observing with KMOS on the VLT should be a relatively straightforward process for the end-user. The spectrally dependent pixel scale, the spatial independence of wavelength coverage and the absence of choice in the slit-width optimisation against R implies the only real complexity for the observer comes in the planning of exposure times and choice of arm allocation (which, due to the ad-hoc nature of pick-off unit configuration, is easily exchanged for back-up plans due to any unforeseen events during a run). The actual allocation of the pick-of units is also greatly aided by the automated KARMA (Wegner & Muschielok, 2008) front-end software tool. The various modes available with this tool include nod-to-sky, stare mode and a mapping mode, detailed in Davies et al. (2010).

3.4.2 Reconstructing the Data

The reduction steps in KMOS are many and each series of reductions will of course depend on the nature of the observations taking place. The main points I will raise here, however, are the basic reconstruction steps, the calibration steps of tracing and assignment of the slitlets and the potential efficiency of the sky line removal. As stated earlier, a lot of information from work with the SINFONI instrument on the VLT UT4 has been used in the design and manufacture of KMOS

and the observation planning and reduction routines have also drawn heavily on this previous work.

When considering spectral and spatial curvature in raw data, polynomials are usually fit in wavelength or pixel space and the resulting coefficients are used to correct and linearise the data for analysis (as seen in the cluster work in this Thesis, Part II). In the case of a datacube constructed from several slitlets and particularly when constructing datasets made of several datacubes, as in KMOS, the interpolations required by applying corrective functions can result in significant degradation of the final data. To reduce these processes to a single interpolation for each datacube, the KMOS reduction pipeline will involve a look-up table system. This relates each 2D raw data value in an exposure with its position in the 3D reconstructed datacube coordinate system. Initially the raw data are sampled in a regular grid by the detector (pixel grid). In the reference coordinate system of the datacube, these sample points become irregularly gridded. A required grid is then defined in the datacube system and the irregular sample points can then be mapped/interpolated onto the required regular grid via some form of neighbour interpolation process (type of interpolations will depend on the required end datacube and the raw data itself). Thus, there is only one interpolation in setting up the final regularly gridded data and the ability to define the regular grid in the datacube system enables a free choice of pixel scale to compare any data with samples from other instruments.

The slit curvature seen in the KMOS test frames indicates that the datacube reconstruction will change the wavelength range available for an observation. The KMOS specifications for λ range and resolving power were not specified with location in the field. Thus, the design of the instrument appears to have been conducted to ensure the central slitlet would meet the specifications. This is worth noting for future science case considerations, as some diagnostic features may be lost.

3.4.3 Calibrations

The main calibrations of the KMOS data are the same as the standard calibrations of other spectroscopic instruments, with the primary addition being the tracing of the slitlets for accurate reconstruction of the datacubes. The steps initially involve dark frame construction and flat fielding. These allow the determination of bad pixels, a measure of the noise in the electronics and

a measure of any variation in the calibration sources. The flat field also allows a mapping of the spatial curvature across each of the three spectrographs. The flat field results in the slitlets being traced along the full entrance slit of a spectrograph.

The wavelength calibration for each pixel in separate slitlets follows a similar method to standard long-slit calibrations, where separations between arc lines are compared to line lists. This was performed during the testing phases for the wavelength solutions in section 3.1.4. The calibrations on-sky include sky flats to measure possible vignetting towards the edges of the patrol field or from closely packed arms and standard star measurement that can allow determination of spectral transmissions and flux calibration scaling factors. More detail on long-slit spectroscopic reductions are given in the description of my work with the GMOS-N instrument in Chapter 5.

3.4.4 Sky subtraction

One of the largest areas of influence from the work carried out with SINFONI will be the in the sky subtraction from the KMOS target frames. A novel technique outlined in Davies (2007) allows for a significant reduction in the noise left around the OH emission line wavelengths after sky frame subtraction. The procedure exploits the fact that most of the variation in the relative line ratios of the OH emission features is due to variations in the vibrational temperature of the OH radical. Any lines from a given vibrational transition occupy a well defined wavelength range (to a certain degree of accuracy), so a single scaling can be applied to each range. Once the vibrational states have been taken out, the rotational transition lines of the molecule can also be identified and corrected. The scaling functions are constructed from the sky cubes and from low-flux (sky) areas in the object/target cubes. These are then applied to the sky cube only before it is subtracted from the final object cube.

The results from some SINFONI data can be seen in Figure 3.15. The (+) indicate the noise after a basic sky subtraction after each object frame taken at various times, the ($\diamond$) indicate the noise remaining after subtracting the same sky frames after using the OH scaling technique and the ($*$) indicate the noise left after using the same single, OH scaled sky frame at a time (S) on all of the object frames over the 24 exposures (each 5 minutes in length). It can be seen that the

noise is significantly reduced with the scaling technique of Davies (2007), in some cases by a factor of 3. The (∗) data also show that this method is still better than simple subtraction up to an hour after the object frame has been obtained.

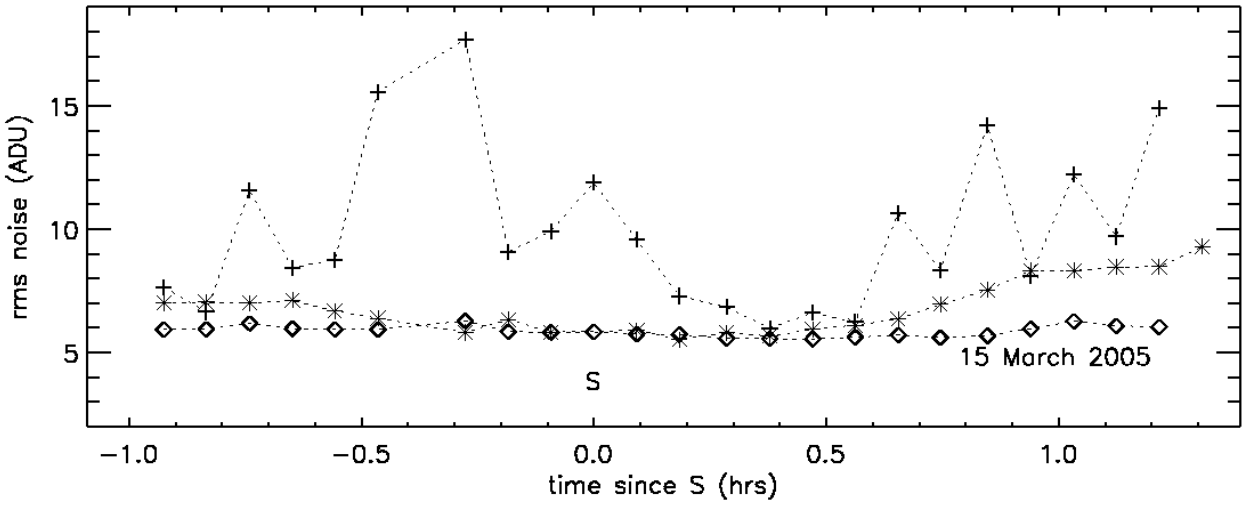

Figure 3.15: Data-cube reconstruction. Reproduced from Davies (2007).

The availability of the routines for the reconstruction of the KMOS data cubes across the many possible variations in the acquisition configuration of the IFUs, the limited interpolation steps, robust calibration processes and powerful noise reduction techniques touched on here indicate the strong potential for success of KMOS in the science cases outlined in the next section.

3.4.5 Science Cases for KMOS

KMOS will have uses in many key science areas. I will now outline a few of these and will highlight the importance of the multiplexing capability, wavelength range and IFS nature of the instrument. Broadly, the main fields of investigation for the proposed science cases have included the masses and growth of galaxies, extremely high redshift galaxies & re-ionisation, the connection between galaxy formation and active galactic nuclei (AGN), accurate age-dating at z = 2 to 3, stellar populations and spectroscopic investigations of extra-solar planets (see Lehnert et al. (2003)).

KMOS will also be well suited to investigations of early type galaxies (ETGs) and the understanding of their formation and evolution. Global scaling relations have allowed us to begin to understand the ensemble characteristics of galaxy formation & evolution and the ability to internally resolve the objects going into these relations is beginning to help us improve the scatter in these relations through effective velocity dispersion (σ_e) determinations (Cappellari et al., 2006). σ_e is obtained by measuring velocity dispersions in circular apertures out to R_e (the effective radius), providing a measure of the mass within R_e (I explain more about these parameters and scaling relations in Part II of this Thesis). In addition to this, however, is the ability of IFU-aided studies to explain internal structure and break classification degeneracies in galaxy populations. In recent times, local studies of ETGs in the SAURON project and ATLAS3D survey (Emsellem et al., 2007, 2011; Cappellari et al., 2007) have discovered so-called *slow and fast rotators*, dividing the ETG samples into two distinct evolutionary types, providing a physical mechanism for ETG classification. These studies have crucially linked the observed velocity fields of the ETGs to their merger history.

Continuing these investigations out to intermediate redshift clusters, in some of the densest environments, where ETGs comprise the bulk of the population, will be possible with KMOS. Calculation of the specific angular momentum (λ), used in classifying the slow and fast-rotator populations, has not been carried out at intermediate redshifts. The IFU nature and multiplexing capability of the instrument will allow large surveys to be built up quickly, providing important observations of the evolution of the slow/fast rotator fraction - allowing us to trace the merger events affecting the build up of the ETG population.

The traditional rest-frame optical diagnostic tools of the 400 nm continuum break, the Balmer, Na and Mg II lines and Oxygen & Nitrogen abundance ratios for age dating are shifted into the I, J, H&K bands for objects in the severely under-sampled *redshift desert* at $1.0 \lesssim z \lesssim 2.0$, easily accessible by KMOS. Investigating the dynamics of galaxies at z= 2 is possible using some of these lines as kinematic tracers and datacubes produced would provide kinemetry on these objects to probe the V/σ asymmetries indicative of mergers. The spectral resolution across the bands ($R \sim$ 3500 - 4500) would allow for accurate measurements of any of these emission features, providing velocity resolutions around 65-85 kms^{-1}. Measurement of early-type galaxy CO Tully-Fisher relations (Davis et al., 2011) could be used to trace the dynamical evolution of the mass-to-light ratio of galaxies and this could be compared to current investigations of stellar M/L from spectral energy distribution (SED) fitting and line strength measurements.

Extremely high redshift Lyα emitting objects in the range 5.6 <z <19.5, have their emission lines (Ly$\alpha \sim$ 1216Å) observable in the I/z to K band range (Sharples et al., 2005; Bender & Sagila, 2007). A deployable MOS IFS would allow investigation of these sources, probing the epoch of re-ionisation, without the prior need for deep imaging on a significant scale. The availability of arms for simultaneous sky measurement would also aid deep probing of the spectra of these objects. The high sensitivity in the KMOS bands would also aid in the detection of these objects with reasonable total exposure times.

The Iz/YJ configurations will allow investigation of Population III stars and active galactic nuclei (AGN) using HeII at $z \sim 4 - 7.5$ and the H band will allow investigation of these objects above redshift 8. The full KMOS range can be used to investigate [OII] lines, an indicator of star formation rate (SFR), metallicity and density from $z \sim 1 - 6$. Over the same range, Hβ and [OIII] are accessible as measures of metallicity and stellar dynamics. There are also the standard stellar population indicators of the 4000Å break, the G-band (CH) at 4300Å and Mgb all from $z \sim 0.9 - 5$.

3.5 Summary

In this Chapter I have presented a representative sample of the range of tests carried out on the individual spectrograph modules at the test facility in Oxford and on the full instrument setup at the UK ATC. The majority of the tests were conducted with a faulty component (the incorrectly manufactured L6 in the camera barrel), but I was able to demonstrate the achievability of the required spectral and spatial image quality of the spectrographs in the centre of the field. The correction of the faulty component allowed me to demonstrate the achievability across the entire field, through mapping the focal plane. Although the data presented is mainly from one grating configuration, the methods were applied across the wavelength range, with the variation between bands remaining within the specifications outlined in Ramsay Howat et al. (2005a).

As a preliminary investigation, I have also presented work on hyper-sampling the KMOS spectral PSF using the instrumental flexure. The results look promising, but much more work on improved data will be required to explore the uses of this technique in future science cases.

I finally presented details of the planned operational procedures for KMOS, along with outline science cases that will hopefully be undertaken in future proposals. KMOS is due for commissioning on site at the VLT UT2 in mid 2012.

Part II

Scaling Relations in the Rich Cluster MS0451.6-0305

Chapter 4

Introduction

This part of the thesis focusses on the investigation of galaxies in the richest environments. Specifically, I focus on the rich cluster MS0451.6-0305 at a redshift of 0.55. I utilise photometric and spectroscopic information to try and understand the formation histories of the galaxies in this cluster through galaxy scaling relations.

4.1 A Brief Introduction to Galaxies and Clusters

In its simplest form a galaxy is a large system of stars, gas, dust and dark matter, bound by gravity and supported by the rotational or randomised motions of its constituent stellar population. The different types of galaxies were originally classified by Hubble's Tuning fork diagram (Hubble, 1926), where elliptical (E) and lenticular (S0) shaped galaxies (or nebulae as they were designated in the original text) were thought to be the progenitors of older spiral and irregular galaxies. This lead to the designations *early type galaxies* (ETGs) for E/S0s and *late type galaxies* (LTGs) for spirals. This is now known to be the reverse of the evolutionary trajectory of galaxies, however the designations remain the accepted nomenclature. The majority of ETGs and the centres of LTGs are thought to form at high-redshift, with the star formation peaking in the Universe around $z \sim 2$ and disks in LTGs forming around $z \sim 1$ (e.g. see Spergel et al., 1997).

The light profiles of galaxies are generally described by the Sérsic profile (Sersic, 1968), which

has a radial dependency of the form,

$$I(r) = I_0 \exp(-b(r/R_e)^{\frac{1}{n}}) \tag{4.1}$$

where r is distance from the centre, I_0 is the intensity at $r = 0$, b is a constant, R_e is the half-light radius and n is a power-law index that describes the profile (see Section 5.7.2 for a more in-depth discussion). The parameter n describes the shape of the profile through a continuous sequence ranging from Gaussian ($n = 0.5$), through to exponential ($n = 1$) and centrally peakier profiles, such as the de Vaucouleurs profile ($n = 4$, de Vaucouleurs, 19483). Typical ETGs and bulges (centres of LTGs) are generally well fit by $r^{1/4}$ profiles and disks of LTGs follow shallower profiles.

The environments galaxies inhabit vary from the sparse and chaotic field, to groups, clusters and superclusters that are generally thought to be virialised, ordered and stable. The morphology-density and morphology-radius relations (Dressler, 1980; Postman & Geller, 1984) have shown that ETGs dominate in cluster environments and spirals are found predominantly in the field. In addition, the frequency of blue galaxies in dense environments, in cluster centres, is found to increase with redshift. Known as the Butcher-Oemler effect (Butcher & Oemler, 1978). This was subsequently linked to morphology, so the fraction of ETGs in rich environments is seen to decrease with z, while the fraction of spirals increases (e.g., Couch et al., 1994; Dressler et al., 1997; van Dokkum et al., 2000).

Theoretical hierarchical formation models predict that galaxies form from the mergers of smaller galaxies, continuing to intermediate redshift (e.g., Baugh et al., 1996), which would disagree with the observations in clusters. Also, semi-analytic models predict a gradual build up in characteristic mass over cosmic time, underpredicting the observed value at $z \approx 1$ by around a factor of three (Poggianti, 2004). Other simulations have underpredicted the numbers and mass densities of the most massive galaxies ($M > 10^{11.5} M_\odot$) by a factor of over one hundred (Conselice et al., 2007). From findings such as these, the role of early vs late trends or *nature vs nurture*, is expected to be a strong factor in galaxy evolution and is therefore a primary focus of today's galaxy evolution studies (e.g., Thomas et al., 2005b; Baugh, 2006).

4.1.1 Scaling Relations

Galaxies exhibit strong correlations between several physical properties, which prove to be incredibly valuable diagnostic tools when investigating their evolution. Galaxy colour and luminosity make up the colour-magnitude relation (CMR, e.g. Baum, 1959), with ETGs primarily falling on a *red sequence* (RS), having higher metallicities and little to no star formation. For the ETGs, the half-light or *effective* radius (R_e) and mean surface brightness within R_e ($\langle\mu\rangle_e$ in [mags/arcsec^2]) correlate in the Kormendy Relation (KR, Kormendy, 1977) and their central velocity dispersions (σ) and absolute magnitudes fall on the Faber-Jackson Relation (FJR, Faber & Jackson, 1976). These relations all take the form

$$P_1 = \alpha_r P_2 + \beta_r \tag{4.2}$$

where r = relation (CMR, KR or FJR) and

$$\begin{aligned} \{P_1, P_2\} &= \{(m_{\nu 1} - m_{\nu 2}), m_{\nu 2}\} && \text{(CMR)} \\ &= \{\langle\mu\rangle_e\ , R_e\} && \text{(KR)} \\ &= \{\mathcal{M}, \sigma\} && \text{(FJR)} \end{aligned}$$

In addition to these, it was discovered that σ, R_e and $\langle\mu\rangle_e$ all lie on the tight Fundamental Plane relation (FP, Dressler et al., 1987; Djorgovski & Davis, 1987). The FP takes the form

$$\log(R_e) = \alpha_{FP}\log(\sigma) + \beta_{FP}\langle I\rangle_e + \gamma_{FP} \tag{4.3}$$

where R_e is in kpc, σ is in kms^{-1} and $\langle I\rangle_e$ is surface brightness within R_e in L$_\odot$ pc^{-2}. It can also be represented in the form of mass-to-light vs mass via

$$\log\left(\frac{M}{L}\right) \approx \epsilon \log M + \gamma_M \tag{4.4}$$

where γ_M is a constant. There is also a dependence on R_e of M/L, which tends to zero for a fully virialised system, but please see Chapter 6 where all of these relations are explained in greater detail.

The majority of previous studies of these global scaling relations, and their variation with redshift, have shown the evolution of ETGs to be consistent with the predictions of single stellar population (SSP) models, passively ageing from a formation redshift $z_f \gtrsim 2$. The slopes of the relations have appeared to change very little since $z \sim 1$, with only the offset, relative to nearby reference samples, changing. (e.g. Kodama & Arimoto, 1997; Ziegler et al., 1999; Fritz et al., 2003; Bruzual & Charlot, 2003; Maraston, 2005).

A focus of a large fraction of these studies has been on the evolution of the FP (e.g. van Dokkum & Franx, 1996; Jørgensen et al., 1999; Kelson et al., 2000; Ziegler et al., 2001; Holden et al., 2005). However, they have generally only been able to obtain $\sim 5-10$ galaxies per redshift bin. More recent studies of the FP, with larger samples at higher z, have begun to produce evidence that the tilt of this relation *does* depend on epoch. Several authors have shown an increase in tilt (an increase in ϵ or decrease in α_{FP}) with redshift, up to $z \sim 1$ (e.g., van Dokkum & Franx, 1996; Jørgensen et al., 2006; Fritz et al., 2009). The presence of an evolution in the tilt, when interpreted in the form of Equation 4.4 indicates *downsizing* (Cowie et al., 1996), a mass dependence on formation epoch (see Chapter 6). Evidence has also been found for the environmental dependence on the FP with low and high density environments indicating significantly different zero-point offsets (Bernardi et al., 2006) and in some cases a change in the tilt with environment (D'Onofrio et al., 2008). Spatially resolved kinematics of ETGs in the local Universe has enabled the reduction in the scatter of the FP and indicated that the tilt from the Virial prediction is primarily due to real M/L variation (Cappellari et al., 2006).

In addition to these scaling relations there is also the Mg-σ relation (Terlevich et al., 1981), relating an increased luminosity to an increased metallicity for ETGs (although Mg is also sensitive to age and alpha abundance). Other relations include the Photometric Fundamental Plane (Scodeggio et al., 1997) and the Mgb-V_{esc} relation (Scott et al., 2009). Recently, a CO-Tull-Fisher (Tully & Fisher, 1977) relation has been found for local ETGs (Davis et al., 2011). We limit ourselves to the CMR, KR, FJR and FP in the investigations presented here.

4.2 The Gemini/HST cluster project

The Gemini/HST cluster project aims to understand galaxy evolution in the richest environments over the redshift range $z = 1$ to 0 - from around half the age of the Universe until the present. In order to achieve this, an original sample of 15 X-ray luminous, rich clusters were selected for investigation. Each cluster is being investigated using diagnostic tools including morphological classification, scaling relations, line indices and abundance ratios for stellar population analysis. Gemini Multi-Object Spectrograph (GMOS) imaging and high signal-to-noise (S/N) spectroscopy has been obtained on $\sim 20-30$ confirmed member galaxies per cluster. This data is supplemented by archival HST imaging for more detailed photometric measurements.

The Gemini/HST project was first outlined in Jørgensen et al. (2005) and the first investigations involved the rich clusters RX J0152.7-1357 ($z = 0.83$) and RX J1226.9-3332 ($z = 0.89$, Jørgensen et al., 2006, 2007). This was followed by Barr et al. (2005), where the authors investigated the lower redshift cluster RX J0142.0+2131 at $z = 0.28$. Fritz et al. (2009) have investigated the highest redshift cluster in the project to date: RXJ1415.1+3612 at z = 1.013 and most recently Houghton et al. (2012) studied Abell 1689 ($z = 0.183$). The findings of these authors are discussed later, in the context of the work in this thesis (see Section 7.4). My role in the project has been the investigation of MS0451.6-0305 at $z = 0.55$ - addressing the intermediate redshift range of the cluster sample.

4.2.1 X-ray selection of clusters

X-ray emission from thermal bremsstrahlung in intra-cluster gas provides a strong indicator of galaxy cluster richness. The higher the X-ray luminosity over an area, the more gas is at that location. The more gas, the more massive the host cluster drawing it into the centre (Solinger & Tucker, 1972). The luminosity cut for cluster selection in the Gemini/HST project was $L_X > 2.10^{44}$ergs/s in the 0.1-2.4 keV bandpass, which puts a lower limit on the cluster masses of $\sim 3 \times 10^{14} M_{\odot}$. This is indicated by the dashed red line in Figure 4.1. The selection of clusters was from a spread in redshifts across several catalogues, randomly sampling to obtain ~ 3 clusters per 0.2 redshift interval.

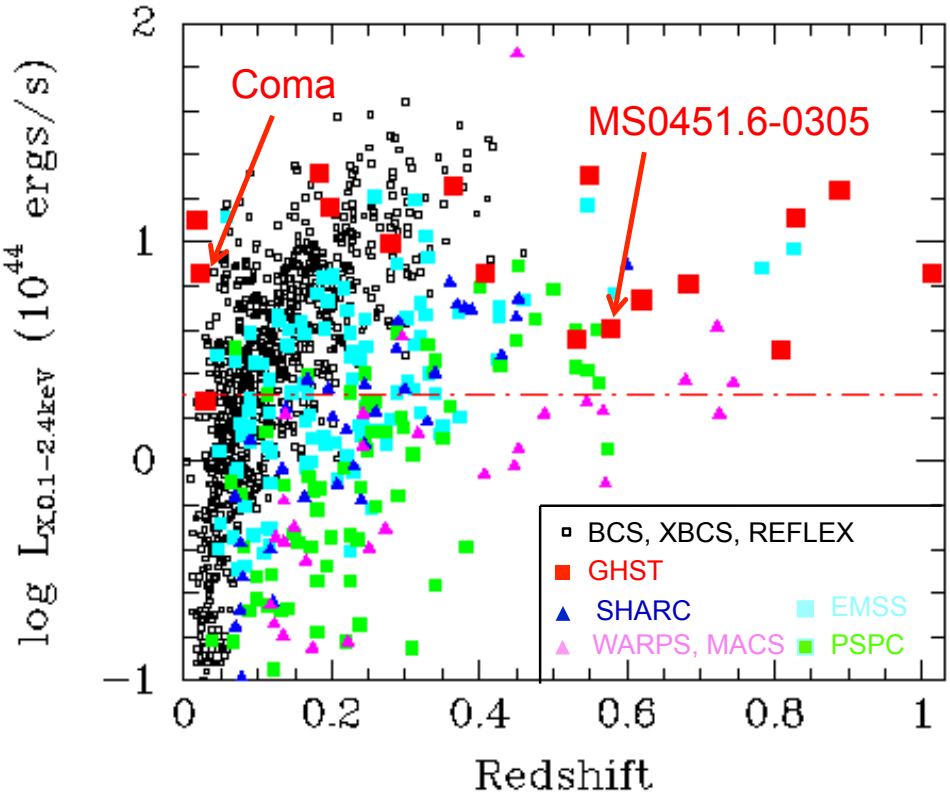

Figure 4.1: Xray surveys and cluster project sample, adapted from Bergmann et al., 2003. The various surveys from which this cluster project sample was drawn are designated, with the luminosity cut given by the dot-dash red line.

4.3 MS0451 - a rich galaxy cluster at $z = 0.55$

The rich cluster MS0451.6-0305 was first identified as part of the Einstein Observatory Extended Medium Sensitivity Survey (EMSS) as the most X-ray luminous cluster in a catalog of 104 (Gioia et al., 1990; Gioia & Luppino, 1994). The cluster centre is located around RA: 04:54:10 DEC: -03:01:00 (J2000). It is an extremely X-ray luminous cluster with $L_X = 4.60 \times 10^{44}$ (erg $s^{-1}h^{-2}$) in the 0.1 to 2.4 keV bandpass, indicating a total mass of (8.6-8.9)$\pm 1.2 \times 10^{14}$ $h^{-1}M_\odot$ (Donahue et al., 2003). Lensing surveys of the cluster have placed the mass within r_{200} at $M_{200} = 4.8 \pm 2.5 \times 10^{15}h^{-1}M_\odot$ (Sereno & Zitrin, 2011). The shape is triaxial, indicated from X-ray and Sunyaev-Zel'dovich studies (Donahue et al., 2003; De Filippis et al., 2005). The high mass and concentration of the cluster has allowed it to be used extensively in gravitational lensing investigations (e.g. Borys et al., 2004; Berciano Alba et al., 2007, 2010). Importantly, X-ray studies have indicated that MS0451 resembles a relaxed Coma-like cluster, with no large scale substructure, cooling flow or single dominant galaxy (Donahue & Stocke, 1995). The heating of the intra-cluster medium (ICM) by active galactic nuclei (AGN) activity has been suggested by Martini et al. (2004), which could explain the lack of a cooling flow, although this evidence is currently weak and requires followup AGN searches.

MS0451 has been found to be a remarkably well evolved cluster for its epoch (Moran et al., 2007b). It has been shown to exhibit significant star formation as evidenced by an excess of mid-infrared sources (Geach et al., 2006). However, the dense intra-cluster medium (ICM) seems to limit this compared to clusters at similar epochs (Geach et al., 2006). Indeed, the cluster environment appears to suppress star formation in late-type galaxies that are not dust obscured mid-IR sources or luminous infrared galaxies (LIRGS) (Wardlow et al., 2010). The most in depth study of the cluster has been carried out in a large survey of two rich clusters at $z = 0.4$ and $z = 0.55$ (Cl 0024+17 and MS0451 respectively, Moran et al., 2007a,b, 2008), where the authors identified the transformation of spirals into ETGs (S0s), highlighting the role of the ICM in quickening the process. Moran et al. (2007b) managed to construct some scaling relations from their data, but did not investigate these in detail. However, the authors did indicate evidence for a mass dependency on formation epoch of the ETG population (discussed later in Section 6.2).

The structure of the remainder of this part of the thesis is as follows: Chapter 5 details the reduction processes and analytical techniques used in deriving the photometric & spectroscopic parameters for the galaxies in MS0451, Chapter 6 presents the results of the scaling relation fits (CMR, KR, FJR and FP) to the data, comparing them to stellar population model predictions and Chapter 7 summarises the findings, while putting the results in the context of previous cluster evolution studies and also details some caveats & future work.

Chapter 5

GMOS/HST reductions and analysis

This Chapter describes the photometric and spectroscopic data, the reduction techniques used and the analysis techniques developed during the investigations of MS0451 and Abell 1689 at $z = 0.183$ (Houghton et al., 2012). Many of the techniques in the following sections can also be found in Houghton et al. (2012), with whom I collaborated on the development of the methods laid out here.

5.1 The Data

I have used Hubble Space Telescope (HST) imaging, through the Advanced Camera for Surveys (ACS) Wide Field Channel (WFC), Gemini-Multi-Object Spectrograph (North) (GMOS-N) imaging and GMOS-N spectroscopy to conduct an analysis of the rich cluster MS0451. I begin by briefly outlining the specifications of the HST ACS and GMOS-N and their instrumental setups during the observing runs.

The ACS is a 3rd generation imaging instrument on the HST. The WFC detector contains two chips (WFC1 and WFC2) of dimensions 2048 x 4096 pixels (15 x 15 μm pixel dims) at a plate scale of $0.05''$ per pixel. This provides a full field of view of 202 x 202 square arcseconds. The chip layout is given in Figure 5.1. The observations of MS0451 utilised the F814W filter on the WFC. The central wavelength of the F814W filter is given as 8332Å with a width of 2510Å . This allows observation of the V-band features of objects at the redshift of the cluster, $z \approx 0.55$.

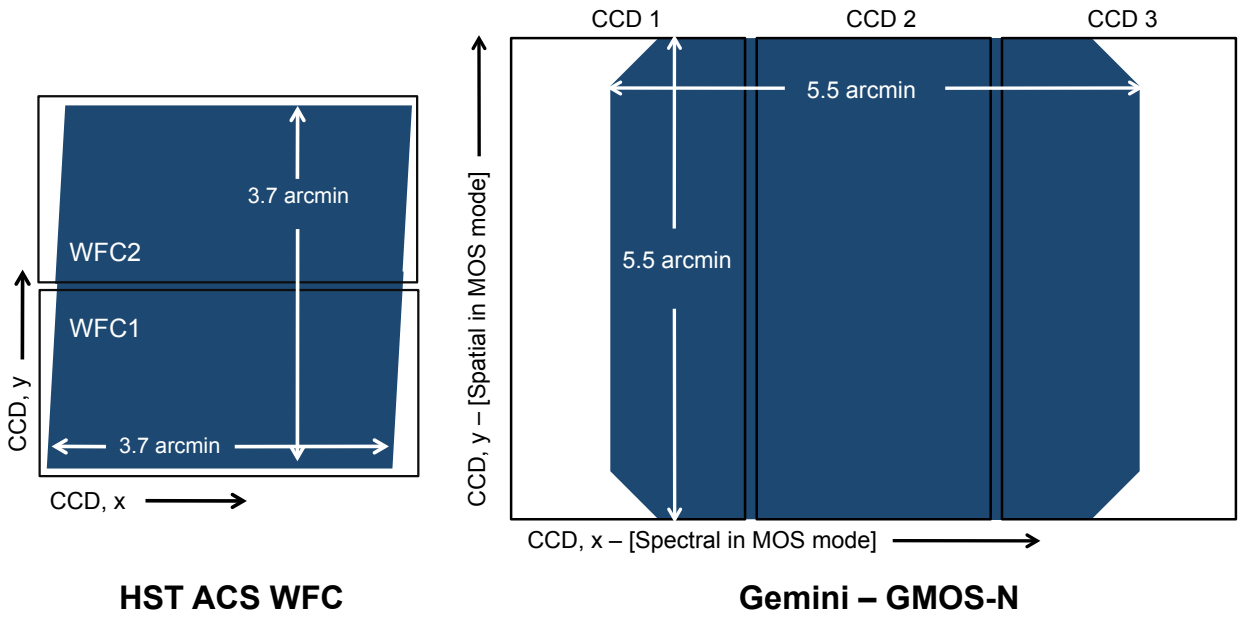

Figure 5.1: Layouts of the HST ACS WFC and GMOS-N Chips - relative FOVs. The chip layouts are to scale, indicating the available relative FOV for each. The chips are given as black rectangles, while the accessible FOVs are given in blue.

The imaging data on MS0451 was obtained from the HST Guessed Observer programs 9836 (part of Cycle 12 - P.I. R. Ellis, CalTech - related paper: Moran et al., 2007b) and 10493 (part of Cycle 14 - P.I. A. Gal-Yam, Weizmann Institute - related paper: Zitrin et al., 2009). The raw data files were downloaded as Multi-Extension Fits (MEF) files from the HST legacy archive. Observations of the cluster in program 10493 were conducted on 31st July 2005 and observations in program 9836 were conducted on the 27th, 28th and 30th January 2004. The exposure times, coordinates and other information on the pointings of the images are given in Table 5.1.

File Prefix	Date-Obs.	Object Name	α	δ	Exp. Time [s]	Proposal I.D.
j9dd14b	2005-07-31	MS0451.6-0305	4:54:8.136	-3:1:58.404	540	10493
j8rq22m	2004-01-27	MS0451-22	4:54:6.624	-2:58:19.416	509	9836
j8rq23m	2004-01-27	MS0451-23	4:54:12.780	-3:1:17.400	509	9836
j8rq30i	2004-01-30	MS0451-30	4:54:24.120	-2:59:32.280	509	9836
j8rq24u	2004-01-28	MS0451-24	4:54:18.900	-3:4:15.096	509	9836
j8rq31j	2004-01-30	MS0451-31	4:54:30.240	-3:2:30.012	509	9836

Table 5.1: Summary of HST ACS F814W imaging data from the two proposals obtained from the HST Legacy Archive.

Parameter	
Readout Noise	(3.5, 3.3, 3.0) e^-
Gain	(2.04, 2.32, 2.19) e^-/ADU
Nominal Pixel Scale	0.0727″/pixel
Slit Width	1″
Slit Height	5″
Wavelength range	5000 - 10 000 Å

Table 5.2: GMOS-N instrumental setup.

The Gemini Multi-Object Spectrographs (GMOS - North and South) are multi-functional instruments with capabilities in imaging, long-slit spectroscopy, multi-object spectroscopy (MOS) and integral field spectroscopy. We use data from imaging and MOS observations with GMOS-North. In depth instrumental specifications and capabilities can be found in Hook et al. (2004). The full field of view is approximately 5.5×5.5 arcminutes^2 over three chips, with ∼2.9″chip gaps (or 40 pixels) The chip layout is given in Figure 5.1. Each raw GMOS-N data file comes in the form of a 3 extension MEF file, with header. Each extension corresponds to one of the three CCD chips that make up the GMOS-N detector. This is the standard format for the bias, flat and science frames.

GMOS-N images of MS0451 were taken as part of observing programmes GN-2003B-Q-21 (g'-band images: the g_{G0301} filter) and GN-2002B-Q-29 (r'-band images: the r_{G0303} filter). The science data and calibration data, along with observing logs and proposal information are available for download from the Canadian Astronomical Data Centre (CADC) archive. There were 6 exposures available in the g'-band (observing date 2003-12-24) and 15 exposures available in the r'-band (observing dates 2002-09-12,15,16). The images were dithered around the position angle (PA) of the cluster to cover the two chip-gaps. All of the image files were 2x2 binned on chip. Details of the raw files used in the GMOS imaging are listed in Table 5.3.

The spectroscopic sample of potential cluster members was initially selected through a magnitude cut of $r' < 23$ (see Section 5.3). A random selection of 42 of the objects (plus two bright stars) within the selection criteria made up our sample. The spectra were taken using the multi-object mode (R400_G5305 grating, R $\sim$ 2000 giving resolution $\sigma \sim 65$ km s^{-1}) of GMOS-N. MOS functionality is achieved by employing a mask plate with laser-cut slitlets at the projected coordinates

of the objects of interest. The spectral range covers 5000Å to 10000Å with two central wavelength configurations for each slit to cover the chip gaps, λ_c = 733 and 741nm. This translates to a rest-frame diagnostic range of $\sim$ 3200 Å to 6500 Å at the redshift of the cluster. The nights of observation covered the 19th, 21st and 23rd December 2003.

Filename	Airmass	Moffat FWHM (″)	Gaussian FWHM (″)	Scaling	Relative Through-put	Filter	Obs. Time	Exp. Time (s)
N20020912S0156	1.124	0.62	0.64	1.00	1.00	r′	14:44:34	600
N20020912S0157	1.111	0.62	0.64	1.36	0.73	r′	14:55:30	600
N20020912S0158	1.101	0.59	0.62	1.69	0.59	r′	15:06:25	600
N20020915S0088	1.189	0.58	0.60	0.44	2.26	r′	13:57:41	600
N20020915S0089	1.165	0.55	0.57	0.44	2.25	r′	14:08:37	600
N20020915S0090	1.145	0.59	0.62	0.43	2.28	r′	14:19:32	600
N20020915S0091	1.128	0.54	0.56	0.91	1.09	r′	14:30:27	600
N20020915S0092	1.114	0.50	0.52	0.76	1.30	r′	14:41:22	600
N20020915S0093	1.103	0.49	0.52	0.44	2.22	r′	14:52:18	600
N20020915S0095	1.092	0.52	0.54	0.44	2.26	r′	15:06:29	600
N20020916S0131	1.122	0.50	0.52	0.44	2.25	r′	14:30:47	600
N20020916S0132	1.109	0.54	0.56	0.44	2.27	r′	14:41:42	600
N20020916S0133	1.099	0.49	0.52	0.45	2.19	r′	14:52:37	600
N20020916S0134	1.092	0.50	0.52	0.44	2.24	r′	15:03:27	600
Combined	1.099	0.56	0.57	1.0	1.0	r′	-	8400
N20031224S0032	1.135	0.71	0.72	1.00	1.00	g′	10:08:19	600
N20031224S0033	1.153	0.75	0.77	0.97	1.03	g′	10:19:14	600
N20031224S0034	1.175	0.73	0.75	1.01	0.99	g′	10:30:10	600
N20031224S0035	1.200	0.80	0.83	0.99	1.01	g′	10:41:06	600
N20031224S0036	1.230	0.88	0.90	1.00	0.99	g′	10:52:02	600
N20031224S0037	1.263	0.84	0.88	0.96	1.05	g′	11:02:57	600
Combined	1.135	0.81	0.90	1.0	1.0	g′	-	3600

Table 5.3: Details of the GMOS-N raw imaging data in the r' and g' bands.

Object	α	δ	# files	Airmass	Exptime [s]	Date Obs.	m_{zp} [mags]	σ	Filter
SA110-361	18:42:47.34	+00:08:05	8	1.26	1 or 3	2002-09-15/16	27.929	0.040	r’
SA110-361	18:42:47.34	+00:08:05	8	1.28	1 or 3	2002-09-15/16	27.576	0.030	g’
PG0231+051	02:33:38	+05:18:33	12	1.44	1 or 3	2002-09-15/16	27.939	0.060	r’
PG0231+051	02:33:38	+05:18:33	9	1.44	1 or 3	2002-09-15/16	27.559	0.113	g’

Table 5.4: Details of the GEMINI/GMOS imaging standard stars used to determine the r' and g' band magnitude zero-points.

5.2 GMOS data reduction

5.2.1 GMOS imaging

We created a set of **IRAF** scripts, involving modified versions of the standard GMOS reduction package, to reduce the GMOS-N imaging data. The reduction process began with preparation of all of the raw files with the `gprepare` task. This task designated the raw data as science (SCI) extensions, created variance extensions (VAR) and data quality (DQ) extensions.

The VAR images were created using the read-noise, gain and raw SCI extensions. The calculation of the variance array takes the form,

$$\mathrm{VAR} = \left(\frac{\mathrm{RDNOISE}}{\mathrm{GAIN}}\right)^2 + \frac{\mathrm{SCI}}{\mathrm{GAIN}} \tag{5.1}$$

where the keywords RDNOISE (e^- rms) and GAIN (e^-/ADU) are extracted from the image header and SCI is the raw science data array (for values greater than 0.0). A set of N exposures eventually combined into a final reduced image would therefore have an effective variance of $\sqrt{N}\times$VAR.

The DQ images were constructed by using a bad pixel mask (BPM) file, available as part of the standard GMOS reduction package, for the chips in combination with a saturation map created from the SCI exposures. Pixels whose counts exceeded the 65000 ADU limit were flagged as bad. These extensions had the good data pixels set to 0 and the BPM & saturated pixels set to 1. The VAR and DQ extensions were propagated through all of the reduction steps.

The raw bias frames were combined into a mosaicked bias frame using the task `gbias`. The raw flat field images were combined into normalised flat-field response maps for each night and filter using the `giflat` task. Dome-flats of equal exposure time were available for the g'-band images and scaled Twilight flats (of differing exposure times) were available for the r'-band images.

The science frames were reduced with the task `gireduce`, involving bias frame subtraction (with overscan trimming), flat-fielding and mosaicking the three chips into a single image (for all of the SCI, VAR and DQ extensions) using *nearest* interpolation to prevent pixel correlations. This type of interpolation introduces a maximum error of half a pixel, which is typically less than 15% of the seeing FWHM (see Section 5.3) .

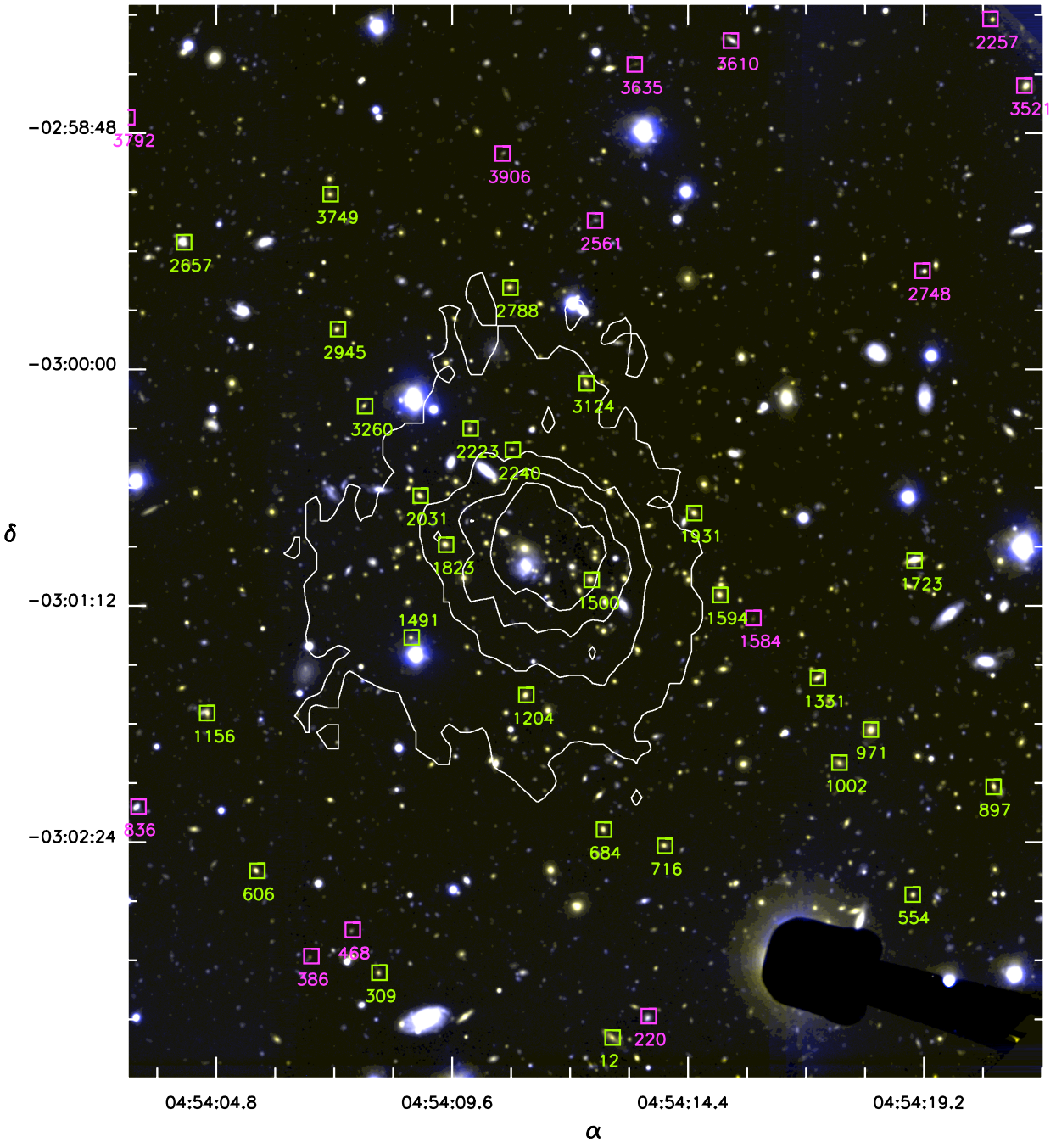

Figure 5.2: A false colour image of MS0451.6-0305, produced using the final g' and r' band reduced images. The objects marked are all found in the spectroscopic mask. The pink squares indicate galaxies that are not members of MS0451 and the green squares indicate the spectroscopically confirmed cluster members. The white contours indicate the central X-ray emission location, taken from *ROSAT* archival data Reese (2000).

Scattered Light

For r' and g' band images taken with GMOS-N, fringing is not generally a significant problem (Hook et al., 2004) and, indeed, in our data fringing is not apparent. However, the images did display non-uniform scattered light patterns across the mosaicked fields of view (Jørgensen et al., 2005, 2006). To remove the scattered light structure in the backgrounds, we used a 1σ cut above the modal sky level to identify non-background pixels. This identified the galaxies and stars. These identifications enabled masks to be produced via various `imexpr` task manipulations. An initial ID mask was produced with objects signalled with 1 and background set to 0. To remove spurious single-pixel identifications and to ensure adequate masking of more extended objects (whose light profiles may have had wings fading into the background), the masks were smoothed with a Gaussian kernel with $\sigma_{kern} = 10$ pixels via the `gauss` task. The smoothed masks were then thresholded, setting values above 0.7 to 1 and the rest of the pixels to 0.

The mosaicked, reduced images were stacked in pixel coordinate space, not using world coordinate system (WCS) alignment. The final masks were used to reject the non-background (object) pixels, by inputting them as bad-pixel masks (BPMs) in `gemcombine`. The *average* combination operation was applied, with a *minmax* rejection algorithm along the stacked dimension to reject the lowest and highest valued pixels in each image. The output from this was a map for the g'-band and a map for the r'-band of the scattered light and any intra-cluster light, particularly present towards the centre of the cluster, across the chip.

To measure the scattered light, while rejecting the intra-cluster light, a 2D polynomial surface fitting routine[1] was employed. This routine allowed fitting of each chip in the scattered light frames. A 4th order polynomial in the x and y directions (in the physical coordinate system of the GMOS-N detector) provided a smooth representation of the scattered light, without the intra-cluster light features, in the g'-band image. The r'-band image suffered from a ghost feature, discussed in Section 5.2.1. The polynomial-fit image was then subtracted from each of the g'-band science frames at various scalings ranging from 60% to 120% of the original level in 5% increments until the background levels appeared uniform across the chips (typically $\sim 1-2\%$ between chips 1,2,3).

[1] Developed using `Python` by Ryan Houghton.

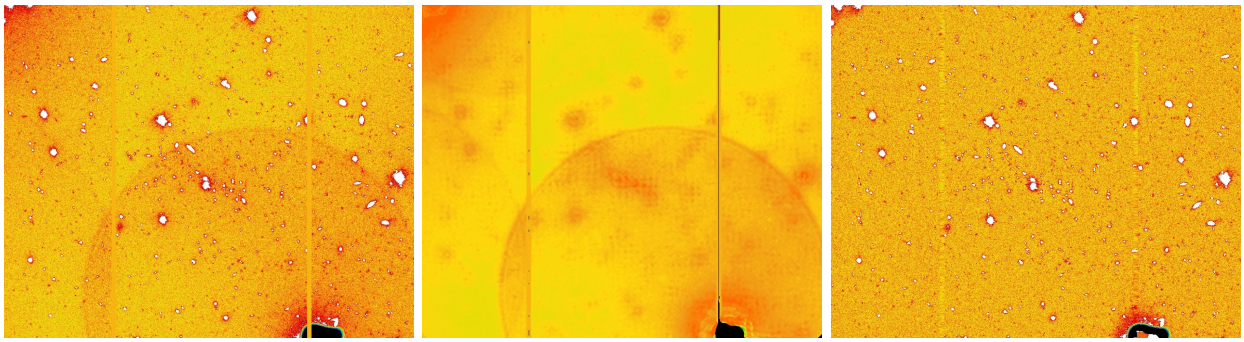

Figure 5.3: GMOS r'-band scattered light removal. False-colour images highlighting the ring-feature. The vertical lines in each image indicate the chip gaps, interpolated over during the reduction and filtering. The OIWFS can be seen as the black region at the bottom of each image.

r'-band ring feature

Figure 5.3 shows images of a mosaicked r'-band exposure. The far left image highlights the frame before scattered light removal. A ring feature is visible in the middle to lower right quarter of the field. The origin of the feature is believed to be a ghost image of a bright guide star covered by the on-instrument wavefront sensor (OIWFS, black region in the bottom right, $\sim$ 20 arcseconds wide when fully in view). As a 2D polynomial fit to the r'-band scattered light frame would not account for this feature, we median filtered the scattered light frame with a 10x10 pixel window. The resulting filtered, scattered light image had reduced levels of the intra-cluster light, while maintaining the prominent ring feature, as seen in the centre image in Figure 5.3. This image was then subtracted at various scalings from the science frames until the background levels were constant across the chip and the ring feature was removed, as seen in the right hand image in Figure 5.3.

Once the scattered light had been removed from all of the images, the task `imcoadd` was used to combine the dithered frames, (across different nights, in the r'-band, with similar seeing), into a single mosaic for each band. The header keyword RELINT was used to scale the images.

Flux calibration

The flux calibration of the images followed a similar process to Jørgensen (2009). The standard stars used are listed in Table 5.4 and are taken from the Landolt faint star catalogue (Landolt,

1992).

The reduction of each image followed the same method as the cluster image reduction. A Moffat profile was fit to the star in each image and the FWHM and eccentricity (e) from this fit was used to define the circular aperture for the photometry. The radius of this aperture was,

$$R_{ap} = 4 \times \text{FWHM} \times \sqrt{(1+e)/(1-e)} \tag{5.2}$$

The magnitude derived from the flux through this aperture is given by,

$$m_{ap} = -2.5\log\left(\frac{N}{t}\right) - k(\alpha_{air} - 1) + m_{band}^{zpt} \tag{5.3}$$

This involves the counts above sky within R_{ap} aperture (N), the exposure time (t), the atmospheric extinction at site (Mauna Kea) in the given band (k), the airmass (α_{air}) and the magnitude zero point in the given observation band (m_{band}^{zpt}), explained later in Section 5.3. The known magnitudes of the stars in the V-band and their (B − V) colours were found in the Landolt catalogue and transformed to their equivalent g' and r' magnitudes via the conversions,

$$g' = \text{V} + 0.54(\text{B} - \text{V}) - 0.07$$

$$r' = \text{V} - 0.44(\text{B} - \text{V}) + 0.12$$

from Smith (2005). No aperture correction was applied as the flux within R_{ap} of a Moffat profile is $> 99.9\%$ of the total.

Resolution

The average seeing across the g' and r' band exposures was $0.81''$ and $0.56''$ respectively, found from Gaussian fits to stars and listed in Table 5.3. To ensure reliable colour measurements, we convolved the r' band reduced image with an appropriate Gaussian kernel to match the g' band seeing. The alignment of the images was confirmed by coordinate matching common features and performing transformations to tweak the alignment with `imcombine`. As an additional check, the matching

of sources was performed using each original image's WCS information to transform the MDF celestial coordinates of each object into pixel coordinates. Over-plotting these pixel coordinates enabled visual confirmation of object matches.

5.2.2 Spectroscopic Reduction

The spectroscopic sample of potential cluster members was initially selected through a magnitude cut of $r' < 23$. A random selection of 42 of the objects (plus two bright stars) within the selection criteria made up our sample. The spectra were taken using the multi-object mode of GMOS-N (R400_G5305 grating, R $\sim$ 2000 giving resolution $\sigma \sim 65$ km s^{-1}). MOS functionality is achieved by employing a mask plate with laser-cut slitlets at the projected coordinates of the objects of interest. The nights of observation covered the 19th, 21st and 23rd December 2003.

The data was obtained via the Canadian Astronomy Data Centre (CADC) archive retrieval service [2]. To reduce the GMOS spectra, we created a pipeline of modified GMOS reduction tasks and automated scripts. The files were first split into the individual nights of observation and then again into the two central wavelengths. The initial preparation involved the use of `gprepare` to attach the mask definition files (MDF - listing slitlet properties) and create the variance and data quality (DQ) frames for each bias, flat, arc and science image. The gradient of the combined flat image was used to locate the slit edges along with the aid of the MDF. The resulting file, an output from `gscut`, was used as a reference image for the reduction of the science and arc frames, as part of the `gsreduce` task. This task applied bias subtraction, flat fielding (science frames only) and separation of the arc and science files into MEF files containing the propagated science, variance and DQ extensions for each slitlet. Once reduced, the arc frames were used to obtain the wavelength solution by identifying the emission lines with respect to a CuAr line list. I performed a 4th order Legendre polynomial fit in the spectral direction and a 2nd order fit in the spatial direction. The residuals of the fits were typically $\sim$ 0.2 Å rms. The output from `gswavelength` was used by `gstransform` to apply the wavelength solution to the science frames, logarithmically binning along the dispersion direction. For MS0451 the wavelength grid began at 5000 Å and finished at 10000 Å over 3650 elements, giving a dispersion of 1.37 Å when regularly gridded. This grid was the

[2] http://cadcwww.dao.nrc.ca/cadcbin/gsa/wdbi.cgi/gsa/dssc_GMOS/form

same for both wavelength settings. The interpolation of this grid onto a logλ grid was the only interpolation in the reduction process. This helped maintain the statistical independence of the pixels and to minimise correlations.

I used `gsskysub` to subtract the sky counts. This task subtracts a linear fit to pixels between the areas containing galaxy counts at each wavelength. Fringe frames were not required for the wavelength range (Hook et al., 2004). The chip gaps in the DQ frames were corrected, as they were slanted by the wavelength transformation. The 1D spectra were then extracted from the 2D fields of the slits, collapsed over an aperture of $1.4''$ to encompass the peak flux of each galaxy (accomplished by `gsextract`).

The extracted 1D spectra for each night and wavelength range were combined, scaling by their median fluxes, via a custom made `IDL` version of `scombine`. This routine also flagged bad pixels and allowed visual inspection of the spectra as they were stacked. The results were individual spectra and error-spectra (derived from the variance extensions) fits files for each slitlet.

5.3 Integrated Photometry

To perform integrated photometry on the GMOS images, we used the *SExtractor* software package (Bertin & Arnouts, 1996). This package is able to find objects in an image and create a catalogue containing several photometric properties for each detection. We were primarily interested in finding the aperture magnitudes and total magnitudes for each galaxy in MS0451.

The basic list of operations *SExtractor* performs is as follows. Initially, the sky background structure is evaluated and subtracted. The sky-subtracted image is then filtered and thresholded to detect sources. An object is classified when a certain number of pixels exceeds the local threshold (e.g. a threshold of 3σ above the local sky level, with, in our case, a requirement of least 8 pixels meeting this cut). The sources are then deblended to aid detection of close-packed objects, extended objects or faint objects. We set 64 de-blending sub-thresholds, which split the area of the detection into 64 exponentially-spaced levels for measurement/separation. The detected and deblended objects are then logged to a catalogue that contains user-specified information on the flux within certain apertures, positions (celestial and physical) and object-type classifications (star,

galaxy).

The input to my *SExtractor* runs involved the reduced r'-band and g'-band images, resolution and coordinate matched. The variance image produced in the reduction of the images was used to create a *weight-image* to aid detection and produce real errors in the final photometry, passed as an inverse variance map (IVM) to *SExtractor*. The photometric zero-points were used from Section 5.2.1. These were corrected for galactic extinction in the region of MS0451 and exposure time (t_{exp} =600s) via,

$$m_{band}^{zpt} = m_{band}^{std} - A_{band} + 2.5\log(t_{exp}) \tag{5.4}$$

The magnitude corrections in the appropriate bands were obtained from the NASA/IPAC Infrared Science Archive (Cardelli et al., 1989; Alexov et al., 2005). They are given here as $A_g = 0.183$ and $A_r = 0.124$. The adopted zero-points were therefore, $m_{g'}^{zpt} = 34.380$ and $m_{r'}^{zpt} = 34.913$.

The requested outputs from *SExtractor* were the pixel coordinates (x and y) of each member, for easy matching with the MDF coordinates, fixed-aperture magnitudes (with error) and automatic-aperture magnitudes (with error). The fixed-aperture magnitudes were defined by Equation 5.2. With a seeing FWHM of $\sim 0.81''$, plate scale of $0.1454''$ and a small measured ellipticity of ~ 0.01, the fixed aperture diameter was set to 22.5 pixels ($\sim 3.3''$). The automatic-aperture is based on the definition of the Kron radius (Kron, 1980) that is varied in size to obtain a total magnitude for the object (based on a scaling of the the intensity-weighted 1st moment radius). The fixed-aperture is required for colour calculations (ensuring the flux in each band is calculated from the same region) and the Kron magnitude provides a total determination of the magnitudes in a given band.

5.4 Determining velocities and velocity dispersions

The original spectroscopic sample had been selected purely through a magnitude cut. The objects in the mask next required spectroscopic confirmation of their membership of MS0451. The CaH+K (singly ionized Calcium lines (CaII) at rest-λ 3933.7Å and 3969 Å) and G4300 (several electronic transitions in the CH radical at 4300 Å) lines were used as the absorption features for initial line of sight velocity (V_{los}) determinations. The constant velocity resolution (with a velocity scale of $\sim$

57 kms^{-1}) enabled the shift in array indices of the spectra to be directly converted into V_{los}. The rough V_{los} were required for fitting the velocity dispersions, explained next.

5.5 Extracting kinematics

To extract the stellar kinematics from galaxy spectra, in particular velocity dispersions, we make the assumption that each spectrum (G) can be modelled by the convolution of a single stellar template, (T) with a distribution of velocities ($L(v)$). When sampling G in logλ (and therefore regularly sampling in velocity space), we can represent this as,

$$G(\log\lambda) = T(\log\lambda) \otimes L(v) \tag{5.5}$$

$L(v)$ has the form of a parameterised Gaussian with a mean velocity (V) and standard deviation σ or its *velocity dispersion*. A library of stellar template spectra is usually used with a weightings in the convolution to determine an appropriate match - by minimising residuals between the model and observed spectrum. An accurate template can only be found if the spectral resolutions match. This can be achieved by observing several stars with the same instrument used to obtain the galaxy spectra, or by using an archival library of stellar spectra obtained at higher resolution and then convolving this library with an appropriate line profile. We chose to use the latter method and adopted the Indo-U.S. Library of Coudé Feed Stellar Spectra (CFLIB) (Valdes et al., 2004). These 1273 spectra have a spectral resolution FWHM of 1.35 Å (updated from the nominal 1.0 Å in a study by Beifiori et al. (2011)) across a wavelength range of 3465.0 to 9469.0 Å giving a velocity resolution of $\sim$ 30km/s at λ_c and $R \sim 4200$.

Usually, the stellar library is convolved with a Gaussian kernel to match the spectral resolution of the observed galaxy spectrum. This will only provide the best possible match if the line shape of the stellar template matches the line shape of the observed spectrum (both Gaussian). Any deviations in the spectra are usually accounted for by an extra term in the galaxy model to describe

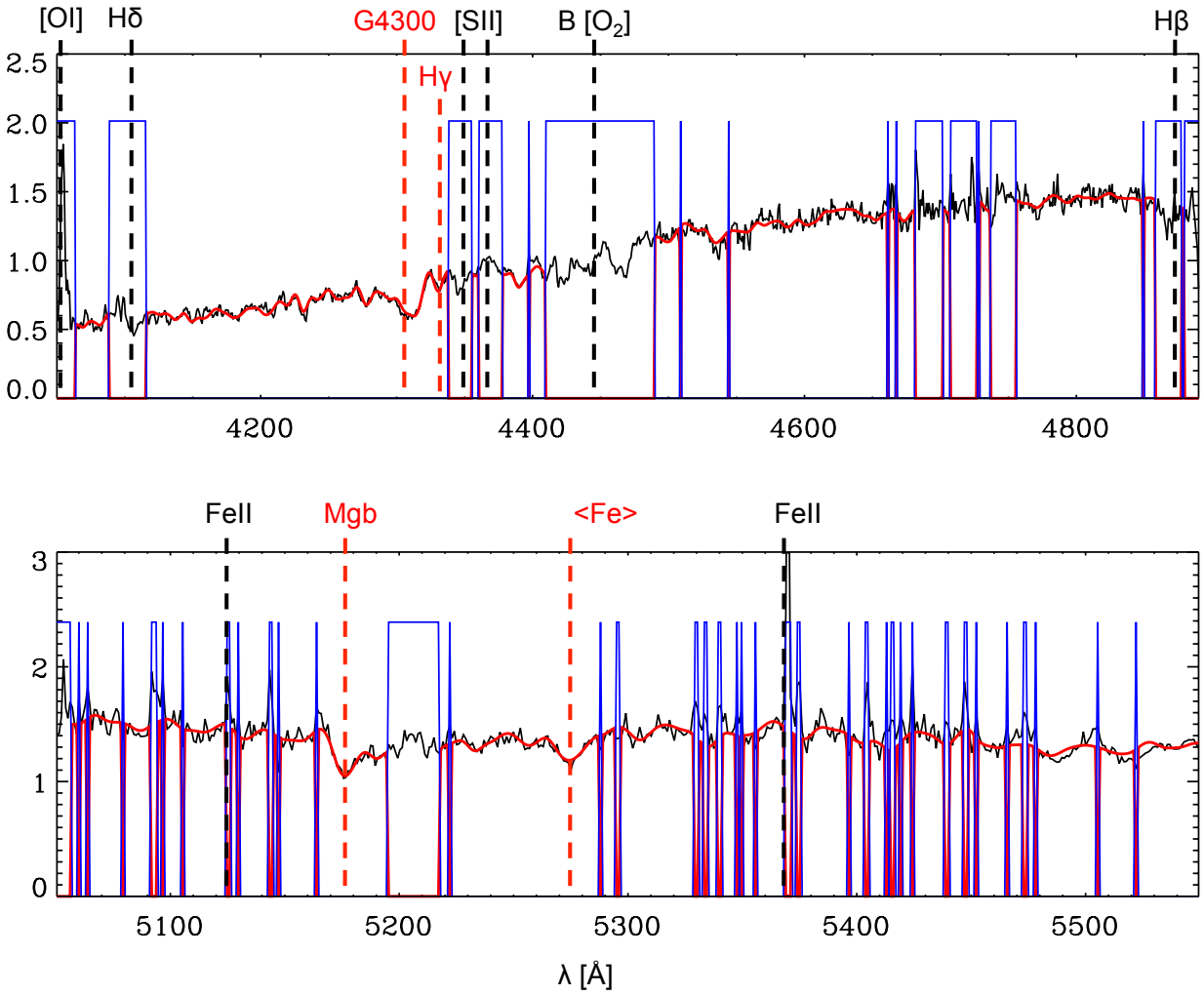

Figure 5.4: Example spectra for Galaxy I.D. 1931, highlighting the quality of the GMOS-N spectra. The blue lines indicate masked/bad regions and the red line indicates the best-fitting stellar template.

continuum variation from Equation 5.5,

$$G' = G + \sum_{i=0}^{N} a_i P_i(\log\lambda) \tag{5.6}$$

where P_i are Legendre polynomials of order i. If the line shape of the galaxy spectra deviates significantly from Gaussian, then there is a chance of template mismatch - leading to incorrect velocity determinations. If we are able to adjust the stellar library line shape to the galaxy line shape, before the matching of templates, then in combination with Equation 5.6, template mismatch can be minimised.

The line profiles seen in the arc spectra from GMOS-N are not purely Gaussian. They appear to be a convolution of the telescope PSF with the top-hat function of the slits. To parameterise the form of the GMOS instrumental profile, and thus determine a suitable kernel for convolution with our stellar library spectra, we adopted a truncated Gauss-Hermite (GH) expansion, of the form,

$$A(x) = \frac{\gamma}{\sqrt{2\pi}\sigma_{sd}} \exp\left[-\frac{1}{2}\left(\frac{x-\bar{x}}{\sigma_{sd}}\right)^2\right] \sum_{i=0}^{N} h_i H_i(x-\bar{x}) \tag{5.7}$$

which we can see is a regular Gaussian with mean $\bar{x}$ (in wavelength, velocity or pixel space), standard deviation σ_{sd} and scale factor γ weighted by the sum of Hermite polynomials H_i. We set $h_0 = 1$, $\{h_1, h_3, h_5\} = 0$ and allow $\{h_2, h_4, h_6\}$ to vary. The odd members of the Hermite series pertain to non-symmetric irregularities in the line profile. As, upon inspection, the GMOS arc lines were symmetric, we could reduce the parameterisation of the fitting to the even coefficients and standard Gaussian parameters only. We fit the GH series to GMOS arc lines across the spectral range of the CuAr spectra and across all 44 slits in the mask. We fit the lines in pixel space and utilised the `IDL MPFIT` implementation of the Levenberg-Marquardt algorithm that finds the best fit parameters by minimising the rms difference between the model function and the data profile. The high degree of freedom in these fits leads to the availability of several local minima, resulting in a degree of sensitivity to the initial values of the h_i coefficients. To reduce this sensitivity we noted that negative h_i produce profiles with large wings and sharp peaks, whereas positive h_i move the line spread function to a top-hat-like shape. So, we limited the h_i coefficients to positive values

only.

An example of a fit to one of the arc lines can be seen in Figure 5.5a . The poorer fitting Gaussian profile can be seen in red and the much better GH-parameterised fit can be seen in blue (over the line profile in black). Figure 5.6 shows the variation of these fits with wavelength. The line shape is quite stable across the wavelength range.

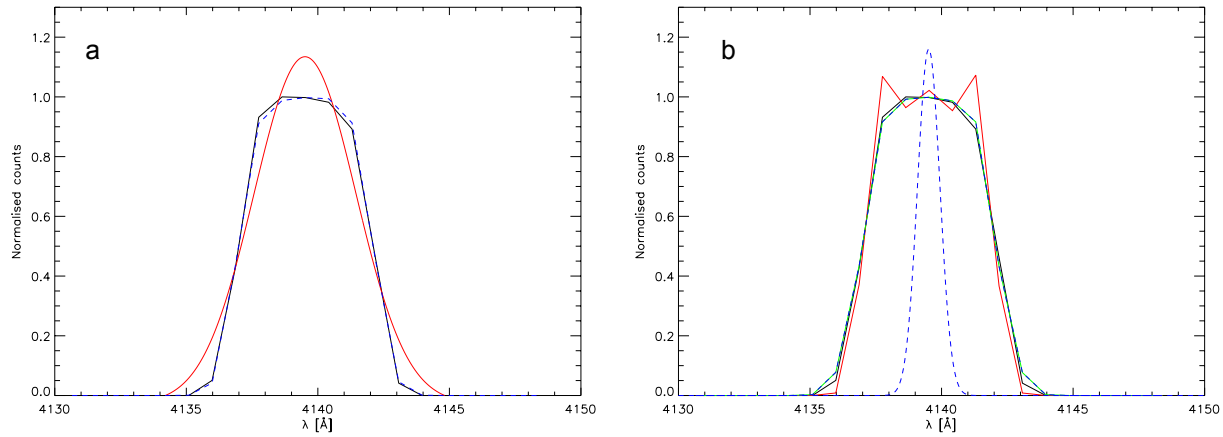

Figure 5.5: a.) GH fit (blue) to a GMOS arc line (dashed black). The inadequacy of a Gaussian line profile is highlighted in red. b.) The TF is given in red and is applied to the dashed-blue CFLIB instrumental profile to produce the dashed-green GH fit to the GMOS arc line.

The spectral resolution is also quite stable across the range in λ, but this indicates a strong variation of the resolution in velocity space(σ) - reducing from around 105kms^{-1} to 75 kms^{-1}.

To determine the kernel for convolution with the spectral templates, we needed to adopt the above method. This kernel takes the form of a transfer function (TF). Prior to deriving the TF we needed to account for the decreasing velocity resolution with wavelength. If we simply matched the resolution of the stellar library to that of an arc line in the *observed* wavelength range of the galaxy spectra, when we redshifted the template spectra to the redshifts of the galaxies, their spectral resolutions would still be too high (resulting in larger velocity dispersion determinations). To prevent this we blue-shifted the arc spectra by the cluster z, before performing our TF determination. To determine the TF we created a model profile by convolving the GH-expanded Gaussian with a Gaussian of FWHM = 1.35 Å (that of the CFLIB) and minimised the χ^2 between this model

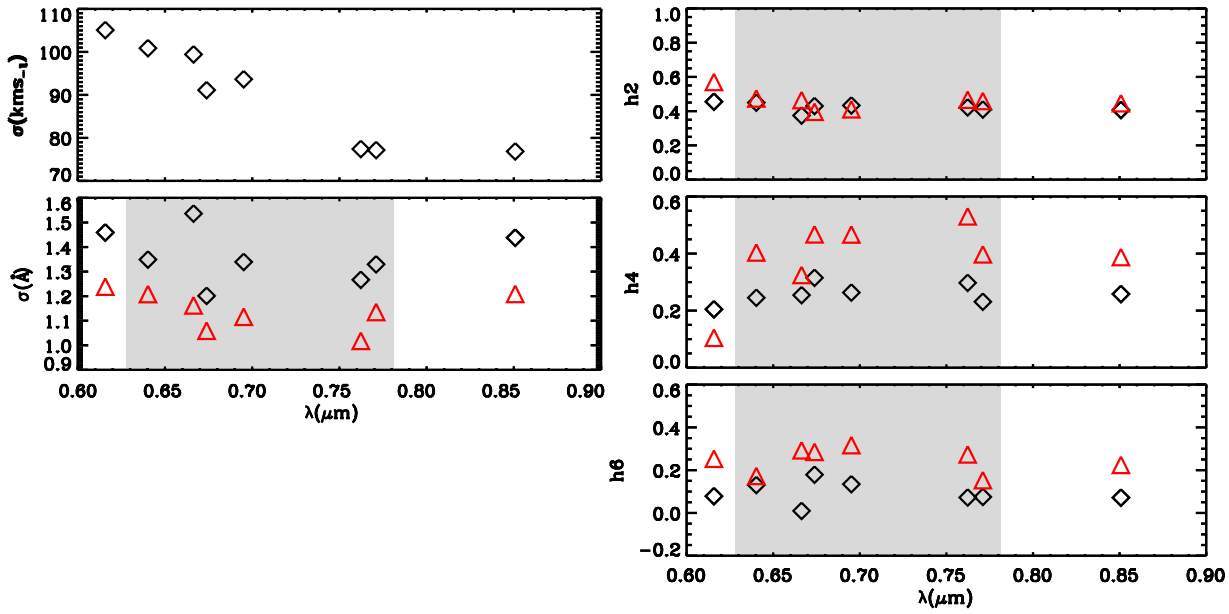

Figure 5.6: σ, σ_λ and the even GH parameters as a function of λ. The grey region indicates the GH parameters used for the first wavelength interval.

convolution and the data via,

$$\chi^2 = \sum_{i=1}^{N} [D_i - (C_i(\bar{x}, \sigma) \otimes A_i(\sigma', h'_j))]^2 \tag{5.8}$$

for each arc line. Where the profile of the template library is represented by C_i, assuming a pure Gaussian profile in the CFLIB spectra, the GH-parameterised Gaussian from Equation 5.7 by A_i and the arc line data by D_i. The A_i that minimised χ^2 was adopted as the TF. An example of the TF for an arc line is given in red Figure 5.5b. The blue dotted line is the Gaussian CFLIB profile and the green line indicates the CFLIB profile convolved with the TF, fitting the arc line well. The derived parameters for the transfer function are shown in red in Figure 5.6. The grey shaded region indicates the first wavelength range over which we extracted the velocity dispersions. We chose to extract the kinematics over the well studied rest-wavelength ranges of 4050 to 5050 Å and 5050 to 5550Å and as a check or in case of poor fitting in either of these bands we also fit across both λ intervals (4050 - 5550Å) simultaneously (beyond this rest-frame limit the spectra were prohibitively contaminated by skylines). This set of ranges would provide a more reliable fit to the

template library and avoids the CaHK lines that exhibit intrinsic broadening in stellar atmospheres. Shifted to the redshift of MS0451, this covers the range shown in the figure. The parameters for the TF averaged over these ranges were found to be $\{\sigma, h_2, h_4, h_6\} = \{1.1\text{Å}\ , 0.46, 0.47, 0.29\}$ and $\{1.2\text{Å}\ , 0.4, 0.41, 0.2\}$.

Once the TF had been determined, we were ready to perform the template matching and extract the galaxy line of sight velocities (V_{los}) and dispersions σ. We used the freely available penalised pixel fitting code of Cappellari & Emsellem (2004) (pPXF) in an `IDL` wrapper to fit the parameterised kinematics. The wrapper script prepared the galaxy spectra by masking out telluric features (such as the 6867Å and 7594Å molecular Oxygen B & A lines), identifying NaNs and estimating S/N per pixel prior to their input into the routine. The V_{los} determined for each galaxy when confirming cluster membership earlier were used as the initial V_{los} guesses.

pPXF also adopts GH fitting in determining the V_{los} and σ of the input galaxies. The code implements Equation 5.6 and expands the velocity distribution, $L(v)$, as a GH series. The $L(v)$ has all its parameters (or to user-defined maximum order) $\{V, \sigma, h_3, ..., h_N\}$ fit simultaneously and an adjustable penalty term is added to the χ^2 measure to bias the solution towards a Gaussian shape in the event of low S/N (below a certain threshold). This prevents the tendency of the GH coefficients towards local minima in low S/N regions, thus preserving only the statistically significant non-Gaussian features in the V_{los} and σ determinations. We initially ran pPxf with a random CFLIB template to obtain a better starting estimate of the V_{los} and σ. The full library was subsequently run through the routine. The V_{los} and dispersions obtained from pPXF were then used as the starting values for another template fitting routine called GANDALF (Gas And Absorption Line Fitting, Sarzi et al. (2006)). GANDALF performs penalised pixel fitting while also allowing the fitting and masking of emission lines that can affect nearby absorption features. The use of an emission-line lookup table aids the identification of emission and skylines in the wavelength ranges of interest. The routine was initially created for measuring gas kinematics from emission line spectra, but is also useful for removing these lines if we are only interested in the stellar absorption features. The final velocities and dispersions across the the three fitting intervals were then compared. If the derived values were of comparable magnitude and error then they were

averaged for the final value to go into the analysis. If the error was particularly large on a value across one or more intervals ($> 15\%$) due to a lack of absorption features or noisy regions, then the best fitting (lowest error) interval out of the three was used to provide the kinematics for that particular galaxy. The results across the three intervals were used to find the most robust V_{los} and σ for each galaxy by selecting the values that had the smallest error, indicating the best template match. The final selected outputs from the template fitting are given in Table 5.5 at the end of this Chapter.

ETGs display radial gradients in their velocity dispersions, with σ decreasing out from the centre(Davies & Birkinshaw, 1988; Davies et al., 1993). Thus, the size of the aperture used for extraction of spectra and the distance to the object(s) affect what is *measured* as the central σ. This measured value will depend on the dispersion profile in the galaxy. A general form is assumed for the galaxies being measured. We referenced the findings of Jorgensen et al. (1995b), who used kinematic models to derive their corrections - sourcing literature data.

As stated earlier, each spectrum had been extracted from a rectangular aperture of dimensions $1''$ by $1.4''$. The equivalent circular aperture for this size is given by

$$R_{ap} \approx 1.025\sqrt{\frac{xy}{\pi}} \tag{5.9}$$

where x and y are the rectangular aperture dimensions ($''$). The factor 1.025 is given in Jorgensen et al. (1995b), where the authors constructed two-dimensional models of the surface brightness, velocity dispersion and rotational velocity projected on the sky and an empirical dependence of velocity dispersion measurement on aperture shape and size was determined. We then corrected our aperture dispersion measurements, σ_{ap}, to a dispersion measured within an aperture of diameter $2R_n = 1.62$kpc. This is the standard size given by Jorgensen et al. (1995b), where they define it as $1.19h^{-1}$ kpc. This projects to a diameter of $3.40''$at the distance of Coma, our comparison sample, for the adopted cosmology. The final correction to σ_{ap} follows a power law,

$$\sigma = \sigma_{ap}\left(\frac{R_{ap}^{kpc}}{R_n}\right)^{\mathcal{C}_\sigma} \tag{5.10}$$

where the constant $\mathcal{C}_\sigma$ is given as -0.04, the normalising radius is $R_n = 0.81$ kpc and R_{ap}^{kpc} is R_{ap} in kpc, converted using the scale at $z = 0.55$ of 6.394 kpc/″.

5.6 HST imaging

5.6.1 HST Reduction and *MultiDrizzling*

The primary individual image files were downloaded as flat-fielded images (*flt*), containing the exposures for each chip (EXP), their error (ERR) and data quality (DQ) extensions in multi-extension fits (MEF) files. The raw images and associated calibration files were also obtained and checked against the available *flt* files. Calibration of the images was achieved using the standard `PyRAF/CALACS` pipeline made available by the Space Telescope Science Institute (STScI). The initial reduction steps for each flat fielded image involved bias subtraction, dark current subtraction and flat-fielding as described in the ACS instrument handbook (Gonzaga, 2005) and the ACS data handbook (Pavlovsky, 2005).

Each pointing consisted of 4 exposures at different positions, dithering over the chip gap. We began with the only pointing available from program 10493. Four other pointings from program 9836 were reduced for analysis of galaxies in the spectroscopic mask that fell outside of the 10493 field.

The `PyRAF` task *MultiDrizzle* (Koekemoer et al., 2002) was used to combine all of the flat-fielded exposures into a single image. Essentially, *MultiDrizzle* corrects the images for geometric distortions and removes cosmic ray events, resamples onto a finer grid to correct for the under-sampling of the PSF, before combining the images into a final reduced image for analysis. The steps taken are given here, including our modifications to the regular routine:

- *Initialisation:* The first step determines input file type and status of the files themselves (to ensure they are flat-fielded). The DQ is also assigned as well as any initial coordinate shifts if a shift-file is presented.

- *BPM creation:* Bad pixels are flagged and added to the DQ files.

- *Sky subtraction:* Each chip has its sky level determined via modal pixel counts in sparse regions and subtracted.

- *Drizzling onto separate images:* Distortions in each image are corrected and drizzled onto the same coordinate system as a reference image (the first image in the input list). The WCS for each image were then updated to share the same reference using this information

It is at this point that we interrupt the standard *MultiDrizzle* run. The task `LACOS_IM` (van Dokkum, 2001) was run to clean cosmic rays from the drizzled images. The resulting cleaned images were then suitable for the task `starfind` to identify stellar objects, avoiding spurious detections. The stellar object lists for each image were then matched with `xyxymatch` and the shifts and rotations relative to the reference image were determined from the output using `geomap`. The shift-file created was then fed into the *MultiDrizzle* routine in order to apply initial offsets to the WCS to improve alignment. *MultiDrizzle* was run for a second time and beyond the first drizzle step, the rest of the process followed:

- *Median image:* The separate drizzled images are median combined - taking into account the static BPM created earlier.

- *Median image copying:* The median image is copied back to the frame of the original (*flt*) images, geometrically distorting the image. This provides cleaned versions of the original distorted images.

- *Compare:* The cleaned distorted images were compared to the originals to create cosmic ray masks.

- *Final drizzle:* The cosmic ray masks are used in the final drizzle combination, with the images weighted by exposure time.

In the final drizzle step, a square drizzle kernel was employed. The fraction by which the input pixels were shrunk prior to being drizzled onto the output image was defined by the `pixfrac` keyword and set to 1.0. To Nyquist sample the PSF, the drizzle scale was set to sample at a higher resolution than the pixel scale ($0.05''\text{pixel}^{-1}$) at $0.03''\text{pixel}^{-1}$. The final, drizzled image for each

pointing was normalized over its total integration time and therefore had units of $e^{-}s^{-1}$. The raw image filenames, exposure times and other useful information are presented in Table 5.1.

5.7 R_e and $\langle I \rangle_e$ Determination

There are two primary methods of R_e and $\langle I \rangle_e$ determination from flux calibrated images. Differential surface fitting via bulge-disk decomposition (e.g. using GASP2D, Méndez-Abreu et al., 2008) or curve of growth profile fitting (COG, Dressler et al., 1987; Jorgensen et al., 1992). As the majority of earlier work on scaling relation has focussed on COG fitting, we chose to adopt this method. COG fitting software, written in `IDL`, was initially devised by Houghton et al. (2012).

5.7.1 Preparing the galaxies

The program used the mask file from the GMOS spectroscopic observations to obtain the coordinates of the objects, after applying a slight shift due to HST/GMOS WCS misalignment. Each object in the mask is cycled through and a region around the galaxy of interest is marked out by the user. Four other user-defined regions are used to obtain a sky value in the immediate vicinity of the galaxy. The modal pixel values are found in each region, by fitting a Gaussian to a histogram of pixel counts (binned up with a resolution of - x), and averaged. This enables us to account for the intracluster light towards the center of the cluster. 2D Gaussian and ellipsoid centroids are fit to the object, and the position angle (PA) and ellipticity ϵ are measured over a series of isophotes. The best fitting ellipse is used to define the final PA and ϵ.

The objects in the field of MS0451 are densely packed. Some of the regions around the selected members were therefore contaminated by other objects. In the sparser regions, the contaminating objects were point-source like, as they tended to be background objects that were most likely not cluster members. The removal of these objects was achieved by clipping pixels above the modal sky value outside the galaxy of interest. For objects in the denser, central cluster regions, the contamination affected the background light profiles, as the wings of the brighter galaxies (potentially cluster members) would affect the COG integrations. To remove these contaminating sources, we manually selected the regions for masking. To replace the clipped/masked pixels, we

performed a 2-fold reflection about the galaxy centroid, thus filling in the masked regions with sky pixels. For severe masking, for example when contaminants were visibly overlapping with the galaxy of interest's profile, we azimuthally binned the image with a fixed radial binned size and a fixed azimuthal bin size, using the PA and centroid of the galaxies. The average of the bins at each radius was then used as the value for any masked pixels located at that radius. An example of contamination removal in one of the galaxies is given in Figure 5.7. The cleaned, centred galaxies were then ready for COG fitting.

5.7.2 The COG Algorithm

The curve of growth method for fitting R_e and $\langle I \rangle_e$ involves integrating radially outward from the centre of the galaxy and fitting some analytically derived model profile to the data. A best fit profile is found by simply minimising the squares between the model and the data. We chose to fit the Sérsic profile (Sérsic, 1963; Sersic, 1968),

$$I(r) = I_0 \exp(-(r/\alpha)^{\frac{1}{n}}) \tag{5.11}$$

where r is the radial distance from the centre, I_0 is the central intensity, α is the scale length (r at which I drops to $I_0 e^{-1}$) and n is the Sérsic index. We fixed $n = 4$ to fit the case of the de Vaucouleurs profile (de Vaucouleurs, 1948). The *total* luminosity is given by,

$$L = \int_0^{2\pi} \int_0^{\infty} I(r) r \mathrm{d}r \mathrm{d}\theta \tag{5.12}$$

incorporating Equation 5.11 and using the substitution $x = (r/\alpha)^{\frac{1}{n}}$,

$$L = 2\pi I_0 \alpha^2 n \int_0^{\infty} x^{2n-1} \exp(-x) \mathrm{d}x \tag{5.13}$$

This integral is easily recognised as the Gamma function $\Gamma(2n)$. Recall, R_e is defined as the half-light radius, thus we can write,

$$L/2 = L(< R_e) = 2\pi \int_0^{R_e} r I(r) \mathrm{d}r \tag{5.14}$$

R_e will depend on n and can be given as $R_e = b^n \alpha$, where $b \approx 2n - 0.324$ & n varies over the range $2 < n < 10$ (Ciotti, 1991). Incorporating this into an expression for α in Equation 5.11,

$$I(r) = I_0 \exp(-b(r/R_e)^{\frac{1}{n}}) \tag{5.15}$$

If we take the radius limit of the total luminosity as the radius at which the galaxy counts equals the sky level, we are then able to measure the total luminosity and then obtain a value for R_e using Equations 5.14 and 5.15. The area under the best fit COG up to this radius enables the calculation of the average surface brightness within R_e, $\langle I \rangle_e$.

The instrumental PSF of the HST images would create a systematic difference between the true R_e and $\langle I \rangle_e$ of each galaxy and those determined from the measured COG - a convolution of the instrumental PSF and the true profile. If the instrumental PSF were well approximated by a single Gaussian or Moffat profile, the correction for this effect would be straightforward. However, this is not the case for HST images. Therefore, we created a representative PSF for our data by approximating the form by a multi-Gaussian expansion (MGE, Bendinelli (1991), with the effectiveness of MGE for HST restoration presented in Zavatti et al. (1991)). The details of the PSF creation are given in Section 5.7.3. The 1D MGE fitting routines made available by Cappellari (2002) were used to calculate the radial MGE approximation. The MGE method assumes the PSF is representable as a sum of Gaussian profiles, minimising the quantity,

$$\Delta_G = \sum_{pixels} \left[\frac{\sum_{i=0}^{N} G_i(r) - PSF(r)}{PSF(r)} \right]^2 \tag{5.16}$$

where G_i are 1D Gaussian profiles (each with $\{I_i, \sigma_i\}$) and $PSF(r)$ is the 1D profile of the HST PSF. The number of Gaussians (N) was left as a free parameter in the fit. Once the form of the HST PSF had been constructed as a 1D profile, we were able to convolve the Sérsic function (in its intensity form) $I(r, R_e, n)$ with the individual Gaussian profiles that formed our MGE profile and fit this to the sampled points for each galaxy.

$$I'(r, R_e, n, \sigma) = \frac{1}{\sigma^2} \int_{r=0}^{r=\infty} I(r) \exp\left[\frac{1}{2}\left(\frac{r^2 + R_e^2}{\sigma^2}\right)\right] B\left(\frac{r R_e}{\sigma}\right) \mathrm{d}r \tag{5.17}$$

where B is a modified Bessel function of the first kind, zeroth order (Moffat, 1969; Bendinelli et al., 1982). Summing this according to the amplitudes of the MGE provides a good approximation to the full PSF convolution. Ellipticity is not accounted for in the fitting process. An azimuthal average of multiple HST/ACS PSFs can be seen in the left plot in Figure 5.8 (black points). The radially binned points are given by the red line and the MGE approximation is given by the blue line. The right plot in Figure 5.8 shows how the residuals to the COG fit are affected when we account for the PSF (red triangles). Towards the central pixel the MGE COG residuals remain close to 2-4%, whereas the fit without accounting for the PSF deviates drastically as the centre of the galaxy is approached (black triangles). The results given in the plot are for de Vaucouleurs fitting. The residuals when fitting variable Sérsic profiles are even smaller (close to zero).

We perform the fitting of the COG model profile to the data, by employing the Levenberg-Marquardt algorithm, implemented in the MPFIT[3] procedure release for `IDL`. The method for the creation of the PSF is given in the next sub-section.

5.7.3 PSF creation

To create the PSF for use in our COG fitting code, we created a range of `PyRAF` scripts and `IDL` procedures. We began by utilising the TinyTim PSF Modelling code (Krist, 1995), available from (STSCI). The programme is fed information on the instrumental setup of the ACS observations and a list of coordinates in pixel space for the positions of the model PSFs across the detector. Each pointing consisted of four dithered images (to cover the chip gap). The coordinates of the cluster members, in pixel space, were taken from the first flat-fielded frame (with header keyword POSTARG = 0.0). These were transformed to the correct pixel coordinates in each of the three other dithered images via their POSTARG keywords. PSFs of diameter $3''$ were created. Once each coordinate had a PSF created, dummy flat-field MEF files were produced. These were essentially the same as the science flat-field files, but with the EXP extensions containing null arrays of the same dimensions as the chips. The PSF images produced by TinyTim were inserted into these arrays at the relevant positions, thus creating 'model star observations' . To achieve the same distortions as those applied to the cluster members during the reduction, *MultiDrizzle* was run

[3]http://www.physics.wisc.edu/ craigm/

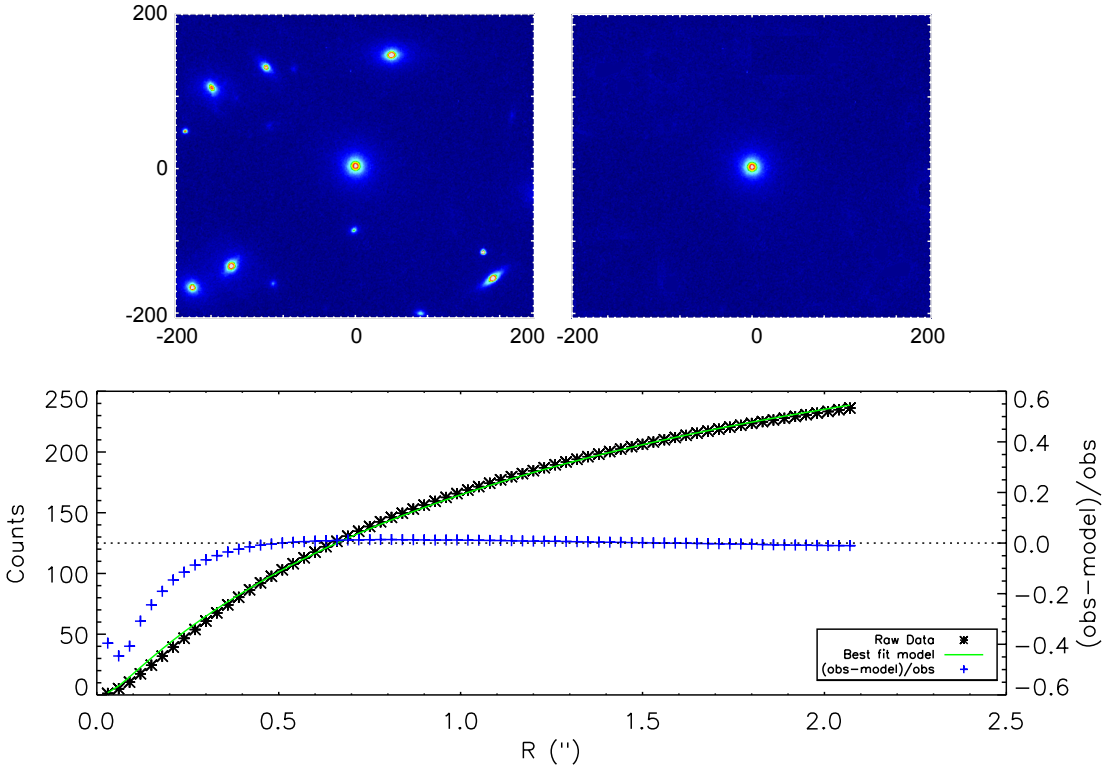

Figure 5.7: Example of source contamination and COG fit. *Top images:* Galaxy I.D. 1500 is located towards the centre of the cluster. Contamination by other sources is potentially significant, as seen in the left image. The contamination removal routine leaves a smooth background with the object of interest ready for COG fitting in the centre, seen in the right image. *Bottom plot:* de Vaucouleurs COG fit (green) to galaxy data (black points). The residuals of the fit are given in blue.

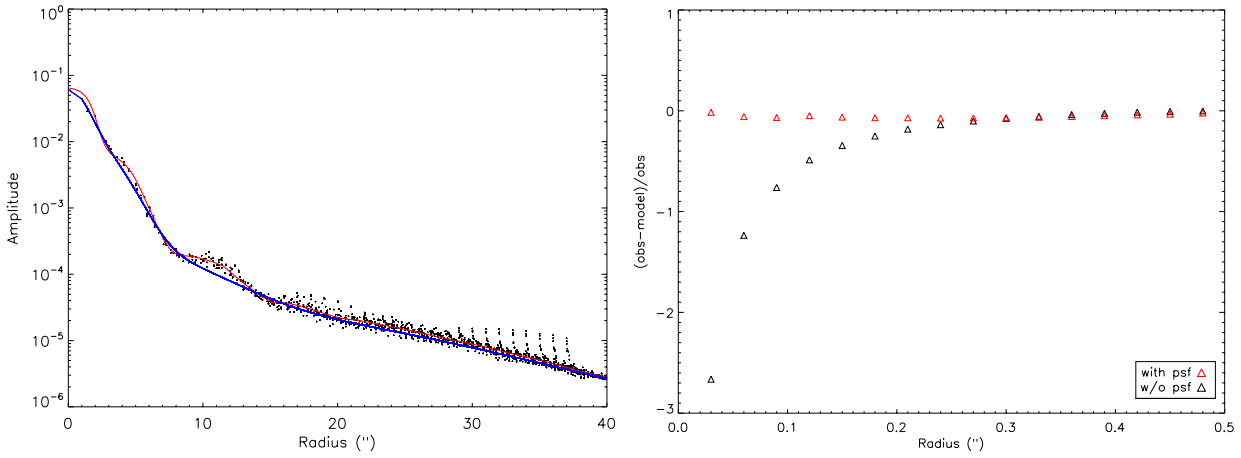

Figure 5.8: MGE approximation and residuals to COG fits.

twice in exactly the same process as in Section 5.6.1.

The PSFs were extracted from the drizzled images, rotated by 90° three times, and mean combined to produce symmetric PSFs for each location. These were all finally averaged into a representative PSF for the full field of view.

5.8 HST Photometric zero-points, corrections and conversions

Direct comparison of the MS0451 data and the local sample in Coma requires differences in the observations to be corrected. The filters used for each set differ in central λ, bandpass & magnitude system and there are also the effects of cosmological dimming & evolution in the stellar population of MS0451 to account for.

5.8.1 Magnitude systems

The zero-point (zp) used for the $\langle I \rangle_e$ determinations in the COG algorithm was obtained via the method of Sirianni et al. (2005). Here, the *PHOTFLAM* header keyword is used, along with the filter pivot wavelength (F814W, $\lambda_p = 8060$Å) to obtain the AB magnitude zp (zp_{AB}) through the equation,

$$zp_{AB} = -2.5\log(PHOTFLAM) - 21.10 - 5\log(\lambda_p) + 18.6921 \tag{5.18}$$

For all of the observations across the two HST proposals, the zp_{AB} was found to be 25.9593. The I-band galactic extinction (A_I) in the region of MS0451, taken from the NASA/IPAC dust extinction map archive (Cardelli et al., 1989; Alexov et al., 2005), is found to be 0.066. The final zp for each HST image is then derived via Equation 5.4, as with the GMOS imaging.

The initially measured, extinction corrected, apparent magnitude within an aperture defined by a radius R_e is thus given by,

$$m_m = -2.5\log(\text{counts}) + zp_{AB} - A_I \tag{5.19}$$

5.8.2 Cosmological corrections

The effects of expansion and redshift on derived magnitudes are significant for $z = 0.55$ objects. Firstly, the cosmological Tolman surface brightness dimming (Tolman, 1930) has a marked effect on measured magnitudes. It is found that the observed bolometric magnitude is related to the rest-frame bolometric magnitude by,

$$m^o_{bol} = m^r_{bol} + 10\log(1+z) \tag{5.20}$$

indicating four $(1+z)$ scaling factors acting to dim the rest frame surface brightness. This term is accounted for by three effects: diminished arrival rate of photons, the redshifted energy of the photons and the expansion of the observed surface area (providing a factor of $(1+z)^2$). To convert the above relation (Equation 5.20) to the bandpass limited case, we need to consider two effects on our bandpass limited observations. The first is the stretching of the rest-frame bandpass of the high-redshift objects (relative to the local rest-frame bandpass) in frequency space and the difference in the effective wavelength (or colour) of the local and high-redshift observations. The correction for these effects is known as a K-correction, K (Frei & Gunn, 1994). Defined over a frequency range ($\Delta\nu$) as,

$$m^r_{\Delta\nu} = m^o_{\Delta\nu} - 10\log(1+z) + K \tag{5.21}$$

where the bandpass limited (or measured) $m^o_{\Delta\nu}$ is obviously equal to the result in Equation 5.19 (m_m). K can be split into two effects, the bandpass correction (K_b) and the colour correction (K_c). K_b is obtained by considering the fact that the bandpass is stretched by a factor $(1+z)$. This would cause the object being observed to appear brighter by the same factor. By setting $K_b = -2.5\log(1+z)$, we are reducing the observed brightness (i.e. increasing m) by the appropriate amount to remove the stretching effect.

The second term, K_c, depends on the underlying stellar population. Usually this is determined by 'observing', via convolution with a standard filter curve, simulated galaxy spectral energy distributions (SEDs) through a standard filter in the rest-frame and then redshifting the SED to that of the object of interest and observing that shifted SED with the appropriate filter used for the

real observations (in our case we would observe the un-shifted SED in with a V-band filter curve and observe the shifted SED with the F814W filter curve). The magnitude difference in these measurements provides a colour correction, K_c. However, this assumes *no* SED evolution and the constant shape of the underlying SED itself. As MS0451 is at $z = 0.55$, these assumptions can introduce large errors. K_c is omitted from the corrections here and instead is considered in the analysis later. See section 6.2.2.

To convert the measured, extinction, bandpass and cosmological dimming corrected apparent magnitude into $\langle m \rangle_e$ (average magnitude within R_e) we need to divide the surface brightness by the surface area within R_e. In magnitudes this translates to an additional term,

$$m_a = 5\log(R_e/\mathcal{R}_{0.55}) + 2.5\log 2\pi \tag{5.22}$$

where $\mathcal{R}_{0.55}$ is the angular scale in kpc/$''$. For our adopted cosmology and redshift, $\mathcal{R}_{0.55} = 6.3945$ kpc/$''$. Thus our final expression for $\langle m \rangle_e$ is,

$$\langle m \rangle_e = m_m + m_a - 7.5\log(1+z) \tag{5.23}$$

which can be converted from mags/arcsec^2 to $L_\odot$/kpc^2 by,

$$\langle I \rangle_e = 10^{-0.4(\langle m \rangle_e - \gamma_z)} \tag{5.24}$$

The constant $\gamma_z = \log(64800/\pi) + \mathcal{M}_\odot$. The V-band absolute magnitude of the Sun, $\mathcal{M}_\odot = 4.83$, giving $\gamma_z = 26.4$ to convert the surface brightness to the rest frame V.

When determining the absolute magnitude ($\mathcal{M}$) of the objects in MS0451, we must consider the effects on the distance modulus (DM). Considering *bolometric* magnitudes,

$$\begin{aligned} DM_{bol} &= m^r_{bol} - \mathcal{M}_{bol} \\ &= 5\log D_L - 5 \end{aligned} \tag{5.25}$$

where D_L is the luminosity distance. D_L is related to the transverse comoving distance (D_M) via

$D_L = (1+z)D_M$ (Peebles, 1993). For a flat universe D_M is equal to the line-of-sight comoving distance D_C, thus

$$DM_{bol} = 5(\log D_C - 1 + \log(1+z)) \tag{5.26}$$

For our adopted cosmology and redshift, we obtained $DM_{bol} = 42.505$. The absolute magnitude in the bandpass limit of our observations is given by,

$$\mathcal{M}_e = m_e - DM_{bol} \tag{5.27}$$

where $m_e = \langle m \rangle_e - m_a$.

5.8.3 Photometric Errors

To estimate the errors on the photometric results, a Monte-Carlo (MC) approach was adopted. Data was simulated by generating galaxies with Sérsic profiles at various combinations of R_e, apparent magnitude (m) and Sérsic index (n) along with random sky level offsets. As $\langle I \rangle_e$ depends on n, parameterising by $\langle I \rangle_e$ across a definite range in the simulations would result in varying completeness for the simulations. To ensure the same level of completeness in magnitude for the simulated data across varying n, $\langle I \rangle_e$ needed to be allowed to vary across an indefinite range. Thus, the simulations were parameterised by m instead of $\langle I \rangle_e$.

Poisson noise was added to the galaxy and background counts, along with read noise. The simulated galaxies are then convolved with the HST PSF created in Section 5.7.3. The simulated galaxies, with known initial parameters, are then analysed with the same COG code used for the real data. For each value of R_e, m and n, 100 MC simulations were run. The radius at which the COG is stopped (R_{max}) is also varied following the same statistics of the real data, over a normal distribution of the ratio R_{max}/R_e with mean 3.5 and standard deviation 1.8. This method allows a combination of the systematic errors (from fitting a de Vaucouleurs profile to a Sérsic-like galaxy) and random errors arising from noise.

5.9 The Local Reference Sample

To understand the results we present for the high redshift cluster MS0451, we need to have a comparison sample that best represents the local analogue of the cluster. The Coma cluster (Abell 1656 at $z = 0.024$, Thomsen et al. (1997)) was chosen. It has been used as the benchmark comparison sample for other high-z massive cluster evolution studies in the Gemini/HST project and other projects. Photometric data, in the Gunn r-band, on the ETG population in Coma are available from a study conducted by Jorgensen et al. (1995a). We correct the gunn magnitudes to AB magnitudes via,

$$r(\mathrm{AB}) = r(\mathrm{Gunn}) - 0.226 \tag{5.28}$$

(Frei & Gunn, 1994). Velocity dispersions are available from Jørgensen et al. (1999). 114 galaxies, matched between the photometric and kinematic datasets, were used as our full comparison sample. The work of Barr et al. (2005, 2006) involved a comparison of the results of their study of RX J0142.0+ 2131 ($z \sim 0.28$), as part of the Gemini/HST cluster project, to the same dataset. The availability of the Coma data allowed us to compare our results to the full sample or to mass-limited subsets. It also allowed us to incorporate the data in our fitting routines, which differ in places from previous studies.

I.D.	α	δ	$\log\sigma$ [km^{-1}]	$\sigma_{\log\sigma}$	$\log\langle I\rangle_e$ [$L_\odot$pc^{-2}]	$\sigma_{\log\langle I\rangle_e}$	$\log R_e$ [kpc]	$\sigma_{\log R_e}$	r' [mags]	$g'-r'$ [mags]
12	04:54:12.64	-03:03:20.12	2.434	0.123	1.674	0.292	1.453	0.203	21.008	1.295
309	04:54:08.42	-03:03:00.53	2.069	0.156	2.338	0.158	0.730	0.092	22.420	1.019
554	04:54:19.10	-03:03:41.03	2.071	0.161	2.722	0.166	0.591	0.100	22.164	1.089
606	04:54:05.94	-03:02:29.43	2.314	0.071	2.808	0.168	0.631	0.102	21.764	1.146
684	04:54:12.98	-03:02:16.80	2.133	0.124	2.633	0.168	0.683	0.102	21.786	1.136
716	04:54:14.22	-03:02:21.73	2.185	0.118	2.377	0.169	0.828	0.096	21.937	1.131
897	04:54:20.90	-03:02:03.69	2.276	0.067	3.010	0.171	0.498	0.106	21.762	1.233
971	04:54:18.40	-03:01:46.45	2.345	0.058	2.541	0.168	1.036	0.091	20.519	1.270
1002	04:54:17.76	-03:01:56.53	2.112	0.106	2.129	0.168	1.008	0.091	21.531	1.245
1156	04:54:04.91	-03:01:41.51	2.368	0.069	2.463	0.169	0.854	0.096	21.293	0.643
1204	04:54:11.39	-03:01:36.08	2.274	0.064	2.818	0.168	0.692	0.102	21.404	1.272
1331	04:54:17.32	-03:01:30.61	2.199	0.177	2.540	0.169	0.737	0.100	21.388	1.070
1491	04:54:09.06	-03:01:18.62	2.352	0.156	3.121	0.229	0.260	0.160	22.301	1.311
1500	04:54:12.72	-03:01:00.80	2.279	0.078	2.604	0.169	0.871	0.096	21.344	1.382
1594	04:54:15.33	-03:01:05.48	2.364	0.049	2.685	0.169	0.824	0.096	21.183	1.326
1723	04:54:19.28	-03:00:54.86	2.288	0.056	2.632	0.168	0.991	0.091	20.109	0.952
1823	04:54:09.76	-03:00:50.25	2.401	0.055	2.994	0.168	0.610	0.102	21.297	1.333
1931	04:54:14.80	-03:00:40.53	2.242	0.085	2.829	0.168	0.672	0.102	21.511	1.176
2031	04:54:09.24	-03:00:35.42	2.428	0.061	3.131	0.171	0.467	0.106	21.538	1.348
2223	04:54:10.25	-03:00:15.04	2.200	0.126	2.644	0.168	0.662	0.102	21.927	1.241
2240	04:54:11.11	-03:00:21.31	2.173	0.201	2.774	0.229	0.388	0.160	22.970	1.174
2788	04:54:11.05	-02:59:32.10	2.164	0.086	2.586	0.169	0.772	0.100	21.689	1.325
2945	04:54:07.55	-02:59:44.90	2.105	0.133	2.832	0.168	0.590	0.102	21.855	1.252
3124	04:54:12.61	-03:00:01.04	2.274	0.082	2.579	0.169	0.788	0.100	21.494	1.204
3260	04:54:08.10	-03:00:08.13	2.239	0.128	2.698	0.229	0.558	0.160	22.561	1.234
3749	04:54:07.39	-02:59:03.70	2.371	0.063	2.262	0.169	0.869	0.096	22.005	1.084

Table 5.5: Overview of cluster data.

Chapter 6

GMOS/HST Results

This Chapter details the results of the analysis of the photometric and spectroscopic data on MS0451. An attempt at determining some ensemble characteristics of the cluster (namely the X-ray luminosity prediction and mass) is presented and then various galaxy scaling relations and the fitting methods employed are illustrated.

6.1 Ensemble characteristics of MS0451

The V_{los} measured for the cluster members enable an approximate determination of the cluster dispersion (σ_{clust}). For a first, crude estimation, we assume the sample is from a Gaussian distribution, simply taking the standard deviation of the V_{los}. This provides a σ_{clust} of $1681 \pm 329 \mathrm{kms}^{-1}$.

For a more robust determination of σ_{clust}, we refer to Beers et al. (1990), who in turn reference Mosteller & Tukey (1977) for the underlying statistical justifications. If the velocity distribution of the population in the cluster was Gaussian, then the standard deviation would be the optimal estimator of the cluster dispersion. However, our sub-sample of $n = 26$ galaxies is likely to deviate from a purely Gaussian distribution. The authors define a *biweight scale estimator*. This takes the form,

$$S_{Bi} = n^{1/2} \frac{[\sum_{|u_i|<1}(v_i - V_M)^2(1-u_i^2)^4]^{1/2}}{\mid \sum_{|u_i|<1}(1-u_i^2)(1-5u_i^2) \mid} \tag{6.1}$$

where v_i are the V_{los}, V_M is the sample median and u_i is defined as,

$$u_i = \frac{v_i - V_M}{\mathcal{T} MAD} \tag{6.2}$$

$\mathcal{T}$ is a tuning constant that is set to provide the estimator, S_{Bi}, with a high efficiency across a broad range of distributions and is set to 9.0. The efficiency relates to the deviation of the estimated variance of the sample from the true variance of the underlying distribution. The acronym MAD refers to the median absolute deviation of the sample (i.e. the median of $\mid v_i - V_M \mid$). Performing iterations of Equation 6.1 by substituting S_{Bi} in for V_M after the first calculation produces a rapid convergence of S_{Bi}, allowing an estimate of σ_{clust}. And thus, for the sample in MS0451, we find $\sigma_{clust} = 1538 \pm 143.6 \mathrm{kms}^{-1}$. The 68% confidence interval is determined via a standard t-test.

The furthest galaxy from the cluster centre (projected on the 2D FOV) is at a radius $R_c \sim$ 1.14Mpc. So, the radius encompassing the velocity field of our sample of galaxies encloses an approximate dynamical mass of $3.04^{+0.44}_{-0.39} \times 10^{15} \mathrm{M}_{\odot}$, which is consistent with the measured r_{200} mass (Sereno & Zitrin, 2011), scaling to R_c, following the $\rho \propto 1/r$ relation of the inner cluster halo (Navarro et al., 1996).

A determination of the cluster dispersion, allows us to predict the X-ray luminosity of MS0451 and compare the value to previous studies. We assume that the galaxies in our sample trace the total mass distribution in the cluster and that the X-ray source in the cluster is a spherically symmetric ball of gas, with,

$$\mathrm{L}_X \propto f^2 \sigma^3 T^{1/2} \tag{6.3}$$

f being the gas fraction of the cluster (M_{gas}/M_{tot}). The gas temperature, T, is proportional to the depth of the gravitational potential, thus following $T \propto \sigma^2$. This results in the X-ray luminosity predicted to follow $\mathrm{L}_X \propto \sigma^4$ (Solinger & Tucker, 1972).

Ortiz-Gil et al. (2004) show the $\mathrm{L}_X - \sigma_{clust}$ relation in the *ROSAT* 0.1-2.4 keV band is

$$\mathrm{L}_X = 10^{32.72 \pm 0.08} \sigma_{clust}^{4.1 \pm 0.3} \mathrm{erg\ s}^{-1} \mathrm{h}_{50}^{-2} \tag{6.4}$$

from a study of 171 clusters from the ROSAT-ESO Flux-Limited X-ray (REFLEX) cluster survey.

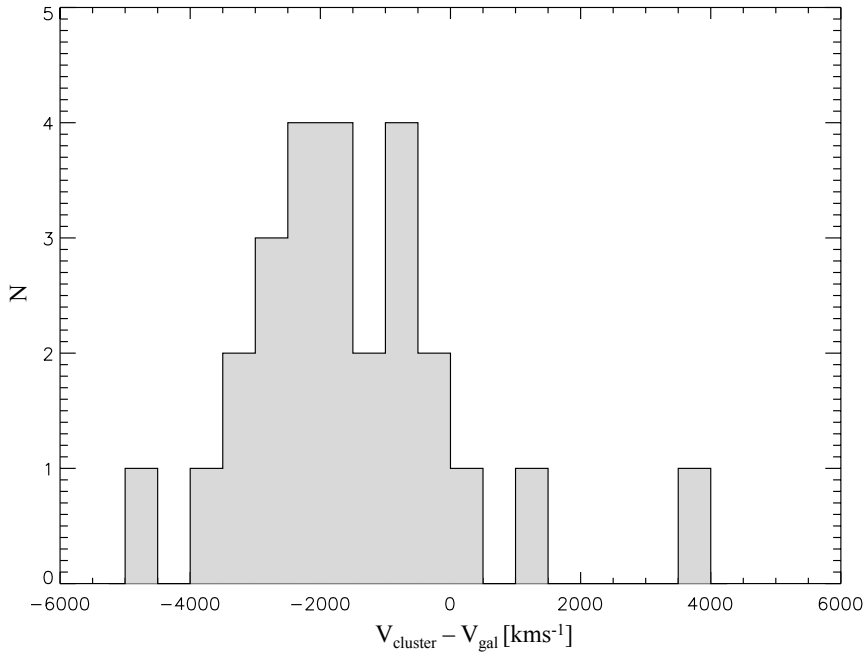

Figure 6.1: Histogram of the V_{los} of the confirmed cluster members of MS0451.

From the measured σ_{clust} of MS0451, we obtain a value of $L_X^{MS0451} \sim 1.53 \times 10^{45}$ erg s^{-1}. The error on the power of σ_{clust} translates to a large error on L_X^{MS0451}. The result here is consistent with the results of Donahue et al. (2003).

6.2 Galaxy Scaling Relations

The primary focus of the investigation of MS0451 has been in the use of scaling relations to probe the evolutionary history of the galaxies in the cluster. Here I give a brief introduction to each of the scaling relations used to study MS0451, the fitting methods used and a brief interpretation of the results. All of the results are also discussed in the next Chapter, to put the evolution of the galaxies in MS0451 into context.

6.2.1 The Colour-Magnitude relation (CMR)

Galaxy colour as a function of magnitude in a given band (or as a function of mass) indicates that brighter (more massive) galaxies are redder than fainter (less massive) galaxies (Baum, 1959). A

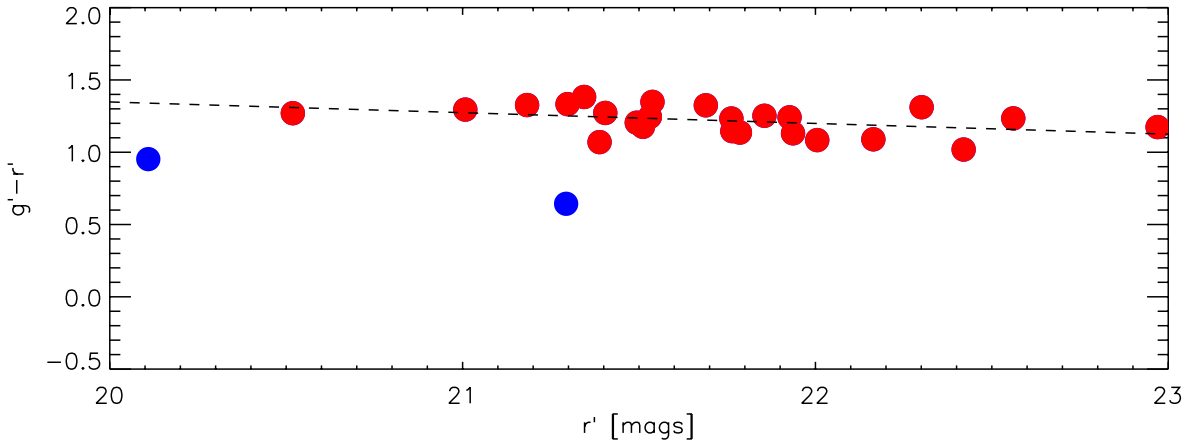

Figure 6.2: The $g' - r'$ vs r' CMR for the spectroscopically confirmed cluster members of MS0451. The dashed line is the fit to the RS members. The blue points are galaxies with $g' - r' < 1$, and represent galaxies 1723 and 1156, exhibiting spiral structure.

strong distinction between a *red sequence* (RS) of galaxies and a *blue cloud* (BC) has been found to be ubiquitous in the local Universe (Visvanathan & Sandage, 1977) and out to high-z (Ellis et al., 1997). Importantly, it has been shown that galaxy morphology is, in general, split between these two colour regions, with E/S0 galaxies dominating the RS (Bower et al., 1992) and spirals dominating the blue cloud and *green valley* in between (e.g. Wyder et al., 2007). The CMR of the RS has been found to be a tight local relation (with a scatter ~ 0.04 mags in $U - V$), which continues out to redshifts beyond $z > 1$, with the scatter nearly always remaining below ~ 0.1 mags (Ellis et al., 1997; Mei et al., 2009).

The tightness of the CMR for early-type galaxies (ETGs) makes it a useful tool for probing the evolution of these galaxies in the centres of rich clusters. Interpreting its tilt can tell us about the mass-metallicity relation (Faber, 1973) or potentially indicate age effects (although this is unlikely given the findings of Kodama & Arimoto, 1997) and changes in the scatter of the RS can indicate age spread at a given mass or changes in epoch of star formation episodes.

The CMR for MS0451 in r' vs $g' - r'$ ($\sim$ rest frame $U - B$) is shown in Figure 6.2. We perform a least squares fit to the galaxies in the spectroscopic sample with $g' - r' > 1.0$, thus omitting two bluer galaxies (I.D.s 1723, 1156 - which actually display spiral structure in their HST imaging).

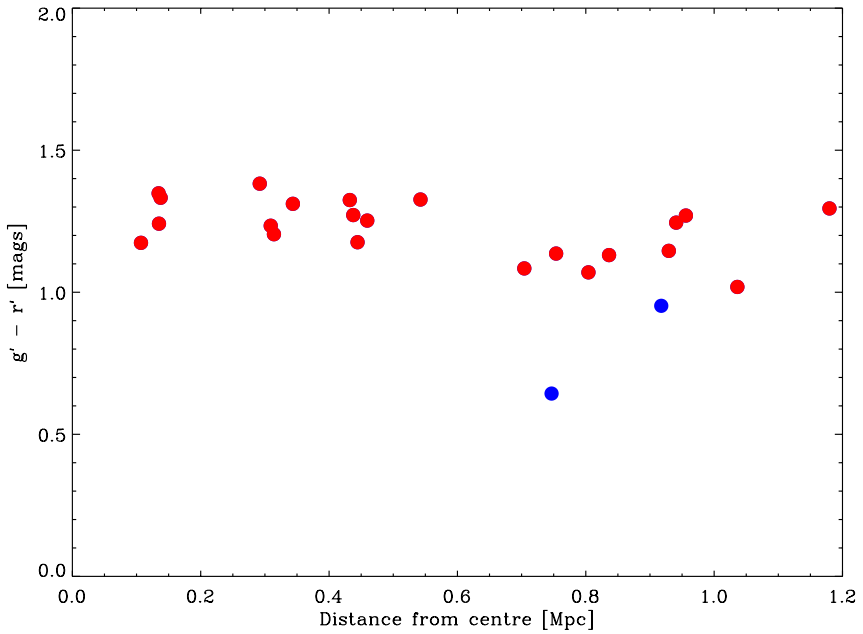

Figure 6.3: $g' - r'$ colour as a function of projected cluster distance. A negative correlation is seen in the RS (red points) at the 2σ level.

The CMR relation for the RS is found to be,

$$(g' - r') = (-0.074 \pm 0.002)r' + 2.83 \pm 0.048 \tag{6.5}$$

with an rms scatter of 0.08 mag about the line. The red points represent the RS galaxies in the spectroscopic sample. The blue points are galaxies 1723 and 1156, off the RS. The derived errors are smaller than the plot-point sizes. The scatter agrees with the findings of Mei et al. (2009): that the scatter in rest-frame $U-B$ is generally less than 0.1 mags up to $z \sim 1.0$ in cluster environments, but it is larger than the average value they find across their clusters of 0.05-0.06 mags. The tilt of the CMR for MS0451 is large at -0.074, when compared to the trend in redshift of Mei et al. (2009) and to the models of Kodama & Arimoto (1997) (giving a slope ~ 0.05 for $z = 0.4 - 0.6$). The zero-point for our CMR is also 0.2 mag lower than the predictions of Kodama & Arimoto (1997) for a formation redshift $z_f \sim 2$, though they admit the zero-point calibration in their results can differ by ~ 0.1 mag.

The tilt in the CMR and increased scatter, particularly in members dimmer than $r' > 22$ (increasing to 0.12 mags), could indicate recent star-formation in the lower-mass members of MS0451, although this is not statistically significant with the small sample in the lower luminosity members. The location in the cluster of the bluer members is further from the cluster centre (defined as the centre of the X-ray contours - see Figure 5.2), with the scatter in colour also increasing with distance (Figure 6.3). The correlation in colour with cluster-centric distance is significant at the 2σ level for the RS galaxies.

6.2.2 The Kormendy and Faber-Jackson Relations

The Kormendy Relation (KR) was discovered as a log-linear relation between galaxy R_e and the surface brightness *at* R_e (Kormendy, 1977). The form of the KR has been modified, for contemporary studies, to represent the relation between R_e and the *average* surface brightness *within* R_e. This is essentially the same for de Vaucouleurs profiles, but requires consideration of the Sérsic index, n, for Sérsic models. For consistency with the majority of previous studies and for meaningful comparison to our reference sample in Coma, we limit our considerations to de Vaucouleurs fixed $n = 4$. The form of the KR is,

$$\langle\mu\rangle_e = \alpha_{KR}\log R_e + \beta_{KR} \tag{6.6}$$

where the average surface brightness within R_e ($\langle\mu\rangle_e$) is given in mags/arcsec^2. The trend of the relation indicates that larger galaxies have lower surface brightnesses. The slope appears to be maintained out to intermediate redshift, while the zero-point changes (Barrientos et al., 1996), indicating ETGs were more luminous in the past and have evolved passively since $z \approx 1 - 2$.

The Faber Jackson Relation (FJR) is a log-linear relation between the luminosity of a galaxy and it's central velocity dispersion (σ_c) and takes the form,

$$\mathcal{M}_\nu = \alpha_{FJR}\log\sigma_c + \beta_{FJR} \tag{6.7}$$

where $\mathcal{M}_\nu$ is absolute magnitude in band ν (Faber & Jackson, 1976). The trend for the FJR indicates that more luminous galaxies have higher velocity dispersions (which traces the dynamical

mass). Investigations of the redshift evolution of the FJR have also found a consistent slope, with zero-point offsets indicating a dimming of the ETGs (Bender et al., 1996).

To compare the KR and FJR of MS0451 to the KR and FJR of Coma, we adopted a Markov Chain Monte Carlo method (MCMC) to fit a *double linear model* (DLM). The description of the fitting method that follows is adapted from Hogg et al. (2010) and follows Houghton et al. (2012). In a linear model (LM), we assume that a dataset $\{x_i, y_i\}$ with normally distributed uncertainties $\{\sigma_{xi}, \sigma_{yi}\}$ and covariance $\sigma^2_{xyi} = \rho_{xyi}\sigma_{xi}\sigma_{yi}$ (where ρ_{xyi} is the *correlation coefficient*) obey a linear relation,

$$y = \alpha_R x + \beta_R \tag{6.8}$$

where, in our case, α_R and β_R correspond to the constants in the KR or FJR when considered with respect to Equations 6.6 and 6.7, with an intrinsic variance V_I. For a given point x_i, with uncertainty σ_{xi}, we can define the probability of observing the point in the range $[y_i, y_i + \mathrm{d}y]$ with uncertainty σ_{yi}, given the model parameters $\{\alpha_R, \beta_R, V_I\}$, as,

$$p(y_i|x_i, \sigma_{xi}, \sigma_{yi}, \alpha_R, \beta_R, V_I) = \frac{1}{\sqrt{2\pi(V_{\rm di} + V_I)}} \exp\left[-\frac{\Delta_i^2}{2(V_{\rm di} + V_I)}\right] \tag{6.9}$$

where the parameter Δ_i^2 measures the perpendicular distance between the linear model and a data point. It is defined as $\mathbf{v}^{\rm T} \cdot \mathbf{Z}_i - \beta'_R$, where $\mathbf{v}^{\rm T} = [\cos\theta, \sin\theta]$, $\mathbf{Z}_i^{\rm T} = [x_i, y_i]$ and $\beta'_R = \beta_R \cos\theta$. It follows that $\alpha_R = \tan\theta$. $V_{\rm di}$ is the projected variance of the data point involving the covariance matrix (Σ_i): $\mathbf{v}^{\rm T} \cdot \Sigma_i \cdot \mathbf{v}$.

The likelihood $(\mathcal{L})$ of observing all of our points in the set, $\{x_i, y_i\}$, given the linear model in Equation 6.8 is then simply the product of the probabilities p in Equation 6.9. However, instead of just maximising the likelihood (locating the peak of the likelihood function), we chose to adopt a Bayesian approach, sampling from a posterior probability distribution defined as being proportional to the prior probability times the likelihood. The prior probability is given by $p(\alpha_R, \beta_R|Q)$, where Q represents all other knowledge of the problem (x_i, errors, etc). For N data points (26 in the case of MS0451 and 114 in the case of Coma), we normalise the posterior probability distribution by dividing by $p(\{y_i\}_{i=1}^N|Q)$. Thus, the posterior distribution we aimed to explore through MCMC

sampling takes the form,

$$p(\alpha_R, \beta_R, V_I | \{y_i\}_{i=1}^N, Q) = \frac{p(\alpha_R, \beta_R | Q) \times \mathcal{L}}{p(\{y_i\}_{i=1}^N | Q)} \tag{6.10}$$

In the implemented code[1], we sample the parameters θ, β' and V_I. The prior constraints we place on the parameters are that θ varies between $\pm\pi/2$ of the initial guess, β' is finite and $V_I > 0$. The best fit is the median of the resulting samples. We sampled the posterior distribution 2×10^5 times. To apply this LM to the two datasets for MS0451 and Coma simultaneously, fitting the DLM, we simply produced probability distributions p_1 and p_2 for the two sets, defined by Equation 6.9 and defined the double likelihood as $\mathcal{L} = \prod_{i=1}^N (p_1 \times p_2)$. α_R is thus constrained to be the same for the MS0451 and Coma datasets. The output from the fits are then the α_R and β_R values, with an offset $\Delta\beta_R$ between the two datasets.

Size Evolution

Size evolution in galaxies with cosmological time suggests that they were more compact in the past. It was initially suggested that disk galaxies were fixed in size relative to their dark matter halos (Mo et al., 1998). Recent studies have found that this appears true for ETG morphological types as well (Longhetti et al., 2007; van der Wel et al., 2008). The effect of size evolution takes the form of a simple power law,

$$\log(R_e) = \log(R_{e,z}) + \zeta \log(1+z) \tag{6.11}$$

where R_e is the effective radius *now* and $R_{e,z}$ is the effective radius at some redshift, z. We represent size evolution in $\langle\mu\rangle_e$ as,

$$\langle\mu\rangle_e = \langle\mu\rangle_{e,z} + 5\zeta \log(1+z) \tag{6.12}$$

If, at a fixed mass, a galaxy increases in size between some redshift, z, and the present, then the central mass concentration is expected to decrease. This translates to a decrease in the central

[1]Written in Python by Ryan Houghton

velocity dispersion and again takes the form of a simple power law,

$$\log(\sigma) = \log(\sigma_z) - 0.5\eta\log(1+z) \tag{6.13}$$

This is true assuming simple dynamical models of Sérsic galaxies (Ciotti, 1991). If the size evolution and velocity dispersion evolution were to follow cosmological expansion alone, then the values of ζ and η are expected to be $\sim$0.75 (Fan et al., 2010). Values of ζ are generally found to be around 1.0 for massive ($\sim 10^{11}\mathrm{M}_{\odot}$), highly concentrated galaxies (Bouwens et al., 2004; van der Wel et al., 2008). The most recent large survey (1100 ETGs, $n \gtrsim 2.5$, Maier et al. (2009)) over the range $0.5 < z < 0.9$ and a mass range of $3 \times 10^{10}\mathrm{M}_{\odot} < \mathrm{M} < 3 \times 10^{11}\mathrm{M}_{\odot}$ finds a slower evolution with $\zeta \sim 0.8$. The velocity dispersion evolution is found to be *weaker* in several studies with $\eta \sim 0.6$ (Cenarro & Trujillo, 2009) or even negligible (Cappellari et al., 2009), highlighting the uncertainty in the determination of velocity evolution in ETGs.

Some explanations for these differences in evolution involve a mechanism forcing the baryonic matter out from the central regions, acting to increase the size while reducing the central potential slightly (counteractions by the evolution of the mass function, increase in Sérsic index with size and dynamical friction with the dark matter component may occur). Supernovae could dominate this process at lower masses while AGN activity could explain the observations at higher masses (Fan et al., 2010). Merger events could also be involved across the mass function (van der Wel et al., 2008). Also, some suggest galaxies may form 'inside out' and accrete material in their outer regions. Due to the uncertainty in the size evolution, we fit the scaling relations here with and without size evolution corrections before comparing to models (initially adopting $\zeta = 1.0$ and $\eta = 1.0$, but varying during the investigation, when we do correct our data). The results of the DLM with and without size evolution are given in Table 6.2.2.

Without correcting for size evolution, we find a disagreement in the Coma-MS0451 offsets ($\Delta\beta$) between the KR and FJR. The inclusion of size evolution results in the offsets converging, but adopting an η value of 1.0 in the σ correction presents too strong an evolution. As stated earlier, the value of η is not well constrained in the literature, whereas ζ is generally accepted to be around 1.0. Table 6.2.2 shows the results for smaller values of η, indicating a value around 0.3-0.4 agrees

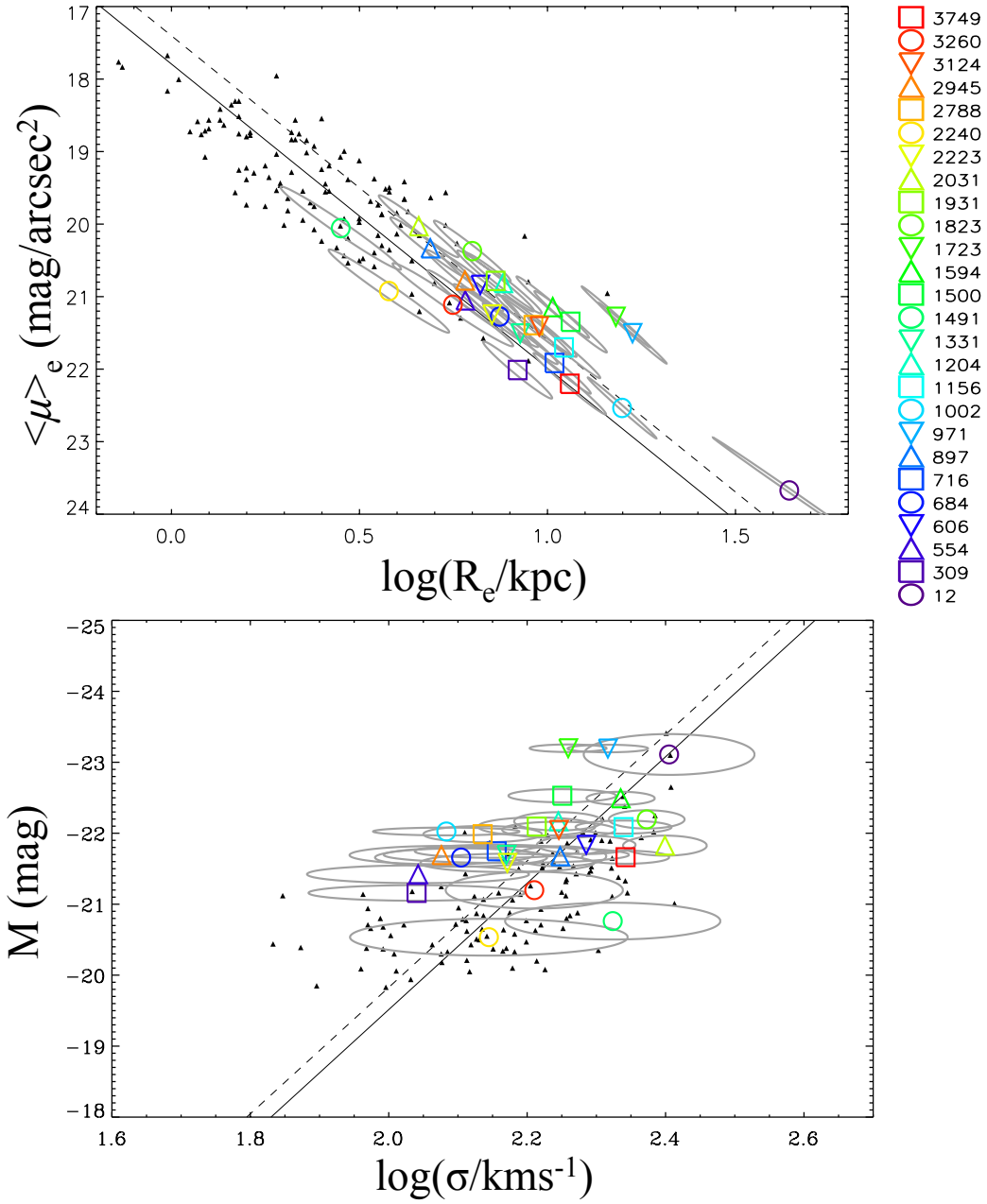

Figure 6.4: The data for MS0451 presented as coloured symbols and the data for the reference Coma sample is presented as black points. *Upper Plot*: The Kormendy Relation for the size evolution corrected data ($\zeta = 1.0$). The black solid line is the KR for the Coma sample. The dashed black line is the offset KR for the MS0451 sample. *Lower Plot*: The Faber-Jackson Relation for the size evolution corrected data ($\eta = 0.3$). The black solid line is the FJR for the Coma sample. The dashed black line is the offset FJR for the MS0451 sample.

α_{KR}	β_{KR}	$\Delta\beta_{KR}$	ζ
$4.12^{+0.24}_{-0.25}$	$17.30^{+0.22}_{-0.21}$	$-0.53^{+0.15}_{-0.15}$	0.0
$4.19^{+0.33}_{-0.30}$	$17.40^{+0.29}_{-0.33}$	$-0.39^{+0.21}_{-0.20}$	1.0
$4.17^{+0.30}_{-0.26}$	$17.44^{+0.27}_{-0.30}$	$-0.36^{+0.20}_{-0.20}$	1.1
α_{FJR}	β_{FJR}	$\Delta\beta_{FJR}$	η
$-8.78^{+1.29}_{-1.07}$	$-2.03^{+2.47}_{-2.95}$	$-0.065^{+0.30}_{-0.27}$	0.0
$-8.75^{+1.08}_{-1.12}$	$-2.95^{+2.46}_{2.41}$	$-0.89^{+0.24}_{-0.23}$	1.0
$-8.41^{+0.95}_{-0.89}$	$-3.35^{+1.98}_{2.10}$	$-0.59^{+0.23}_{-0.23}$	0.6
$-8.91^{+1.11}_{-0.92}$	$-2.01^{+2.09}_{2.56}$	$-0.31^{+0.27}_{-0.26}$	0.3

Table 6.1: KR and FJR parameters.

with the results of size evolution in the KR. Figure 6.4 shows the KR and FJR for MS0451 and the full Coma sample. The data presented in these plots has been corrected for size evolution using $\zeta \sim 1.0$ and $\eta \sim 0.3$. The intrinsic scatter (σ_I) in the FJR and KR is 0.088 and 0.129 respectively. On applying the size evolution corrections, it can be seen that the MS0451 sample appears to occupy a different region on each relation to the Coma sample (particularly in the KR). However, the uncorrected data in the KR, for example, occupies the range 0.2 - 1.0 in $\log R_e$ (kpc) and 22 to 19 mag/arcsec^2 in $\langle\mu\rangle_e$.

We compare these offsets to those predicted by the models of Bruzual & Charlot (2003, BC03) and Maraston (2005, M05). Briefly, the outputs from these models allow magnitude offsets to be related to formation epochs and ages of ETGs, given certain input parameters (metallicities, initial mass function (IMF), stellar libraries for spectral energy distribution (SED) construction etc). Specification of observation filter is possible, along with the epoch of the SED being observed. The models incorporate the colour corrections (K_c - see Section 5.8.2) in how they interpret observations through these filters. Hence no colour correction was applied to our data here, only for the increased bandpass at high-z (Section 5.8.2).

Comparing the F814W magnitude of galaxies at $z = 0.55$ to the r(AB) magnitude of galaxies at $z = 0$ (equivalent to $\Delta\beta$) in the models, allows a prediction of the formation redshift (z_f). Figure 6.2.2 shows the BC03 and M05 models for a range of metallicities. Without the corrections for size evolution, the KR and FJR predict different z_f of ~ 1 and ~ 3 respectively (taking the average BC03 and M05 solar metallicity (Z=0.02) model fits). Correcting for size evolution (with

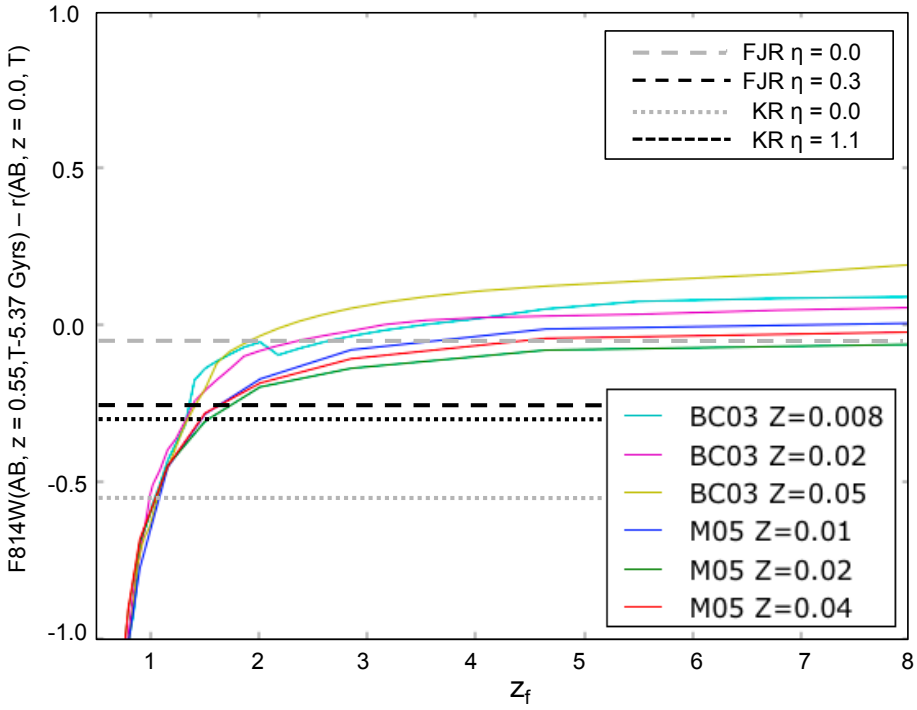

Figure 6.5: The BC03 and M05 stellar population model results, indicating the predicted formation redshift (z_f) given a $\Delta\beta$ magnitude offset in F814W-r(AB). A range of metallicities were used for the model runs, each indicated by a different colour, with the legend in the bottom right. The grey lines (long dashed and short dashed) indicates the FJR and KR model predictions prior to correcting for size evolution. The black lines indicate the FJR and KR offsets when the size evolution corrections have been made.

$\zeta \sim 1.0$ and $\eta \sim 0.3$), we see a prediction of $z_f = 1.7^{+\infty}_{-0.6}$.

6.3 The Fundamental Plane

The Fundamental Plane (FP) (Dressler et al., 1987; Djorgovski & Davis, 1987) is a correlation between the three galaxy parameters mentioned previously, with the KR and FJR being projections of this more 'fundamental' relation. These are the effective radius (R_e), the average surface brightness within R_e ($\langle I \rangle_e$ - in solar luminosities ($L_\odot$) per parsec^2) and the central line-of-sight velocity dispersion (σ). R_e is also known as the half-light radius and so is the radius within which half of the *total* luminosity of the galaxy lies. This definition of an R_e allows photometric and kinematic quantities of galaxies to be compared at the same scale. Projections along the axes of

the FP produce the previously discovered FJR and KR relations. The relation between all three parameters in the FP forms a relatively tight plane in logarithmic space compared to just the projected parameters in the FJR or KR. This originally enabled the FP to act as a more robust distance indicator for distant objects, subtending small, difficult to measure angles. Crucially, the FP relates dynamical properties (kinematics, masses) with photometric properties (morphologies, sizes, surface brightnesses (SBs)) in a single representative parameter space, thus allowing detailed study of evolutionary processes across different epochs and environments. The derivation of the Virial prediction of the FP is now given.

If we are to represent the FP variables as a log-linear relation, we expect the the form to be,

$$\log R_e = \alpha \log \sigma + \beta \log \langle I \rangle_e \ + \gamma \tag{6.14}$$

We can derive the expected values of the coefficients (α, β and γ) from the scalar Virial Theorem. Early type galaxies (ETGs) are assumed to be purely self gravitating, symmetric systems. Importantly, we assume that they are relaxed and completely pressure supported resulting from the random motions of their stellar components. The energy balance equation for a self gravitating system is given by,

$$\frac{\mathrm{d}^2 l}{\mathrm{d}t^2} + 2K = U \tag{6.15}$$

where l is the angular moment of the stellar component, K is the kinetic energy and U is the gravitational potential. In a relaxed system, the time development of the angular momentum ceases and $\frac{\mathrm{d}^2 l}{\mathrm{d}t^2}$ tends to 0, resulting in the system being well represented as a virialised (time-averaged) model. Writing the kinetic energy in terms of the velocity dispersion and the gravitational energy of the system within a given radius (in the case of ETGs we use the border of R_e), we have

$$k\sigma^2 = \frac{GM}{R_e} \tag{6.16}$$

where k is a constant, M is the total mass enclosed within R_e, σ is the line of sight velocity dispersion of the central stellar population within R_e and G is the gravitational constant. The average surface brightness within R_e, $\langle I \rangle_e$, is simply related to the luminosity via,

$$L = 2\pi R_e^2 \langle I \rangle_e \tag{6.17}$$

Rearrangement of equation 6.16 provides us with an expression for the dynamical mass (M) of the system within R_e and combining this with Equation 6.17 results in an expression for the Mass-to-light ratio,

$$\frac{M}{L} = \frac{k\sigma^2}{2\pi G R_e \langle I \rangle_e} \tag{6.18}$$

A simple rearrangement to make R_e the subject and taking logs gives,

$$\log R_e = 2\log\sigma - \log\langle I \rangle_e \ - \log\left(\frac{2\pi G(M/L)}{k}\right) \tag{6.19}$$

which can be related to Equation 6.14, giving the Virial predictions as $\alpha = 2$, $\beta = -1$ and $\gamma = 2\pi(M/L)/Gk$. The FP of nearby galaxies (Dressler et al., 1987; Djorgovski & Davis, 1987), indicates a significant deviation in the values of the FP coefficients from the Virial prediction. For optical band observations (B, V), the values of α and β have been found to be ~ 1.24 and ~ -0.81 respectively for local samples across several studies (Lucey et al., 1991; Jorgensen et al., 1996; Jørgensen et al., 1999; Kelson et al., 2000). This could indicate deviation from homology, anisotropies or initial mass function IMF variation or different ages as a function of mass. The tightness of the FP, indicated primarily from larger local samples (Jorgensen et al., 1996), means that it is sensitive to small variations and thus a dependence on the luminosity evolution with mass would be seen in the variation of the FP coefficients (Renzini & Ciotti, 1993; Fritz et al., 2009).

We can use the relations above to reform the general FP into a M/L vs Mass representation. From Equation 6.18, we have

$$\frac{M}{L} \propto \sigma^2 R_e^{-1} \langle I \rangle_e \ ^{-1} \tag{6.20}$$

and from Equation 6.16,

$$M \propto \sigma^2 R_e \tag{6.21}$$

Substituting for $\langle I \rangle_e$ in Equation 6.20, using Equation 6.14,

$$\frac{M}{L} \propto \sigma^{(2+\alpha/\beta)} R_e^{-(1+1/\beta)} \tag{6.22}$$

From Equation 6.21, we can substitute for σ,

$$\frac{M}{L} \propto M^{(1+\alpha/2\beta)} R_e^{-(2+\alpha)/(2\beta)-2} \tag{6.23}$$

The power on R_e tends to zero for the virial case and for observed values of α and β is negligible, with a tight relation found between M/L and σ only (e.g. see Jorgensen et al., 1996). Thus we recover Equation 4.4,

$$\log M/L = \epsilon \log M + \gamma_{ML} \tag{6.24}$$

The gradient, $\epsilon = 1 + \alpha/2\beta$, is found to be around 0.28±0.05 locally (Jorgensen et al., 1996; Jørgensen et al., 2007). Cappellari et al. (2006) find that this observed tilt in the FP is due to a real variation in the M/L, through studies of local galaxies, incorporating the effective velocity dispersion (σ_e, see Section 3.4.5). The constant γ_{ML} allows us to measure the luminosity evolution of galaxies at fixed mass (or by taking the median of a population) and compare the offsets between higher-z samples and the local relation with stellar population models (Bruzual & Charlot, 2003; Maraston, 2005; Thomas et al., 2005a). This is valid assuming the *tilt* of this relation is the same for low and high-z samples. It has been suggested, in recent studies, that the tilt in the FP evolves with redshift - steepening at higher-z (Jørgensen et al., 2006, 2007; Fritz et al., 2009, $z = 0.8 - 0.9$ and 1, cluster environments, Fernández Lorenzo et al., 2011, in field ETGs). This provides evidence for galaxy *downsizing* in clusters - at higher-z the more massive galaxies are forming stars and at lower-z the lower mass galaxies are still forming stars. Jørgensen et al. (2006, 2007) suggest formation redshifts (the z at which star formation ceases and passive fading of the ETGs occurs) range from around 1.25 for $10^{10.3}$M$_\odot$ galaxies up to $\gtrsim 1.6$ for high-mass members ($\gtrsim 10^{11.3}$M$_\odot$). However, other studies have not seen this variation in the FP tilt (Barr et al., 2005; Holden et al., 2010). They indicate passive evolution across the entire mass distribution of their samples, with luminosity offsets in agreement with formation redshifts around $z \sim 2$.

The FP at intermediate redshift (around $z \sim 0.5$) is not well studied, particularly in individual clusters. The original FP studies around this redshift involved 13 galaxies at $z = 0.58$ and 5 at $z = 0.4$ (van Dokkum & Franx, 1996; Kelson et al., 1997). Moran et al. (2007c) looked at evolution of S0 galaxies into E-type galaxies over two clusters around $z \sim 0.5$ (with MS0451 being one of them), but did not study the FP in great detail and did not investigate the KR, FJR or CMR at all.

It is important to note, that when we fit the FP for MS0451, we included all of the spectroscopically confirmed cluster members. *No* morphological selection or colour cut is deliberately applied[2]. This is to avoid the so called *progenitor bias* (van Dokkum & Franx, 1996), which indicates that by selecting only ETGs or RS galaxies in high-z samples, it is incorrect to assume that the sample is comparable to the local reference ETGs. Progenitors could therefore be missed and the assumption that the sample galaxies/cluster could evolve into the local galaxies/cluster would be wrong. Evolution between z and now can cause late-type galaxies to change into ETGs and migrate onto the RS.

The FP was fit by minimising the absolute residuals perpendicular to the plane, given by Equation 6.14. The points were weighted by their individual errors, input via the covariance matrix. The likelihood of the fit was maximised by minimising the χ^2 following,

$$\chi^2 = \sum_i^N \frac{(\log R_{e,i} - \alpha \log \sigma_i - \beta \log \langle I \rangle_{e,i} \ - \gamma)^2}{\mathrm{Var}(R_{e,i}) + \alpha^2 \mathrm{Var}(\sigma_i) + \beta^2 \mathrm{Var}(\langle I \rangle_{e,i} \ )} \tag{6.25}$$

Where Var(X) represents the variance on the parameter X. Fitting the full sample of 26 galaxies using equation 6.25 we find,

$$\log R_e = (0.80 \pm 0.18) \log \sigma - (0.76 \pm 0.09) \log \langle I \rangle_e + 0.93 \tag{6.26}$$

This indicates a steepening of the slope of the FP towards $z = 0.55$. The scatter in $\log R_e$ is found to be 0.12 for the full ETG population. When we measure the scatter in the RS only, the scatter in $\log R_e$ reduces to 0.09 dex, comparable to that found in Coma (Barr et al., 2006). The tilt is more

[2]Although in practice there is a potential cut in colour caused by the resolution of our velocity dispersion determinations; bluer galaxies are known to have lower σ.

easily seen in the representation of the FP as stellar M/L vs dynamical Mass. Rearrangement of the standard FP form in Equation 6.14 and the equations for M and M/L given previously allow the coefficients in Equation 6.24 to be written as,

$$\epsilon = 1 + \frac{\alpha}{2\beta} \tag{6.27}$$

and

$$\gamma_{ML} = \gamma/\beta - 0.74 - 6.06(1 + \frac{\alpha}{2\beta}) \tag{6.28}$$

These allow us to present the M/L vs mass FP for MS0451 as,

$$\log M/L = (0.47 \pm 0.09)\log M - 4.82 \pm 0.87 \tag{6.29}$$

whereas for the full Coma sample we find,

$$\log M/L = (0.27 \pm 0.03)\log M - 2.35 \pm 0.37 \tag{6.30}$$

Clearly indicating a steepening. The scatter in $\log M/L$ for MS0451 is 0.16 for the full sample and 0.13 for the RS only - as opposed to 0.10 found for the Coma sample, agreeing with Jørgensen et al. (2006) & Barr et al. (2006) .

Previous works have tended not to weight by errors when fitting the FP (Jørgensen et al., 2006; Barr et al., 2006). For consistency, we re-fit without error weighting. We obtain,

$$\log R_e = (1.05 \pm 0.25)\log\sigma - (0.72 \pm 0.08)\log\langle I\rangle_e + 0.25 \tag{6.31}$$

indicating a shallower tilt, but still steeper than for Coma. The scatter is similar in R_e for the full sample and RS (at 0.12 and 0.09 dex respectively). The difference in the error-weighted and the non-error-weighted fits reduces drastically when we fit the RS only (see Table 6.2), though this introduces the progenitor bias explained earlier and is not used to determine offsets.

α	β	γ	Comment
No Size Evolution			
0.80 ± 0.18	-0.76 ± 0.09	$+0.93 \pm 0.34$	MS0451, With Errors, Free fit, Full sample
1.05 ± 0.25	-0.72 ± 0.08	$+0.25 \pm 0.58$	MS0451, Without Errors, Free fit, Full sample
1.60 ± 0.18	-0.81 ± 0.04	-0.92 ± 0.37	Coma, Mass-cut (M$> 10^{10.8}$M$_\odot$)
0.91 ± 0.23	-0.77 ± 0.09	$+0.69 \pm 0.48$	MS0451, With Errors, Free fit, RS only
0.92 ± 0.23	-0.71 ± 0.07	$+0.25 \pm 0.58$	MS0451, Without Errors, Free fit, RS only
1.24	-0.81	$+0.08 \pm 0.03$	MS0451, Fixed gradient
1.24	-0.81	-0.11 ± 0.01	Coma, Fixed gradient
1.60	-0.81	-0.74 ± 0.03	MS0451, Fixed gradient (Mass-cut Coma)
With Size Evolution	($\zeta = 1.0$, $\eta = 0.3$)		
0.81 ± 0.22	-0.73 ± 0.09	$+0.80 \pm 0.46$	MS0451, With Errors, Free fit
1.05 ± 0.25	-0.72 ± 0.08	$+0.21 \pm 0.57$	MS0451, Without Errors, Free fit
1.24	-0.81	$+0.01 \pm 0.03$	MS0451, Fixed gradient

Table 6.2: FP parameters.

Formation Epoch and Size Evolution in the FP

A common method for determining the magnitude offset between the FPs for the two clusters is to fix the slope to that of the local reference and fit this to the high-z sample (e.g. Barr et al., 2006). To determine the magnitude offset between the MS0451 FP and that of Coma, we fixed the FP slope parameters to the established values for Coma, $\{\alpha, \beta\} = \{1.24, -0.81\}$, and allowed the zero-points to vary in the fitting routine. This returned the FP γ values, $\{\gamma_{0.55}, \gamma_0\} = \{0.08, -0.11\}$ for the MS0451 and Coma samples respectively. Converting the difference in these two values to a magnitude difference via $\Delta\gamma = \Delta\mu/0.4\beta$, results in $\Delta\beta_{FP} = -0.58 \pm 0.03$ mags, which indicates a $z_f \sim 1$ from the BC03 and M05 models shown in Figure 6.2.2.

The evident mass-dependence on formation epoch can be investigated through Equations 6.29 and 6.30. The $\Delta\log M/L$ value obtained at a fixed mass translates directly to a magnitude offset. Adopting the free-fit slopes for the two cluster samples indicates a magnitude offset of -0.78 mags for the lowest mass members of the MS0451 sample ($10^{10.8}$M$_\odot$) and an offset of < -0.28 mags for the highest mass members ($> 10^{11.8}$M$_\odot$). These correspond to formation redshifts around 0.8 and > 1.7 respectively.

When we correct for size evolution using the values determined from the literature & consistent with the KR and FJR DLM fits ($\zeta = 1.0$ and $\eta = 0.3$), we obtain $\gamma_{0.55}^{SE} = 0.01 \pm 0.03$ for the median offset. This converts to $\Delta\beta_{FP}^{SE} = -0.28^{+0.03}_{-0.09}$ mags, in agreement with $\Delta\beta_{KR}^{SE}$ and $\Delta\beta_{FJR}^{SE}$

given in Table 6.2.2 and a median formation redshift ~ 2. The coefficients obtained from the size evolution-corrected fits indicate magnitude offsets of -0.59 mags and -0.14 mags for the low and high mass limits respectively in the M/L vs Mass view of the FP. These correspond to $z_f = 1.0$ and $z_f > 2.5$ respectively. A summary of the main FP parameters (α, β, γ) can be seen in Table 6.2 and the traditional FP projections in the Coma parameter space ($\{\alpha, \beta\} = \{1.24, -0.81\}$) are shown in Figure6.6.

Mass-cuts

Our sample in MS0451 has a lower mass limit of $10^{10.8}\mathrm{M}_{\odot}$. It is important to compare the FP across the same mass distribution if we are assuming the population in our high-z sample will evolve into the local sample. So, we apply a mass-cut of $M > 10^{10.8}\mathrm{M}_{\odot}$ to the Coma sample, leaving 44 galaxies. Fitting the FP to this mass-cut sample actually brings the Coma coefficients nearer to the Virial prediction, as is expected for more massive galaxies, giving $\{\alpha, \beta\} = \{1.60, -0.81\}$ (equal when fitting with or without the errors on the Coma data (Jorgensen et al., 1996)). Thus, when probing the same mass-distribution, the change in FP tilt at $z = 0.55$ compared to $z = 0$ is still evident. The offsets for the size evolution corrected and non-size-evolution corrected MS0451 data are the same when comparing to the mass-cut Coma sample - indicating that the results here are not affected by any bias introduced in the mass limits of the high-z and local cluster samples.

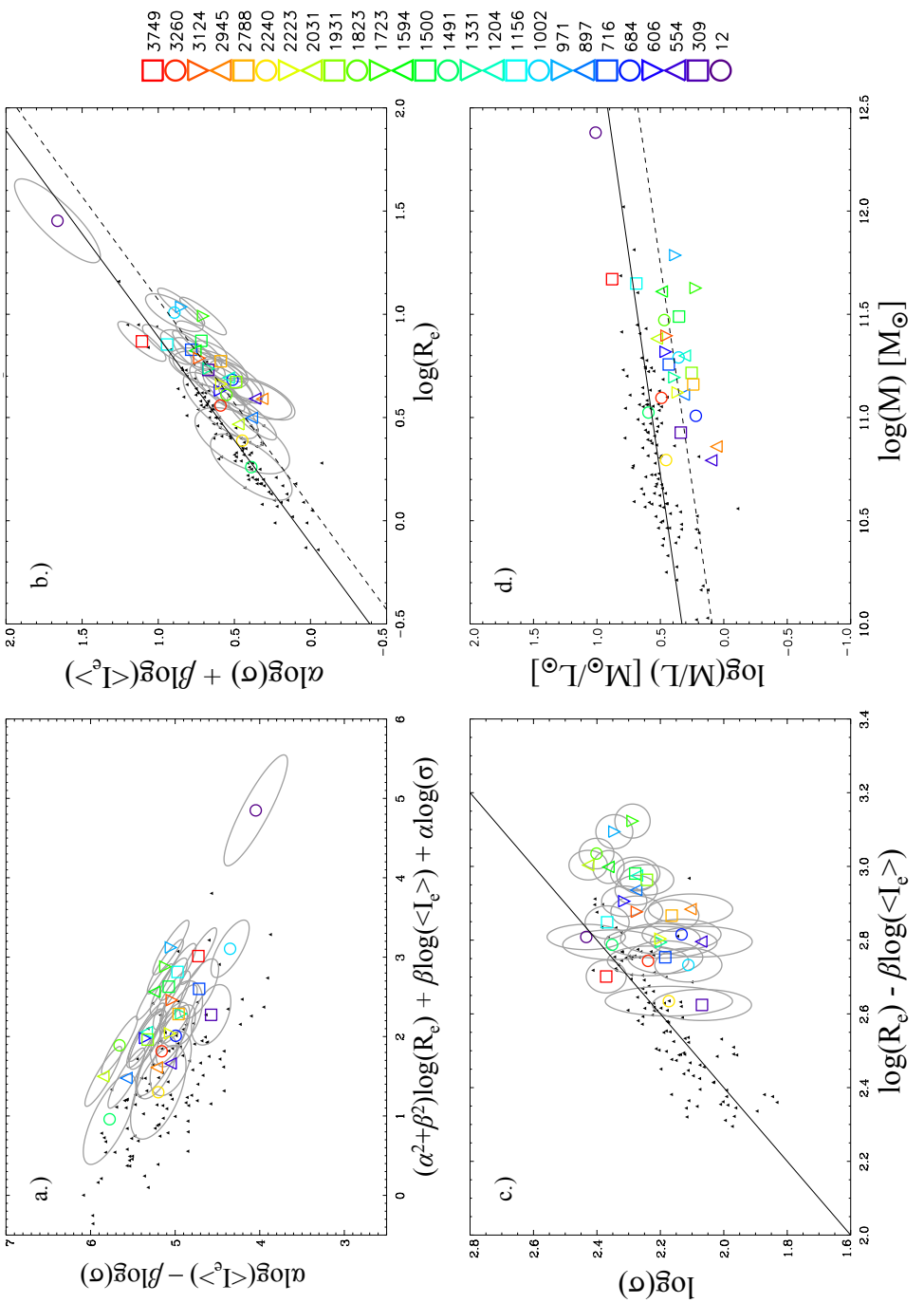

Figure 6.6: The traditional FP projections in the Coma parameter space ($\{\alpha, \beta\} = \{1.24, -0.81\}$). The black dots indicate the full Coma sample, the colour-coded shapes indicate the MS0451 sample, with a legend in the right for reference. The error ellipses are indicated in grey. a.) indicates the standard *face-on* view of the FP (Jorgensen et al., 1996), b.) and c.) are *edge-on* views, with the black solid lines indicating the Coma FP fit and the dashed line in b.) indicating the MS0451 FP offset at a fixed Coma gradient (with no correction for size evolution), d.) gives the $\log M/L$ vs $\log M$ view, with the solid and dashed black lines indicating the zero-points of the Coma and MS0451 samples respectively.

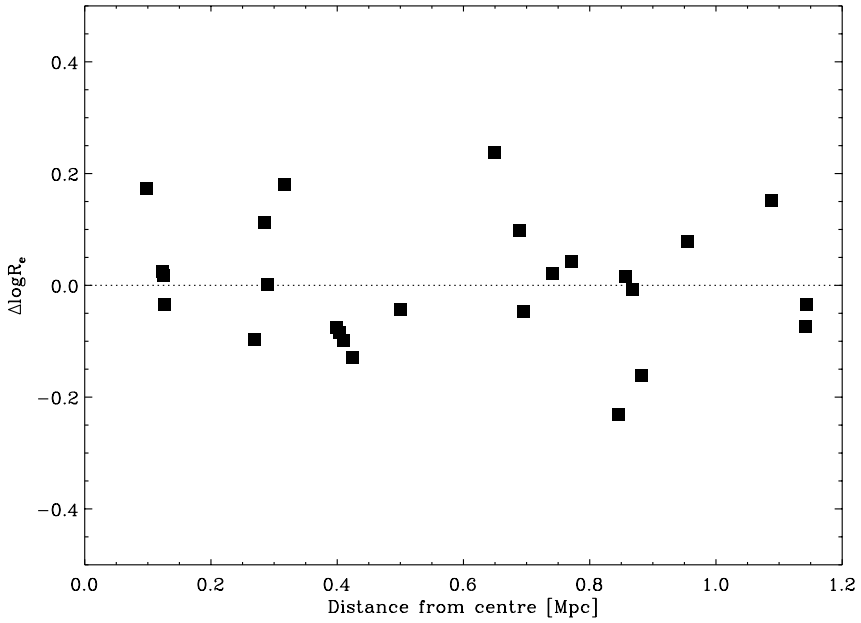

Figure 6.7: FP residuals as a function of cluster-centric distance (projected).

Environmental effects

It was seen in Section 6.2.1 that galaxy colour appears to correlate with distance from the cluster centre. To help confirm the correlation follows the cluster metallicity gradient, it is worth investigating other possible environmental correlations that could also explain the trend. van Dokkum et al. (2001), Treu et al. (2002) and van de Ven et al. (2003) show from FP studies that field ETGs are younger than their cluster counterparts. Infall from field galaxies could explain the increased scatter in $\log R_e$ for MS0451 compared to the scatter in Coma. If this were true, an increase in scatter with cluster-centric distance might be expected along with an increase in a scatter in colour. However, Figure 6.7 shows no correlation between the FP residuals and cluster-centric distance. There is no appreciable difference in scatter between central galaxies and peripheral members at $\sim$ 1Mpc. There is also no significant correlation between velocity dispersion or Sérsic index with distance. However, the measured n do not change much for the RS members and the two blue ($g' - r' < 1.0$) galaxies do exhibit lower n.

Chapter 7

Discussion and Conclusions

Here I present a review of the results of the investigation into scaling relations in MS0451. I then compare these results to the previous Gemini/HST project findings, discuss some caveats on the work and briefly present some ideas for future investigations.

7.1 The CMR

We have presented the first optical CMR of the confirmed cluster members of MS0451. It is in agreement with previous investigations of optical colour evolution in cluster ETGs, although it does indicate a slightly more recent formation epoch for this particular cluster, with $z_f \approx 1.8$. This formation epoch supports the findings of the KR and FJR fits to the size-evolution corrected (GMOS-N) spectroscopic and (HST F814W) photometric data. The steeper and slightly larger scatter than is found in clusters at similar redshifts (Mei et al., 2009) would also indicate a lower z_f and significant ongoing star formation (SF), as found for MS0451 by Geach et al. (2006). This is interesting when we consider the remarkably relaxed nature of MS0451, indicated by it's X-ray contours (Donahue et al., 2003; Moran et al., 2007b). However, the SF in MS0451 is still lower than that found in another cluster at a similar z (CL0024+16 at $z = 0.4$, Geach et al., 2006). The gradient of the colour-distance relation, at a 2σ significance, would indicate a tracking of the metallicity gradient in the cluster. De Grandi & Molendi (2001) investigate the metal content of the intra-cluster medium (ICM) and find an enrichment towards the cluster core in cooling-flow

clusters, stemming from ejection of metals from the central galaxies. This could lead to a flattening in the colour profile of the galaxies themselves as we move radially outward. The observed gradient here, although weak, supports the non-cooling flow nature of MS0451.

7.2 The Kormendy Relation and Faber-Jackson Relation

The KR and FJR for MS0451 differ in their magnitude offsets relative to the Coma reference sample at the 2.1σ level. This is the same discrepancy found for Abell 1689 (Houghton et al., 2012). After correcting the data for size-evolution, the KR and FJR indicate that the galaxies in MS0451 are brighter in the F814W band than the Coma galaxies in rest-frame r', by 0.33 ± 0.23 mags (taking the average of the two $\Delta\beta$ values), suggesting an average formation redshift of the galaxies of $1.7^{+\infty}_{-0.6}$ and an age of $9.8^{+4.5}_{-1.69}$ Gyrs. The inclusion of size evolution agrees with other studies that incorporate it, particularly in the KR, with $\zeta \approx 1$ (Longhetti et al., 2007; van der Wel et al., 2008; Saglia et al., 2010). The FJR is in agreement with previous works, but exhibits slightly weaker evolution than has been found in some high-redshift studies, with $\eta \approx 0.3$ (Cenarro & Trujillo, 2009; Saglia et al., 2010). Houghton et al. (2012) highlight several mechanisms that could play a part in the size-evolution of the members of Abell1689. The effects of adiabatic and cosmological expansion may be drivers of size evolution in MS0451, along with gradual accretion processes. In addition, the ICM of MS0451 is particularly dense and acts to rapidly curtail star formation across the central 1 Mpc of the cluster, with strong quenching and evidence of ram-pressure stripping occurring within the central 0.6 Mpc (Geach et al., 2006; Moran et al., 2007b). This may help to explain the slower size evolution in the FJR (or σ) for the MS0451 sample. The ram-pressure stripping of the disks, as passive spirals enter the dense central ICM, would leave ETGs with lower central σ than ETGs formed through other processes (e.g. mergers, accretion).

7.3 The Fundamental Plane

We have found that the FP for MS0451 is offset and rotated relative to the FP of the local reference sample in Coma. When interpreted as the relation between M/L and Mass, the galaxies in MS0451

follow a steeper gradient than the local sample. The evidence for downsizing in MS0451 was first presented by Moran et al. (2007b). We have quantified the slope here, with improved GMOS-N spectroscopy, and we see that the increase in FP tilt in rich clusters, at high-z, discovered by Jørgensen et al. (2006), is seen at $z = 0.55$ over a mass range spanning an order of magnitude ($\sim 10^{10.8} - 10^{11.8}M_{\odot}$). The slope is shallower than the cluster samples at $z = 0.8 - 0.9$ (clusters RX J0152.7-1357 and RX J1226.9-3332) in the previous work. The $\Delta \log M/L$ value obtained at a fixed mass translates directly to a magnitude offset. Thus, the different slopes for MS0451 and Coma indicate a magnitude offset of -0.78 mags for the lowest mass members of the high-z sample ($10^{10.8}$M$_{\odot}$) and an offset of < -0.28 mags for the highest mass members ($> 10^{11.8}$M$_{\odot}$). These correspond to formation redshifts around 0.8 and > 1.7 respectively. We find a lower scatter in $\log M/L$ for MS0451 than Moran et al. (2007b), but it is still higher than that in the local Coma Cluster. This may indicate different formation histories for different cluster members, again depending on the action of the dense ICM. When accounting for the mass-limit on our high-z sample, we see that the evolution in the FP tilt is still evident.

We also fit the FP for the size-evolution corrected data. Taking the coefficients derived from the KR and FJR, we find that the offset in the FP (after fixing the slope to that of the local Coma sample) indicates the galaxies in MS0451 are $0.28^{+0.03}_{-0.09}$ mags brighter in the F814W filter than the Coma galaxies in rest-frame r'. This is in agreement with the KR and FJR derived offsets (derived by the DLM). The mass-dependent offsets (from the $\log M/L$ v Mass relation) become -059 mags and -0.14 mags for the low and high-mass limits respectively. These indicate formation epochs of around 1.0 and > 2.5 from the BC03 and M05 models. We can apply this to galaxies of mass $10^{11.3}$M$_{\odot}$ for a comparison with the findings of Jørgensen et al. (2006, 2007); Fritz et al. (2009). We see an offset at this mass of -0.37 mags translates to a $z_f \sim 1.6$, indicating a similar formation epoch for members of MS0451 to the equivalent mass members in the higher-z (0.8-1.0) clusters (Jørgensen et al., 2005).

Cluster	z	α	β	ϵ
Coma	0.024	1.24 ± 0.07	-0.81 ± 0.02	0.23 ± 0.07
RX J0142.0+2131	0.28	1.29 ± 0.07	-0.83 ± 0.03	0.22 ± 0.08
MS0451.6-0305	0.55	0.80 ± 0.18	-0.76 ± 0.09	0.47 ± 0.09
RX J0152.7-1357 / RX J1226.9+3332	0.83, 0.89	0.66 ± 0.22	-0.70 ± 0.06	0.54 ± 0.07
RXJ1415.1+3612	1.013	-	-	0.54 ± 0.07

Table 7.1: Summary of Fundamental Plane coefficients across the Gemini/HST Cluster Project sample to date. The coefficients for the FP in Fritz et al. (2009) are not provided by the authors.

7.4 MS0451 in the context of Previous Gemini/HST Rich Cluster Studies

The first two studies of the galaxy members of rich clusters as part of the Gemini/HST cluster project found, for the first time, galaxies in intermediate redshift rich clusters (RX J0152.7-1357 and RX J0142.0+2131 at $z = 0.83$ and 0.28 respectively) that could not evolve passively to resemble the galaxy populations in today's rich clusters (Jørgensen et al., 2005; Barr et al., 2005). From the analysis of metal line index realtions, σ and the strength of the 4000Å break, it appeared as though the merger of two sub-clumps was affecting the evolution in both clusters. For RX J0142.0+2131, this interpretation was strengthened through an analysis of the FP of the cluster members (Barr et al., 2006), where the mean stellar ages of galaxies differed depending on location within the cluster, with two distinct regions. They found no dependence on mass of the formation epoch. The analysis of the FP at higher redshift followed, revisiting RX J0152.7-1357 ($z = 0.83$) and including new data on RX J1226.9+3332 ($z = 0.89$) indicated a *rotation* in the FP relation relative to the local sample in Coma (Jørgensen et al., 2006). This was supported by Fritz et al. (2009) through the study of RXJ1415.1+3612 at $z \approx 1$. The conclusions of these studies to date is that none of these clusters could evolve passively, across their entire mass functions, to become a Coma-like cluster at the present epoch. The plots of the FP as viewed in the parameter space of M/L vs Mass are given in Figure 7.1.

The most recent investigation using the GMOS spectroscopy obtained as part of the project is by Houghton et al. (2012) of Abell 1689 at $z = 0.183$. The authors find that this rich cluster could possibly evolve into the local Coma sample. They provide evidence against any large merger

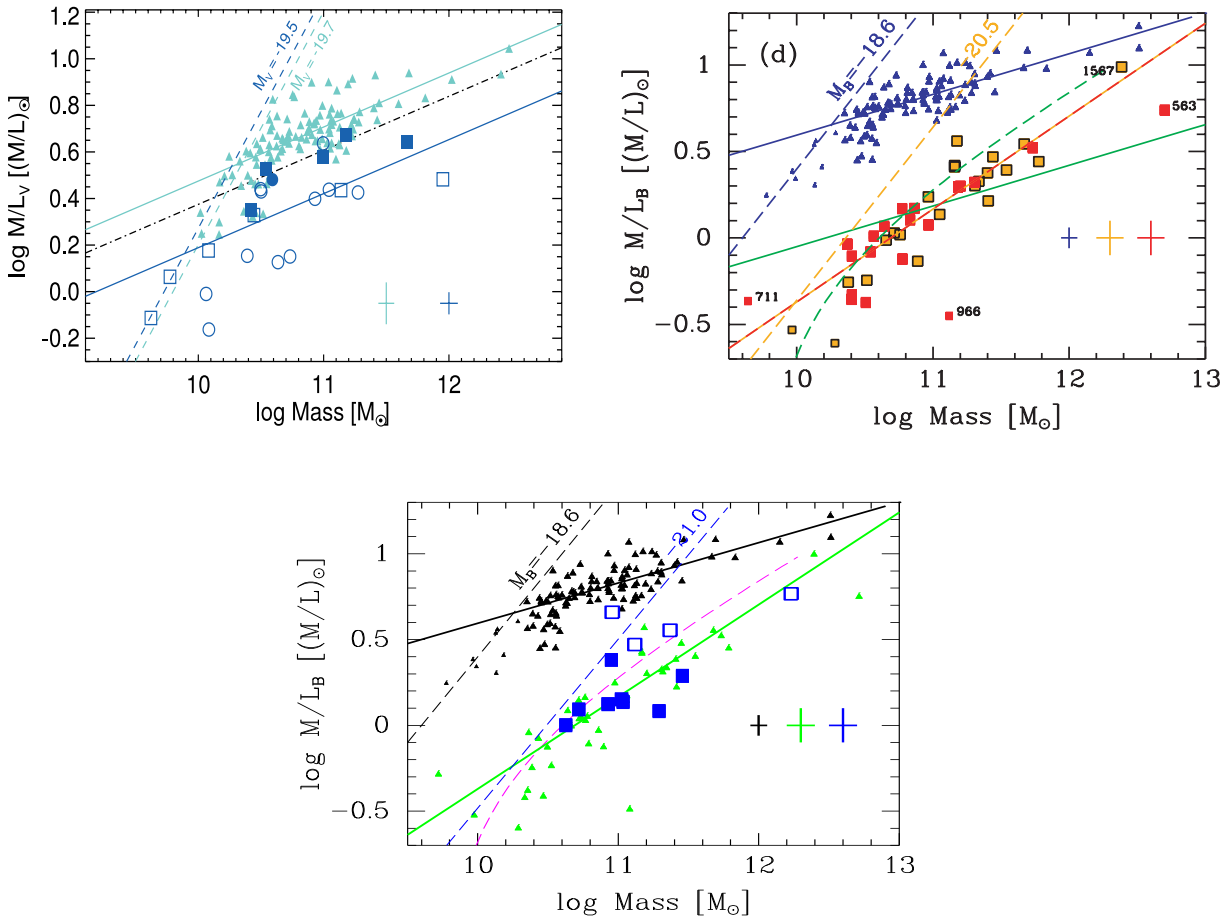

Figure 7.1: The FP for RX J0142.0+2131 ($z = 0.28$, top left), RX J0152.7-1357 & RX J1226.9+3332 ($z = 0.83, 0.89$, top right) and RXJ1415.1+3612 ($z \approx 1$). In each plot, the triangles and solid line of the same colour represent the Coma sample (in the bottom plot, the green triangles represent the high-z sample from Jørgensen et al., 2006). The sources of each of the plots are Barr et al. (2005); Jørgensen et al. (2006); Fritz et al. (2009): top left, top right and bottom plots respectively.

scenarios, with the evolution driven by more gradual processes. The investigation of the FP for Abell 1689 has yet to be concluded.

This series of rich cluster studies is the first to use such high quality spectra over a range of epochs with large samples of galaxies ($\sim$ 30 per cluster). Our investigation of MS0451.6-0305 has produced some interesting results in the context of the specific cluster structure, evolutionary history and is important as an intermediate redshift sample for the study of the evolution of scaling relations in rich cluster environments. The coefficients for the Fundamental Plane of galaxy members of MS0451, along with the coefficients found in previous studies, are given in Table 7.4, highlighting the evolution in the FP tilt. Of the studies so far presented as part of the Gemini/HST cluster project, the investigation of MS0451 is the first to display the evolution of FP tilt in a cluster that is not undergoing some sort of large scale merger event. Speculatively, the galaxy downsizing in this cluster could be explained by AGN activity (quasar mode) in the more massive cluster members, quenching star formation early ($z \sim 3-4$) and keeping the ICM hot through the radio-AGN phase, preventing a cooling flow (Silk, 2011). Small starbursts in the lower mass population could have maintained star formation until more recently ($z_f \sim 1$). Of course, to investigate the star formation history of the cluster members thoroughly, we must analyse their absorption line strengths and scaling relations therein (e.g. Bender et al., 1993; Barr et al., 2005). This is yet to be conducted for MS0451, however the spectra are available for future work.

7.5 Caveats

Here I present some caveats for our work on the various scaling relations of MS0451.

7.5.1 Outliers

Galaxies 12 and 1491 (see Figures 6.4 and 6.6) had poor photometry & spectroscopy respectively, appearing as potential outliers in the KR, FJR and FP relations. To test their influence on the conclusions and the robustness of the the fitting, the KR, FJR and FP were fit again without the two galaxies. No variation was seen of the parameters derived with the full sample outside of the errors. Galaxy 12 was located in a noisy part of the HST ACS chip, towards the edge of the field,

and galaxy 1491 had low S/N spectra.

7.5.2 Colour gradients

An important difference between the KR and FJR is that the former is potentially sensitive to internal colour gradients. There is the possibility of this being a source of error in the work presented here, as the F814W observations of MS0451 are approximately rest-frame V-band and the Coma observations are rest-frame r-band. Colour gradients in ETGs cause them to be redder towards the centre (e.g. Vader et al., 1988). Therefore, at bluer wavelengths R_e will be larger. Using the Coma data from Jorgensen et al. (1995a), Houghton et al. (2012) find that R_e in Gunn-g is a mean of $5\pm15\%$ (or a median of 2%) larger than R_e in Gunn-r. Increasing R_e by 5% leads to an apparent magnitude evolution of $\log(1.05) = 0.02$ mag in the KR. Calculating the mean difference between the central colour ($\langle\mu\rangle_e$(g)$-\langle\mu\rangle_e$(r)) and the global colour (g-r) from Coma data, Houghton et al. (2012) find a value of 0.05 ± 0.35 mag. This agrees with the evolution resulting from an increase in R_e of 5% and so the combined effects of the colour gradient in R_e and luminosity cancel to first order. Hence Houghton et al. (2012) do not correct for colour gradients and neither do we for MS0451.

7.5.3 Sample effects

As stated in Section 6.3, Holden et al. (2010) presented an investigation of the FP of the high-z cluster MS 1054-03 at $z = 0.83$. They concluded that there is no sign of evolution in the FP tilt between the present day and $z = 0.83$ and that previous findings of such a change were due to sample effects. They state that corrections must be applied to account for the potential loss to the sample of higher M/L galaxies in the low-mass populations, due to the luminosity limits imposed during selection. The corrections are,

- Weighting the data in the FP fit by the completeness fraction as a function of magnitude.
- Cutting the sample in velocity dispersion at the typical σ for a galaxy at the magnitude limit.

We applied these corrections to the MS0451 data to investigate the affect on our FP results. The completeness fraction $\mathcal{F}$ was taken as,

$$\mathcal{F}_i = \frac{N_{\rm MS0451}(< r'_i)}{N_{\rm GD}(< r'_i)} \tag{7.1}$$

where $N_{\rm MS0451}(< r'_i)$ is the number of cluster members brighter than galaxy i in the r'-band and $N_{\rm GD}(< r'_i)$ is the total number of galaxy detections (using *SExtractor*) brighter than galaxy i in the r'-band. This ranges from $\sim 5\%$ at the magnitude limit ($r' = 23$) up to $\sim 20\%$ for the brightest cluster members.

For the faintest galaxy in our sample, $\log\sigma = 2.17$. Applying a cut at this velocity dispersion left 20 cluster members to go into the FP fit. The fit was carried out as in Section 6.3, weighting by $\mathcal{F}_i$ only and then weighting by the determined errors in combination with $\mathcal{F}_i$. We find $\{\alpha, \beta\} = \{1.14 \pm 0.26, -0.61 \pm 0.06\}$ and $\{1.05 \pm 0.25, -0.76 \pm 0.08\}$, respectively. Although α does increase towards the Coma value when we apply the corrections of Holden et al. (2010), the β value still indicates a change in the FP slope. When converted to the slope of the M/L vs mass representation, we actually see this as a *flattening* of the FP slope.

7.6 Summary and Future Work

I have presented the spectroscopic and photometric reduction methods, results and analysis of an investigation of scaling relations in the rich galaxy cluster MS0451.6-0305, as part of the Gemini/HST cluster project. The results agree with previous findings of a relaxed cluster environment, with evidence, from studies of the FP, of mass-dependence on formation epoch of the galaxy population. The role of size-evolution has been investigated and it is found that without the inclusion of size-evolution corrections, the KR and FJR are inconsistent, possibly placing constraints on the mechanisms at work in the evolution of cluster members.

Work on investigating other scaling relations involving metal line indices such as Hβ, Mgb and $\langle$Fe$\rangle$ with σ and the strength of the 4000Å break would be the next step in understanding the formation histories of the cluster members. The spectra are available for this, but the analysis is potentially involved (see e.g., Barr et al., 2005) and beyond the scope of this Thesis.

The previous clusters studied as part of the Gemini/HST project would be interesting candidates for the investigation of size evolution, as they have larger samples with higher quality spectra than the majority of previous investigations at similar redshifts.

So far, six of the originally selected 15 X-ray clusters have been investigated. The rest of the sample needs to be investigated to continue to constrain the evolution of the global scaling relations and the formation histories of the galaxies in these dense environments. The reduction and fitting routines, set up as part of the investigations of MS0451 and Abell 1689 (Houghton et al., 2012), would aid this process greatly.

Bibliography

Alexov, A., Berriman, G. B., Chiu, N.-M., Good, J. C., Jarrett, T. H., Kong, M., Laity, A. C., Monkewitz, S. M., Tahir-Kheli, N. D., Norton, S. W. & Zhang, A., 2005. The NASA/IPAC Infrared Science Archive (IRSA): The Demo. In P. Shopbell, M. Britton, & R. Ebert, ed., *Astronomical Data Analysis Software and Systems XIV*, vol. 347 of *Astronomical Society of the Pacific Conference Series*, 7.

Baade, D., Balestra, A., Cumani, C., Eschbaumer, S., Finger, G., Geimer, C., Mehrgan, L., Meyer, M., Stegmeier, J., Reyes, J. & Todorovic, M., 2009. NGC-ESO's New General Detector Controller. *The Messenger*, **136**, 20–24.

Bacon, R., Adam, G., Baranne, A., Courtes, G., Dubet, D., Dubois, J.-P., Georgelin, Y., Monnet, G., Pecontal, E. & Urios, J., 1988. The integral field spectrograph TIGER. In *Very Large Telescopes and their Instrumentation, Vol. 2*, vol. 2, 1185–1194.

Bacon, R., Copin, Y., Monnet, G., Miller, B. W., Allington-Smith, J. R., Bureau, M., Carollo, C. M., Davies, R. L., Emsellem, E., Kuntschner, H., Peletier, R. F., Verolme, E. K. & de Zeeuw, P. T., 2001. The SAURON project - I. The panoramic integral-field spectrograph. MNRAS, **326**, 23–35.

Barr, J., Davies, R., Jørgensen, I., Bergmann, M. & Crampton, D., 2005. RX J0142.0+2131. I. The Galaxy Content of an X-Ray-luminous Galaxy Cluster at z = 0.28. AJ, **130**, 445–474.

Barr, J., Jørgensen, I., Chiboucas, K., Davies, R. & Bergmann, M., 2006. The Fundamental Plane in RX J0142.0+2131: A Galaxy Cluster Merger at z=0.28. ApJL, **649**, L1–L4.

Barrientos, L. F., Schade, D. & Lopez-Cruz, O., 1996. Luminosity Evolution in Cluster Galaxies From z=0.41 to z=0.02. ApJL, **460**, L89.

Baugh, C. M., 2006. A primer on hierarchical galaxy formation: the semi-analytical approach. *Reports on Progress in Physics*, **69**, 3101–3156.

Baugh, C. M., Cole, S. & Frenk, C. S., 1996. Evolution of the Hubble sequence in hierarchical models for galaxy formation. MNRAS, **283**, 1361–1378.

Baum, W. A., 1959. Population Inferences from Star Counts, Surface Brightness and Colors. PASP, **71**, 106–117.

Beers, T. C., Flynn, K. & Gebhardt, K., 1990. Measures of location and scale for velocities in clusters of galaxies - A robust approach. AJ, **100**, 32–46.

Beifiori, A., Maraston, C., Thomas, D. & Johansson, J., 2011. On the spectral resolution of the MILES stellar library. A&A, **531**, A109.

Bender, R., Burstein, D. & Faber, S. M., 1993. Dynamically hot galaxies. II - Global stellar populations. ApJ, **411**, 153–169.

Bender, R. & Sagila, R., 2007. Surveying the High Redshift Universe with KMOS. *Astronomische Nachrichten*, **328**, 707–+.

Bender, R., Ziegler, B. & Bruzual, G., 1996. The Redshift Evolution of the Stellar Populations in Elliptical Galaxies. ApJL, **463**, L51–L54.

Bendinelli, O., 1991. Abel integral equation inversion and deconvolution by multi-Gaussian approximation. ApJ, **366**, 599–604.

Bendinelli, O., Parmeggiani, G. & Zavatti, F., 1982. The deconvolution of brightness profiles of galaxies from seeing - Application to M32. Ap&SS, **83**, 239–246.

Bennett, R. J., Davidson, G. H., Rees, P. & Todd, S. P., 2008. Mechanical design and testing of the cryogenic pick-off arms for the VLT KMOS. In *Society of Photo-Optical Instrumentation Engineers (SPIE) Conference Series*, vol. 7018 of *Society of Photo-Optical Instrumentation Engineers (SPIE) Conference Series*.

Berciano Alba, A., Garrett, M. A., Koopmans, L. V. E. & Wucknitz, O., 2007. Highly-magnified, multiply-imaged radio counterparts of the sub-mm starburst emission in the cluster-lens MS0451.6-0305. A&A, **462**, 903–911.

Berciano Alba, A., Koopmans, L. V. E., Garrett, M. A., Wucknitz, O. & Limousin, M., 2010. Radio counterpart of the lensed submm emission in the cluster MS0451.6-0305: new evidence for the merger scenario. A&A, **509**, A54.

Bergmann, M. P., Jorgensen, I., Barr, J., Davies, R. L., Crampton, D., Takamiya, M. & Miller, B., 2003. Galaxy Evolution During Half the Age of the Universe. In *American Astronomical Society Meeting Abstracts*, vol. 35 of *Bulletin of the American Astronomical Society*, 131.08.

Bernardi, M., Nichol, R. C., Sheth, R. K., Miller, C. J. & Brinkmann, J., 2006. Evolution and Environment of Early-Type Galaxies. AJ, **131**, 1288–1317.

Bertin, E. & Arnouts, S., 1996. SExtractor: Software for source extraction. A&A, **117**, 393–404.

Borys, C., Chapman, S., Donahue, M., Fahlman, G., Halpern, M., Kneib, J.-P., Newbury, P., Scott, D. & Smith, G. P., 2004. The nature of a gravitationally lensed submillimetre arc in MS0451.6-0305: two interacting galaxies at z˜ 2.9? MNRAS, **352**, 759–767.

Bouwens, R. J., Illingworth, G. D., Blakeslee, J. P., Broadhurst, T. J. & Franx, M., 2004. Galaxy Size Evolution at High Redshift and Surface Brightness Selection Effects: Constraints from the Hubble Ultra Deep Field. ApJL, **611**, L1–L4.

Bower, R. G., Lucey, J. R. & Ellis, R. S., 1992. Precision Photometry of Early Type Galaxies in the Coma and Virgo Clusters - a Test of the Universality of the Colour / Magnitude Relation - Part Two - Analysis. MNRAS, **254**, 601.

Bruzual, G. & Charlot, S., 2003. Stellar population synthesis at the resolution of 2003. MNRAS, **344**, 1000–1028.

Burch, K., Cliffe, M., Todd, S. & Henry, D., 2006. Infrastructure II Sub-System Design and Analysis Document. *KMOS Design Documentation V1.0*.

Bureau, M., Jeong, H., Yi, S. K., Schawinski, K., Houghton, R. C. W. et al., 2011. The SAURON project - XVIII. The integrated UV-line-strength relations of early-type galaxies. MNRAS, **414**, 1887–1902.

Butcher, H. & Oemler, Jr., A., 1978. The evolution of galaxies in clusters. I - ISIT photometry of C1 0024+1654 and 3C 295. ApJ, **219**, 18–30.

Cappellari, M., 2002. Efficient multi-Gaussian expansion of galaxies. MNRAS, **333**, 400–410.

Cappellari, M., Bacon, R., Bureau, M., Damen, M. C., Davies, R. L., de Zeeuw, P. T., Emsellem, E., Falcón-Barroso, J., Krajnović, D., Kuntschner, H., McDermid, R. M., Peletier, R. F., Sarzi, M., van den Bosch, R. C. E. & van de Ven, G., 2006. The SAURON project - IV. The mass-to-light ratio, the virial mass estimator and the Fundamental Plane of elliptical and lenticular galaxies. MNRAS, **366**, 1126–1150.

Cappellari, M., di Serego Alighieri, S., Cimatti, A., Daddi, E., Renzini, A., Kurk, J. D., Cassata, P., Dickinson, M., Franceschini, A., Mignoli, M., Pozzetti, L., Rodighiero, G., Rosati, P. & Zamorani, G., 2009. Dynamical Masses of Early-Type Galaxies at z ˜ 2: Are they Truly Superdense? ApJL, **704**, L34–L39.

Cappellari, M. & Emsellem, E., 2004. Parametric Recovery of Line-of-Sight Velocity Distributions from Absorption-Line Spectra of Galaxies via Penalized Likelihood. PASP, **116**, 138–147.

Cappellari, M., Emsellem, E., Bacon, R., Bureau, M., Davies, R. L., de Zeeuw, P. T., Falcón-Barroso, J., Krajnović, D., Kuntschner, H., McDermid, R. M., Peletier, R. F., Sarzi, M., van den Bosch, R. C. E. & van de Ven, G., 2007. The SAURON project - X. The orbital anisotropy of elliptical and lenticular galaxies: revisiting the (V/σ, ϵ) diagram with integral-field stellar kinematics. MNRAS, **379**, 418–444.

Cardelli, J. A., Clayton, G. C. & Mathis, J. S., 1989. The relationship between infrared, optical, and ultraviolet extinction. ApJ, **345**, 245–256.

Cenarro, A. J. & Trujillo, I., 2009. Mild Velocity Dispersion Evolution of Spheroid-Like Massive Galaxies Since z ˜ 2. ApJL, **696**, L43–L47.

Ciotti, L., 1991. Stellar systems following the R exp 1/m luminosity law. A&A, **249**, 99–106.

Clark, P., Rees, P. & Team, C. K., 2007. KMOS Pick-Off Sub-System Design and Analysis Document. *KMOS Design Documentation V4.0*.

Conselice, C. J., Bundy, K., Trujillo, I., Coil, A., Eisenhardt, P., Ellis, R. S., Georgakakis, A., Huang, J., Lotz, J., Nandra, K., Newman, J., Papovich, C., Weiner, B. & Willmer, C., 2007. The properties and evolution of a K-band selected sample of massive galaxies at z ˜ 0.4-2 in the Palomar/DEEP2 survey. MNRAS, **381**, 962–986.

Content, R., 1998. Advanced image slicers for integral field spectroscopy with UKIRT and GEMINI. In A. M. Fowler, ed., *Society of Photo-Optical Instrumentation Engineers (SPIE) Conference Series*, vol. 3354 of *Society of Photo-Optical Instrumentation Engineers (SPIE) Conference Series*, 187–200.

Couch, W. J., Ellis, R. S., Sharples, R. M. & Smail, I., 1994. Morphological studies of the galaxy populations in distant 'Butcher-Oemler' clusters with HST. 1: AC 114 AT Z = 0.31 and Abell 370 at Z = 0.37. ApJ, **430**, 121–138.

Cowie, L. L., Songaila, A., Hu, E. M. & Cohen, J. G., 1996. New Insight on Galaxy Formation and Evolution From Keck Spectroscopy of the Hawaii Deep Fields. AJ, **112**, 839.

Davies, R., Agudo Berbel, A., Wiezorrek, E., Ott, T. & Förster-Schreiber, N. M., 2010. KMOS data flow: reconstructing data cubes in one step. In *Society of Photo-Optical Instrumentation Engineers (SPIE) Conference Series*, vol. 7735 of *Society of Photo-Optical Instrumentation Engineers (SPIE) Conference Series*.

Davies, R. I., 2007. A method to remove residual OH emission from near-infrared spectra. MNRAS, **375**, 1099–1105.

Davies, R. L., Allington-Smith, J. R., Bettess, P., Chadwick, E., Content, R. et al., 1997. GMOS: the GEMINI Multiple Object Spectrographs. In A. L. Ardeberg, ed., *Society of Photo-Optical Instrumentation Engineers (SPIE) Conference Series*, vol. 2871 of *Society of Photo-Optical Instrumentation Engineers (SPIE) Conference Series*, 1099–1106.

Davies, R. L. & Birkinshaw, M., 1988. The orientations of the rotation axes of radio galaxies. II - Stellar rotation curves and velocity dispersion profiles. ApJS, **68**, 409–447.

Davies, R. L., Sadler, E. M. & Peletier, R. F., 1993. Line-strength gradients in elliptical galaxies. MNRAS, **262**, 650–680.

Davis, T. A., Bureau, M., Young, L. M., Alatalo, K., Blitz, L. et al., 2011. The ATLAS^{3D} project - V. The CO Tully-Fisher relation of early-type galaxies. MNRAS, **414**, 968–984.

De Filippis, E., Sereno, M., Bautz, M. W. & Longo, G., 2005. Measuring the Three-dimensional Structure of Galaxy Clusters. I. Application to a Sample of 25 Clusters. ApJ, **625**, 108–120.

De Grandi, S. & Molendi, S., 2001. Metallicity Gradients in X-Ray Clusters of Galaxies. ApJ, **551**, 153–159.

de Vaucouleurs, G., 1948. Recherches sur les Nebuleuses Extragalactiques. *Annales d'Astrophysique*, **11**, 247–+.

de Zeeuw, P. T., Bureau, M., Emsellem, E., Bacon, R., Carollo, C. M., Copin, Y., Davies, R. L., Kuntschner, H., Miller, B. W., Monnet, G., Peletier, R. F. & Verolme, E. K., 2002. The SAURON project - II. Sample and early results. MNRAS, **329**, 513–530.

Dials, M. A., Gille, J. C., Barnett, J. J. & Whitney, J. G., 1998. Description of the High Resolution Dynamics Limb Sounder (HIRDLS) instrument. In M. Strojnik Scholl & B. F. Andresen, ed., *Society of Photo-Optical Instrumentation Engineers (SPIE) Conference Series*, vol. 3437 of *Society of Photo-Optical Instrumentation Engineers (SPIE) Conference Series*, 84–91.

Djorgovski, S. & Davis, M., 1987. Fundamental properties of elliptical galaxies. ApJ, **313**, 59–68.

Donahue, M., Gaskin, J. A., Patel, S. K., Joy, M., Clowe, D. & Hughes, J. P., 2003. The Mass, Baryonic Fraction, and X-Ray Temperature of the Luminous, High-Redshift Cluster of Galaxies MS 0451.6-0305. ApJ, **598**, 190–209.

Donahue, M. & Stocke, J. T., 1995. ROSAT Observations of Distant Clusters of Galaxies. ApJ, **449**, 554.

D'Onofrio, M., Fasano, G., Varela, J., Bettoni, D., Moles, M., Kjærgaard, P., Pignatelli, E., Poggianti, B., Dressler, A., Cava, A., Fritz, J., Couch, W. J. & Omizzolo, A., 2008. The Fundamental Plane of Early-Type Galaxies in Nearby Clusters from the WINGS Database. ApJ, **685**, 875–896.

Dressler, A., 1980. Galaxy morphology in rich clusters - Implications for the formation and evolution of galaxies. ApJ, **236**, 351–365.

Dressler, A., Lynden-Bell, D., Burstein, D., Davies, R. L., Faber, S. M., Terlevich, R. & Wegner, G., 1987. Spectroscopy and photometry of elliptical galaxies. I - A new distance estimator. ApJ, **313**, 42–58.

Dressler, A., Oemler, Jr., A., Couch, W. J., Smail, I., Ellis, R. S., Barger, A., Butcher, H., Poggianti, B. M. & Sharples, R. M., 1997. Evolution since Z = 0.5 of the Morphology-Density Relation for Clusters of Galaxies. ApJ, **490**, 577.

Dubbeldam, M., Content, R., Allington-Smith, J. R., Pokrovski, S. & Robertson, D. J., 2000. Integral field unit for the Gemini near-infrared spectrograph. In M. Iye & A. F. Moorwood, ed., *Society of Photo-Optical Instrumentation Engineers (SPIE) Conference Series*, vol. 4008 of *Society of Photo-Optical Instrumentation Engineers (SPIE) Conference Series*, 1181–1192.

Ellis, R. S., Smail, I., Dressler, A., Couch, W. J., Oemler, Jr., A., Butcher, H. & Sharples, R. M., 1997. The Homogeneity of Spheroidal Populations in Distant Clusters. ApJ, **483**, 582.

Emsellem, E., Cappellari, M., Krajnović, D., Alatalo, K., Blitz, L. et al., 2011. The ATLAS^{3D} project - III. A census of the stellar angular momentum within the effective radius of early-type galaxies: unveiling the distribution of fast and slow rotators. MNRAS, **414**, 888–912.

Emsellem, E., Cappellari, M., Krajnović, D., van de Ven, G., Bacon, R., Bureau, M., Davies, R. L., de Zeeuw, P. T., Falcón-Barroso, J., Kuntschner, H., McDermid, R., Peletier, R. F. & Sarzi, M., 2007. The SAURON project - IX. A kinematic classification for early-type galaxies. MNRAS, **379**, 401–417.

Faber, S. M., 1973. Variations in Spectral-Energy Distributions and Absorption-Line Strengths among Elliptical Galaxies. ApJ, **179**, 731–754.

Faber, S. M. & Jackson, R. E., 1976. Velocity dispersions and mass-to-light ratios for elliptical galaxies. ApJ, **204**, 668–683.

Fan, L., Lapi, A., Bressan, A., Bernardi, M., De Zotti, G. & Danese, L., 2010. Cosmic Evolution of Size and Velocity Dispersion for Early-type Galaxies. ApJ, **718**, 1460–1475.

Fernández Lorenzo, M., Cepa, J., Bongiovanni, A., Pérez García, A. M., Ederoclite, A., Lara-López, M. A., Pović, M. & Sánchez-Portal, M., 2011. Evolution of the fundamental plane of $0.2 < z < 1.2$ early-type galaxies in the EGS. A&A, **526**, A72.

Finger, G., Dorn, R. J., Meyer, M., Mehrgan, L., Stegmeier, J. & Moorwood, A. F. M., 2004. Performance of large-format 2Kx2K MBE grown HgCdTe Hawaii-2RG arrays for low-flux applications. In J. D. Garnett & J. W. Beletic, ed., *Society of Photo-Optical Instrumentation Engineers (SPIE) Conference Series*, vol. 5499 of *Society of Photo-Optical Instrumentation Engineers (SPIE) Conference Series*, 47–58.

Frei, Z. & Gunn, J. E., 1994. Generating colors and K corrections from existing catalog data. AJ, **108**, 1476–1485.

Fritz, A., Jørgensen, I., Schiavon, R. P. & Chiboucas, K., 2009. The evolution of cluster early-type galaxies over the past 8 Gyr. *Astronomische Nachrichten*, **330**, 931–+.

Fritz, A., Ziegler, B. L., Bower, R. G., Smail, I. & Davies, R. L., 2003. The Evolutionary Status of Early-type Galaxies in Abell 2390. Ap&SS, **285**, 61–66.

Froud, T. R., Tosh, I. A. J., Edeson, R. L. & Dalton, G. B., 2006. Cryogenic mounts for large fused silica lenses. In *Society of Photo-Optical Instrumentation Engineers (SPIE) Conference Series*, vol. 6273 of *Society of Photo-Optical Instrumentation Engineers (SPIE) Conference Series*.

Geach, J. E., Smail, I., Ellis, R. S., Moran, S. M., Smith, G. P., Treu, T., Kneib, J.-P., Edge, A. C. & Kodama, T., 2006. A Panoramic Mid-Infrared Survey of Two Distant Clusters. ApJ, **649**, 661–672.

Gilmozzi, R., 1999. The first six months of VLT science operations. *The Messenger*, **98**, 25–27.

Gioia, I. M. & Luppino, G. A., 1994. The EMSS catalog of X-ray-selected clusters of galaxies. 1: an atlas of CCD images of 41 distant clusters. ApJS, **94**, 583–614.

Gioia, I. M., Maccacaro, T., Schild, R. E., Wolter, A., Stocke, J. T., Morris, S. L. & Henry, J. P., 1990. The Einstein Observatory Extended Medium-Sensitivity Survey. I - X-ray data and analysis. ApJS, **72**, 567–619.

Gonzaga, S. e. a., 2005. *Advanced Camera for Surveys Instrument Handbook, Version 6.0, (Baltimore:STScI).*

Hogg, D. W., Bovy, J. & Lang, D., 2010. Data analysis recipes: Fitting a model to data. *ArXiv e-prints.*

Holden, B. P., van der Wel, A., Franx, M., Illingworth, G. D., Blakeslee, J. P., van Dokkum, P., Ford, H., Magee, D., Postman, M., Rix, H.-W. & Rosati, P., 2005. The Fundamental Plane of Cluster Elliptical Galaxies at z=1.25. ApJL, **620**, L83–L86.

Holden, B. P., van der Wel, A., Kelson, D. D., Franx, M. & Illingworth, G. D., 2010. M/L_B and Color Evolution for a Deep Sample of M ^{sstarf} Cluster Galaxies at z ˜ 1: The Formation Epoch and the Tilt of the Fundamental Plane. ApJ, **724**, 714–729.

Hook, I. M., Jørgensen, I., Allington-Smith, J. R., Davies, R. L., Metcalfe, N., Murowinski, R. G. & Crampton, D., 2004. The Gemini-North Multi-Object Spectrograph: Performance in Imaging, Long-Slit, and Multi-Object Spectroscopic Modes. PASP, **116**, 425–440.

Houghton, R. C. W., Davies, R. L., Dalla Bonta, E. & Masters, R., 2012. The GEMINI-HST cluster survey of Abell 1689: data and 2D scaling relations. *In prep.*.

Howell, J. R., 1982. *A Catalog of Radiation Heat Transfer Configuration Factors (2nd Edition).*

Hubble, E. P., 1926. Extragalactic nebulae. ApJ, **64**, 321–369.

Jørgensen, I., 2009. Calibration of Photometry from the Gemini Multi-Object Spectrograph on Gemini North. PASA, **26**, 17–30.

Jørgensen, I., Bergmann, M., Davies, R., Barr, J., Takamiya, M. & Crampton, D., 2005. RX J0152.7-1357: Stellar Populations in an X-Ray Luminous Galaxy Cluster at z = 0.83. AJ, **129**, 1249–1286.

Jørgensen, I., Chiboucas, K., Flint, K., Bergmann, M., Barr, J. & Davies, R., 2006. The Fundamental Plane for z = 0.8-0.9 Cluster Galaxies. ApJL, **639**, L9–L12.

Jørgensen, I., Chiboucas, K., Flint, K., Bergmann, M., Barr, J. & Davies, R., 2007. Erratum: "The Fundamental Plane for z = 0.8-0.9 Cluster Galaxies" (<A href="/abs/2006ApJ...639L...9"> ApJ 639, L9 [2006]</A>). ApJL, **654**, L179–L180.

Jørgensen, I., Franx, M., Hjorth, J. & van Dokkum, P. G., 1999. The evolution of cluster E and S0 galaxies measured from the Fundamental Plane. MNRAS, **308**, 833–853.

Jorgensen, I., Franx, M. & Kjaergaard, P., 1992. CCD surface photometry for E and S0 galaxies in the Coma cluster. A&A, **95**, 489–534.

Jorgensen, I., Franx, M. & Kjaergaard, P., 1995a. Multicolour CCD surface photometry for E and S0 galaxies in 10 clusters. MNRAS, **273**, 1097–1128.

Jorgensen, I., Franx, M. & Kjaergaard, P., 1995b. Spectroscopy for E and S0 galaxies in nine clusters. MNRAS, **276**, 1341–1364.

Jorgensen, I., Franx, M. & Kjaergaard, P., 1996. The Fundamental Plane for cluster E and S0 galaxies. MNRAS, **280**, 167–185.

Kelson, D. D., Illingworth, G. D., van Dokkum, P. G. & Franx, M., 2000. The Evolution of Early-Type Galaxies in Distant Clusters. III. M/L_V Ratios in the z=0.33 Cluster CL 1358+62. ApJ, **531**, 184–199.

Kelson, D. D., van Dokkum, P. G., Franx, M., Illingworth, G. D. & Fabricant, D., 1997. Evolution of Early-Type Galaxies in Distant Clusters: The Fundamental Plane from Hubble Space Telescope Imaging and Keck Spectroscopy. ApJL, **478**, L13+.

Kodama, T. & Arimoto, N., 1997. Origin of the colour-magnitude relation of elliptical galaxies. A&A, **320**, 41–53.

Koekemoer, A. M., Fruchter, A. S., Hook, R. N. & Hack, W., 2002. MultiDrizzle: An Integrated Pyraf Script for Registering, Cleaning and Combining Images. In S. Arribas, A. Koekemoer, & B. Whitmore, ed., *The 2002 HST Calibration Workshop : Hubble after the Installation of the ACS and the NICMOS Cooling System*, 337–+.

Kormendy, J., 1977. Brightness distributions in compact and normal galaxies. II - Structure parameters of the spheroidal component. ApJ, **218**, 333–346.

Krist, J., 1995. Simulation of HST PSFs using Tiny Tim. In R. A. Shaw, H. E. Payne, & J. J. E. Hayes, ed., *Astronomical Data Analysis Software and Systems IV*, vol. 77 of *Astronomical Society of the Pacific Conference Series*, 349–+.

Kron, R. G., 1980. Photometry of a complete sample of faint galaxies. ApJS, **43**, 305–325.

Landolt, A. U., 1992. UBVRI photometric standard stars in the magnitude range 11.5-16.0 around the celestial equator. AJ, **104**, 340–371.

Larkin, J., Barczys, M., Krabbe, A., Adkins, S., Aliado, T. et al., 2006. OSIRIS: a diffraction limited integral field spectrograph for Keck. In *Society of Photo-Optical Instrumentation Engineers (SPIE) Conference Series*, vol. 6269 of *Society of Photo-Optical Instrumentation Engineers (SPIE) Conference Series*.

Le Fevre, O., Saisse, M., Mancini, D., Vettolani, G. P., Maccagni, D. et al., 2000. VIMOS and NIRMOS multi-object spectrographs for the ESO VLT. In M. Iye & A. F. Moorwood, ed., *Society of Photo-Optical Instrumentation Engineers (SPIE) Conference Series*, vol. 4008 of *Society of Photo-Optical Instrumentation Engineers (SPIE) Conference Series*, 546–557.

Lehnert, M., Ivison, R., Sharples, R., Bender, R., S. R., Bremer, M. & Ramsay Howat, S., 2003. KMOS Science Case. *Ksci*.

Lewis, I., Tosh, I. & Ferlet, M., 2007. Spectrograph Optics Sub-System Design and Analysis Document. *KMOS Design Documentation V2.0*.

Lewis, I. J., Cannon, R. D., Taylor, K., Glazebrook, K., Bailey, J. A. et al., 2002. The Anglo-Australian Observatory 2dF facility. MNRAS, **333**, 279–299.

Longhetti, M., Saracco, P., Severgnini, P., Della Ceca, R., Mannucci, F., Bender, R., Drory, N., Feulner, G. & Hopp, U., 2007. The Kormendy relation of massive elliptical galaxies at z ˜ 1.5: evidence for size evolution. MNRAS, **374**, 614–626.

Lucey, J. R., Bower, R. G. & Ellis, R. S., 1991. The fundamental plane of cluster ellipticals. MNRAS, **249**, 755–762.

Maier, C., Lilly, S. J., Zamorani, G., Scodeggio, M., Lamareille, F. et al., 2009. The Dependence of Star Formation Activity on Stellar Mass Surface Density and Sersic Index in zCOSMOS Galaxies at $0.5 < z < 0.9$ Compared with SDSS Galaxies at $0.04 < z < 0.08$. ApJ, **694**, 1099–1114.

Maraston, C., 2005. Evolutionary population synthesis: models, analysis of the ingredients and application to high-z galaxies. MNRAS, **362**, 799–825.

Martini, P., Kelson, D. D., Mulchaey, J. S. & Athey, A., 2004. New Results on the AGN Population in Clusters of Galaxies. In R. Mújica & R. Maiolino, ed., *Multiwavelength AGN Surveys*, 413–416.

Masters, R. J., Lewis, I. J., Tosh, I. A. J., Tecza, M., Lynn, J., Watkins, R. E. J., Clack, A., Davies, R. L., Thatte, N. A., Tacon, M., Makin, R., Temple, J. & Pearce, A., 2010. KMOS: assembly, integration and testing of three 0.8-2.5 micron spectrographs. In *Society of Photo-Optical Instrumentation Engineers (SPIE) Conference Series*, vol. 7735 of *Society of Photo-Optical Instrumentation Engineers (SPIE) Conference Series*.

Mei, S., Holden, B. P., Blakeslee, J. P., Ford, H. C., Franx, M., Homeier, N. L., Illingworth, G. D., Jee, M. J., Overzier, R., Postman, M., Rosati, P., Van der Wel, A. & Bartlett, J. G., 2009. Evolution of the Color-Magnitude Relation in Galaxy Clusters at z ˜ 1 from the ACS Intermediate Redshift Cluster Survey. ApJ, **690**, 42–68.

Méndez-Abreu, J., Aguerri, J. A. L., Corsini, E. M. & Simonneau, E., 2008. Structural properties of disk galaxies. I. The intrinsic equatorial ellipticity of bulges. A&A, **478**, 353–369.

Mo, H. J., Mao, S. & White, S. D. M., 1998. The formation of galactic discs. MNRAS, **295**, 319–336.

Moffat, A. F. J., 1969. A Theoretical Investigation of Focal Stellar Images in the Photographic Emulsion and Application to Photographic Photometry. A&A, **3**, 455.

Monnet, G., 1984. Fabry-Perot Spectrographs for Very Large Telescopes / VLT. In M.-H. Ulrich & K. Kjaer, ed., *IAU Colloq. 79: Very Large Telescopes, their Instrumentation and Programs*, 493–+.

Moran, S. M., Ellis, R. S. & Treu, T., 2008. Observing the Transformation of Spirals into S0s in Two z∼0.5 Clusters. In T. Kodama, T. Yamada, & K. Aoki, ed., *Panoramic Views of Galaxy Formation and Evolution*, vol. 399 of *Astronomical Society of the Pacific Conference Series*, 344.

Moran, S. M., Ellis, R. S., Treu, T. & Smith, G. P., 2007a. Reflections of Cluster Assembly in the Stellar Populations and Dynamics of Member Galaxies. In N. Metcalfe & T. Shanks, ed., *Cosmic Frontiers*, vol. 379 of *Astronomical Society of the Pacific Conference Series*, 243.

Moran, S. M., Ellis, R. S., Treu, T., Smith, G. P., Rich, R. M. & Smail, I., 2007b. A Wide-Field Survey of Two z ˜ 0.5 Galaxy Clusters: Identifying the Physical Processes Responsible for the Observed Transformation of Spirals into S0s. ApJ, **671**, 1503–1522.

Moran, S. M., Miller, N., Treu, T., Ellis, R. S. & Smith, G. P., 2007c. Dynamical Evidence for Environmental Evolution of Intermediate-Redshift Spiral Galaxies. ApJ, **659**, 1138–1152.

Morian, H. F., Mackh, R., Mueller, R. W. & Hoeness, H. W., 1997. Performance of the four 8.2-m ZERODUR mirror blanks for the ESO/VLT. In A. L. Ardeberg, ed., *Society of Photo-Optical Instrumentation Engineers (SPIE) Conference Series*, vol. 2871 of *Society of Photo-Optical Instrumentation Engineers (SPIE) Conference Series*, 405–415.

Mosteller, F. & Tukey, J. W., 1977. *Data analysis and regression. A second course in statistics.*

Navarro, J. F., Frenk, C. S. & White, S. D. M., 1996. The Structure of Cold Dark Matter Halos. ApJ, **462**, 563.

Ortiz-Gil, A., Guzzo, L., Schuecker, P., Böhringer, H. & Collins, C. A., 2004. The X-ray luminosity-velocity dispersion relation in the REFLEX cluster survey. MNRAS, **348**, 325–332.

Pasquini, L., Avila, G., Allaert, E., Ballester, P., Biereichel, P. et al., 2000. FLAMES: a multi-object fiber facility for the VLT. In M. Iye & A. F. Moorwood, ed., *Society of Photo-Optical Instrumentation Engineers (SPIE) Conference Series*, vol. 4008 of *Society of Photo-Optical Instrumentation Engineers (SPIE) Conference Series*, 129–140.

Pasquini, L., Avila, G., Blecha, A., Cacciari, C., Cayatte, V. et al., 2002. Installation and commissioning of FLAMES, the VLT Multifibre Facility. *The Messenger*, **110**, 1–9.

Pavlovsky, C. e. a., 2005. *ACS Data Handbook, Version 6.0, (Baltimore:STScI).*

Peebles, P. J. E., 1993. *Principles of Physical Cosmology.*

Poggianti, B., 2004. Evolution of galaxies in clusters. In R. Dettmar, U. Klein, & P. Salucci, ed., *Baryons in Dark Matter Halos.*

Postman, M. & Geller, M. J., 1984. The morphology-density relation - The group connection. ApJ, **281**, 95–99.

Ramsay Howat, S., Rees, P. & Pirad, J. F., 2005a. KMOS Technical Specifications. *KMOS Requirements Documentation V1.0.*

Ramsay Howat, S., Rees, P. & Pirad, J. F., 2005b. KMOS Technical Specifications. *KMOS Spectrograph Requirements Documentation V1.0.*

Ramsay Howat, S., Rees, P. & Pirad, J. F., 2007. KMOS Spectrograph Requirements Specification. *KMOS Requirements Documentation V2.0.*

Rees, P., 2007. KMOS IFU Sub-System Design and Analysis Document. *KMOS Design Documentation V2.0.*

Rees, P., 2011. KMOS Mass Budget. *KMOS Requirements Documentation V1.0*.

Rees, P., Content, R., Dubbeldam, M., Lewis, I., Rolt, S., Todd, S. & Tosh, I., 2008. Management of optical interfaces in the VLT KMOS instrument. In *Society of Photo-Optical Instrumentation Engineers (SPIE) Conference Series*, vol. 7017 of *Society of Photo-Optical Instrumentation Engineers (SPIE) Conference Series*.

Reese, E., 2000. Sunyev-Zel'dovich Determined Direct Distances to High Redshift Galaxy Clusters: Implications for the Hubble Constant. In *American Astronomical Society Meeting Abstracts*, vol. 32 of *Bulletin of the American Astronomical Society*, 119.03.

Renzini, A. & Ciotti, L., 1993. Transverse Dissections of the Fundamental Planes of Elliptical Galaxies and Clusters of Galaxies. ApJL, **416**, L49.

Saglia, R. P., Sánchez-Blázquez, P., Bender, R., Simard, L., Desai, V. et al., 2010. The fundamental plane of EDisCS galaxies. The effect of size evolution. A&A, **524**, A6.

Sarzi, M., Falcón-Barroso, J., Davies, R. L., Bacon, R., Bureau, M., Cappellari, M., de Zeeuw, P. T., Emsellem, E., Fathi, K., Krajnović, D., Kuntschner, H., McDermid, R. M. & Peletier, R. F., 2006. The SAURON project - V. Integral-field emission-line kinematics of 48 elliptical and lenticular galaxies. MNRAS, **366**, 1151–1200.

Scodeggio, M., Giovanelli, R. & Haynes, M. P., 1997. An Economical Technique for the Estimate of Galaxy Distances: The Photometric Fundamental Plane. AJ, **113**, 2087–2093.

Scott, N., Cappellari, M., Davies, R. L., Bacon, R., de Zeeuw, P. T., Emsellem, E., Falcón-Barroso, J., Krajnović, D., Kuntschner, H., McDermid, R. M., Peletier, R. F., Pipino, A., Sarzi, M., van den Bosch, R. C. E., van de Ven, G. & van Scherpenzeel, E., 2009. The SAURON Project - XIV. No escape from V_{esc}: a global and local parameter in early-type galaxy evolution. MNRAS, **398**, 1835–1857.

Sereno, M. & Zitrin, A., 2011. Triaxial strong-lensing analysis of the z > 0.5 MACS clusters: the mass-concentration relation. *ArXiv e-prints*.

Sérsic, J. L., 1963. Influence of the atmospheric and instrumental dispersion on the brightness distribution in a galaxy. *Boletin de la Asociacion Argentina de Astronomia La Plata Argentina*, **6**, 41–+.

Sersic, J. L., 1968. *Atlas de galaxias australes*.

Sharples, R., Bender, R., Agudo Berbel, A., Bennett, R., Bezawada, N. et al., 2010. Recent Progress on the KMOS Multi-object Integral Field Spectrometer. *The Messenger*, **139**, 24–27.

Sharples, R., Bender, R., Bennett, R., Burch, K., Carter, P. et al., 2005. Surveying the High-Redshift Universe with KMOS. *The Messenger*, **122**, 2–5.

Silk, J., 2011. Feedback in Galaxy Formation. In C. Carignan, F. Combes, & K. C. Freeman, ed., *IAU Symposium*, vol. 277 of *IAU Symposium*, 273–281.

Sirianni, M., Jee, M. J., Benítez, N., Blakeslee, J. P., Martel, A. R., Meurer, G., Clampin, M., De Marchi, G., Ford, H. C., Gilliland, R., Hartig, G. F., Illingworth, G. D., Mack, J. & McCann, W. J., 2005. The Photometric Performance and Calibration of the Hubble Space Telescope Advanced Camera for Surveys. PASP, **117**, 1049–1112.

Smith, G. P., 2005. Hubble, Chandra and Keck Constraints on Massive Galaxy Clusters at z=0.2 and z=0.5. In Y. Mellier & G. Meylan, ed., *Gravitational Lensing Impact on Cosmology*, vol. 225 of *IAU Symposium*, 161–166.

Solinger, A. B. & Tucker, W. H., 1972. Relationship Between X-Ray Luminosity and Velocity Dispersion in Clusters of Galaxies. ApJL, **175**, L107.

Spergel, D. N., Lilly, S. J. & Steidel, C., 1997. The Epoch of Galaxy Formation. *Proceedings of the National Academy of Science*, **94**, 2783–2784.

Terlevich, R., Davies, R. L., Faber, S. M. & Burstein, D., 1981. The metallicities, velocity dispersions and true shapes of elliptical galaxies. MNRAS, **196**, 381–395.

Thatte, N., Tecza, M., Clarke, F., Davies, R. L., Remillieux, A. et al., 2010a. HARMONI: a single-field wide-band integral-field spectrograph for the European ELT. In *Society of Photo-Optical Instrumentation Engineers (SPIE) Conference Series*, vol. 7735 of *Society of Photo-Optical Instrumentation Engineers (SPIE) Conference Series*.

Thatte, N., Tecza, M., Clarke, F., Goodsall, T., Fogarty, L., Houghton, R., Salter, G., Scott, N., Davies, R. L., Bouchez, A. & Dekany, R., 2010b. The Oxford SWIFT Spectrograph: first commissioning and on-sky results. In *Society of Photo-Optical Instrumentation Engineers (SPIE) Conference Series*, vol. 7735 of *Society of Photo-Optical Instrumentation Engineers (SPIE) Conference Series*.

Thatte, N. A., Tecza, M., Eisenhauer, F., Mengel, S., Krabbe, A., Pak, S., Genzel, R., Bonaccini, D., Emsellem, E., Rigaut, F. J., Delabre, B. & Monnet, G., 1998. SINFONI: a near-infrared AO-assisted integral field spectrometer for the VLT. In D. Bonaccini & R. K. Tyson, ed., *Society of Photo-Optical Instrumentation Engineers (SPIE) Conference Series*, vol. 3353 of *Society of Photo-Optical Instrumentation Engineers (SPIE) Conference Series*, 704–715.

Thomas, D., Maraston, C. & Bender, R., 2005a. Stellar Population Models with Variable Element Abundance Ratios. *Highlights of Astronomy*, **13**, 189–3.

Thomas, D., Maraston, C. & Bender, R., 2005b. The Epochs of Early-Type Galaxy Formation in Clusters and in the Field. In A. Renzini & R. Bender, ed., *Multiwavelength Mapping of Galaxy Formation and Evolution*, 296.

Thomsen, B., Baum, W. A., Hammergren, M. & Worthey, G., 1997. The Distance to the Coma Cluster from Surface Brightness Fluctuations. ApJL, **483**, L37.

Tolman, R. C., 1930. On the Estimation of Distances in a Curved Universe with a Non-Static Line Element. *Proceedings of the National Academy of Science*, **16**, 511–520.

Tosh, I., 2011. KMOS Lens Barrel Alignment and Testing. *Report by the Optical System Group, RAL Issue 2.0*.

Treu, T., Stiavelli, M., Casertano, S., Møller, P. & Bertin, G., 2002. The Evolution of Field Early-Type Galaxies to z˜0.7. ApJL, **564**, L13–L16.

Tully, R. B. & Fisher, J. R., 1977. A new method of determining distances to galaxies. A&A, **54**, 661–673.

Vader, J. P., Vigroux, L., Lachieze-Rey, M. & Souviron, J., 1988. Three-color surface photometry of a selected sample of early-type galaxies. II - Color gradients. A&A, **203**, 217–225.

Valdes, F., Gupta, R., Rose, J. A., Singh, H. P. & Bell, D. J., 2004. Indo-US library of coude feed stellar spectra (Valdes+, 2004). *VizieR Online Data Catalog*, **2152**, 20251–+.

van de Ven, G., van Dokkum, P. G. & Franx, M., 2003. The Fundamental Plane and the evolution of the M/L ratio of early-type field galaxies up to z˜ 1. MNRAS, **344**, 924–934.

van der Wel, A., Holden, B. P., Zirm, A. W., Franx, M., Rettura, A., Illingworth, G. D. & Ford, H. C., 2008. Recent Structural Evolution of Early-Type Galaxies: Size Growth from z = 1 to z = 0. ApJ, **688**, 48–58.

van Dokkum, P., Franx, M., Kelson, D., Illingworth, G. & Fabricant, D., 2001. Evolution of Early-Type Galaxies in Clusters. In S. Cristiani, A. Renzini, & R. E. Williams, ed., *Deep Fields*, 194.

van Dokkum, P. G., 2001. Cosmic-Ray Rejection by Laplacian Edge Detection. PASP, **113**, 1420–1427.

van Dokkum, P. G. & Franx, M., 1996. The Fundamental Plane in CL 0024 at z = 0.4: implications for the evolution of the mass-to-light ratio. MNRAS, **281**, 985–1000.

van Dokkum, P. G., Franx, M., Kelson, D. D., Illingworth, G. D. & Fabricant, D., 2000. Evolution of Cluster Early-Type Galaxies. *ArXiv Astrophysics e-prints*.

Visvanathan, N. & Sandage, A., 1977. The color-absolute magnitude relation for E and S0 galaxies. I - Calibration and tests for universality using Virgo and eight other nearby clusters. ApJ, **216**, 214–226.

Wardlow, J. L., Smail, I., Wilson, G. W., Yun, M. S., Coppin, K. E. K. et al., 2010. An AzTEC 1.1-mm survey for ULIRGs in the field of the Galaxy Cluster MS0451.6-0305. MNRAS, **401**, 2299–2317.

Wegner, M. & Muschielok, B., 2008. KARMA: the observation preparation tool for KMOS. In *Society of Photo-Optical Instrumentation Engineers (SPIE) Conference Series*, vol. 7019 of *Society of Photo-Optical Instrumentation Engineers (SPIE) Conference Series*.

Wyder, T. K., Martin, D. C., Schiminovich, D., Seibert, M., Budavári, T. et al., 2007. The UV-Optical Galaxy Color-Magnitude Diagram. I. Basic Properties. ApJS, **173**, 293–314.

Zavatti, F., Bendinelli, O., Gatti, M. & Parmeggiani, G., 1991. Deconvolution of HST Images - Simulations with Observed and Analytical PSF. In P. J. Grosbøl & R. H. Warmels, ed., *European Southern Observatory Conference and Workshop Proceedings*, vol. 38 of *European Southern Observatory Conference and Workshop Proceedings*, 179–+.

Ziegler, B. L., Bower, R. G., Smail, I., Davies, R. L. & Lee, D., 2001. The early-type galaxy population in Abell 2218. MNRAS, **325**, 1571–1590.

Ziegler, B. L., Saglia, R. P., Bender, R., Belloni, P., Greggio, L. & Seitz, S., 1999. Probing early-type galaxy evolution with the Kormendy relation. A&A, **346**, 13–32.

Zitrin, A., Broadhurst, T., Rephaeli, Y. & Sadeh, S., 2009. The Largest Gravitational Lens: MACS J0717.5+3745 (z = 0.546). ApJL, **707**, L102–L106.